# Modelling and Performance Evaluation of a Three-phase Capacitive Voltage Sensor Topology

S van der Merwe

Thesis presented in partial fulfilment of the requirements for the degree of

**Master of Science in Engineering**

at the

**University of Stellenbosch**

Supervisor: Prof. H.J. Vermeulen

December 2006

# Declaration

I, the undersigned, hereby declare that the work contained in this thesis is my own original work, and has not previously, in its entirety or in part, been submitted at any university for a degree.

_____ _____

S van der Merwe Date

## Abstract

This research project investigates the design, modelling and application of an open-air capacitive voltage sensor assembly for the measurement of wideband High Voltage signals on three-phase transmission lines. The advantages and disadvantages of conventional methods used to measure these voltages are reviewed and the advantages of the open-air capacitive sensor are established. The main research objective of this project involves extending the application of previously developed single-phase capacitive sensor topologies to three-phase applications. A three-phase set of mobile, compact and relatively inexpensive capacitive voltage sensors for open-air application under overhead transmission lines are designed and constructed, including a data acquisition triggering system for the measurement of transient waveforms. Equivalent circuit models, using a Thévenin equivalent approach, are developed for the three-phase sensor topology and the associated three-phase transmission line configuration. A number of different methods for simplifying the associated Thévenin equivalent impedance and voltage equations are evaluated.

The decoupling of the voltage waveforms measured by the individual sensors for a three-phase transmission line configuration is subsequently examined with the view to derive mathematical relationships for determining the phase conductor voltages from the measured sensor voltages. The performance of the sensor assembly is experimentally evaluated under laboratory conditions as well as field conditions. An outdoor HV test facility, representing a scaled three-phase flat transmission line structure, is developed for evaluation of the three-phase sensor topology in a controlled environment. The methodology for decoupling the phase voltages and reconstructing the phase conductor voltages from the voltages induced on the sensors is evaluated using measured data obtained with this HV test facility. It is shown that the three-phase capacitive voltage sensor topology as applied in the test facility delivers good results for the measurement of three-phase transient voltage waveforms.

## Opsomming

Hierdie navorsingsprojek ondersoek die ontwerp, modelering en toepassing van ‘n opelug kapasitiewe spanningsensor samestelling vir die meting van wyeband hoogspanning seine op driefasige transmissielyne. Die voordele en nadele van konvensionele metodes wat gebruik word om hierdie spannings te meet word bestudeer en die voordele van 'n opelug kapasitiewe sensor word bevestig. Die hoof navorsingsdoelstelling van hierdie projek behels die uitbreiding van die toepassing van vorige ontwikkelde enkelfasige kapasitiewe sensortopologië na driefasige toepassings. 'n Driefase stel van mobiele, kompakte en relatief goedkoop kapasitiewe spanningsensors vir opelug aanwending onder oorhoofse transmissie lyne is ontwerp en gebou, sowel as 'n dataversamelaar snellersisteem vir die meting van oorgangsverskynsels. Ekwivalente stroombaan modelle is ontwikkel, deur gebruik te maak van 'n Thévenin ekwivalente benadering, vir die driefasige sensortopologie en die meegaande driefasige transmissielyn konfigurasie. 'n Aantal verskillende metodes vir die vereenvoudiging van die gepaardgaande Thévenin ekwivalente impedansie- en spanningsvergelykings word ge-evalueer.

Die ontkoppeling van die spanninggolfvorms gemeet deur die individuele sensors vir 'n driefasige transmissielyn konfigurasie word vervolgens ondersoek ten einde wiskundige verbande af te lei vir bepaling van die fasegeleier spannings vanaf die gemete sensorspannings. Die gedrag van die sensorsamestelling is eksperimenteel geëvalueer onder laboratoriumtoestande asook veldtoestande. 'n Buitelug hoëspanning toetsfasiliteit, wat ‘n geskaleerde driefasige plat transmsissielyn struktuur voorstel, is ontwikkel vir evaluering van die drie-fasige sensortopologie in 'n gekontroleerde omgewing. Die metodiek vir ontkoppeling van die fasespannings en hersamestelling van die fasespannings vanaf die spannings geinduseer op die sensors is geëvalueer deur gebruik te maak van gemete data verkry met hierdie fasiliteit. Daar word gewys dat die driefasige kapasitiewe spanningsensor topologie soos aangewend in die toetsopstelling goeie resultate lewer vir die meting van driefasige oorgangspanning golfvorms.

## Acknowledgements

I would like to thank the following individuals and institutions for their contributions and support

- Prof HJ Vermeulen for his guidance and support through this project.
- Ferdinand and Family for all the help in finalising the thesis.
- Dr Melanie Botha for her ideas and support of the project.
- ESKOM for their contribution throughout this project.
- Petrus Pieterse for all the help in the HV Lab as well as with the planning, construction and measurements of the HV Test Facility.
- Fransois Siebrit for all of his support and assistance, especially with triggering system.
- Petro, William, Johnny, Murray and especially Andre for all their effort and skill in the workshop. Without them the construction of the HV Test Facility and the new sensors would not have been capable.
- Mr J.M. Strauss for his support and assistance.
- Dr Holtzhauzen for his comments and help.
- Wilhelm for all his information on HV Towers.
- The University of Stellenbosch for laboratory and other research facilities.
- Andrew Gailbraith for his friendship, ideas and support.
- The Vissers for all their support through my studies.
- My parents for believing in me and providing opportunities.
- Janke for her friendship, inspiration and understanding.

# Table of Contents

**LIST OF ABBREVIATIONS**

| | |
|---|---|
| ACSR | Aluminium Conductor Steel Reinforced |
| BEM | Boundary Element Method |
| CAE | Computer Aided Engineering |
| CM | Common Mode |
| D/I | Differential / Integrating |
| EHV | Extra High Voltage |
| EMC | Electromagnetic Compatibility |
| FEA | Finite Element Analysis |
| GIS | Gas Insulated Switchgear |
| GMD | Geometric Mean Distance |
| GMR | Geometric Mean Radius |
| HV | High Voltage |
| LV | Low Voltage |
| MV | Medium Voltage |
| MVT | Magnetic Voltage Transformer |
| PCB | Printed Circuit Board |
| PVC | Polyvinyl Chloride |
| PD | Partial Discharges |
| RMS | Root Mean Square |
| VFT | Very Fast Transient |
| VT | Voltage Transformer |
| UHV | Ultra High Voltage |

# 1. Project overview

## 1.1. Project motivation

The demand for electric power is increasing rapidly throughout the world. To meet this ever-increasing demand, larger power stations are being built. Transmission lines connect these power stations into an integrated network over an entire country or group of countries. The requirement of power transmission and distribution industries is to provide a reliable, high quality and economical supply. High Voltage (HV) electrical transmission and distribution systems must thus be monitored for metering and protection purposes.

Although modern power systems are very reliable, abnormal operation can result in a poor quality of supply. Many phenomena generate high frequency signals on high voltage lines, such as harmonic distortion, switching-, lightning- and fault transients, partial discharges and corona noise. The location and correction of these faults must happen as fast as possible. Fault location and analysis are thus important parts of power system operation.

The phase voltages on the conductors are important parameters indicating the behaviour of a power system. Conventional methods for measuring these voltages require physical connections to the high voltage source. To prevent discharges at high voltages, these measurement devices must be well insulated. This increases the size and cost of the equipment and thereby limits the number of locations where measuring equipment are installed. Standard voltage transducers also have limited bandwidth as they are designed and specified for 50Hz operation.

In order to address the shortcomings of conventional voltage transducers for the measurement of wideband HV signals, less expensive, mobile HV measuring equipment with very wide measuring bandwidths are required. Recent research has focussed on the development and application of non-intrusive capacitive sensors. Botha [1] researched wideband modelling of capacitive voltage sensors for single-phase, open-air transmission line applications. A mobile, compact and relatively inexpensive differential parallel plate sensor was designed. The differential sensor was a three-element parallel plate sensor (middle element being a separate Faraday cage). Botha [1] proved that this sensor has a very wide bandwidth that facilitates the measurement of high frequency phenomena.

Further research must be done in implementing the single-phase topology investigated by Botha [1] for a three-phase transmission line topology. It is necessary to examine the constraints and

difficulties represented by decoupling the three-phase transmission line waveforms from the three measured sensor voltages. The practical work can be conducted for relatively low frequencies. Once the sensor topology has been successfully studied for low-frequency measurements, the experimental work research can be extended to include high frequency measurements.

## 1.2. Project description

The main research objective of this project involves extending the application of the single-phase capacitive sensor topology developed by Botha [1] to three-phase applications. This implies the following main tasks:

- Development of a three-phase model topology.
- Design and construction of a three-phase sensor assembly.
- Evaluation of the associated model parameters.
- Laboratory and field evaluation of the measuring performance of the three-phase sensor assembly for three-phase topologies.

Equivalent circuit models for the three-phase, three-element sensor topology are derived. These models are then used to develop equations for the Thévenin equivalent voltage and impedance of the topology. This is required to clarify the relationship between the transfer function characteristics of the sensors and the individual parameters defining the sensor topology, as discussed by Botha [1]. The equivalent circuit models formulated are directly derived from the sensor topologies, model approximations and mathematics developed by Botha [1]. The equivalent equations derived for three-phase power systems are however very complex and must be simplified. Different methods and techniques are discussed for simplifying the Thévenin equivalent impedance and voltage equations.

To evaluate the capacitive coupling factors between the sensors and overhead phase conductors the underlying theory of transmission line parameters are reviewed in the literature section. By characterizing the coupling capacitive matrix, the voltage transfer functions between the individual phase conductors and the sensors can be determined. The results, i.e. coupling capacitances, obtained by analytical methods are compared with results obtained by finite-element field software. Finally, different methods are proposed and evaluated for decoupling the waveforms of a three-phase sensor topology to discriminate between the different phase voltages.

Field tests showed that the physical size of the original differential, three-element parallel plate sensor designed by Botha [1] can be reduced, thereby making the sensors more mobile and thus easier to use. Three smaller sensors were therefore designed and constructed for three-phase open-air measurements in the laboratory and in the field. A triggering system was developed to enable the data acquisition system to capture transient waveforms such as switching waveforms on the HV phase conductors.

The characteristics of the three-phase sensor topology, i.e. three capacitive sensors positioned under three phase conductors, were modelled and quantified using analytical methods as well as software packages. The electric field profile underneath three-phase power systems was researched with the view to find the optimal positions for placement of the three sensors.

A high voltage test facility was designed and built for experimental evaluation of the three-phase capacitive voltage measuring topologies and accurate evaluation of the three-element parallel plate sensor models.

### 1.3. Thesis structure

This thesis document has the following structure:

- Chapter 2 presents a literature review on standard HV measuring topologies as well as capacitive voltage sensing techniques. The measurement of electric field strength is discussed as well as the operation of typical AC voltage sensors. A detailed discussion is given on open-air applications of capacitive voltage sensors. Chapter 2 also reviews some basic principles of electrostatic theory. Various limitations in development of capacitive sensors are discussed. Two approaches used in this thesis for determining capacitive coupling, namely analytical and numerical approaches respectively, are discussed. The capacitive sensor assembly as well as the equivalent circuit equations developed by Botha are reviewed in detail.
- Chapter 3 reviews the different approaches for determining the capacitive coupling components in line configurations. The approaches in determining the electric field strength underneath power lines are also discussed. Analytical and numerical methods are evaluated. Two software packages, namely ELECTRO and EMFP are critically reviewed.

- Chapter 4 presents the design and evaluation of the new three-element open-air capacitive sensor assembly. Results are given for field evaluation of the performance of the original sensor developed by Botha for steady-state power line frequencies. The design and construction of a new, smaller sensor are presented and the interface instrumentation used in conjunction with the sensors is discussed. The design of a triggering system to facilitate the measurement of switching transients is presented.
- Chapter 5 evaluates the generic capacitive coupling components for three sensors positioned underneath a three-phase transmission line. Different methods are evaluated for decoupling the measured voltages into phase voltages. Details are given of the application of various software packages used to assist in determining the various capacitive coupling elements.
- Chapter 6 develops the detailed equivalent circuit models for the three-phase topology of three-element parallel plate sensors underneath a three-phase transmission line. The associated Thévenin equivalent voltage and impedance equations are subsequently derived. Different methods to simplify these equivalent equations are also discussed.
- Chapter 7 presents the experimental evaluation of the sensor assembly. Since a controlled environment is required for calibration and evaluation of the sensor assembly, these tests are performed in the HV laboratory. The practical performance of the triggering system is reviewed and the calibration and evaluation of the optical-link interface are discussed. Some results are presented for the three-phase field tests.
- Chapter 8 discusses the development and construction of the high voltage test facility including all research, construction constraints and test procedures. The various single-phase and three-phase tests performed using the test facility are reviewed.
- Chapter 9 presents the final conclusion and recommendations.

Figure 1.1 shows a block overview of the main research activities of project.

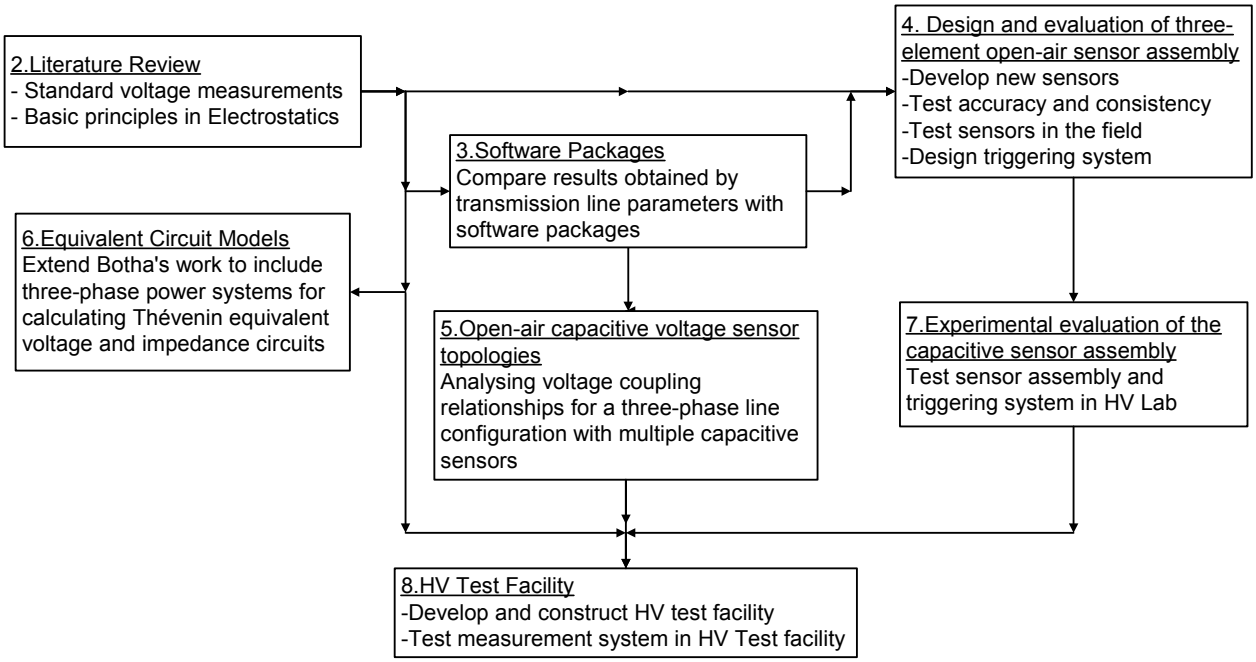


**Figure 1.1: Block diagram overview of research project research activities.**

# 2. Literature Review:

## 2.1. Overview

The objective of this thesis is the research and development of an open-air capacitive high voltage measuring device. The use of open-air, capacitive voltage measurements, on high voltage transmission lines has recently gained popularity. This has resulted in a marked increase in research due to the small size, reliability, safety, good EMC properties and low cost of these methods versus traditional methods

Many techniques have been developed to measure high voltages on power transmission systems. Each technique is suited to a particular application, e.g.

- DC electric-field or voltage measurements
- AC electric-field or voltage measurements
- Partial discharge measurements

As a precursor to this research a background study was done on high voltage and traditional voltage measurement techniques. An outlay of the sections to follow is:

- Section 2.2 **High voltage measurement techniques**: gives an overview of conventional high voltage transducer technologies, emerging high voltage measurement technologies and wideband capacitive sensor topologies.
- Section 2.3 **Electrostatic theory of capacitive sensor design**: gives an overview on different constraints that must be taken into account while designing capacitive sensors.
- Section 2.4 **Capacitive sensor and data acquisition instrumentation developed by Botha**: gives a detailed overview of the three-element sensor developed by Botha [1]

## 2.2. High voltage measurement techniques

### 2.2.1. Conventional high voltage transducer technologies

#### 2.2.1.1. Introduction

This section reviews the conventional high voltage transducer technologies used in electrical power system applications. A description of the available technology, its advantages and disadvantages are given. Although the developed sensors are only used for 50Hz, three-phase power system measurements, future research will focus on measuring high voltage transients. It

is thus necessary to critically evaluate the existing HV transducer principles and equipment in the context of wideband HV measuring applications.

Many authors have contributed to the discussions on conventional voltage transducers, such as Schwab [16], Kuffel & Zaengl [8], Gallagher & Pearmain [17], Botha [1], Gerrard [10] and Naidu and Kamaraju [7]. There are obvious difficulties in measuring voltage and current in high-voltage circuits due to the isolation required between the voltage to be measured and conventional measuring instruments. Voltages can only be measured directly by an absolute electrostatic voltmeter. All other methods, using transformers or potential dividers and low-voltage meters require some calibration with reference to a standard. Research has confirmed the reliability of the flashover voltage in air between spheres as the working standard for calibration [1].

The above mentioned two methods, electrostatic voltmeters and sphere gaps, are illustrated in Figure 2.1(g) and (h). Figure 2.1(g) demonstrates an electrostatic voltmeter, which is primarily a research instrument and not commonly used in commercial power systems [7]. An electrostatic voltmeter utilizes the force existing between oppositely charged plates. The sensor is not electrically connected to the high voltage line, but uses the electric field, produced by the high voltage lines, to exert forces on charged objects. Figure 2.1(g) demonstrates that the device consists out of two parallel plates. One is fixed and the other has a very small movable part that is restrained by a spring. The movable part, to which a mirror is attached, is displaced proportional to the force of attraction created by the applied voltage. An incident light beam will therefore be reflected toward a voltage scale via the mirror. Electrostatic voltmeters have very high internal resistance and low capacitance. The meters measures direct voltages or the RMS value of alternating voltages and will give accurate measurements up to MHz frequencies. A more detailed description of the electrostatic voltmeter is given by Anis [41].

Figure 2.1(h) demonstrates a sphere gap. When sphere gaps are used in high-voltage measurement, one of the spheres is earthed and the other is connected to the high voltage [41]. Sphere gaps are not able to produce an instantaneous voltage measurement and are usually used for calibration and research purposes only. The unknown high voltage is applied across the spheres and the distance, *d*, is decreased until the air between the spheres breaks down. For a particular test circuit, a relation between the peak voltage, determined by the spark over between the spheres, and the reading of a voltmeter on the primary or input side of the high-voltage source

is established. The breakdown field of air is a function of temperature, humidity and pressure, thus for accurate measurements it is necessary to correct for these factors. This instrument is thus only a research instrument.

Most high voltage measuring techniques are extensions of low voltage methods. For HV measurements, the physical dimensions of the measuring components must be increased to prevent dielectric breakdown. This typically results in increased stray capacitances and leakage inductances. Special construction methods therefore are required to minimize the above mentioned effects. Conventional techniques require that a connection must be made to both the source under test and the ground. Figure 2.1 illustrates the different conventional methods discussed in this section.

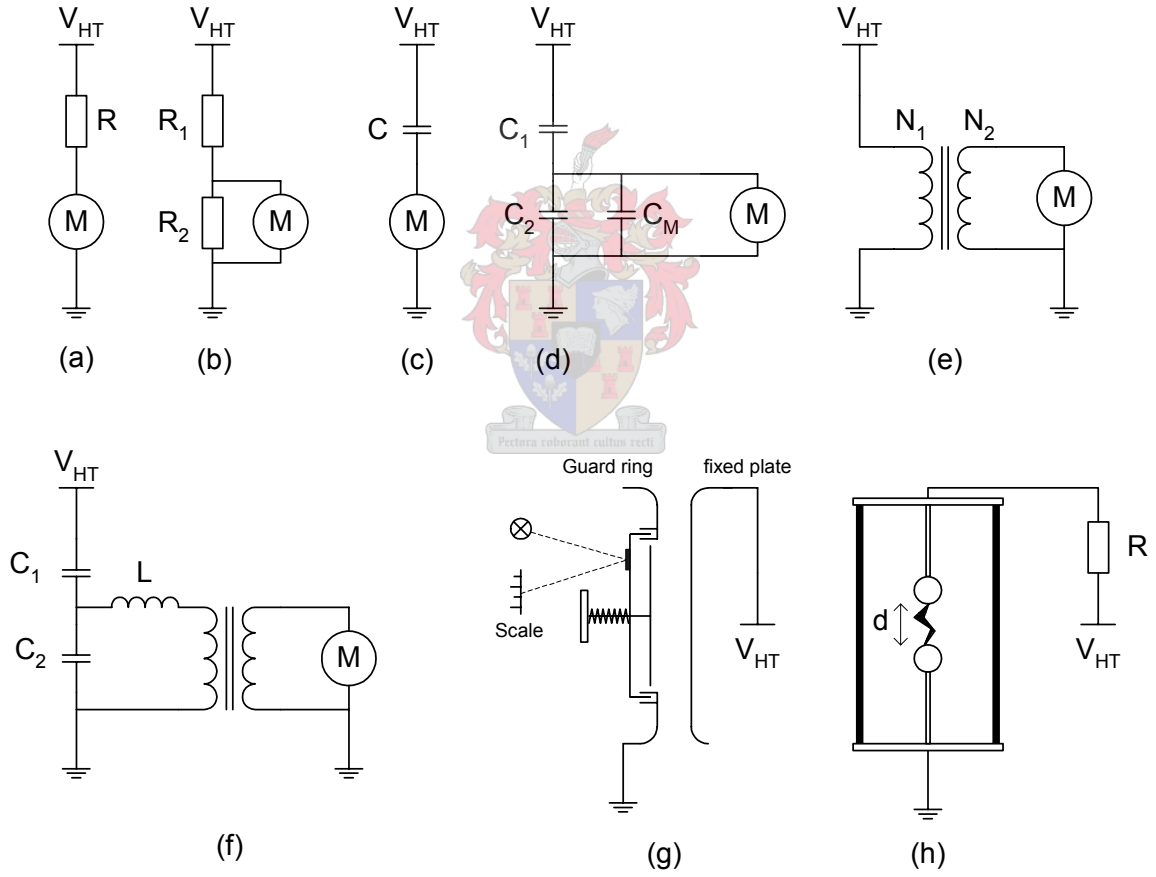


**Figure 2.1: Conventional methods of measuring high voltages [1]. (a) Resister in series with Micro ammeter; (b) resistor divider; (c) capacitive voltage current transformer (d) Capacitive divider (e) Voltage transformer (f) Capacitive voltage transformer (g) Electrostatic voltmeter (h) Sphere gaps.**

Existing high voltage transducer principles and equipment, commonly used in the industry, must be reviewed and discussed in the context of wideband HV measuring applications The following conventional voltage transducers are used in substations to measure AC waveforms:

- Resistive divider devices
- Capacitive divider devices
- Magnetic voltage transformers
- Capacitive voltage transformers

These methods are discussed in the following sections.

#### 2.2.1.2. Resistive devices

Two methods for resistive voltage measurements exist. Figure 2.1(a) illustrates the first method where the high voltage is applied across a large resistance. The current that flows is then measured by the ammeter. This current is proportional to the voltage and calculated by Ohm's law. This method is limited by the availability of high value resistors with suitable temperature coefficients. As current flows through the resistor power is dissipated as heat. If the temperature of the resistor increases, the resistance increase and hence the ratio $I:V_{HT}$ of the device changes.

Using the highest resistive value possible will reduce the current flow through it and hence the heating effect as well. The insulation supporting the resistor has however a finite resistance and current will also flow through it. High resistance units for HV also have stray capacitances which limits the high frequency response. Freedom from corona discharge and improved cooling may be achieved by immersing the resistor in insulating oil [41].

For the second method, two resistors are used in a divider arrangement as illustrated in Figure 2.1(b). If the current drawn by the voltmeter, V, is small, the heating effects in both resistors will be similar and the effect of the temperature variations will be minimized. To limit the electrical field effect around the resistors, large dimension resistors are required. This is commonly achieved by constructing chains of smaller resistive elements [8]. These electric fields are produced by the high voltage and should not exceed the breakdown voltage of the resistor material or the surrounding medium. Insulation resistance is largely determined by surface conditions which vary with deposits on the surface, changes in humidity and other environmental conditions. For AC or transient excitation the distributed capacitances ("stray"), between the nodes on the resistors and ground, result in a ratio between input and output voltage that changes

with frequency [41]. Resistive dividers are thus not suitable for high frequency alternating voltages and generally used for DC measurements only [10].

Figure 2.2 shows how the effect of stray capacitances is cancelled by screening the resistors. This is accomplished by surrounding the high-voltage resistor with a conducting screen maintained at the mean potential of the resistor. Capacitive currents will flow between the screen and the resistor in one direction within the upper portion of the resistor and in the opposite direction within the lower portion. It is however preferred to divide the resistor into identical smaller units, each containing its own screen that is maintained at the mean potential of the unit. This action poses less risk of flashover between the resistor and the screen extremities [41].

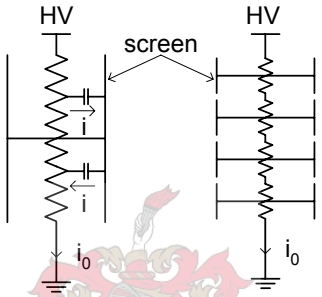


**Figure 2.2: Screened high-voltage resistance by one piece [41].**

Resistance potential dividers suffer from the same disadvantages as series resistance voltmeters for AC applications. Moreover, stray capacitances and inductances associated with the resistances make it inaccurate and compensation has to be provided. Hence, resistance potential dividers are not generally used [7].

### 2.2.1.3. Capacitive devices

For measuring high AC voltages, capacitive voltage to current (V/I) converters and capacitive dividers can be used as illustrated in Figure 2.1(c) and (d) respectively. Figure 2.1(c) illustrates how a series capacitor can be used instead of a resistor for AC high voltage measurements. The relationship between the current, $I$, and the high voltage, $H_{VT}$ is given by

$$I = j\omega C V_{HT} \tag{2.1}$$

where ω is the angular frequency of the voltage. If the frequency changes the ratio $I{:}V_{HT}$ of the device will also change. If the voltage contains harmonics, the ratio will differ for each one producing an error in the indicated RMS value.

The errors due to harmonic voltages can be eliminated by the use of capacitive voltage dividers. Figure 2.1(d) illustrates how two capacitors are used to form a divider. The measuring equipment is connected across the low-voltage capacitor. The relationship between the measured voltage $V_m$ and the high voltage $V_{HT}$ is given by

$$V_m = \left( \frac{C_1}{C_1 + C_2 + C_m} \right) V_{HT} \tag{2.2}$$

where $C_m$ is the capacitance of the meter, connecting cable and leads. The input capacitance of the measuring instrument must thus be taken into account, as it influences the dividing ratio of the divider. As with the resistive divider, stray capacitances exist between the terminals and ground, but these stray components mostly influence the high frequency behaviour of the voltage divider. If these capacitances are small compared to the capacitances of the divider their influence on the response of the device is negligible.

The response of the capacitive dividers, particular for measurement of transient voltages, has been greatly improved [16, 18, 3 and 20]. High voltage capacitors can be either screened or unscreened. Screening capacitors with parallel-plate electrodes (by enclosing it in a metal case) is one method where voltages up to 30kV (peak) can be measured. When the metal case is filled with dried gas, the capacitor has almost a zero power-factor and a highly stable value of capacitance. At higher voltages a capacitor with coaxial cylindrical electrodes may be used as the high-voltage component. The outer cylinder is flared at the ends to avoid discharges. The capacitor can function with voltage gradients at the inner electrode surface of about 14kV/cm peak without partial discharges at atmospheric pressure and with smooth clean electrode surfaces. If the gas pressure is increased higher voltage gradients can be obtained [41].

The two main drawbacks of resistive dividers, power losses and stray capacitance to earth, limit their use to voltages below 100kV at 50 Hz and even lower voltages at higher frequencies. Capacitive potential dividers are therefore more suitable to use with AC voltages, particular at high voltages and high frequencies. Capacitive potential dividers are limited only by their internal inductances or the dielectric losses of their components [41].

#### 2.2.1.4. Magnetic voltage transformers

Magnetic voltage transformers (MVT) are the oldest devices for high voltage AC measurements. Figure 2.1(e) illustrates how the primary winding is connected to the high voltage to be measured

and the secondary winding is connected to an AC voltmeter. Voltage and phase angle errors can be caused by the magnetizing and leakage impedances of the transformer windings. These errors can be compensated for by adjusting the turn-ratio with the tappings on the HV side under load conditions [7].

MVT do not permit fast rising transients or high frequency voltages along with the normal supply frequency, but harmonic voltages are usually measured with sufficient accuracy. The MVT thus has a low bandwidth, typically a few kHz, with a deteriorating response for higher frequency components [1]. At high voltages the amount of insulation between the two windings and the number of turns required on the primary winding result in large physical size and hence cost.

#### 2.2.1.5. Capacitive voltage transformers

Figure 2.1(f) illustrates how a capacitive divider and a MVT can be combined to form a capacitive voltage transformer (CVT). By combining a capacitive divider, with $C_1$ and $C_2$ as the high and low voltage arms respectively, in conjunction with a magnetic voltage transformers, the problem of constructing a sensor for high voltages, which are able to connect to low impedance loads, is overcome. The voltage divider is used to reduce the voltage (intermediate voltage) while a transformer across the low voltage capacitor reduces the intermediate voltage even further. A transformer of moderate size and cost can then be used for this purpose. This arrangement is often used in transmission networks to monitor the line voltage and connect the power line communications to the HV line. Capacitive voltage transformers work well at their designed operating frequency but if the frequency changes the response of the device changes [21]. These sensors are commonly used as a measuring device for meter and relaying purposes [7].

#### 2.2.1.6. Conclusion

Table 2.1 lists some of the most common methods of measuring high voltage, discussed in the above sections, together with the modes of usage.

The traditional voltage transducers, discussed in this section, have the following shortcomings:

- The equipment is expensive.
- The equipment is large and bulky.
- Most of the transducers are limited to certain voltages.
- The transducers have limited bandwidth when used in the standard configurations.

- These transducers are intrusive as some form of impedance is connected to the HV [1].

**Table 2.1: Methods of measuring high voltages.**

| Method of measurement | DC | | AC | | | Impulse | |
|---|---|---|---|---|---|---|---|
| | Mean | Peak | rms | Peak | Waveform | Peak | Waveform |
| Resistor in series with milliameter | x | | x | | | | |
| Reistive divider | x | x | x | x | x | x | x |
| Capacitive divider | | | x | | x | | x |
| Voltage transformer | | | x | x | x | | |
| Electrostatic voltmeter | x | | x | | | | |
| Sphere gaps | | x | | x | | x | |
| Peak voltmeter | | | | x | | | |

Most of these transducers operate well at their designed operating frequency but if the frequency changes the response of the device normally changes. Thus, for low frequency measurements these voltage sensors are ideal and are commonly used for metering. Alternative methods must however be found for optimal wideband measuring.

### 2.2.2. Emerging high voltage measurement technologies

Optical sensing is an alternative form for measuring HV. Optical fibre allows the transmission of optical energy over a flexible dielectric filament efficiently over long distances. This provides a convenient method of transmitting signals from high voltage to ground and vice versa. The cost-effective production of optical fibres in the late 1970's lead to the development of a large number of sensors for measuring voltage, current and temperature on power systems. Many of these techniques have been reviewed by Moghisi [23] and Pilling [24]. As the physical connection between the high voltage system and earth provides a potential discharge path, insulators have to be fitted to the fibre to guard against surface tracking on the fibre resulting in a flash over. This increase the size and cost of the fibre.

Optical fibre is usually installed on the high voltage line and the processing instrument placed at ground potential. Two categories may be used to classify sensors namely active (hybrid) and passive.

*Active (hybrid) sensors* contain conventional electronics and sensors and the value of the measurement is transmitted to ground via an optical fibre. These sensors required a source of electric power to supply the electronics in the sensor. For short term testing, batteries have been used, but any device attached to a high voltage power system must have a high reliability and be

maintenance free, battery power is thus not possible. Long term methods of powering the sensor have been reported by Moulton [25] and Casper & Neuman [26]. Moulton describes a line powered current sensor where the line passes through a coil in the sensor. As current flows through the line a secondary current is induced in the coil which is used to power the sensor electronics. Casper and Neuman used an optical energisation scheme to transmit optical energy to the sensor through an optical fibre. Photo-diodes convert this to electrical energy which is used to power the sensor electronics. Optical energisation offers the advantage that the sensor operates with zero line current.

An optical hybrid voltage and current sensor, using a capacitive divider to determine voltage, has been reported by Pilling [24]. Distributed capacitances exist between the conductor and internal electronics. A second capacitance exists between the case of the sensor and ground. A capacitor was connected between the conductor and the case and a signal proportional to the line voltage developed across it. To measure the line current, a current transformer was used to provide a signal proportional to the line current. Both signals were encoded using pulse width modulation and transmitted to a receiver at ground potential using two optical fibres. The measured capacitance had to be calibrated for the installation, as it is determined by the environment in which it was installed.

*Passive sensors* use physical characteristics of electric or magnetic fields to modulate an applied light signal. Anisotropic optical materials exist in which the relative index in one plane is determined by an applied electric or magnetic field. If a polarised beam is passed through the material the plane of polarisation will rotate as the refractive index changes. The Pockels and Kerr effects are of interest for voltage measurements, as the rotation is proportional to the electric field for Pockels materials and the square of the field for Kerr materials [27, 41]. Figure 2.3 shows an electro-optical system to measure electrical quantities.

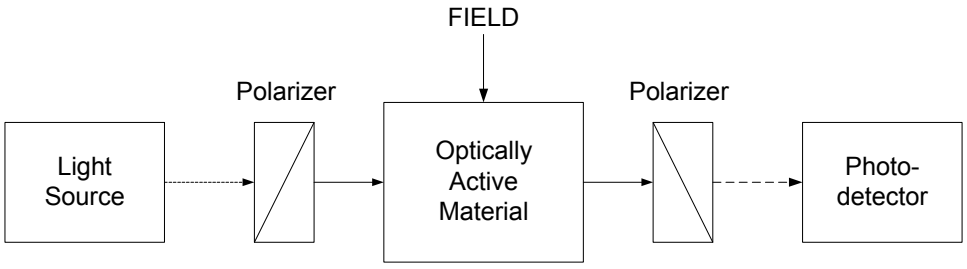


**Figure 2.3: Typical electro-optical measurement system [41].**

The optical material or element must be positioned such that an applied high voltage generates a known field across it. Thus for practical use in a power system, this may be accomplished by placing the sensors between points connected to the high voltage and ground. This type of installation requires insulation both between the sensor and ground and between the sensor and the instrumentation. Optical fibres are used in a power system to address the element from a distance. No reference has been found to the successful implementation on commercial power systems of passive materials, but it has had many implementations in laboratories [28, 29].

Optical sensing has the following drawbacks

- To guard against flash-over the size and cost of the fibre must be increased.
- The sensors are not always maintenance free and require energisation.
- The measured capacitance requires calibration.

### 2.2.3. Wideband capacitive sensor topologies

#### 2.2.3.1. Introduction

In this section AC voltage sensors that work on the principles of electric field strength and capacitive coupling measurements will be discussed. The differential plate sensor developed by Botha falls in this category.

Fixed electrode sensors work on these principles. These sensors are used to measure high voltage and can either be constructed as an integral part of high voltage equipment or as separate units [1]. The fixed electrode sensors can be subdivided into three types, namely the gas-insulated switchgear voltmeters, open-air voltage sensors and open-air electric field strength meters [1].

#### 2.2.3.2. Gas-insulated switchgear

Gas-insulated switchgear (GIS) that uses compressed sulphur hexafluoride ($SF_6$) gas overcomes many of the limitations of the conventional open-type HV switchgear, as it offers the following advantages [41]:

- The space occupied by the switchgear is greatly reduced.
- It is totally unaffected by atmospheric conditions such as polluted or saline air in industrial and coastal areas, or desert climates.
- It possesses a high degree of operational reliability and safety to personnel.
- It is easier to install in difficult site conditions.

- In addition to having dielectric strength much greater than that of air, $SF_6$, has the advantages of being non-toxic and non-flammable.

All these advantages have led to an increase in GIS applications and thus instruments had to monitor these applications. The instruments designed for GIS applications were designed exclusively to measure Very Fast Transients (VFTs) as well as voltage waveforms or partial discharges (PDs) and have bandwidths ranging from a few kHz to hundreds of MHz. Many of the GIS sensors were designed to investigate the breakdown of GIS equipment due to the fact that switching transients are a larger problem in GIS switchgear than in conventional switchgear.

Developments in voltage and current transformers has seen to it that the function of traditional high-voltage current and voltage instrument transformers has been replaced by an advanced generation of current and voltage sensors combining both the functions in a single component. The inductive instrument transformers are being replaced by optical or electrical sensors which reduce the weight and size considerably. For current measurements a Rogowski coil is used [45] which measure the current with the highest precision and without saturation across the entire operating range. The Rogowski coil output is a voltage proportional to the time derivative of the magnetic flux passing through the coil and hence the current in the high voltage lead as well. The voltage is measured by means of a metal-enclosed capacitor voltage divider, which avoids any ferromagnetic resonance. A similar instrument was constructed by Van Deursen *et al* [32] where an integrator is necessary to obtain a copy of the original current waveform. The voltage sensing element is a ring shaped electrode embedded concentrically in the side of the current coil.

Voltages are commonly being measured at the same location as the protective switchgear. Tokoro *et al* [30] report a capacitive divider for attachment to gas insulated switchgear (GIS). A hemispherical conducting probe surrounded by an insulating flange was attached to a port on the GIS. A distributed capacitance exists between the outside of the probe and the bus bar. A second capacitor was connected between the outside of the probe and ground forming the lower arm of a capacitive divider. A conventional electronic system was used to produce a signal proportional to the line voltage. Shielded plates were used in the GIS structure to shield each sensing element from the other phases. From the results reported, the authors conclude the system is suitable for use on live power systems, however no record of its commercial implementation has been found. Hall [31] indicates that this is due to the reluctance of the power system industry to make any modifications to GIS enclosures that may compromise their integrity.

A VFT sensor was designed by Osmokrovi *et al* [33] where the high voltage capacitor is formed by the stray coupling between the GIS bus bar and a ring sensor, which is symmetrical. An integrated approach was taken to prevent oscillations at the higher frequencies.

Botha [1] concluded that the capacitive sensors designed and tested for GIS offers the following advantages:

*It has good EMC properties:*

*the sensors are well-contained and shielded*

*optical data transmission is used*

*D/I principles easily implemented*

*Low cost*

*Small size*

*Simple construction*

*It is clear from the above discussions that capacitive sensors have yielded excellent results for wideband applications in GIS. According to Botha [1], important differences exist between the GIS environment and open-air applications which included the following*

*The physical environment where GIS sensors are implemented are well-defined and confined to small spaces with well-defined ground references*

*Connections to GIS sensors can be made as an integral part of the sensor topology due to the well-defined ground reference, which accounts for the excellent response achieved with D/I galvanic coupling*

*The above advantages unfortunately do not exist in open-air applications [1].*

### 2.2.3.3. Open air applications

Van Heesch [15] describes a low cost, easy to install high-voltage measuring system for open air substations and overhead lines. Three free-standing capacitive pickup electrodes are used to sense the three phase to ground voltages based on the Differentiating/Integrating (D/I) principle. Electrical coupling from all three phases are made with each pickup electrode. After integration the original phase voltages have to be calculated from the measurements done by the three electrodes.

The transported signal of Van Heesch's system is integrated at the input of the measuring cabinet, thus interference pickup is strongly reduced. The coupling between measuring electronics and

common mode currents on signal cables, grounding wires and power supply cables is sufficiently avoided if a special EMC cabinet is used with low transfer impedance between Common Mode (CM) current instruments.

In a fixed geometry of sensors and phase conductors, a matrix of coupling capacitances can be defined and evaluated. The inverse of this matrix, applied to the sensed D/I signals then yields the original phase voltages. Successful application of the system to measure phase voltages in a 380kV GIS substation was reported earlier [19]. The three phase D/I system was applied successfully for substation measurements. High bandwidth transient phenomena and over voltages, as well as the 50Hz power frequency can be measured and due to its linearity the system basically has a very wide dynamic range. Detection of lightning strokes is a particular application for which these sensors could be implemented.

Van Heesch system has a very low cost, simple installation, a large bandwidth, is linear and has excellent EMC qualities.

Feldman *et al* [35] reports the development of an instrument to estimate the potential of a high voltage DC line without a direct electrical contact to either the high voltage line or to ground. An electric field sensor was suspended on an insulating pole and inserted into the field of the conductors. The sensor was calibrated by changing the line potential and recording the sensor output. The incident field on the sensor is a function of position within the field distribution, thus a slight change in the position of the probe would have an effect on the measured electric field. This problem was neutralized by using analytical models to select areas, 'sweet-spots', where the field did not change much with a change in position. By placing a calibrated sensor in a sweet-spot the line potential was successfully estimated to an accuracy of ±10% over a range of 0 to 500kV.

Gerrard [10] implemented a multiple point electric field measurement system for monitoring voltage changes on three-phase power systems. Unshielded electrical power systems generate electric fields which can be measured accurately at distances from conductors that are an order of magnitude greater than typical system dimensions. The field at a particular location and time is a function of the instantaneous voltages on all conductors and depends on the transmission line topology, i.e. conductors and tower structures, as well as objects and structures in the immediate environment.

An array of electric field sensors were installed at ground level below a scale model of such a three-phase bus-bar system. The electric field at each sensor position is shown to be the same as that below a full-size system provided that the dimensions and voltages are scaled in the same proportions. Using the output of the array of sensors the voltages on the individual conductors could be determined, in real time, over an extended period. The deduced voltages agreed with direct measurements obtained using conventional resistive divider networks and particular events occurring on a single conductor were reliably detected.

The above investigation adopts an inverse approach and demonstrates that the voltages on the individual conductors of a three-phase power system can be determined by measuring changes in the electric field distribution at a number of locations remote from the power lines. As the sensor array is not directly connected to the high voltage system, measurements of voltages are made without the use of cumbersome and expensive insulating structures. Hence, Gerrard's technique can be used where cost or physical location difficulties preclude the use of conventional methods.

A system of eight sensors was used to monitor a three-phase power system which had a single set of conductors, as illustrated in Figure 2.4. The sensors were arranged in a linear array orthogonal to the conductor axes and extend over a distance exceeding the conductor spread.

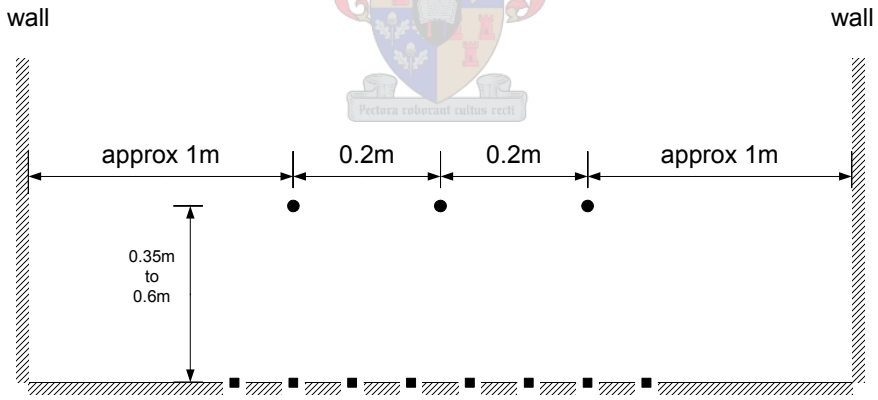


**Figure 2.4: Cross-section of the scale model power system and the sensor array [14].**

Eight sensors were used, as this number was convenient for implementation and data processing and provided a degree of sensor redundancy. Each sensor element consisted of a parallel plate capacitor with one plate exposed to the electric field.

Gerrard demonstrated with the model system that the prototype electric field measuring instrument could successfully monitor the voltages on the individual conductors of a power system.

Differential coaxial voltage sensors were discussed by Shimada, Furukawa & Ohchi [36]. The differential sensors were mounted on the conductor of a 66kV test system. Detailed numerical simulations were performed to determine the expected phase shift between the conductor voltage and the measured voltage for each of the sensors. According to Shimada *et al* [36], each sensor is supposed to detect only a single phase voltage.

Botha [1] developed a differential parallel plate sensor with a floating faraday cage for the interface instrumentation as well as a coaxial sensor mounted around the earth conductor with a faraday cage connected to the earth conductor. Botha also investigated a single element sensor and a differential sensor. According to Botha [1] the single element sensors seem to work well, but the capacitive coupling parameters are very sensitive to the actual coupling of the ground level. The differential sensor, similar to those of Shimada *et al*, will be less sensitive to ground plane variations as the reference is less important in differential topologies. This was an important aspect of the approach followed by Botha [1]. From the three parallel plate sensors discussed by Botha the differential plate sensor with faraday cage (three-element sensor) was declared as the more superior sensor topology.

Botha [1] described the wideband modelling of the above mentioned capacitive voltage sensors. Interface instrumentation was developed with a fibre optic link to obtain a flat frequency response from very low frequencies (less than 5 Hz) to very high frequencies (several MHz). It is important that the interface instrumentation has a high input impedance and that galvanic isolation is maintained. The termination and interface instrumentation (fibre optic link) is placed inside the faraday cage of the three-element sensor. Usually other systems that use optical isolation interfaces employ analogue transmission. Botha however used a digitising topology which offers an improved accuracy and versatility but is more complex and has a high power supply requirement. According to Botha the system has a bandwidth of approximately 6 MHz, with an optional anti-aliasing filter at 1 MHz.

The conclusion reached is that capacitive sensors can be applied effectively in power system applications. This equipment is smaller, cheaper and has wider bandwidth than traditional transducers.

#### 2.2.3.4. Field sensing technologies

DC field measurements will be briefly discussed. Only three sensors are discussed to illustrate the concept of field measurements in a DC environment. Most electric field measuring devices

are based on the principle that the electric field is proportional to the electric flux density *D*. When this changes due to natural phenomena or by mechanical movement, a displacement current occurs. The three sensors are:

- The *passive capacitance probe* is essentially a small disk mounted level with the surface of an electrode or a screen. The device measures the displacement charge induced on the probe surface due to the electric flux density.
- The *electric field mill* consists of a grounded multi-vane rotor turning in front of a multi-segment sensor plate where the grounded rotor alternately exposes the sensor plates to the ambient electrostatic field and shields them. When its sensor plate is shielded its charge is expelled.
- The *free body press* (electrical dipole sensors) normally have no electrical connection to ground. These types of probes generally consist of two electrodes of a specific geometry separated by a small insulating gap.

The principles used for DC electric field measurements are used for AC electric field measurements as well. Different electric field sensors for AC applications have been developed.

A spherical potential-free sensor, i.e. a sensor that is floating, was developed by Feser *et al* [3]. This instrument was used to measure the localised electric field, but the voltage on a nearby HV electrode could also be determined. The accurate measurement of front oscillations on lightning impulses is a major problem in HV impulse measurements. The importance of these oscillations is their effect on the crest voltage and both international [64] and IEEE [65] standards require that the amplitude of oscillations on standard full impulses must be less than 5% of the crest value at crest value. Fortunately, these oscillations usually decay quite quickly. However it is still necessary to measure the oscillations sufficiently accurate to ensure that they have decayed to less than 5% of the crest value.

Damped capacitor dividers are used in many HV laboratories to measure the crest voltage of full impulses to within ±3%. However some variations of damped capacitor dividers are not able to measure front times within the permitted ±10%. McComb [1] indicated that damped capacitor dividers can give sufficiently accurate values of the time parameters even when they do not transmit front oscillations, but independent confirmation is required. A significant contribution towards a solution for this problem has been made by Feser, Pfaff & Weyreter [3], where the electric field probe offered at least ten fold increased bandwidth, measures the two orthogonal

components of the electric field vector, and has a dynamic range which is higher by a few order of magnitudes.

### 2.2.4. Conclusion

As stated by Gerrard [10], all high voltage measurement systems, can be classified into one of three systems:

- Full contact
- No-electrical contact
- Non contact

These classifications depend on the relative position of each of the four components of the sensor, namely:

- High voltage system
- Ground reference
- Sensor
- Instrumentation

*Full contact systems* include all conventional sensors. The sensor is connected to the high voltage system and to the ground reference (the instrumentation is at ground potential) and allows voltage measurements to be made with high accuracy. However the full potential is applied across the sensor and insulation is necessary to prevent breakdowns. As the voltage to be measured increase the physical size, amount of insulation and cost of the device also increases. Development of full contact systems has been limited by the insulation burden. For AC or transient excitation, stray capacitances occur between the resistor/capacitor terminals and ground. The capacitive dividers are sensitive to objects in close proximity, which will increase the stray capacitances. Capacitive voltage transformers have limited bandwidth. According to Botha [1] the bandwidth of the measuring systems may be increased, with limited success, by proper compensation or by using alternative configurations.

*No-electrical contact systems* include optical sensors and devices such as the Nitech power donut [34]. The sensor is physically connected to the high voltage line, but is electrically isolated from both the ground and the instrumentation. The installation burden is reduced by this system because the instrumentation is not connected to a ground reference. This however limits the accuracy with which voltage measurements may be made. Most developments of optical systems

have been for current measurements. Development of hybrid voltage sensors has been limited by the absence of a ground reference and a suitable power supply. Development of passive sensors has been limited by the temperature coefficients of the materials used.

*Non contact systems* include open-air sensors and electric field sensors. No physical contact is made to the high voltage system and the instrumentation is at ground potential. The sensor may be at ground potential or at the potential of the location at which it is placed. The absence of a connection to the high voltage line limits the accuracy with which the measurements are made but the insulation burden of all other methods is removed completely which can result in smaller and potentially cheaper systems.

A variety of methods have been developed to meet the differing requirements of the power industry and the research community. The advantages and disadvantages of the different measuring methods have been discussed and it is clear that capacitive sensors may be applied effectively in power system applications. These sensors fulfil the requirements for smaller and cheaper equipment with wider bandwidths and the sensors can usually be implemented to be non-intrusive.

Conventional voltage measuring sensors worked well for their intended functions, but require large amounts of insulation to ensure safe operation and are usually large and costly.

This literature review clearly showed the relevance of using an open air capacitive voltage sensor, for measurements done in high voltage environments on AC power lines.

## 2.3. Electrostatic theory of capacitive sensor design

### 2.3.1. Introduction

The above literature review stated the relevance of the capacitive voltage sensors. Capacitive sensors can be used for many different applications, i.e. proximity sensing, measurement, switches and communications. The scope of this thesis included the development of a capacitive sensor for implementation underneath a three-phase high voltage transmission line environment. For the design of capacitive voltage sensors certain constraints such as the electrostatics of the sensors required investigation. Capacitive sensors measure the capacitance between two or more conductors in a dielectric environment, usually air or liquid.

Electrostatics is the study of electromagnetic phenomena that occur when there are no moving charges, i.e. after a static equilibrium has been established [12]. The mathematical methods of

electrostatics make it possible to calculate the distributions of the electric field and of the electric potential from a known configuration of charges, conductors and insulators. On the other hand the electric fields in regions between a given set of conductors, as well as the charge distribution on the conductors, can be calculated if the potentials of the conductors are known [71].

Most capacitive sensors use simple planar parallel-plate geometry and do not require expertise in electrostatics. The applications that use non-planar electrode geometry, i.e. Feser *et al* [3], will require more extensive electrostatic field analysis. The sensors used in this project will however consist out of simple planar parallel-plate geometry.

### 2.3.2. Maxwell's Equations

Real-world capacitive sensor designs involve moving charges, partially conducting surfaces and AC potential sources. For an accurate analysis of the fields and currents that constitutes a capacitive sensor, Maxwell's equations, relating electric and magnetic fields, charge density and current density should be used. In differential form Maxwell's equations can be given by

$$\nabla \times \mathrm{E} = -\frac{\partial}{\partial t}\mu_0 \mathrm{H} \approx 0 \ , \tag{2.3}$$

$$\nabla \times \mathrm{H} = \frac{\partial}{\partial t}\varepsilon_0 \mathrm{E} + \mathrm{J} \approx 0 \ , \tag{2.4}$$

$$\nabla . \varepsilon_0 \mathrm{E} = \rho \tag{2.5}$$

and

$$\nabla . \mu_0 \mathrm{H} = 0 \ . \tag{2.6}$$

If at an initial instant, electric and magnetic fields are specified throughout all of a source-free space, Maxwell's equations in their differential form predict these fields as they subsequently evolve in space and time. Fields can exist in regions far removed from their sources because they can propagate as electromagnetic waves [13].

Maxwell's equations describe the most intricate electromagnetic wave phenomena; however the analysis of such fields is difficult and not always relevant. Wave phenomena occurring in short time scales or at high frequencies is often of no practical concern e.g. an electromagnetic wave which propagates through a typical dimension of the system, in a time shorter than the time of interest. In such cases the electrical fields may be described by truncated versions of Maxwell's equations applied to relative long time scales and low frequencies (quasistatics). A quasistatic

system composed of perfect conductors and frequencies is either electroquasistatic (EQS) or magnetoquasistatic (MQS). A detailed discussion of EQS and MQS approximations is given in Haus & Melcher [13].

A power transmission system is at high voltage and can be regarded as EQS. However, once electrical breakdown occur, enough current can flow to bring MQS considerations into play. In so far the power frequencies (50Hz) are concerned, the system is quasistatic. Certain parts of the power system is thus MQS and others EQS, although when lightning strikes it is likely that neither approximation is appropriate. The interplay of the laws of Faraday, Ohm and Ampere is used in EQS and MQS analysis [13].

Capacitive sensors with small geometry and measuring high frequency are prone to electromagnetic interference. The open air capacitive sensors used in this project have a relative large geometry. If low frequencies, i.e. 50Hz, are measured, the effect of electrostatics will play an insignificant role and will virtually be eliminated through the use of a faraday cage in this design. However, for high frequency measurements, expertise in electromagnetics will be required for proper capacitive sensor design.

### 2.3.3. Charges and fields

With the simplified Maxwell equations [13], electrostatic analysis reduces to the discovery of the electric field produced by various charge distributions in systems of materials with various dielectric constants. An electric field exists between two charged objects and the electric field **E** a vector quantity is the gradient of the voltage $V$ and is defined as

$$\mathrm{E} = -\nabla V \,. \tag{2.7}$$

When an electric field is produced in any material a current flows. The total flow of charge due to displacement current through a surface is found by Gauss' law [12, 13].

#### Induced charge

When a positive test charge is brought near a conductor a charge is induced on the conductor. The charges come to an equilibrium in which the repulsive force of the surface electrons is balanced by the attraction of the surface electrons to the test charge. Electric fields inside a conductor are usually negligible if current flow is small, in which case the surface of the conductor is an equipotential surface. An equipotential surface is a surface where the voltages are the same. An electric field outside the conductor but near its surface also has equipotential

surfaces which are parallel to the conductor and lines of magnetic flux which intersect the conductor at right angles. The magnitude of the conductor's surface charge is equal to the flux density of the adjacent dielectric [12].

The effect of induced charge is seen in applications such as capacitive proximity detection. The far-field effects on a capacitive sense electrode must also include the contribution to the E-field of the charge that the electrode induces on nearby floating conductors. Sensors positioning is therefore critical [70].

**Superposition**

As for any linear isotropic system, the principle of superposition can be applied to the electric field analysis. This principle states that the electric field of a number of charges can be calculated as the vector sum of the field due to each individual charge. The field in a system of charged conductors can be determined by assuming all conductors are discharged except one, calculating the resultant field and repeating the process with each conductor and calculating the vector sum. Superposition is thus a very useful and powerful technique for simplifying a complex problem into smaller problems that can be solved independently [12, 66, 68].

**Charge images**

The distribution of charge on conductors can often only be determined with considerable difficulty by calculating the electric field distribution. Kelvin [67] suggested a simple graphical method. A charge, $+q$, in a dielectric near a conducting plane produce a charge density of opposite sign on the nearby surface of the plane. The electric field produced in the dielectric is the same as if the charge density on the surface of the plane was replaced by a single charge, $-q$, inside the plane at a symmetrical location. Figure 2.5 illustrates how the charge image is similar to an optical image in a mirror. Kelvin's [67] result can be derived by looking at the field lines around two charges of opposite polarity and noticing that the line *SS* is, by symmetry, an equipotential surface which can be replaced by a conducting surface as illustrated in Figure 2.6. Then no change in the field structure on the $+q$ side of *S* is seen if the charge $-q$ is replaced with the induced surface charge on the conductor *SS* [12, 68, 70].

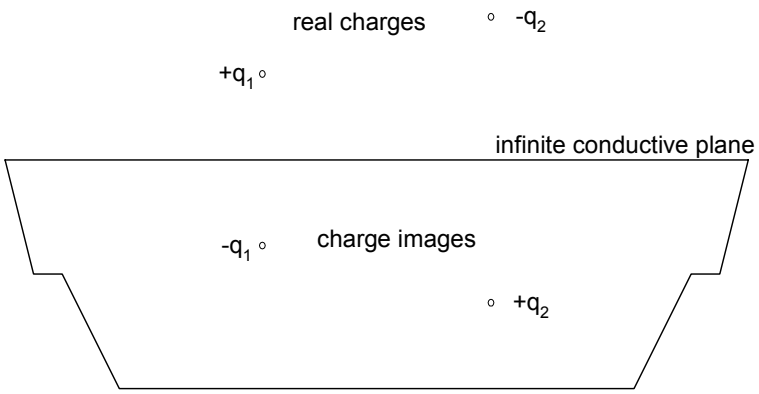


**Figure 2.5 : Charge images [12].**

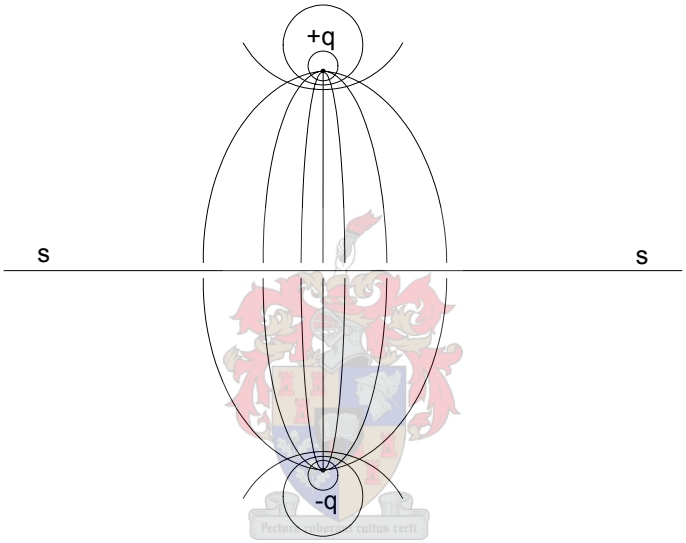


**Figure 2.6 : Fields of opposite charges [12].**

### 2.3.4. Capacitance

For normal parallel plate geometry a voltage $V$ can be applied to the two plates to produce a total flux ψ. The amount of flux in coulombs which is then produced by $V$ volts is given by

$$\psi = Q = CV \quad . \tag{2.8}$$

where $C$ is the capacitance of the plates in coulombs/volt and $Q$ is the charge on the plates. The capacitances for different geometries can be calculated. Baxter [12] provides a detailed discussion on the different methods for calculating the capacitance of various geometries.

### 2.3.5. Approximate solutions

For most capacitive designs, fringe capacitance and stray capacitance can be ignored or approximated without much trouble, but if maximum accuracy is required, or if problems are

encountered with capacitive crosstalk or stray components, it is useful to have an analytical method to evaluate the capacitance of various electrode configurations. Usually it is inconvenient to measure the actual fringe or stray capacitance values, as the strays associated with the measuring equipment are much larger than the strays trying to be measured. Calculating the strays is possible only for simple geometry with spatial symmetry in a given coordinate system, but an approximate solution is generally adequate. Three options that give approximate solutions are field line sketches, Teledeltos™ paper and finite element analysis. Finite element analysis is the only one of these three methods that is used in this thesis and is discussed below.

### 2.3.6. Finite element analysis

Finite Element Analysis (FEA) is appropriate for problems which can be represented by fields which vary smoothly in an area or volume, and which have no direct solution. FEA divides an area into a number of polygons, usually triangles, although squares are sometimes used. The field inside a triangle is assumed to be represented by a low-order polynomial, and the coefficients of the polynomial are chosen to match the boundary conditions of the neighbouring polygons by a method similar to cubic spline curve fitting or polygon surface rendering. The accuracy of the fit is calculated, and in areas where the fit is poorer than a preset constant the polygons are subdivided and the process is repeated. For three-dimensional analysis, the polygons are replaced by cubes and tetrahedrons. This reference shows FEA error compared to analytic solution to be less than 0.18% [12].

FEA has several drawbacks namely [73]:

- Slow response time
- The need for huge amounts of input data
- Inaccurate calculation of derived functions of potential
- Inability to deal with open region problems

### 2.3.7. Boundary element method

The Boundary Element Method (BEM) is a numerical computational method of solving linear partial differential equations which have been formulated as integral equations. It solves field problems by solving an equivalent source problem. In the case of electric fields it solves for equivalent charge, while in the case of magnetic fields it solves for equivalent currents [73].

BEM also uses in integral formulation of Maxwell's equations [13], which allows for accurate field calculations.

The BEM has become more and more popular as it requires calculating only boundary values, rather than values throughout the space defined by a partial differential equation. It is significantly more efficient in terms of computational resources for problems where there is a small surface/volume ratio. Conceptually, it works by constructing a *mesh* over the modelled surface [59]. The matrices generated for the BEM are more complicated than Finite Element Analysis (FEM) for certain amount of elements, but far fewer elements are required as only the boundaries must be discretized, not the entire simulation space [1].

A floating boundary can only be defined by BEM if the boundary is surrounded by a single dielectric. A floating plate must thus be modelled with finite thickness. This increase the complexity of the model and simulation time considerably as the extra volume requires much more elements. Fortunately this is unnecessary when calculating capacitances as no floating boundary conditions are defined then [1].

### 2.3.8. Basics of capacitive sensors

Two basic aspects have to be taken into account during capacitive sensor design namely noise and the stability of the sensor. As the signals to be measured might be very small, the signal to noise ratio is very important. Stability is very important as the sensors will be used in different conditions and over different periods of time.

#### Noise

The input current noise of the amplifier circuit can be a limiting factor in measurement precision in a capacitive sensor. With the high impedance of capacitive sensors, current noise is usually more important than voltage noise however in high capacitance and low frequency applications, current noise is not much of a limiting factor either.

Short duration noise effects, excessive noise in semiconductor junctions, and thermal noise in resistors can affect the actual signal resolution by several orders of magnitude more than voltage and current noise.

**Stability**

The environmental stability of air-dielectric capacitors is quite good. The dielectric constant of dry air at 0˚C and 760 mm pressure is 1.000590, and that of gaseous water (steam) at 110˚C is 1.00785, so the effects of temperature and humidity are minimal. Absolute capacitance measurement is difficult to do accurately, as stray capacitances must be considered. To minimise stray capacitance careful grounding and shielding are required. If stray capacitances are well guarded against, the variation of capacitance due to dielectric constant variation and fringe fields can usually be ignored.

### 2.3.9. Summary:

Correct circuit design will play a very important role in developing a capacitive sensor. The predicted working environment of the sensors should be taken into account when designing the sensor system. As the sensors that will be developed in this project used planar parallel plate geometry, expertise in electrostatics was not required. The principle of superposition and charge images are important techniques that will be used in this project for calculation of the electric fields underneath power systems. Measurement of the capacitance between the different sensor plates will play an important role in this project.

## 2.4. Capacitive sensor and data acquisition instrumentation developed by Botha

### 2.4.1. Introduction

Section 2.2.3 presents the research done by Botha on wideband capacitive sensor topologies. Botha concluded that the three-element parallel plate sensor is the superior sensor of the different topologies presented for measurements underneath a HV transmission line. This section now provides a more detailed discussion on the different topologies for capacitive open air sensors as well as the three-element parallel plate sensor assembly designed and developed by Botha [1].

### 2.4.2. Capacitive sensor assembly developed by Botha

#### 2.4.2.1. Open-air capacitive sensor topologies

Open-air capacitive sensors can be used to accurately monitor high voltage transmission lines for metering and protection purposes. This is achieved by placing the sensor in close proximity and parallel to the ground plane underneath the transmission line. The voltage that is induced on the sensing elements, via the electrostatic induction process, is proportional to the voltage of the HV

conductors. If three-phase transmission lines are monitored, three or more sensors are required in order to decouple the different phase voltages. Section 2.2.3 reviews the advantages of open-air capacitive sensors when compared to conventional voltage transducers.

Figure 2.7(a) illustrates the geometry of the single-element sensor topology. It consists of a single floating conductive plate $s_1$ suspended a height $h$ above a ground plane $g$ underneath a transmission line $l$. Figure 2.7(b) shows a diagram of the capacitive coupling components for this topology. The induced voltage $V_{s1}$ is measured between $s_1$ and $g$ as indicated in Figure 2.7(a). The induced voltage is however very sensitive to changes in $h$ as well as variations in ground conductivity. The single element sensor is simple to analyze and construct.

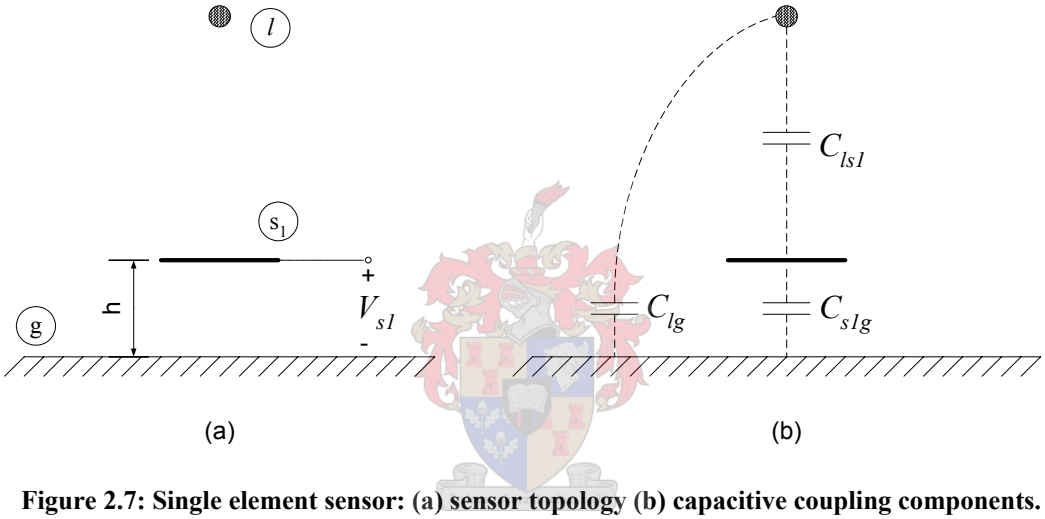


**Figure 2.7: Single element sensor: (a) sensor topology (b) capacitive coupling components.**

A differential parallel-plate sensor topology is suggested to decrease the impact that variations in ground conductivity has on the voltage response of the open-air capacitive sensor. Figure 2.8 illustrates the geometry of the differential sensor topology. It consists of two floating parallel conductive plates $s_1$ and $s_2$ separated a distance $d$ from each other and suspended a height $h$ above a ground plane $g$ underneath a transmission line $l$. Figure 2.8(b) shows a diagram of the capacitive coupling components for this topology. The potential difference $V_{s1s2}$ is measured between $s_1$ and $s_2$. Botha [1] concluded that $V_{s1s2}$ is less sensitive to changes in $h$ as well as variations in ground conductivity if the sensor is placed in close proximity to ground.

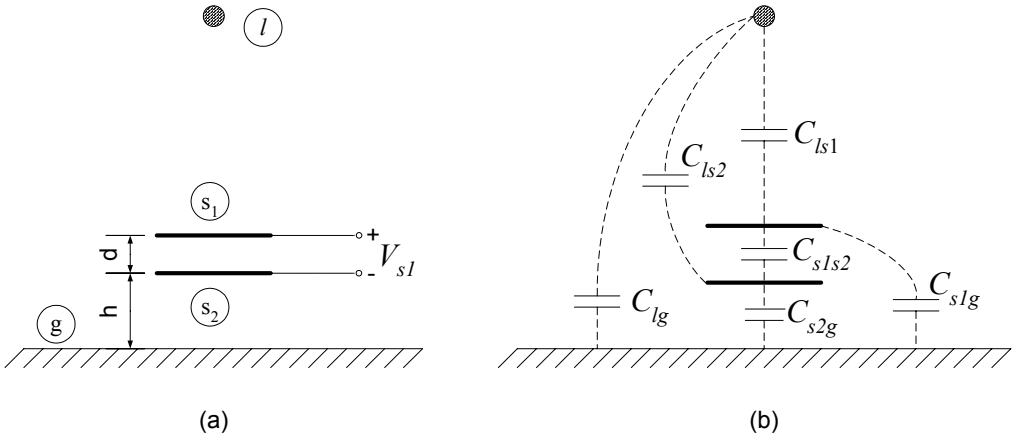


**Figure 2.8: Differential sensor: (a) sensor topology (b) capacitive coupling components.**

A three-element sensor is realised by including a faraday cage in the differential sensor topology. The cage is added as a floating element between the two sensing elements. Figure 2.9(a) illustrates the geometry of the differential sensor including a faraday cage (three-element sensor) topology. It consists of two floating conductive parallel plates $s_1$ and $s_2$ separated a distance $d$ from each other and suspended a height $h$ above a ground plane $g$ underneath a transmission line $l$. The floating conductive faraday cage $s_3$ is inserted parallel between the two plates as shown. Figure 2.9(b) shows a diagram of the capacitive coupling components for this topology. The faraday cage $s_3$ is not a sensing element as the potential difference $V_{s1s2}$ is measured differentially between the top and bottom plates $s_1$ and $s_2$. The instrumentation, i.e. interface instrumentation, used to measure the voltage $V_{s1s2}$ is housed within the faraday cage.

Botha [1] reviewed the main properties, advantages and disadvantages of the three sensor topologies discussed in this section. The following evaluation of the three sensor topologies can be made:

- The single-element sensor is very sensitive to changes in height above the ground plane as well as variations in ground conductivity.
- The differential sensor is less sensitive to ground variations. A faraday cage is still required to house interface instrumentation.
- The three-element sensor has the same robustness than the differential sensor but with the added benefit of a faraday cage inserted between the two sensing plates. Interface instrumentation used to measure the voltage induced on the sensing plates can now be

placed in a known environment which excluded electromagnetic fields from the transmission lines.

It was concluded by Botha that the three-element parallel plate sensor is the superior sensor topology of the three. This sensor has wide bandwidth and is compact, relatively inexpensive and mobile.

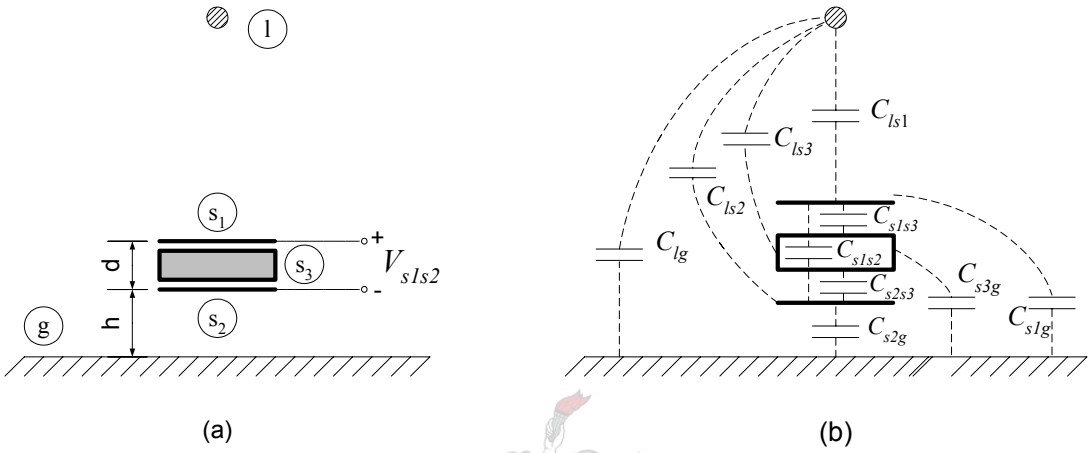


**Figure 2.9: Differential sensor with faraday cage: (a) sensor topology (b) capacitive coupling components.**

The three-element parallel plate sensor is used in this project for capacitive voltage measurements underneath three-phase high voltage transmission lines.

### 2.4.2.2. Equivalent circuit for the three-element sensor

Botha [1] derived and analysed equivalent circuit models for the three-element sensor underneath a single transmission line. A two-dimensional approximation of the sensor topology was made and only resistive and capacitive components were included in these models. All inductive coupling was ignored, as it was assumed that the sensor dimension was electrically small.

Thévenin's theorem was used throughout to determine the equivalent voltage source and impedance to characterise the sensor topologies. The Thévenin equivalent voltage and impedance were both functions of frequency because of the resistive elements in the equivalent circuit models.

If all loss terms were neglected a Thévenin equivalent capacitance was defined. The Thévenin equivalent voltage together with Thévenin equivalent capacitance allowed for easy calculation of the high frequency division ratio or asymptote for any added termination. The low-frequency

cut-off caused by the resistive part of termination impedance could be calculated easily from these equivalent circuit parameters.

Figure 2.9(a) illustrates the geometry of a three-element plate sensor, above a ground plane and underneath a single-phase transmission line. Figure 2.9(b) illustrates the capacitive coupling components of the three-element sensor topology. An equivalent circuit for this sensor geometry can be deduced by arranging the capacitors in circuit format. The shunt loss terms must be included in parallel with the capacitances. The main line capacitance to ground $C_{lg}$ can be omitted as the two systems are completely decoupled and the sensor is regarded as a point element. Figure 2.10 illustrates the resulting circuit where the capacitance and resistance are defined as follows [1]:

| | |
|---|---|
| $C_{ls1}$, $R_{ls1}$ | Capacitance and resistance respectively between the main line and top sensor plate. |
| $C_{ls2}$, $R_{ls2}$ | Capacitance and resistance respectively between the main line and bottom sensor plate. |
| $C_{ls3}$, $R_{ls3}$ | Capacitance and resistance respectively between the main line and faraday cage. |
| $C_{s1g}$, $R_{s1g}$ | Capacitance and resistance respectively between the top sensor plate and ground. |
| $C_{s2g}$, $R_{s2g}$ | Capacitance and resistance respectively between the bottom sensor plate and ground. |
| $C_{s3g}$, $R_{s3g}$ | Capacitance and resistance respectively between the faraday cage and ground. |
| $C_{s1s2}$, $R_{s1s2}$ | Capacitance and resistance respectively between the top and bottom sensor plates. |
| $C_{s1s3}$, $R_{s1s3}$ | Capacitance and resistance respectively between the top sensor plate and the faraday cage. |
| $C_{s2s3}$, $R_{s2s3}$ | Capacitance and resistance respectively between the bottom sensor plate and faraday cage. |

The loss terms between the transmission line and the sensing plates, namely $R_{ls1}$, $R_{ls2}$ and $R_{ls3}$ may be ignored as air is a very good insulator. If the support structure consists of very good insulators, the resistive elements between the sensing plates and ground, namely $R_{s1g}$ and $R_{s2g}$ may be ignored. It is also assumed that the termination resistor $R_t$ is much smaller than $R_{s1s2}$. $R_t$ will therefore dominate the low-frequency behaviour of the transfer function and $R_{s1s2}$ may be ignored as well. The dielectric substrate separating the sensor plates cannot be regarded as a perfect insulator, therefore $R_{s1s2}$ and $R_{s2s3}$ must remain in the model. The Thévenin equivalent voltage and impedance are then calculated between the top and bottom sensing plates.

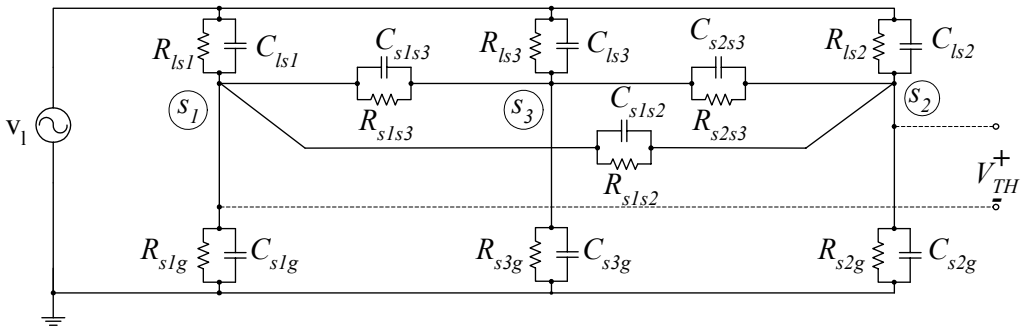


**Figure 2.10: Equivalent circuit model for the three-element sensor topology [1].**

The equations for the high frequency asymptote of the three-element sensor can be derived when all loss terms are ignored and Figure 2.11 shows this equivalent circuit model.

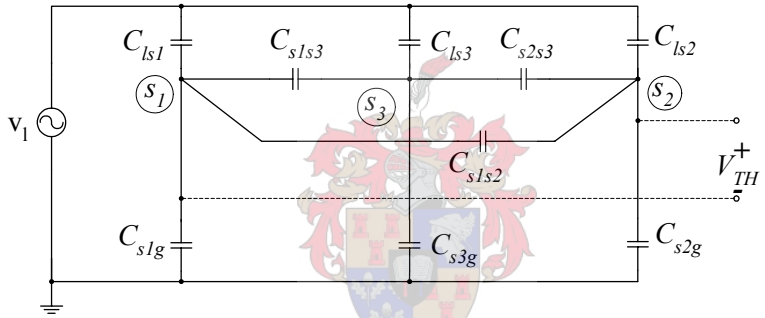


**Figure 2.11: Equivalent circuit model for the three-element sensor topology if all loss terms are omitted.**

Using the notation of Figure 2.11, the Thévenin equivalent voltage of the three-element sensor topology, when all loss terms are omitted, is given by the relationship [1]

$$V_{TH} = V_1 \frac{V_{THn}}{DEN} \tag{2.9}$$

and the Thévenin equivalent impedance is given by the relationship

$$Z_{TH} = \frac{Z_{THn}}{s.DEN} \tag{2.10}$$

where $s = j2\pi f$ and $V_{THn}$ $Z_{THn}$, and $DEN$ are given by the following equations:

$$\begin{aligned} V_{THn} = {} & C_{ls1}\left(C_{s2g}C_{s2s3} + C_{s2g}C_{s3g} + C_{s2g}C_{s1s3} + C_{s3g}C_{s2s3}\right) - \\ & C_{ls2}\left(C_{s1g}C_{s1s3} + C_{s1g}C_{s2s3} + C_{s1g}C_{s3g} + C_{s3g}C_{s1s3}\right) + \\ & C_{ls3}\left(C_{ls1}C_{s2g} + C_{s2g}C_{s1s3} - C_{s1g}C_{ls2} - C_{s1g}C_{s2s3}\right) \end{aligned} \tag{2.11}$$

$$Z_{THn} = \left(C_{s1s3} + C_{s2s3}\right)\left(C_{ls1} + C_{ls2} + C_{ls3} + C_{s1g} + C_{s2g} + C_{s3g}\right) + \left(C_{ls3} + C_{s3g}\right)\left(C_{ls1} + C_{ls2} + C_{s1g} + C_{s2g}\right) \quad (2.12)$$

$$\begin{aligned} DEN = {} & \left(C_{ls1} + C_{ls2} + C_{ls3} + C_{s1g} + C_{s2g} + C_{s3g}\right)\left(C_{s1s2}C_{s1s3} + C_{s1s2}C_{s2s3} + C_{s1s3}C_{s2s3}\right) + \\ & \left(C_{ls1} + C_{ls2} + C_{ls3}\right)\left(C_{s1g} + C_{s2g} + C_{s3g}\right)\left(C_{s1s2} + C_{s1s3} + C_{s2s3}\right) + \\ & C_{s1s2}\left(C_{ls1}C_{s3g} + C_{s2g}C_{ls3} + C_{ls2}C_{ls3} + C_{ls1}C_{ls3} + C_{s1g}C_{s3g} + C_{ls2}C_{s3g} + C_{s2g}C_{s3g} + C_{s1g}C_{ls3}\right) \quad (2.13) \\ & C_{s1s3}\left(C_{s2g}C_{ls3} + C_{ls2}C_{ls3} + C_{s1g}C_{s2g} + C_{s1g}C_{ls2} + C_{ls1}C_{s2g} + C_{ls2}C_{s3g} + C_{ls1}C_{ls2} + C_{s2g}C_{s3g}\right) \\ & C_{s2s3}\left(C_{s1g}C_{s3g} + C_{s1g}C_{s2g} + C_{s1g}C_{ls2} + C_{s1g}C_{ls3} + C_{ls1}C_{ls2} + C_{ls1}C_{s3g} + C_{ls1}C_{ls3} + C_{ls1}C_{s2g}\right) \end{aligned}$$

A Thévenin equivalent capacitance can be defined from this idealised case, denoted by

$$C_{TH} = \frac{DEN}{Z_{THn}}. \quad (2.14)$$

#### 2.4.2.3. Physical design of the three-element parallel plate sensor

Figure 2.12 illustrates the framework of the three-element parallel plate sensor designed by Botha [1]. The sensor had a width of 0.5m, a length of 2m and a height of 0.035m. The framework was constructed from Polyvinyl Chloride (PVC) and Printed Circuit Boards (PCBs) were used for the parallel plates. Two PCBs were placed on either side of the framework. The dielectric between the two plates of the PCB had a thickness of 1.6mm [74]. The distance between the outer plates and the faraday cage was thus 1.6mm.

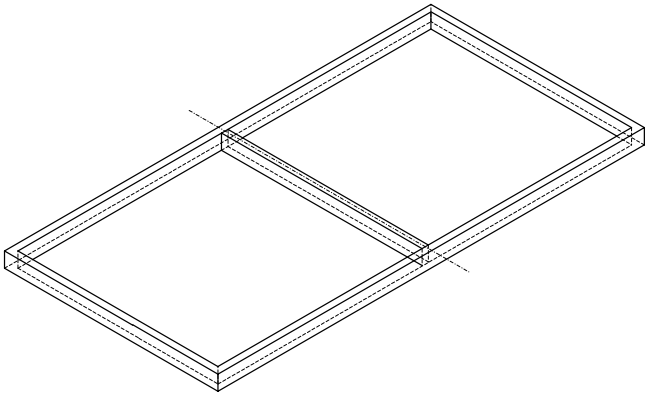

**Figure 2.12: Isometric view of the three-element sensor's structure designed by Botha.**

The Faraday cage was created by connecting the two inner copper plates (inner sides of the two PCBs) with aluminium foil on the inside of the framework. This caused that the cage (formed by the aluminium foil) was interrupted by the inner framework. The aluminium foil also oxidises

easily which can lead to the copper plates not making good contact with the aluminium foil. This can lead to an incomplete Faraday cage.

#### 2.4.2.4. Numerical modelling and analysis

Botha [1] did extensive numerical modelling and analysis of the three-element sensor topology. Botha [1] used the circuit models and Thévenin equivalent parameters to determine time- and frequency domain responses to characterize the topology of the sensors completely. In order to find the output voltage, the termination impedance has to be connected across the Thévenin equivalent circuit. The output voltage $V_{out}$ of the sensor with any arbitrary termination impedance $Z_t$ is given by the relationship [1]

$$V_{out} = V_{TH} \frac{Z_t}{Z_t + Z_{TH}} \tag{2.15}$$

where $Z_{TH}$ and $V_{TH}$ denote the Thévenin equivalent impedance and voltage respectively.

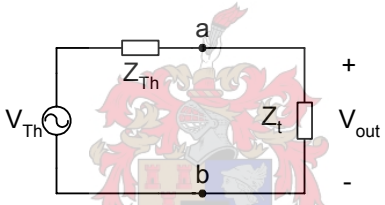


**Figure 2.13: Thévenin equivalent circuit with arbitrary termination impedance [1].**

The termination impedance of the sensor is the input impedance of the interface instrumentation. Capacitances and resistances are both inherent in the input impedance of any buffer or amplifier. In order to increase the division ratio of the sensor topology and lower the pole formed by the parallel connection of $R_t$ and $C_t$, extra capacitances are added in parallel [1].

Botha defined different models with different leakage elements from a mathematical point of view for the three-element sensor topology. The termination resistor $R_t$ was included in the total circuit for all the models. The ideal or default model was defined with no loss term except for the termination resistance. The other models were defined by adding resistors to the default model, presenting the different leakage components. The values that were used for the leakage between the sensor elements and ground were 100MΩ, while 10MΩ was used for the leakage between the different sensing elements and the faraday cage. Botha showed that unbalanced leakage between the sensing plates and faraday cage affects the sensor response adversely and therefore a balanced support structure was proposed by her [1].

The sensor's bandwidth was tested by Botha by means of frequency response tests. The termination impedance (parallel resistor $R_t$ and capacitor $C_t$ combination) adds a zero, cutting of the low frequencies. The position of this zero is determined by the termination resistance $R_t$ and the parallel combination of the Thévenin equivalent capacitance $C_{TH}$ and termination capacitance $C_t$, as given by the relationship [1]

$$f_c = \frac{1}{2\pi R_t \left(C_t + C_{TH}\right)} \ . \tag{2.16}$$

For accurate measurements at 50 Hz this pole should lie at or lower than 5Hz. The termination resistor must therefore have a value given by [1]

$$R_t \geq \frac{1}{2\pi f_c \left(C_t + C_{TH}\right)} \tag{2.17}$$

where $f_c$ is the frequency equal to 5Hz.

Botha graphed the amplitude and phase response for different sensor models of the three-element parallel plate sensor in a closed HV laboratory. The relative sensor height influenced the voltage division ratio, but not the Thévenin equivalent impedance. Graphs for three different termination impedance combinations, namely 10MΩ//30nF, 10MΩ//10nF and 30kΩ//10nF, were presented by Botha. The larger value resistance and capacitance pairs cut off at a lower frequency than the low valued resistance termination. This emphasized the requirement for high input impedance for the interface instrumentation. For both cases where a 10MΩ resistor was used the -3dB frequency was low enough that all impulse measurements were unaffected by this zero. The 30kΩ termination removed a significant amount of low-frequency data and proved very useful in frequency response / parameter estimation routines [1].

When the support structure was connected to the faraday cage, the model was unaffected by the leakage, where-as if the support structure was connected to the top or bottom plate, the models showed unacceptable deviation from the default model. The models that illustrated leakage between the top and bottom plate and ground as well as when the PCBs had leakage across the substrate, showed negligible deviation from the default model. The phase response was influenced negligibly and therefore the leakage of the substrate was regarded as a minor problem. The cut-off frequency of this model was however increased [1].

Botha tested the effect of the termination impedance on time domain signals by using a step response as input for the default model. Figure 2.14 shows the equivalent circuit diagram for the three-element parallel plate sensor with the resistance between the transmission line and the sensing elements already ignored. The termination impedance is presented by the parallel combination of resistor $R_t$ and capacitor $C_t$. It was concluded that high frequency information is transferred correctly. Botha stated that slow impulses have more low frequency components than fast impulses. The slow impulse waveforms were thus less accurate, especially if the exact values of the resistive terms were not known [1].

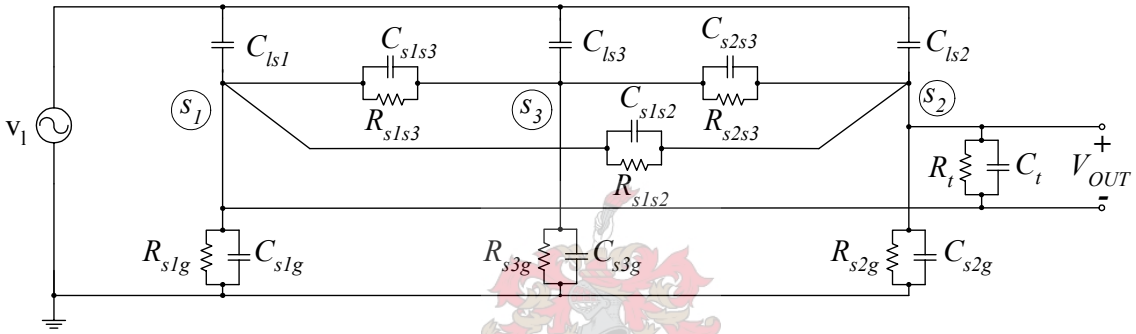


**Figure 2.14: Equivalent circuit of three-element sensor with added termination resistor and capacitor parallel impedance.**

The following factors play a role in the operation of three-element sensors. The sensor has to remain galvanically isolated from the environment. The overall bandwidth is determined by the high frequency -3dB point of the instrumentation and the low-frequency pole formed by the termination impedance and sensor capacitance. Furthermore, the high frequency cut-off is determined by the size of the sensor, the test environment and the bandwidth of the interface instrumentation.

For these conclusions it was assumed that the sensor, as well as the transmission line, is electrically short and that the sensor's main dimension is shorter than one tenth of the wavelength [1]. If the termination impedance and support structure approach the ideal situation, the frequency response of the sensor topology should be flat from 5 Hz to very high frequencies. This will allow the user to do 50 Hz measurements for calibration purposes.

The accuracy of the measured results by Botha may be quantified in terms of the instrumentation accuracy as well as the geometrical positioning accuracy. The Thévenin equivalent impedance is

mostly dependent on the values of the capacitances between the sensor plates and the faraday cage, $C_{s1s3}$ and $C_{s2s3}$ [1]. These values changed negligibly with changes in the geometry. The Thévenin equivalent impedance, which is determined by the sensor capacitance, is the main contributing factor to the magnitude of the output voltage. It is therefore very important to know the exact values of the sensor's capacitances. A faraday cage is required for proper integration of the instrumentation with the sensor [1].

#### 2.4.2.5. Interface instrumentation

The above section reviews the three-element parallel plate sensor assembly, including the signal conditioning instrumentation, i.e. termination impedance, designed and developed by Botha and others [1]. The voltage induced on the plates of the sensor was measured by means of interface instrumentation. Figure 2.15 gives a block diagram overview of the complete interface instrumentation system. The interface system consisted out of a transmitter unit and receiver unit that were interconnected via a fibre-optical link [1].

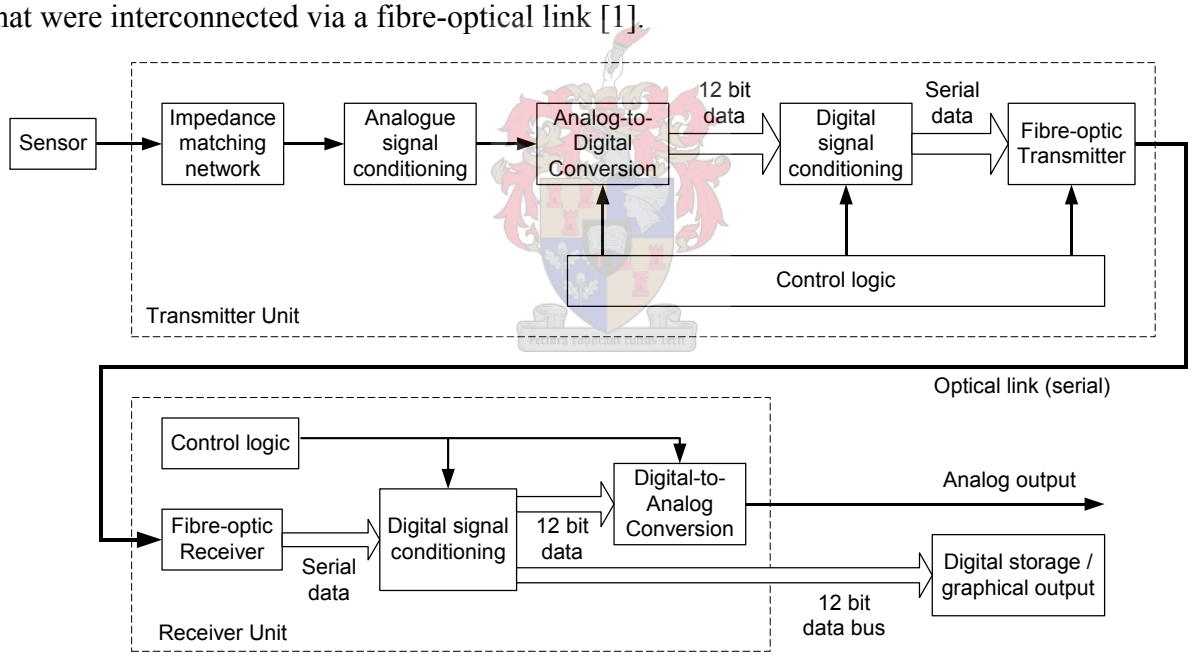


**Figure 2.15: Block diagram of interface system [1].**

The transmitter, located inside the faraday cage of the sensor, had a high input impedance and transmitted the digitised, encoded data via optical fibre. A high termination impedance was used in order to remain in the linear region. The receiver decoded the data and interfaced with the measuring instrumentation [1].

Two modes of operation were available, namely a 12 bit, 5 MHz sampling mode and an 8 bit, 10 MHz sampling mode. The analogue signal conditioning circuitry on the transmitter ensured linear operation for half- and full- scale output voltages. The gain was flat to within 2 % across the entire bandwidth of the system.

The digitising approach used by Botha facilitated improved versatility, linearity and controllability at the cost of power consumption and complexity.

#### 2.4.2.6. Sensor support structure

The termination impedance of the sensor and instrumentation provide a known path for the discharge current. The support structure should not add significantly to this. The support structure may influence the sensor environment in two ways, namely by distorting the field due to charge build-up on itself or by conducting charge away from the sensors. The support structure was therefore designed by Botha to minimize both of these effects. Figure 4.3 illustrates the support structure used in this project. The framework of the structure was constructed from PVC. The PVC had increased resistance and negligible effect on the capacitive coupling, but the surface areas attracted moisture and pollution, which lowered the resistance to much. Glass tubes were thus inserted between the top and bottom part of the framework for galvanic isolation between the sensor and ground. Glass is a good insulating material and has a volume resistivity of approximately $10^{18}$ times that of copper. The support structure, especially the glass tubes, has to be thoroughly cleaned before measurements [1].

### 2.4.3. Instrumental and laboratory evaluation of sensor assembly

Botha did preliminary investigations with a differential sensor. Variable frequency AC excitation was used to evaluate the voltage measuring characteristics of the sensor. Different cables were used to connect the sensor and instrumentation. The key conclusions made by Botha from these measurements were [1]:

- Dedicated optically isolated instrumentation had to be developed due to the fact that a large amount of coupling takes place to the cable itself.
- Instrumentation had to be integrated with the sensor inside a faraday cage.
- A larger test area was necessary due to the fact that boundary conditions in small test areas have significant effect on the output voltage of a capacitive sensor and should be taken into account.

- Three-dimensional simulations were much more accurate than two-dimensional simulations.

The final measurements done by Botha were inside the High Voltage Laboratory (HV Lab). The transmission line was aligned vertically instead of horizontally and a ground plane was suspended in front of the back wall of the laboratory. The three-element sensor was suspended at a fixed distance of 1m in front of the ground plane.

The capacitive coupling parameters for the three-element parallel plate sensor topology in the HV Lab arrangement were determined from 3D simulations. Several models were defined to model the effects of certain of the non-ideal loss terms

Two types of impulses, namely fast and slow impulses, were used to excite the system. The measuring instrumentation discussed in section 2.4.2.5 was used for these measurements. Data processing algorithms used to evaluate the accuracy of the impulse measurements were discussed by Botha. The test conditions were selected for the different impulse tests to allow for the following [1]:

- Different impulse peak values.
- Different transmission line heights.
- Different impulse rise- and fall time characteristics.
- Different loss terms included in the sensor model.

The three-element parallel plate sensor produced very good results in the time-and frequency domains. The means and standard deviations of the impulse peak errors for both sensors in the time domain and the FFT method in the frequency domain were determined. The largest absolute value for the mean error was 1.02% [1].

### 2.4.4. Conclusion

Botha concluded that the three-element parallel plate sensor topology is the superior sensor topology of the different open-air plate topologies. Botha's research only included testing the three-element sensors underneath single-phase excitation in the laboratory. In this project the three-element sensor is implemented underneath three-phase line configurations for capacitive voltage measurements.

# 3. Software packages used for determining capacitive coupling and electric fields underneath transmission lines

## 3.1. Introduction

Botha [1] calculated the coupling capacitances between a single phase transmission line conductor and the sensor elements for various sensor configurations. The objective of this research project is to expand this methodology to the three-phase line configuration. The purpose of the discussions presented in the chapter is to review the methodologies for determining the electric field properties and coupling capacitances for the phase conductors and sensor configurations. The electric field profile underneath a specific transmission line can also be used for determining optimal placement of the sensors.

Computations and measurements of the electric field distribution surrounding power system apparatus are routinely performed for various reasons, including to ensuring that the field strengths are limited to safe levels. Two basic approaches can be used to calculate the coupling capacitances associated with the sensor topology, namely analytical methods and numerical modelling using software packages. These approaches are discussed in section 3.2.

A number of studies [39] have been conducted on the possible biological effects of exposure to power line fields. Deno & Zaffanella [40] calculated the voltages induced on objects in power system electric fields and the currents flowing to ground through them. Computations for electric fields underneath transmission-lines were discussed by Gerrard [10] and Coetzee [38].

Two software programs, namely ELECTRO and EMFP, are used for the FEM simulations in this project. All of the analysis methods used for this project where done for a two-dimensional (2D) approximation of the system. Section 3.3 evaluates ELECTRO by comparing results from analytical calculations with simulated results for various line configurations. Section 3.4 considers various three-phase power line configurations with EMFP and ELECTRO. The simulated results for the electric fields are then compared to values [48] measured by ESKOM personnel underneath equivalent transmission lines.

## 3.2. Approaches to determine capacitive coupling components and electric field distribution

### 3.2.1. Analytical method

Analytical methods for calculating the capacitive matrix and the electric field strength underneath transmission lines have been thoroughly investigated by many researchers [10, 38, 40] and are reviewed in Appendix J.

If the dimensions in the cross section are small compared to the distance over which the cross section remains constant, a two dimensional model may be used to determine the electric field characteristics associated with a particular configuration. Selection of a two dimensional model has many advantages. When numerical methods, such as boundary element methods, are used, computing time increase with the square of spatial resolution for two dimensional models, and with the cube for three dimensional models. Analytical expressions for electric field may be derived for a two dimensional model, though generally not for a system with variation in the third dimension.

The analytical method is limited to situations with simple geometry and with a constant permittivity. Conductors may be located at any location with any peak voltage, including zero. It is however not possible to include conductors with no connection to a voltage source. The floating sensors underneath the transmission line will thus not be included in a model that must be solved analytically. The equations used to calculate the electric field distribution at a sensor location can however be used to formulate an expression that will be useful in determining the coupling capacitances between the transmission line conductors and the sensors. As the conductors are replaced by line charges, the distribution of charges on the lines is ignored and electric fields predicted in the immediate vicinity of the conductors will be incorrect. However, this will not seriously affect the accuracy of the coupling capacitances between the conductors and sensor elements distanced sufficiently from the conductors.

Analytical methods are not suitable for determining coupling capacitances and electric field profiles for the more complex geometrical configurations. Software packages using numerical methods, i.e. FEA and the Boundary Element Method (BEM), are then used for these instances. The analytical calculations are used in this chapter mainly to gain confidence in the results produced with the BEM as implemented in the ELECTRO software package. The remainder of

this chapter gives an overview of the software packages used for calculating the coupling capacitances and electric field profiles of the sensor topologies.

### 3.2.2. Software packages

The software packages used in this research to simulate the electric field distribution and the capacitive coupling components for the various sensor topologies can be divided into the following two groups:

- Programs implementing an analytical approach, i.e. EMFP.
- Programs implementing a numerical approach, i.e. ELECTRO and COULOMB.

#### 3.2.2.1. Overview of the analytical software programs

Coetzee [38] developed an analytical software package called EMFP in MATLAB for determining the electric fields underneath power lines. Gerrard [10] developed a similar program and compared an analytical and a finite element numerical method for calculating the electric field. He concluded that the differences between the results obtained with the two methods are small. However the analytical method was of the order of 3000 times faster compared to the numerical method. Gerrard concluded that both techniques are approximate, except close to conductors and earthed objects. In section 3.4, the validity of the results obtained with EMFP is evaluated and calculated results are compared to values measured by ESKOM personnel [48].

#### 3.2.2.2. Overview of the numerical software programs

ELECTRO and COULOMB are both developed by Integrated Engineering Software and use the boundary element method. ELECTRO is a two-dimensional solver and COULOMB is a three-dimensional solver. COULOMB is not used in this project as a two-dimensional approximation was assumed.

ELECTRO is a two-dimensional/rotational-symmetric, electrostatic field solver with Computer-Aided Engineering (CAE) software features designed to perform cross section simulations of electrostatic and quasi-static physical systems. ELECTRO combines the efficiency of the BEM with a powerful user-interface to alleviate the shortcomings of older methods, i.e. FEA, while offering advanced simulation features. In order to perform a simulation using ELECTRO a *geometric model* of the physical system is required. The model is constructed using the Geometric Modeller of ELECTRO, which allows the user to draw lines, arcs, circles and to re-shape, rotate, displace, mirror, round or scale the model. Once the geometric model has been

built, *physical properties* (such as boundary conditions, materials, sources, operating frequency, etc.) are assigned. The type of model must also be defined, i.e. a two-dimensional or rotationally symmetric model.

After the physical properties have been assigned, the model is *discretized.* In order to use BEM the boundaries must be broken into discrete segments where the sources are defined and the boundary conditions satisfied. The BEM solver ignores any segments that do not contain boundary elements. A model requires boundary elements on all segments that form material interfaces or boundaries with assigned boundary conditions. The solution is subsequently calculated by the *field solver*. The Self-Adapt function can be used in ELECTRO to automatically add elements when the model is solved. ELECTRO creates and tests element distributions until the solution is within predefined accuracy boundaries.

ELECTRO provides users with a wide variety of analysis options, including the ability to create contour plots and graphs of field quantities. Macroscopic parameters such as forces, torques and capacitances can also be calculated. ELECTRO can also perform transmission line analysis and calculate capacitance, inductance, impedance, conductance and admittance.

ELECTRO can be set to perform multiple unattended analyses by running the program in *parametric* or *batch* mode. ELECTRO can perform *phasor* simulations to calculate steady state field solutions that result from sinusoidal sources. However, ELECTRO is not designed to account for radiation or scattering effects. It is assumed that the dimensions of all objects in a model are much smaller than the wavelength for the frequency of simulation.

The following assumptions are made to permit the two-dimensional approximations:

- All structures are infinitely long.
- Variations in the height of line conductors are neglected, i.e. average height is used.
- Wavelength at maximum frequency must be longer than 10 times the actual length of the structure.

### 3.3. Comparison between ELECTRO and theoretical calculations

In order to gain confidence in the results obtained with ELECTRO, simulations of different configurations are performed and the results are compared with approximate analytical results. The configurations that are simulated consist of models with known analytical solutions, including the following:

- Parallel plate configuration.
- Single-phase, two wire line configuration without earth plane.
- Single-phase, two wire line configuration with earth plane.
- Three-phase line configuration with earth plane but no neutral conductors.
- Three-phase line configuration with earth plane and a neutral conductor.

### 3.3.1. Parallel plate configuration

Figure 3.1 shows two parallel plates, each of width $w$ and distance $d$ apart. The capacitance $C$ between these two plates is given by the relationship [47]

$$C = \frac{Q}{V} = \frac{\varepsilon_0 \varepsilon_r A}{d} \tag{3.1}$$

where $Q$ denotes the charge on the plates, $V$ denotes the voltage between the two plates, $A$ denotes the surface area of a plate ($m^2$), $\varepsilon_r$ denotes the relative permittivity of the dielectric between the plates and $\varepsilon_0 = 8.85 \times 10^{-12}$ ($F.m^{-1}$). If distance $d$ is 0.01m, area A of plate is $0.1m^2$ and $\varepsilon_r$ equals 1 for air the capacitance between the two plates is evaluated from equation (3.1) as

$$C = 88.5 \times 10^{-12} F .$$


**Figure 3.1 : Parallel plate geometry with air as dielectric.**

End-effects are neglected in the above calculation. However, simulations with ELECTRO take end-effects into consideration. To eliminate these end-effects a guard ring principle is applied as illustrated in Figure 3.2. Two guard plates, each with width $w_2$, are placed either side of the bottom plate with a distance $w_3$ separating them. The width of the top plate is increased until its edges coincide with those of the two guard plates. The gap $w_3$ between the bottom plate and the guard plates must be small compared to $w_1$ and $w_2$. The width $w_2$ must not be small compared to $w_1$, but it must be large compared to distance $d$. For the case study, the elements of the guard ring had the following dimensions:

- $w_2 = 2\ w_1$
- $w_3 = 0.0001\ w_1$

- $d = 0.1\ w_1$

The ELECTRO simulation for the geometry of Figure 3.2 yields a value of $89.1x10^{-12}$ F for the capacitance between the bottom plate and the top plate. The difference between the analytical value and the simulated result is less than 1%. This discrepancy decreases as the ratios $d/w_1$, $d/w_2$ and $w_3/w_1$ decreases. Thus good correlation is obtained between the analytical and simulated results.

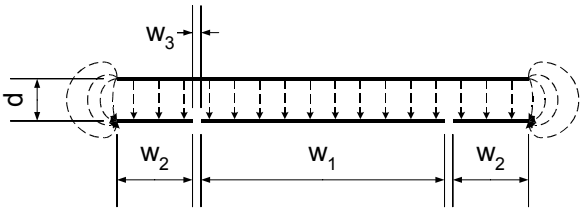


**Figure 3.2 : The geometry used in the ELECTRO simulation for calculating the capacitance of the parallel plate geometry.**

### 3.3.2. Single-phase, two-wire line configuration without earth plane

Figure 3.3 shows a single-phase, two-wire line configuration. The capacitance $C_{xy}$ between conductors $x$ and $y$ is given by the relationship [11]

$$C_{xy} = \frac{\pi\varepsilon}{\ln(D/r)} \quad \text{F/m} \tag{3.2}$$

where ε denotes the permittivity, $D$ denotes the distance between the conductor centres and $r$ denotes the radius of the conductors.

In order to use a representative line configuration for the comparison between the analytical calculation and ELECTRO simulation a single-phase line consists of two 4/0 12-strand copper conductors with a GMR of 5.334mm and a spacing of 1.5m between the conductor centres [11] was used. Thus, for a distance $D$ of 1.5m and a radius $r$ of 5.334mm, the capacitance between the two conductors is

$$C_{xy} = 4.9326\times10^{-12} \quad \text{F/m.}$$

The ELECTRO simulation yields a value of $4.933x10^{-12}$ F. The difference between the analytical value and the simulated result is less than 0.8%. This discrepancy can be ascribed to the analytical method calculating the capacitance between the conductor centres, whereas ELECTRO

calculates the capacitance between the conductor surfaces. Good correlation is obtained between the analytical and simulated results.

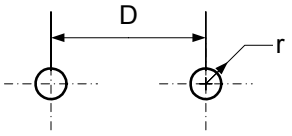


**Figure 3.3 : A single-phase, two-wire line configuration consisting out of two parallel conductors.**

### 3.3.3. Single-phase, two-wire line configuration with earth plane

Figure 3.4(a) shows a single-phase, two-wire line configuration above an earth plane. Figure 3.4(b) shows how the method of images is used to replace the perfect conducting earth plane with image conductors. The capacitance $C_{xy}$ between conductors $x$ and $y$ is given by (refer Appendix J)

$$C_{xy} = \frac{\pi\varepsilon}{\ln(D/r) - \ln\frac{H_{xy}}{H_{xx}}} \quad \text{F/m} \tag{3.3}$$

where ε denotes the permittivity, $D$ denotes the distance between conductors $x$ and $y$, $r$ denotes the radius of the conductors, $H_{xy}$ denotes the distance between conductor $x$ and image conductor $y'$ and $H_{xx}$ denotes the distance between conductor $x$ and image conductor $x'$ as shown in Figure 3.4(b).

The same line dimensions as in the previous section are used for comparing the analytical calculation to the ELECTRO simulation, except for a ground plane being added [11]. Thus, for a distance $D$ of 1.5m, a radius $r$ of 5.334mm and line height of 5.5m, the capacitance between the two conductors is

$$C_{xy} = 5.016\times10^{-12} \quad \text{F/m.}$$

The ELECTRO simulation yields a value of $4.941\text{x}10^{-12}$ F. The difference between the analytical value and the simulated result is less than 1.5%. The discrepancy between the two values can be ascribed to the assumption that the earth plane is infinitely wide in the analytical calculations. However, in the ELECTRO simulation the earth plane is given a finite width. The discrepancy can thus be decreased by increasing the earth width for a given line configuration. Good correlation is obtained between the analytical result and the simulated result.

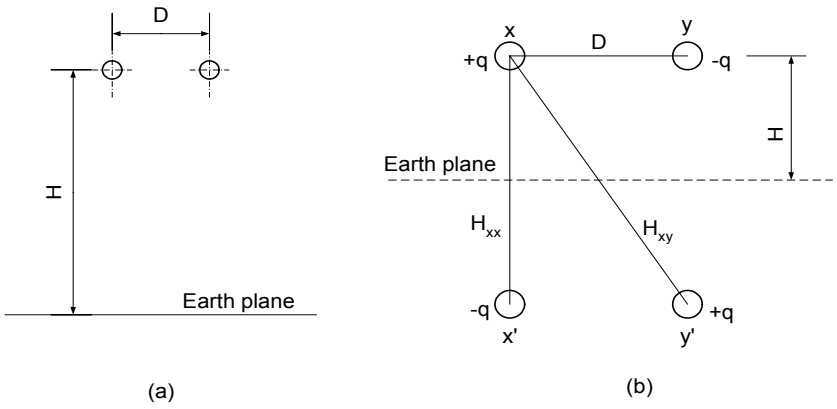


**Figure 3.4: A single-phase, two-wire line configuration: (a) Above a perfect conducting earth plane, (b) With the earth plane replaced by image conductors [11].**

### 3.3.4. Three-phase line configuration with earth plane but no neutral conductors

Figure 3.5 shows a three-phase line configuration, without neutral conductors, above an earth plane. The coupling capacitance matrix of the three-phase line configuration is given by the equations presented in Appendix J.3. The capacitances between the different conductors were calculated analytically and simulated with ELECTRO for $D$ = 2m, $r_p$ = 0.01m and $H_p$ = 5m. Table 3.1 compares the analytical and simulated results. Capacitances $C_{ab}$ and $C_{bc}$ are equal, illustrating the symmetrical property of the capacitive phase matrix.

**Table 3.1: Analytical and simulated results for the capacitances between the different phases of a three-phase line configuration without any neutral conductors.**

| | $C_{ab}$ | $C_{ac}$ | $C_{bc}$ |
|---|---|---|---|
| **Analytical (F)** | -1.84E-12 | -8.00E-13 | -1.84E-12 |
| **Numerical (F)** | -1.86E-12 | -8.19E-13 | -1.86E-12 |
| **Error** | -0.93% | -2.37% | -0.93% |

The discrepancy of -2.37% between the analytical result and the simulated result of capacitance $C_{ac}$ can be ascribed to the assumption made for the analytical calculations, i.e. that the distortion of the electric field introduced by the centre conductor is negligible. ELECTRO take the distortions in the electric field, due to other conductors, into consideration. It can thus be accepted ELECTRO obtains better results. For capacitances $C_{ab}$ and $C_{bc}$ good correlation is obtained between the analytical results and the simulated results. Table A.1 in Appendix A tabulates the capacitive coupling matrices of the two methods. Note that arbitrary dimensions were used in the exercise, i.e. no specific practical line configuration is represented. In section 3.4 various representative three-phase line configurations are used for analytical calculations and ELECTRO simulations.

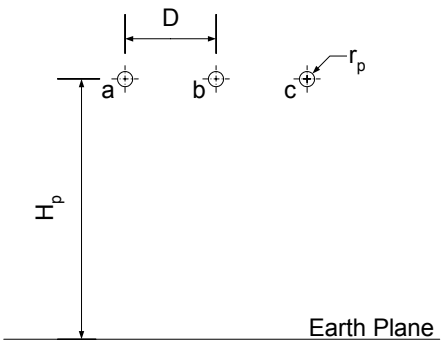


**Figure 3.5 : Three-phase line configuration above an earth plane.**

### 3.3.5. Three-phase line configuration with earth plane and a neutral conductor

Figure 3.6 illustrates a three-phase line configuration with one neutral conductor above an earth plane. The capacitance matrix of this line configuration is given by the equations presented in Appendix J.3. The capacitances between the different conductors were calculated analytically and simulated with ELECTRO for $D$ = 2m, $r_p$ = 0.01m, $r_n$ = 0.006m, $H_n$ = 1m and $H_p$ = 5m. Table 3.2 compares the analytical and simulated results. Capacitances $C_{ab}$ and $C_{bc}$ are equal, illustrating the symmetrical property of the capacitive phase matrix.

**Table 3.2 : Analytical and simulated results for the capacitances between the different phases of a three-phase line configuration with one neutral conductor.**

| | $C_{ab}$ | $C_{ac}$ | $C_{bc}$ |
|---|---|---|---|
| **Analytical (F)** | -1.49E-12 | -6.15E-13 | -1.49E-12 |
| **Numerical (F)** | -1.50E-12 | -6.30E-13 | -1.50E-12 |
| **Error** | -0.69% | -2.38% | -0.69% |

The discrepancy of 2.38% can be ascribed to the same assumption made during analytical calculations as explained in the previous section. For capacitances $C_{ab}$ and $C_{bc}$ good correlation is obtained between the analytical and simulated results. Table A.2 in Appendix A tabulates the capacitance phase matrixes of the two methods.

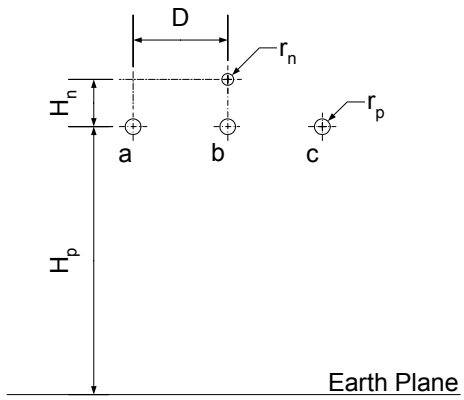


**Figure 3.6 : Three-phase line with one neutral conductor above an earth plane.**

### 3.3.6. Conclusion

Good comparison was obtained between the analytical results and the simulated results. Although the different configurations that are investigated in this section seem trivial, it is regarded as necessary to gain confidence for future analysis with ELECTRO. The discrepancies for each line configuration between the analytical and simulated results are discussed in each section.

## 3.4. Evaluating three-phase line configurations with EMFP and ELECTRO

In this section various simulations of different three-phase power line configurations are conducted. These simulations are done with EMFP, as well as ELECTRO. For each power line configuration the electric field strengths, obtained by EMFP and ELECTRO, are compared to electric field strengths measured underneath equivalent ESKOM power line configurations [48]. The following typical power line configurations are simulated:

- 88kV
- 132kV
- 275kV
- 400kV
- 765kV

Appendix A.2 gives details of the above power line configurations. The 275kV, 400kV and 765kV line configurations feature phase bundle topologies. A bundle can be represented by a single conductor as explained in Appendix J.3. ELECTRO is used to compare the electric field profile for a line configuration consisting out of separate conductors for each bundle to a line

configuration with the bundle replaced by an equivalent conductor. At a height of 1.8m above the ground plane, there is a discrepancy of 0.001% between these two field profiles. This confirms that an equivalent conductor, with a GMR of the bundle, can be used in ELECTRO in order to make the line configuration less complex.

As in the previous sections, analytical values obtained with EMFP are compared with simulated results obtained with ELECTRO. The maximum values of the vertical component of the electric field strength 1.8m above the ground plane, simulated with EMFP and ELECTRO, are compared with the values measured by ESKOM.

Coetzee [38] compared the results obtained with EMFP with the ESKOM results and concluded that in all cases, except for the double circuit 400kV power line configuration, there were good correlation. The discrepancy between the results for the double circuit, 400kV power line might be due to a programming error in EMFP. It can also be ascribed to the assumption made for the analytical calculations that the distortion of the electric field in the vicinity of the other conductors is negligible. Calculated values and measured values will always deviate from each other due to measurement errors and the simplifications and/or assumptions made in calculations. Coetzee indicated that the accuracy between calculated values and outdoor electric field measurements is near 10%, but under controlled conditions it is better than 5%. Table 3.3 tabulates the results from EMFP, ELECTRO and ESKOM measurements.

**Table 3.3: Comparison between electric field strengths simulated by EMFP and ELECTRO and measured by ESKOM [48].**

| | Electric Field 1.8m above ground (kV/m) | | | % difference between | | |
|---|---|---|---|---|---|---|
| Power Line | EMFP | ELECTRO | ESKOM | ELECTRO and EMFP | ESKOM and EMFP | ELECTRO and ESKOM |
| 88kV | 0.859 | 0.8216 | 0.8 | 4.35 | 6.87 | 2.63 |
| 132kV | 1.65 | 1.6493 | 1.3 | 0.04 | 21.21 | 21.18 |
| 275kV | 3.126 | 3.1396 | 3 | -0.44 | 4.03 | 4.45 |
| 400kV | 3.775 | 4.835 | 4.7 | -28.08 | -24.50 | 2.79 |
| 765kV | 6.662 | 6.6936 | 7 | -0.47 | -5.07 | -4.58 |
| | | | | Average difference | | |
| | | | | 5.45 | -0.20 | 3.54 |

The deviations between ELECTRO and ESKOM measurements are smaller than the difference between EMFP and ESKOM measurements. As the average (median) difference between ELECTRO and ESKOM amounts to only 3.54%, ELECTRO proved to be a very accurate

simulation package for calculating the electric field profiles underneath power lines and determining the capacitive coupling matrices.

### 3.5. Conclusion

ELECTRO gives accurate results for the calculation of the capacitive coupling matrices of power lines. Appendix J.4 states that the capacitive matrices are calculated from the electric field profiles. If the electric field strengths simulated by ELECTRO are similar to those measured by ESKOM, it can be concluded that the capacitive matrix obtained by ELECTRO will be accurate.

The deviations between calculated and measured values are due to numerous assumptions made in simplifying the process of calculating the electric field profiles. Conductor sag, the presence of pole structures, tower structures and other objects in the vicinity of the power lines are usually ignored in calculations. In addition a flat horizontal ground level is assumed, while in practice hills and valleys distort the fields close to the ground.

ELECTRO will be used to determine the capacitance matrices of sensors underneath power lines. EMFP would be used in favour of ELECTRO whenever the electric field profiles underneath a power line have to be calculated quickly.

# 4. Design and evaluation of three-element open-air sensor assembly

## 4.1. Introduction

The research in this project focuses on a three-element parallel plate sensor in three-phase transmission line configurations. Botha [1] researched the performance of a three-element sensor extensively under laboratory conditions. However, the sensor was not tested under field conditions underneath a transmission line. A field evaluation of the sensor developed by Botha was therefore performed before introducing design changes to the original sensor.

Following field tests a smaller, more mobile and sturdier sensor is developed. A discussion is presented on the design and development of the new sensor, associated termination impedances and data acquisition instrumentation. A triggering system used for the measurement of switching transients underneath HV transmission lines is developed.

## 4.2. Original sensor developed by Botha

### 4.2.1. Field evaluation of original sensor

The three-element parallel plate sensor has not previously been tested underneath a HV transmission line in the field. It was therefore necessary to determine if the three-element parallel plate sensor measures an adequate voltage level if placed underneath a three-phase HV transmission line. The measurements were conducted for an isolated flat three-phase single-circuit 400kV transmission line, i.e. a line which does not have interference from nearby lines. The instrumentation is connected to the sensor as explained in section 2.4.2.5.

Table 4.1 tabulates the peak values of the voltages induced on the sensing plates at different positions underneath the line and for different termination impedances. The following test configurations were implemented:

- Sensor centralized underneath the centre phase with a 10MΩ resistor in parallel with a 30nF as termination.
- Sensor centralized underneath the left phase with a 10MΩ resistor in parallel with a 30nF as termination.
- Sensor centralized underneath the centre phase with no termination.
- Sensor centralized underneath the left phase with no termination.
- Sensor placed half the phase-to-phase distance (denoted as medium in the table) away from the left phase.

- Sensor placed the full phase-to-phase distance (denoted as far in the table) away from the left phase.

**Table 4.1 : Peak voltages measured with original sensor underneath a three-phase 400 kV transmission line.**

| Position under transmission-line | Termination Impedance | Oscilloscope [V] |
|---|---|---|
| Left phase | 10M ohm, 30nF | 0.231 |
| Centre phase | 10M ohm, 30nF | 0.18 |
| Left phase | None | 0.375 |
| Centre phase | None | 0.555 |
| Not beneath a phase (medium) | None | 0.528 |
| Not beneath a phase (far) | None | 0.36 |

Several practical problems were encountered during the field measurements. These problems included bad connections between the BNC output connector and the differential plates, the BNC connector short-circuiting on the inside of the faraday cage, difficulties in positioning the sensor directly underneath the lines, inadequate fibre optic cable lengths, dynamic input range problems with the fibre optic transmitter equipment and problems due to the uneven terrain. All of these served as inputs for the design of an improved sensor and field test arrangement.

### 4.2.2. Critical review of existing sensor assembly

The original three-element parallel plate sensor can be improved with respect to a number of aspects, including the following:

- The sensor dimensions are relatively large and thus difficult to handle and to transport. The field measurements done with the original sensor shows that the measured voltage is in excess of 0.4V. A voltage of ±0.25V is adequate for transmission and triggering purposes in the measuring system, thus the size of the sensors can be scaled down.
- Installing the optical transmitter and battery pack inside the Faraday cage requires that the entire top sensing plate be removed.
- The connection between the transmitter and the termination impedance is not sturdy enough to avoid the BNC connector short circuiting on the inside of the faraday cage.
- The aluminium foil used for the faraday cage oxidises, causing bad contacts between the sides of the faraday cage and the top and bottom sides.
- Leakage currents exist between ground and the plate on which the sensor rest, thereby forming a leakage path through the support structure. This has an influence on the frequency response of the voltage transfer function of the three-element topology.

- The power consumption of the optical-link is relatively high, thereby limiting the battery lifetime.

The above list gives rise to a set of design objectives for improving the electrical and constructional properties of the new sensor.

## 4.3. New sensor design

### 4.3.1. Design objectives for new sensor

The three-element parallel plate sensor developed by Botha is redesigned and constructed. A smaller, more mobile and sturdy sensor is developed. Three of these new sensors are then constructed for capacitive voltage measurements underneath three-phase high voltage transmission lines.

The design objectives of the new sensor are derived from the problems encountered with the original sensors. The design objectives for the new sensor are the following:

- A smaller, sturdier and more mobile sensor must be constructed for easier handling and transportation of the sensor.
- The sensor must be able to measure adequate voltage levels underneath a HV transmission line.
- A drawer is required which will make the insertion of the transmitters into the faraday cage easier, i.e. one of the plates should not have to be removed every time the transmitter is connected to the sensor.
- The connection between the transmitter and the termination impedance must be made sturdier to avoid the BNC connector short circuiting on the inside of the faraday cage.
- The support structure should rather be connected to the faraday cage than to one of the plate elements in order to achieve better galvanic isolation. A connection to the faraday cage does not have a significant influence on the transfer function of the three-element topology as shown before.
- Interface instrumentation that uses less power than the optical-link can be used.

### 4.3.2. Physical design of the new three-element parallel plate sensor

Figure 4.1 shows an isometric view of the internal framework for the new three-element sensor assembly while the schematic representations given in Figure 4.2 define the dimensions of the framework. This structure is similar to that of the original sensor shown in Figure 2.12, except that it is smaller and it is provided with a slot in which a removable

drawer can be inserted. The drawer facilitates easy removal and insertion of the optical transmitter instrumentation into the faraday cage. Due to the fact that the framework is smaller and because of the extra pieces of PVC used for the slot, the new sensor is also sturdier. As with the original design the framework of the sensor consists out of PVC. Double side Printed Circuit Boards (PCBs) are used at the top and bottom for the sensing plates and to form the top and bottom sides of the faraday cage. The glass fibre body of the PCB thus serves as the dielectric layer separating the sensing plates from the faraday cage. The PCB that is commonly available has a dielectric with a relative permittivity of 5.2 and a thickness of 1.6mm [74]. The PCB has two drawbacks, namely that the dielectric substrate can absorb moisture and become more conducting and the dielectric constant itself is not very predictable.

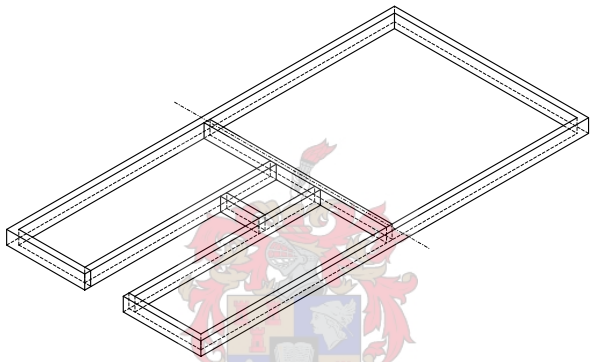

**Figure 4.1: Isometric view of the redesigned three-element parallel plate sensor assembly.**

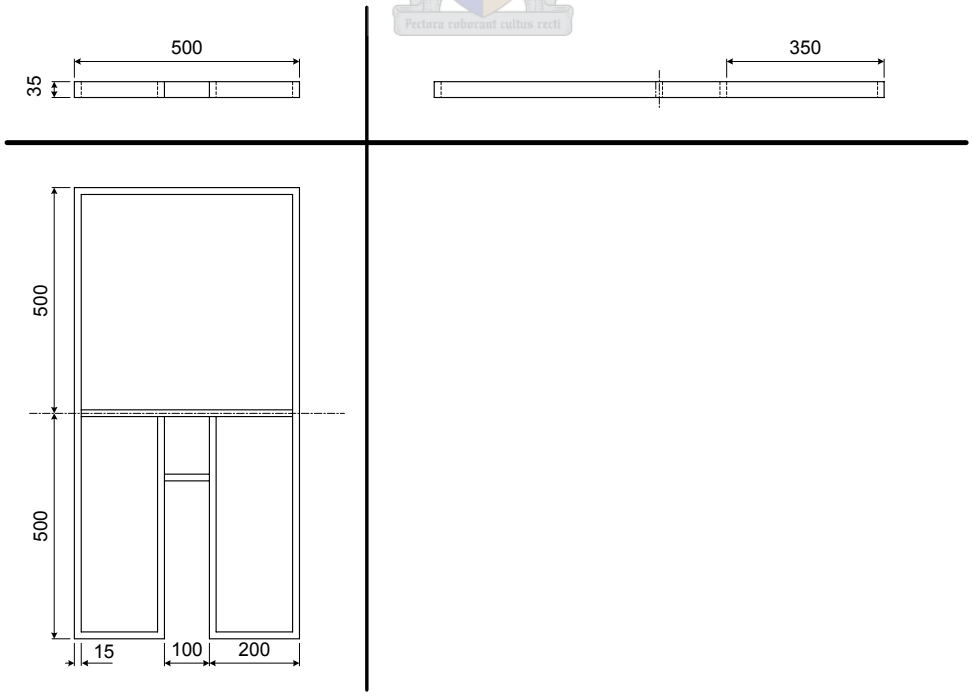


**Figure 4.2: Orthographic projection of the redesigned three-element parallel plate sensor assembly.**

The two inner copper surfaces of the PCB are connected by a thin copper sheet moulded around the outside of the PVC frame work, thereby forming a study Faraday cage. The contact areas between the copper surfaces are tinned in order to minimise the high contact resistance resulting from surface oxidation. In order to minimize surface leakage currents between the sensing plates and the faraday cage, a strip of copper around the outer edges of the two sensing plates is removed to increase the leakage current path length.

The support structure used by Botha was resized to correspond with the smaller sensors. The structure is however still constructed out of PVC tubes, and as in the original design, glass tubes are used for increased insulation. The sensor assembly is placed on top of the support structure. Figure 4.3 shows a photograph of the redesigned sensor assembly and the support structure. Figure 4.4 shows the inside of the faraday cage, including the PVC instrumentation drawer, with the top plate of the sensor is removed.

**Figure 4.3: Photograph of the redesigned three-element parallel plate sensor assembly and support structure.**

**Figure 4.4: Photograph of the inside of Faraday cage and drawer, with the top plate of sensor assembly removed.**

Figure 4.5 shows the optical transmitter and signal connectors inside the drawer. The banana plugs terminations are not ideal from a noise perspective. However, the current emphasis is on low frequency measurements and the banana plugs are regarded as adequate for this

project. This will thus be adequate for the measurements intended in this project. For high frequency measurements better connections will have to be made between the drawer and the sensor.

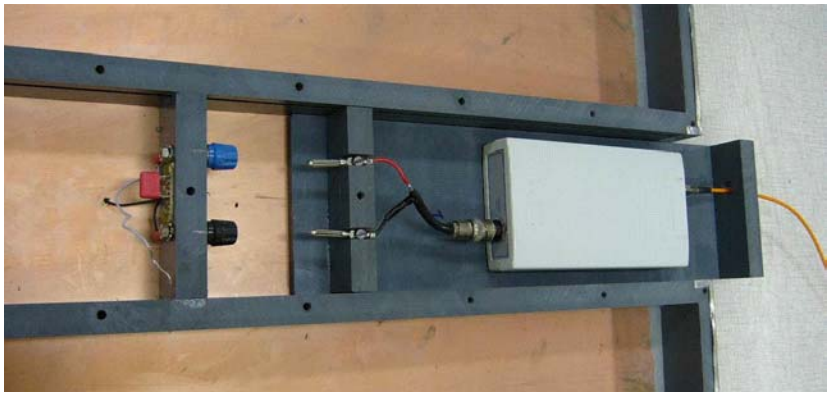

**Figure 4.5: Photograph of the transmitter located in the instrumentation drawer.**

### 4.3.3. Experimental determination of sensor capacitance

Capacitors with liquid or solid insulation exhibit dielectric losses under AC voltage stress. Such lossy capacitors are modelled by a series/parallel combination of an ideal capacitor and ohmic resistors as shown in Figure 4.6. The residual inductance must only be considered at high frequencies and is omitted here. In reality a capacitor possesses both a series and a parallel loss resistance, but depending on the frequency of the applied voltage only one of them dominates. At low frequencies, $1/\omega C_p >> R_s$, and the parallel circuit of $C_p$ and $R_p$ dominates the impedance function. The losses, represented by $R_p$, are generated mainly in the dielectric. The equation used to convert the dissipation factor $tan\delta_p$ ($D$) to the parallel resistor $R_p$ value is given by the relationship [76]

$$R_p = \frac{1}{\tan \delta_p \omega C_p} \tag{4.1}$$

where $C_p$ denotes the parallel capacitor.

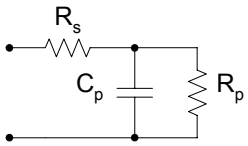


**Figure 4.6: Equivalent circuit for a lossy capacitor.**

The capacitance $C$ between the two plates of a parallel-plate element can also be calculated analytically using the relationship

$$C = \frac{\varepsilon_0 \varepsilon_r A}{d} \tag{4.2}$$

where $\varepsilon_r$ denotes the relative permittivity of the dielectric between the plates, $\varepsilon_0 = 8.85\text{x}10^{-12}$ [F.m$^{-1}$] and $A$ denotes the surface area of a plate [m$^2$]. Measured and calculated values for the capacitive components of the three-element sensor will be compared in this section.

Botha derived a detailed equivalent circuit topology for the three-element sensor assembly in a single-phase phase conductor topology. In order to characterise the Thévenin equivalent circuit of the redesigned sensor, it is necessary to determine parameter values associated with the sensor assembly. Three categories of parameters are of interest, namely the parameters associated with the standalone sensor, the parameters representing the coupling between the sensor and the transmission line and the parameters associated with the sensor termination impedance. Figure 4.7 shows the equivalent circuit topology of the stand-alone sensor and termination impedance. The circuit elements are defined as follows [1]:

| | |
|---|---|
| $C_{s1s2}$, $R_{s1s2}$ | Capacitance and resistance between the top and bottom sensor plates respectively. |
| $C_{s1s3}$ | Capacitance between the top sensor plate and the faraday cage. |
| $C_{s2s3}$ | Capacitance between the bottom sensor plate and the faraday cage. |
| $R_{s1s3}$ | Resistance of the dielectric substrate between the top sensor plate and the faraday cage. |
| $R_{s2s3}$ | Resistance of the dielectric substrate between the bottom sensor plate and faraday cage. |
| $C_t$, $R_t$ | Termination capacitance and resistance respectively inserted between the top and bottom plates. |

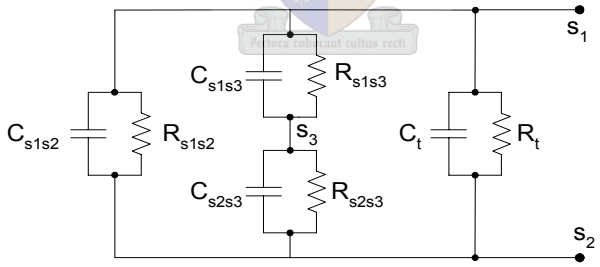


**Figure 4.7: Equivalent circuit of the three-element sensor and termination impedance.**

The values of the circuit elements shown in Figure 4.7 were measured with a Hewlet Packard 4285A, precision LCR meter, whilst taking care to reduce the errors introduced by residual and stray components. The LCR meter measures the dissipation factor $D$ and the parallel capacitance $C_p$ of the equivalent lossy circuit. The parallel resistive value $R_p$ can be obtained from equation (4.1). The measurements with the LCR meter were conducted for all three sensor assemblies and were repeated under different conditions to verify repeatability of the measurements. Note that following two categories of measurements were conducted:

- *Measurements for individual sections of the disassembled sensor:* This includes measurements of the capacitances between the top plate and the bottom surfaces of the two PCBs used in construction of the sensor.
- *Measurements of the integrated sensor:* This include measurements of the total capacitance between the three elements of the fully assembled sensor, i.e. top plate/Faraday cage, bottom plate/Faraday cage and top plate/bottom plate.

To measure the capacitance between the surfaces of a PCB the plate, it is removed from the sensor assembly and measured separately. The dielectric constant of the PCB substrate is not very predictable. With a dielectric constant of 5.2 and a thickness of 1.6mm the capacitance between the two conducting sides of the PCB is calculated with equation (4.2) as 14.38nF. The measured value of this capacitance is 12.29nF, yielding a discrepancy of 14% between the calculated and measured values. This discrepancy can be ascribed to the value of the dielectric constant used and the fact that fringe effects on the edges have been neglected in the calculation.

If loss terms are ignored, the equivalent circuit model shown in Figure 4.7 yields the circuit shown in Figure 4.8 The capacitances $C_{p1p2}$, $C_{p1p3}$ and $C_{p2p3}$ measured between $s_1$ and $s_2$, between $s_1$ and faraday cage $s_3$ and between $s_1$ and faraday cage $s_3$ respectively are given by the relationships

$$C_{p1p2} = C_{s1s2} + \frac{C_{s1s3}C_{s2s3}}{C_{s1s3} + C_{s2s3}} \tag{4.3}$$

$$C_{p1p3} = C_{s1s3} + \frac{C_{s1s2}C_{s2s3}}{C_{s1s2} + C_{s2s3}} \tag{4.4}$$

and

$$C_{p2p3} = C_{s2s3} + \frac{C_{s1s2}C_{s1s3}}{C_{s1s2} + C_{s1s3}} \ . \tag{4.5}$$

The set of simultaneous equations represented by equations (4.3) to (4.5) yields the following results for $C_{s1s2}$, $C_{s1s3}$ and $C_{s2s3}$:

$$C_{s1s2} = \frac{{C_{p1p2}}^2 + \left(C_{p1p3} - C_{p2p3}\right)^2 - 2C_{p1p2}\left(C_{p1p3} + C_{p2p3}\right)}{2\left(C_{p1p2} - C_{p1p3} - C_{p2p3}\right)} \tag{4.6}$$

$$C_{s1s3} = -\frac{{C_{p1p2}}^2 + \left(C_{p1p3} - C_{p2p3}\right)^2 - 2C_{p1p2}\left(C_{p1p3} + C_{p2p3}\right)}{2\left(C_{p1p2} - C_{p1p3} + C_{p2p3}\right)} \tag{4.7}$$

and

$$C_{s2s3} = -\frac{C_{p1p2}{}^2 + \left(C_{p1p3} - C_{p2p3}\right)^2 - 2C_{p1p2}\left(C_{p1p3} + C_{p2p3}\right)}{2\left(C_{p1p2} + C_{p1p3} - C_{p2p3}\right)} \quad . \tag{4.8}$$

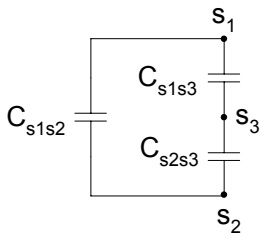


**Figure 4.8: Reduced equivalent circuit of a three-element sensor with loss terms and the termination impedance ignored.**

The capacitance between the sensing plates of the assembled three-element sensor, i.e. $C_{p1p2}$, is measured between nodes $s_1$ and $s_2$. Table 4.2 tabulates $C_{p1p2}$, $D$ and $R_{p1p2}$ for the three sensors with the termination impedance omitted. These three values are denoted respectively as *Csp, D* and *Rsp* in Table 4.2. The differences between the values for the three sensors, using *Sensor A* as the reference, are also tabulated. The biggest difference occurs between *sensor A* and *sensor B,* yielding a small difference of 7.8pF.

**Table 4.2: Parameter values measured with the LCR meter for the three sensors without termination impedances.**

| | Sensor omitting termination capacitance | | | | | |
|---|---|---|---|---|---|---|
| | Csp [nF] | Csp dif [nF] | Csp dif [%] | D | Rsp [Ω] | Rsp dif [%] |
| Sensor A | 6.18824 | | | 0.008282 | 31055.89 | |
| Sensor B | 6.18043 | 0.00781 | 0.126 | 0.008239 | 31255.53 | -0.64 |
| Sensor C | 6.1898 | -0.00156 | -0.025 | 0.008337 | 30841.37 | 0.69 |

### 4.3.4. Interface instrumentation

The waveforms measured by the sensors are transmitted to the measuring unit through an optical-link. The input impedance of the interface instrumentation appears in parallel with the termination impedance of the sensor. The value of the input impedance of the interface instrumentation is therefore required for determining the total termination impedance of the sensor. This section reviews the interface instrumentation used with the three-element sensors, but focuses mainly on the input impedance of the instrumentation.

The fibre optic technology used in this investigation is similar to the interface instrumentation used by Botha [1]. Figure 4.9 shows a block diagram of the optically isolated link used in conjunction with the new sensors [49]. The input stage of the transmitter unit consists of a buffer and anti-aliasing low-pass filter. The buffer determines the input impedance and the low-pass filter serves as a high frequency noise filter. The signal is digitised and serially

transmitted to the receiver unit via an optical fibre. At the receiver unit the serial data stream is translated to parallel data and converted to an analog signal. The resulting analog signal is then measured by the HandyScope 3 oscilloscope developed by TiePie Engineering.

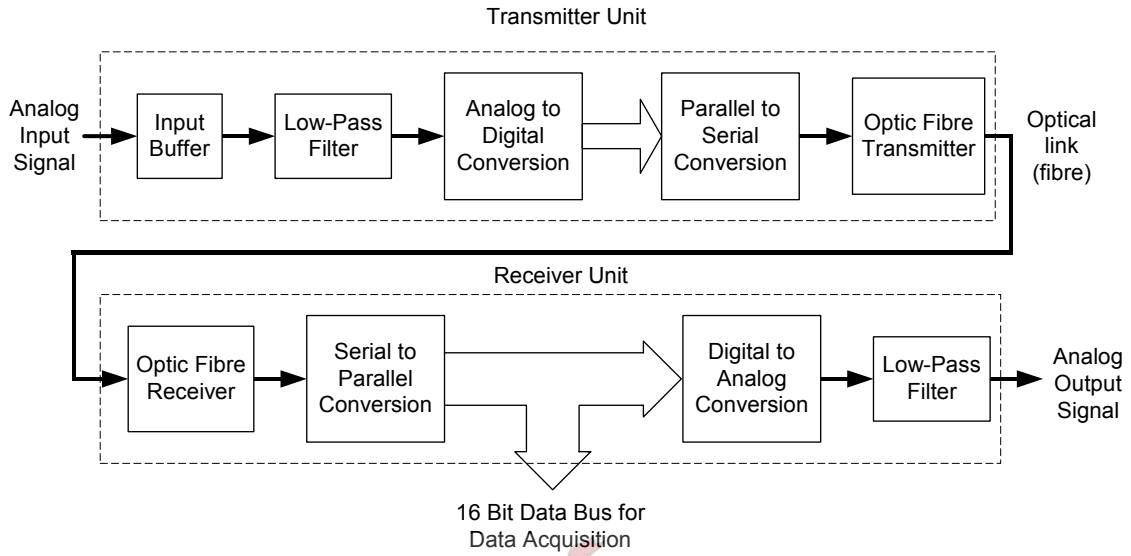


**Figure 4.9: Block diagram of the optically isolated link [49].**

Figure 4.10 shows a circuit diagram of the input buffer, where $R_1$, $R_2$, $C_{trim}$ and $C_1$ represent a voltage divider. The capacitors denoted by $C_{cm}$ represent the common mode input capacitances of the operation amplifier. The low-frequency gain of the non-inverting amplifier is determined by resistors $R_a$ and $R_b$ while capacitor $C_{fb}$ is used for compensation at high frequencies.

In practice, the effect of $C_{cm}$ on the gain response of the non-inverting amplifier is negligible below 1MHz. Since $C_{in}$ was not used in the final design, the input impedance of the circuit is determined by $R_1$, $R_2$ $C_{trim}$ and $C_1$.

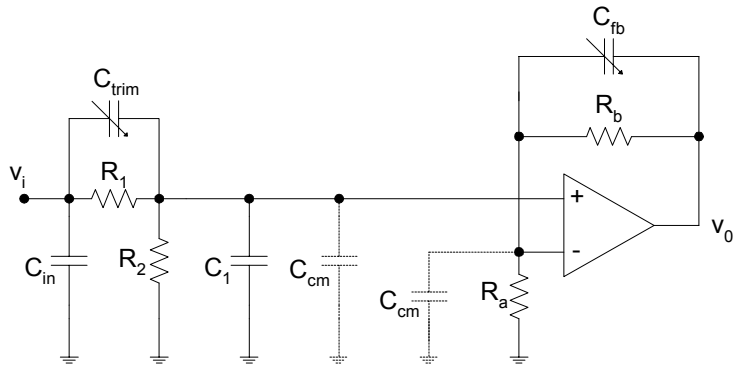


**Figure 4.10: Circuit diagram of the input buffer [49].**

### 4.3.5. Termination impedance of sensor

Determination of the overall voltage transfer function of the sensor and the associated termination impedance can be achieved by combining the Thévenin equivalent circuit of the sensor with a termination impedance representing the input impedance of the instrumentation. This allows the effects of the terminal impedance on the voltage transfer function of the complete system to be investigated. It is shown in section 2.4.2.1 that the Thévenin equivalent voltage and impedance relationships for the single line topologies are relatively complex. For the three-phase topology, these relationships become considerably more complex. Therefore, in order to investigate the effects of the termination impedance on the frequency response of the voltage transfer function of the sensor and the termination impedance, it is convenient to neglect the loss terms associated with the sensor and conduct the investigation for a single-phase topology.

Figure 2.11 shows the equivalent circuit model for a three-element sensor in a single phase line topology if all loss terms are ignored. This circuit diagram can be reduced to the circuit shown in Figure 4.11, where the subscripts *p1*, *g*, *s1*, *s2*, *s3* and *t* denote the line conductor, ground plane, top sensing plate, bottom sensing plate, faraday cage and termination impedance respectively. Capacitance $C_t$ in Figure 4.12(a) and (b) is added to move the pole formed by the input impedance of the interface instrumentation.

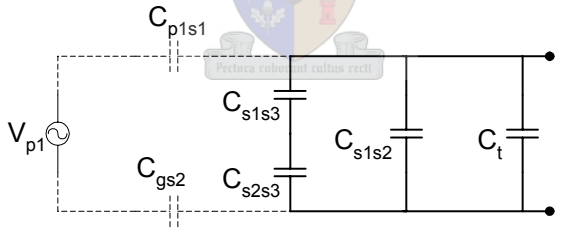


**Figure 4.11: Simplified equivalent circuit of the three-element sensor in a single-phase topology.**

The coupling capacitance between the line conductor and the sensor elements are more than four orders of magnitude smaller than the capacitances between the sensor elements, i.e. sensing plates and the faraday cage. Ignoring the coupling capacitances between the line conductor and the sensor elements will therefore have a negligible effect on the Thévenin equivalent capacitance. This yields the reduced circuit model shown in Figure 4.12(a). Furthermore, because $C_t$ and the series combination of $C_{s1s3}$ and $C_{s2s3}$ are three orders of magnitude greater than $C_{s1s2}$, capacitance $C_{s1s2}$ can be omitted. This yields the reduced equivalent circuit model shown in Figure 4.12(b).

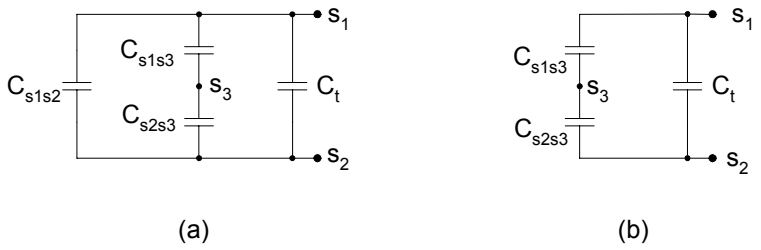


**Figure 4.12: (a) Reduced Thévenin impedance representation of the three-element sensor with all loss terms omitted. (b) Reduced Thévenin impedance representation of the three-element sensor with all loss terms and $C_{s1s2}$ omitted.**

The Thévenin capacitance $C_{TH}$ of the three-element sensor, with termination capacitance $C_t$, can thus be approximated by the relationship

$$C_{TH} \approx C_t + \frac{C_{s1s3}C_{s2s3}}{C_{s1s3} + C_{s2s3}} \tag{4.9}$$

where $C_{s1s3}$ denotes the capacitance between the top plate and the faraday cage, $C_{s2s3}$ denotes the capacitance between the bottom plate and the faraday cage and $C_t$ denotes the termination capacitance.

The overall frequency response of the voltage transfer function of the sensor and instrumentation can be determined using the circuit diagram shown in Figure 4.12(a), where the sensor is represented by the measured impedance values presented in section 4.3.3. Figure 4.14 plots the frequency responses simulated with PSpice for the different values of $C_t$ tabulated in Table 4.3.

**Table 4.3: Thévenin equivalent capacitance of the three-element sensor with different termination capacitors.**

| Ct | Cth |
|---|---|
| 5.00E-09 | 20.6E-9 |
| 10.0E-9 | 25.6E-9 |
| 15.0E-9 | 30.6E-9 |
| 20.0E-9 | 35.6E-9 |
| 30.0E-9 | 45.6E-9 |
| 50.0E-9 | 65.6E-9 |

The output voltage is measured at the non-inverting input of the operational amplifier of the buffer stage as indicated by the voltage probe in Figure 4.13. The results show that the -3dB low-frequency cut-off point decreases as the value of the capacitor increases. Equation (2.16) yields a value of 30nF *for* $C_t$ for an input impedance of 1MΩ in order to achieve a cut-off frequency of 5Hz. This is confirmed by the results given in Figure 4.14. A termination capacitor of 10nF was selected for terminating each of the new sensors. According to the

results given in Figure 4.14 this yields a cut-off frequency of approximately 10Hz, which is regarded as marginal but adequate for measurements at 50Hz. This yields a good combination for measurements at the power-frequency, i.e. 50Hz.

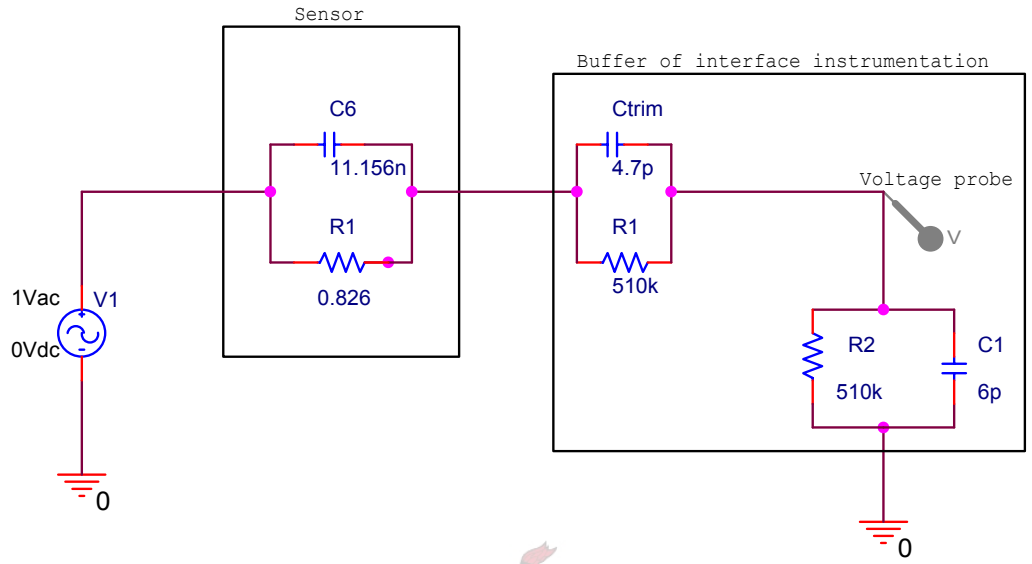


**Figure 4.13: Circuit diagram used in PSpice to do AC sweep simulations for different termination capacitors.**

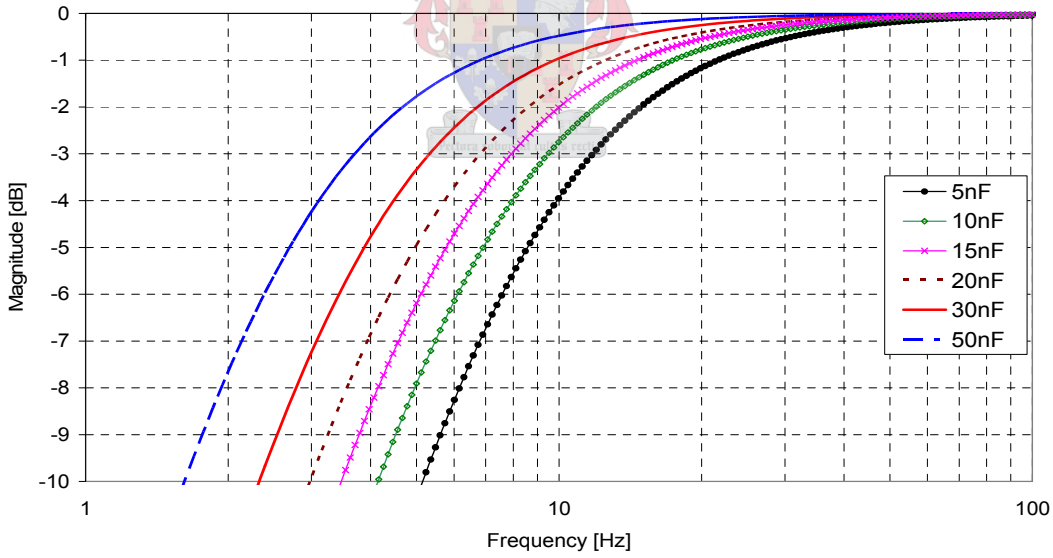


**Figure 4.14: Simulated frequency response of the magnitude of the voltage gain magnitude for termination capacitances of 5nF, 10nF, 15nF, 20nF, 30nF and a 50nF.**

In order to obtain closely matched voltage gains for the three sensors, the values of the termination capacitances must also be matched. Although ceramic (NPO or COG) capacitors have very small tolerances, i.e. as small as 0.1pF for *KEMET* capacitors as shown in

Appendix D.1., *WIMA* capacitors were used due to time and budget constraints. Three 10nF *WIMA* capacitors were hand picked to obtain the capacitors with acceptable tolerances, i.e. 1.13%.

Table 4.4 tabulates the values of $C_{sp}$, $D$ and $R_{sp}$ measured between nodes $s_1$ and $s_2$ for the three sensors with the termination capacitances included. The differences between the values for the three sensors, using *Sensor A* as the reference, are also tabulated. The biggest difference between the capacitances is 0.5%, which is acceptable for the objectives of this project. Better results can be obtained if capacitors with smaller tolerances are used.

**Table 4.4: Parameter values measured with the LCR meter for the three sensor assemblies with termination capacitances included.**

| | Sensor including the termination capacitance | | | | | |
|---|---|---|---|---|---|---|
| | Csp [nF] | Csp dif [nF] | Csp dif [%] | D | Rsp [Ω] | Rsp dif [%] |
| Sensor A | 15.57215 | | | 0.00501 | 20402.21 | |
| Sensor B | 15.644 | -0.07185 | -0.46 | 0.006966 | 14604.57 | 28.42 |
| Sensor C | 15.5513 | 0.02085 | 0.13 | 0.006884 | 14866.63 | 27.13 |

## 4.4. Data acquisition instrumentation design

### 4.4.1. Overview

The complete system topology for evaluating the performance of the sensors consists of the following:

- Three three-element parallel plate sensors.
- Three optical links, each consisting of a transmitter, optical fibre and receiver. The receivers are housed in two two-channel receiver units.
- Two two-channel oscilloscopes.
- A triggering system to trigger the different oscilloscopes simultaneously.

This section reviews the complete data acquisition system.

### 4.4.2. Data acquisition system overview

Two HandyScope 3 (HS3) oscilloscopes are used for measuring the three voltages induced on the sensors in the three-phase topology. The HandyScope 3 is a two channel oscilloscope with a resolution of 12 bits and a maximum sampling rate of 50 MSample/sec. With the accompanying software, the HandyScope 3 can be used as an oscilloscope, a storage oscilloscope, a spectrum analyser, a true RMS voltmeter or transient recorder. The HandyScope connects to a PC through the USB port. The HandyScope does not require an external power supply, but is powered by the computer through the USB port.

The complete measuring system thus consists out of two measuring segments, namely measuring *system#1* and measuring *system#2*, as shown Figure 4.15. A trigger system is used to synchronize the two measuring segments.

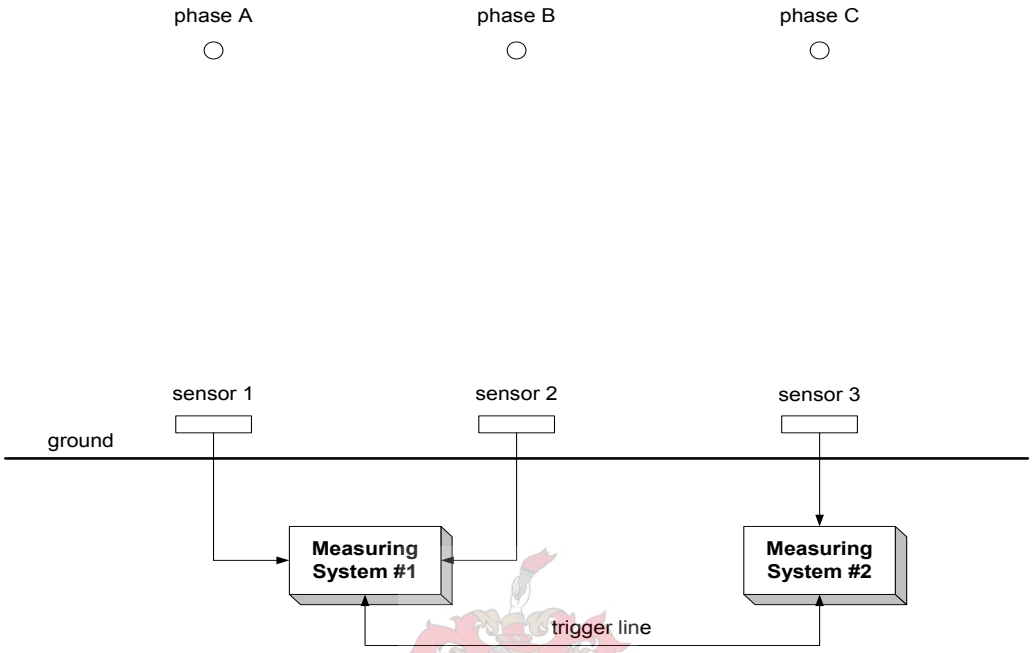


**Figure 4.15 : Block diagram representation of the complete measuring system.**

### 4.4.3. Topology of the individual measurement systems

Figure 4.16 illustrates the connections between measuring systems *#1* and *#2* with the three sensors. Measuring *system#1* consists of *sensor_1, sensor_2, transmitter_1, transmitter_2*, *receiver_1–channel_1* and *receiver_1–channel_2* while measuring *system#2* consists out of *transmitter_3* and *receiver_2–channel_1*.

The three transmitters are located inside the faraday cages of the three three-element sensor assemblies as shown in Figure 4.17 to shield it from capacitive coupling with the overhead conductors. Each transmitter is connected via an optical fibre to a receiver channel on one of the two two-channel receivers units. The output signals from the receiver channels are connected to the two oscilloscopes and the triggering system.

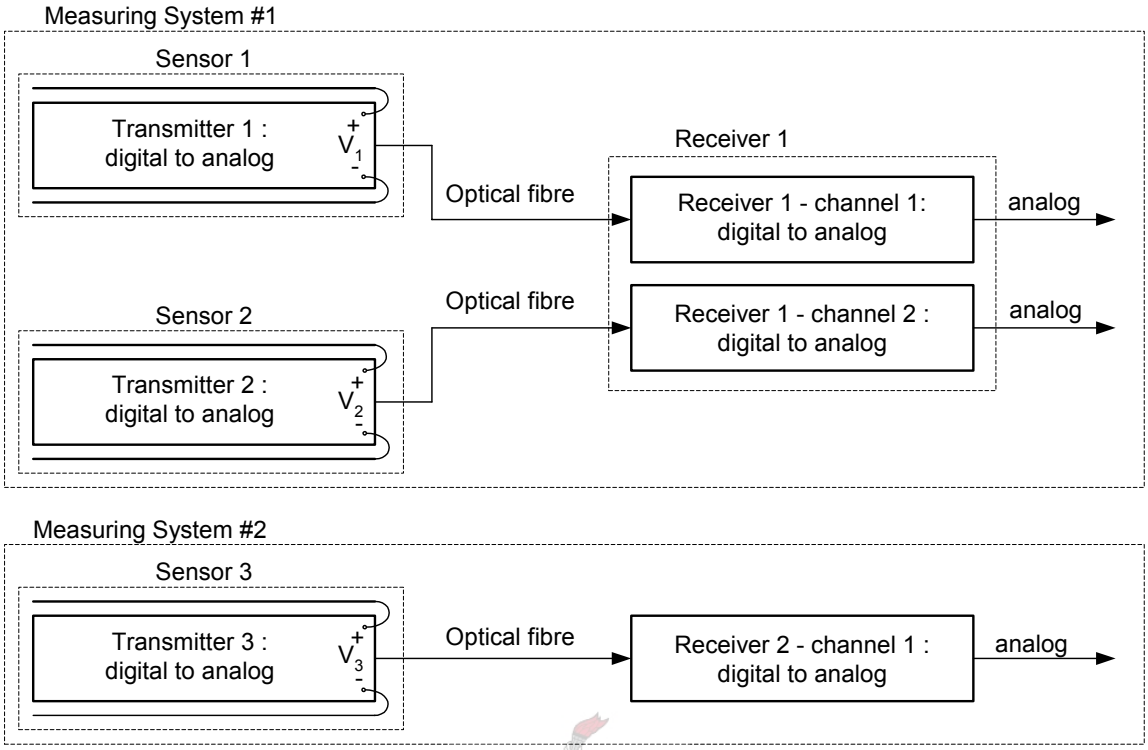


**Figure 4.16 : Block diagram representation of measuring system #1 and #2.**

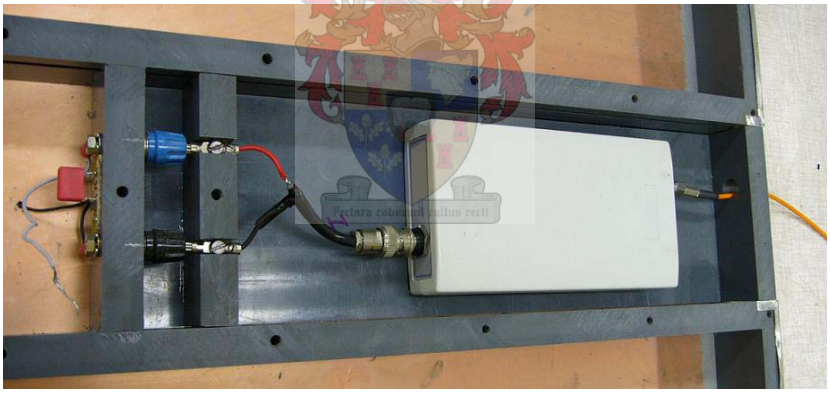

**Figure 4.17 : Photo of a transmitter located inside the faraday cage of a sensor assembly.**

### 4.4.4. Topology of the triggering system

Figure 4.18 shows interconnection between the triggering system and the receivers channel and oscilloscopes. The signal that exits *receiver_2–channel_1* is sent to *oscilloscope_2–channel_1* and to the triggering system. The triggering system is used to trigger the two oscilloscopes via *optocoupler_1* and *optocoupler_2* for electrical isolation purposes. The signal from *sensor_1* is measured by *oscilloscope_1–channel_1,* the signal from *sensor_2* is measured by *oscilloscope_1–channel_2* and the signal from *sensor_3* is measured by *oscilloscope_2–channel 1*

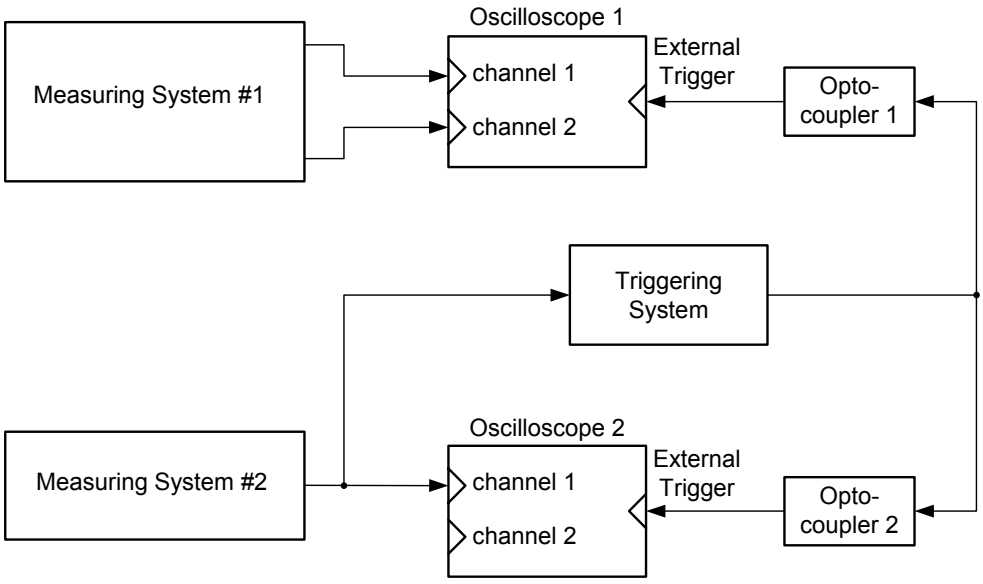


**Figure 4.18 : Block diagram representation of the interconnections between the measurement systems, oscilloscopes and triggering system.**

### 4.4.5. Triggering system design

This section gives a detailed discussion on the development of a triggering system for measuring switching transients. An overview of the triggering system is given and the three main parts of the triggering system are described.

#### 4.4.5.1. System overview

A purpose built triggering system had to be designed to trigger the two oscilloscopes for measuring transient voltage waveforms induced on the sensors by the phase voltages. The triggering system functions to trigger the oscilloscopes simultaneously whenever the following events occur:

- The phase voltages are switched off.
- The phase voltages are switched on.
- A trigger is created manually.

Figure 4.19 shows a block diagram of the topology of the triggering system. The topology consists of the following elements:

- Low-pass filter
- Gain stage
- Window comparator
- Monostable multi-vibrator

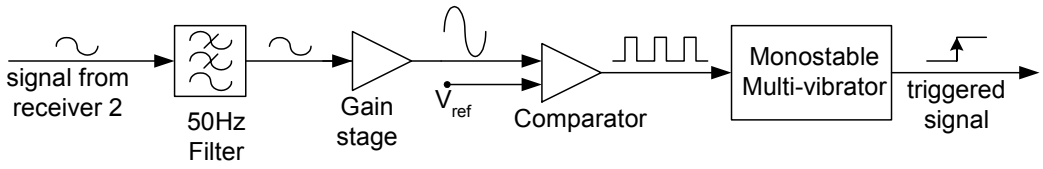


**Figure 4.19: Block diagram representation of the triggering system.**

The triggering system is used to test when one of the signals (measured by one of the sensors) doesn't oscillate anymore, i.e. the voltage equals 0V. The measured waveform must be compared to a specific positive and negative reference voltage to test when the sinusoidal wave is inside specific positive and negative rails. Figure 4.20 illustrates these reference voltages in comparison with the sinusoidal waveform. A reference voltage is chosen because the waveform will almost never equal precisely 0V.

This reference voltage is set at 50% of the amplitude to compensate for the measured voltage's amplitude fluctuations and to ensure no noise would influence the triggering system when the transmission line is switched off. The triggering system will only trigger the oscilloscopes when the waveform is between the rails and stable.

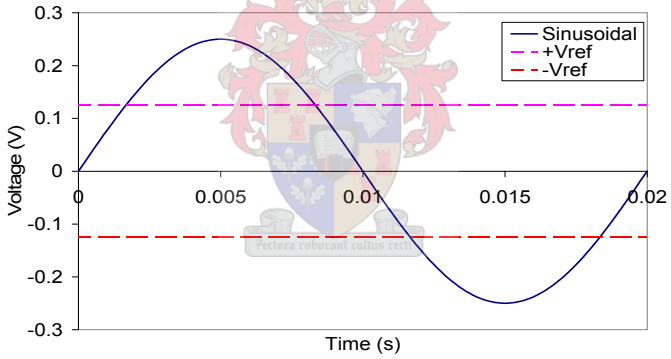


**Figure 4.20 : Comparing the sinusoidal wave with the positive and negative reference voltages.**

### 4.4.5.2. Design of the filter

The input signal to the trigger system requires filtering in order to eliminate false triggers due to high frequency noise and possibly dc offsets. Two options were considered, namely a bandpass filter with a centre frequency of 50Hz and a low-pas filter with a cut-off frequency located above 50 Hz.

The bandpass filter design implemented the second-order biquad topology shown in Figure 4.21 [51], using the design equations presented in Appendix F.1. Figure 4.22 shows the frequency responses of the transfer function of the filter simulated with PSPICE. The magnitude response shown in Figure 4.23 shows -3dB points at 45Hz and 55Hz, yielding a quality factor $Q$ of 5.

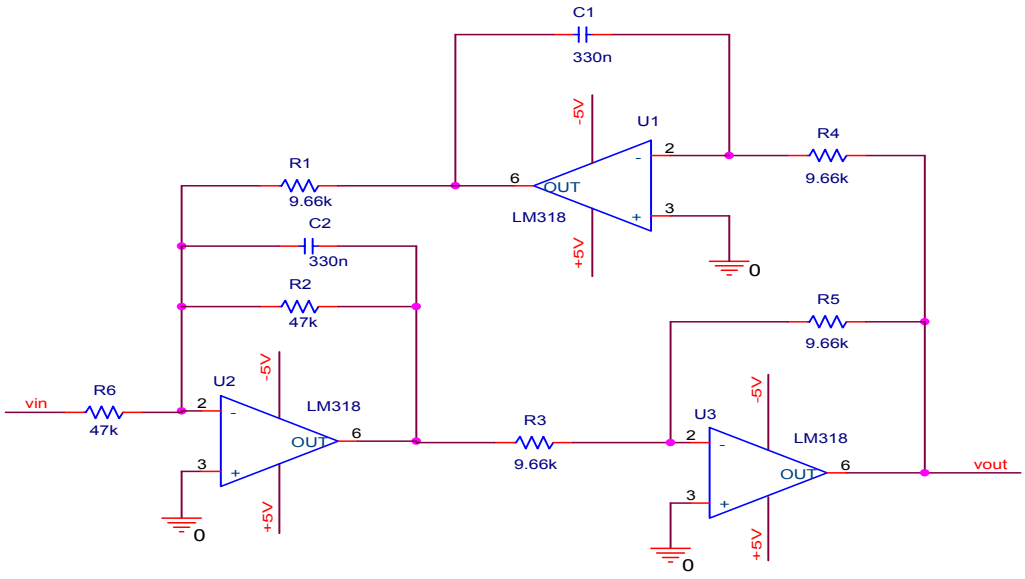


**Figure 4.21 : Circuit diagram of the 50Hz biquad bandpass filter.**

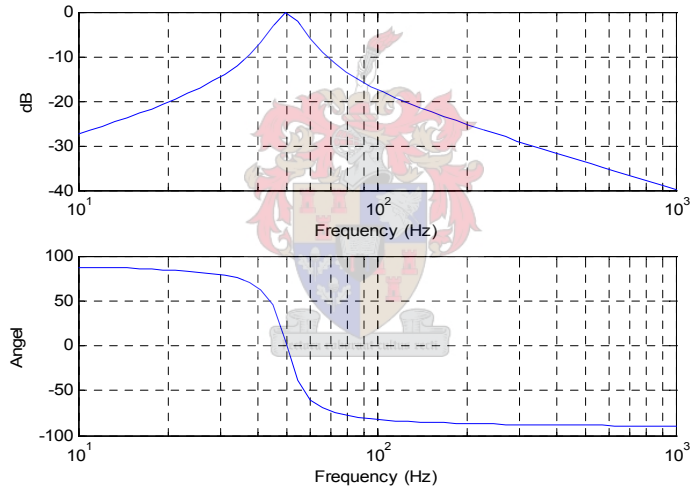


**Figure 4.22 : Simulated frequency responses of the bandpass filter.**

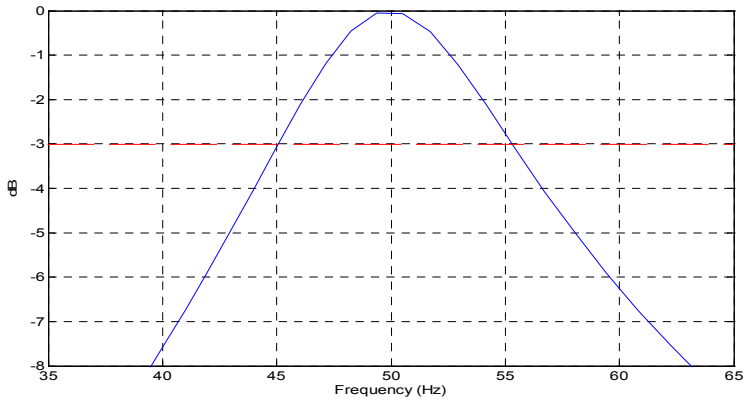


**Figure 4.23 : Simulated magnitude response of the bandpass filter showing the -3dB points.**

Laboratory evaluation of the bandpass filter showed that an oscillation occurs on the output of the filter when the input signal switches off, causing false triggers. The pulse response of the filter was simulated using Simulink, yielding the response shown in Figure 4.24. It is clear that the bandpass filter has a natural 50Hz oscillation whenever a pulse is applied to the input of the filter.

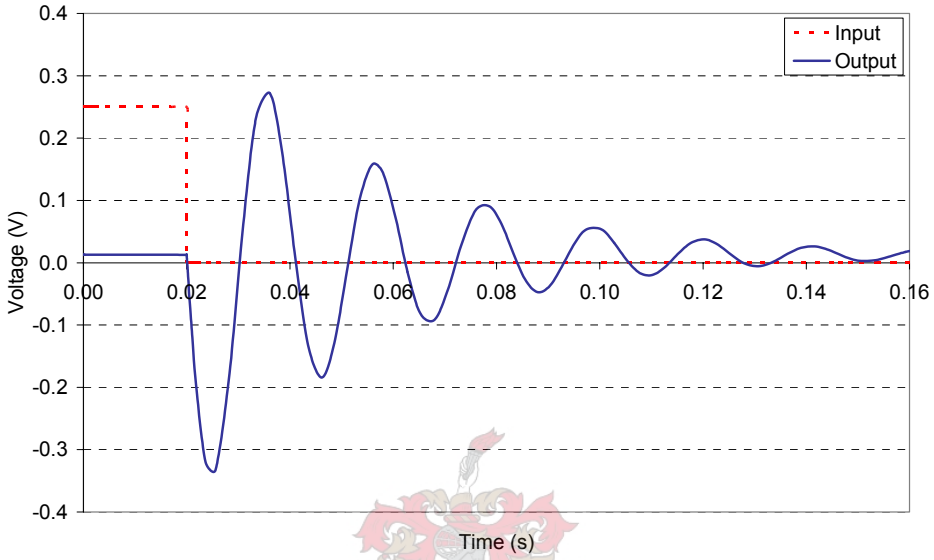


**Figure 4.24 : Simulated pulse response of the 50Hz, biquad bandpass filter.**

To solve the oscillation problem the bandpass filter was replaced by the second-order *VCVS* lowpass filter shown in Figure 4.25 [51]. This yields the transfer function [51]

$$\frac{V_2}{V_1} = \frac{Gb_0}{s^2 + b_1 s + b_0} \tag{4.10}$$

where $V_1$ denotes the input voltage, $V_2$ denotes the output voltage, $s = j\omega_0$, $d_0$ and $d_1$ denotes the filter coefficients and $G$ denotes the gain of the filter. The *VCVS* low-pass filter topology is one of the more popular configurations with non-inverting gain. Appendix F.2 presents the calculations for designing the VCVS, second-order low-pass filter.

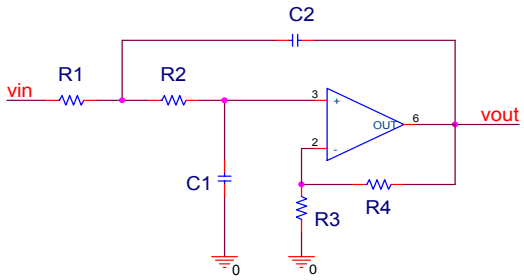


**Figure 4.25 : Circuit diagram of a second-order VCVS low-pass filter [51].**

Although the gain of the *VCSV* can be set precisely with a potentiometer instead of resistors $R_3$ and $R_4$, a non-inverting, adjustable gain stage was added at the output of the low-pass filter to match the output signal of the filter to the window comparator. It requires a minimal number of elements, has a relative ease of adjustment of characteristics and low output impedance. Figure 4.26 shows the complete low-pass filter, including the non-inverting gain stage.

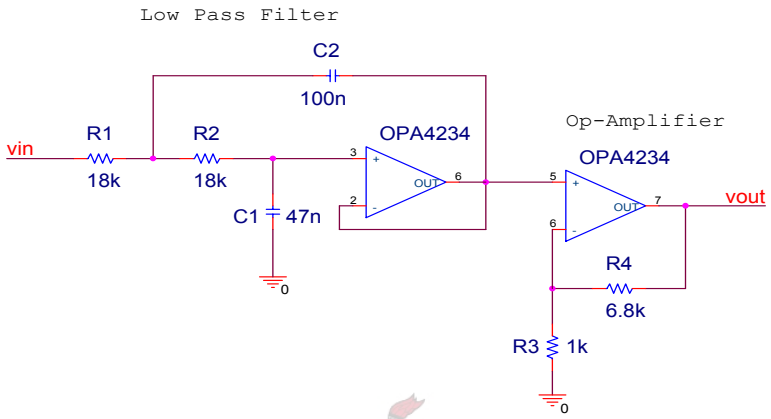


**Figure 4.26 : The VCVS, second-order low-pass filter, including the non-inverting gain stage.**

Figure 4.27 shows the frequency response of the low-pass filter. From Figure 4.27 it can be seen that the -3dB point is at 126 Hz. Figure 4.28 shows the pulse response of the designed low-pass filter and it can be seen that no oscillations were created.

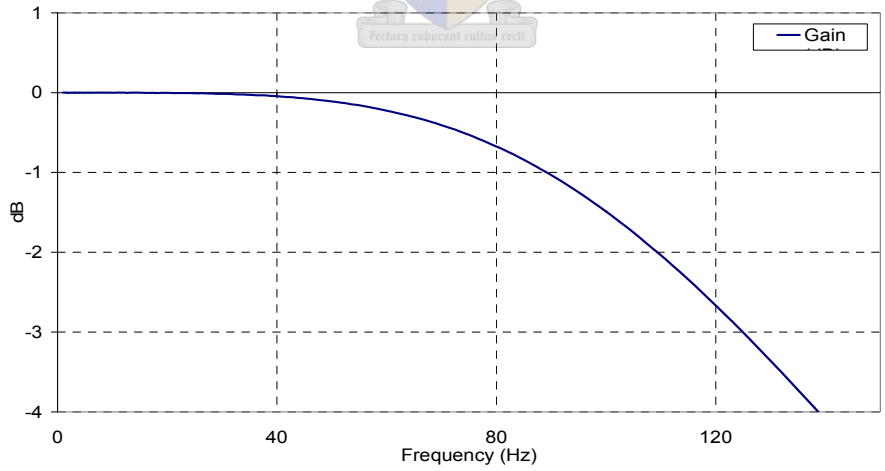


**Figure 4.27 : Frequency response of the VCVS, second-order low-pass filter.**

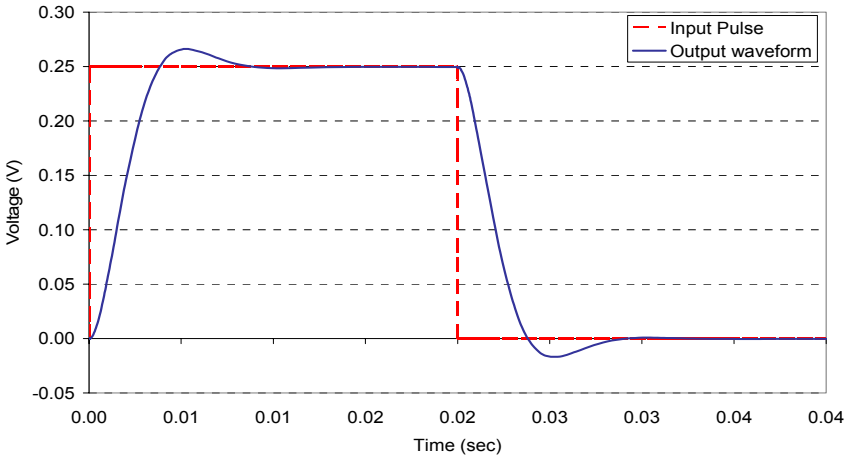


**Figure 4.28 : Pulse response of the VCVS, second-order low-pass filter.**

### 4.4.5.3. Design of the window comparator

The comparator is essentially an operational amplifier (op-amp) operating in an open-loop configuration and as the name implies, a comparator compares two voltages to determine the larger value [52]. For the purpose of this design a window comparator was used. A typical window comparator uses two comparators and a single op-amp to determine whether a voltage is inside or outside a boundary region. Figure 4.29 shows a typical implementation. $IC_1$ is an inverting op-amp with a gain of -1. $V_{REF}$ and - $V_{REF}$ create the window limits. When $V_{IN}$ becomes more positive than $V_{REF}$, the output of $IC_{2A}$ goes low. When $V_{IN}$ becomes more negative than - $V_{REF}$, the output of $IC_{2B}$ goes low. If $V_{IN}$ is lower than $V_{REF}$ and greater than - $V_{REF}$, both outputs of $IC_2$ remain high.

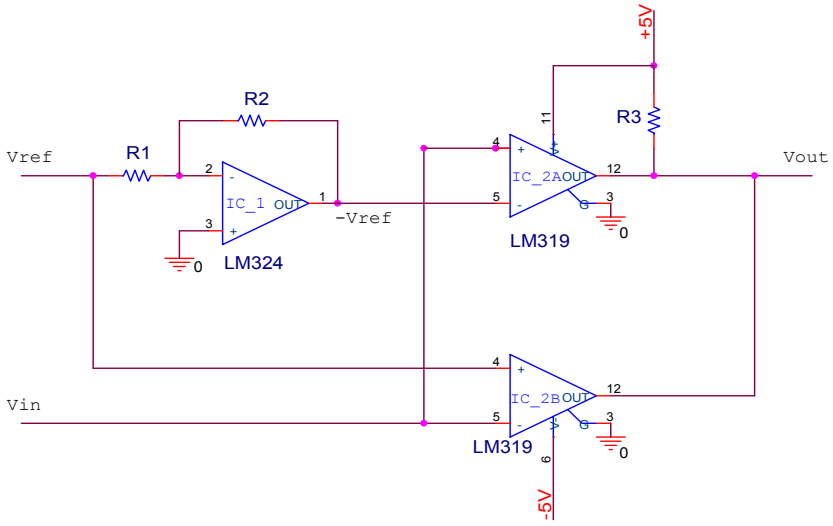


**Figure 4.29 : Circuit diagram of a typical window comparator [53].**

The window comparator was implemented using the LM319, high speed dual comparator, with a typical response time of 80ns [52]. An open-loop comparator circuit may exhibit unacceptable behaviour due to noise in the system. This can be addressed by using a Schmitt trigger. The Schmitt trigger or *bistable multivibrator* uses positive feedback with a loop-gain greater than unity to produce bistable characteristics [52]. Figure 4.30 shows the circuit diagram of the window comparator, including the Schmitt trigger, as implemented. The relevant design equations are given in Appendix F.3.

The reference voltage ($V_{REF}$) was implemented using the circuit shown in Figure 4.31. A zener diode and variable resistor was used to create an adjustable constant reference voltage that could be adjusted between 0V and 1.69V.

Figure 4.32 shows the input and output waveforms of the comparator for a sinusoidal input voltage waveform.

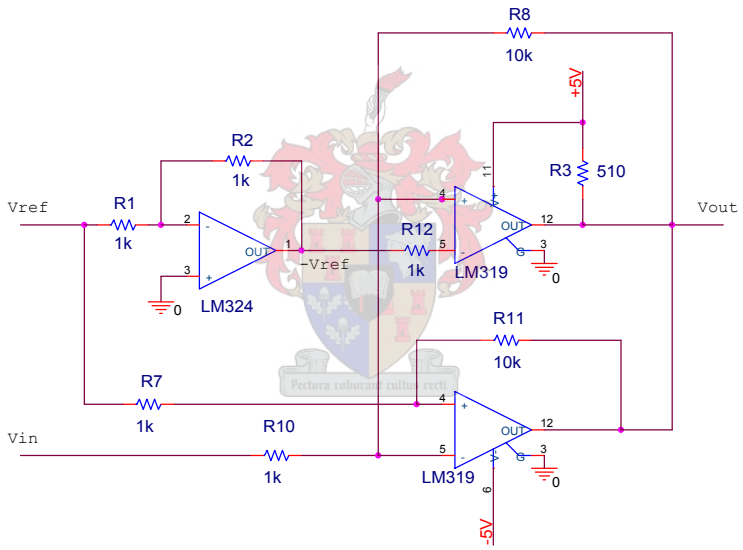


**Figure 4.30 : Circuit diagram of the window comparator with Schmitt trigger.**

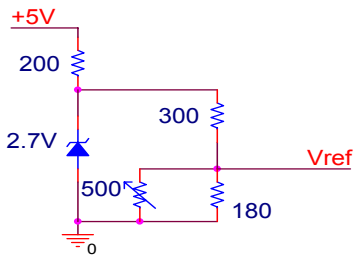


**Figure 4.31 : Circuit diagram of reference voltage source.**

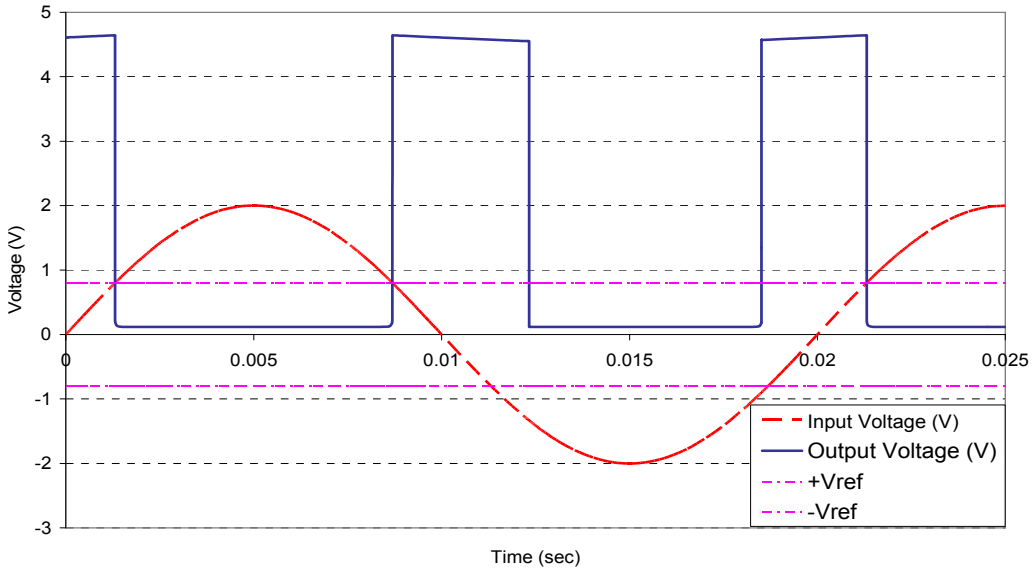


**Figure 4.32 : Input and output waveform of the window comparator.**

### 4.4.5.4. Design of the re-triggerable monostable multi-vibrator

A monostable multi-vibrator has one stable sate in which it can remain indefinitely if not disturbed. However, a trigger pulse can force the circuit into a quasi-stable state for a definite time, producing an output pulse with a particular height and width. The circuit then returns to its stable state until another trigger pulse is applied [52]. The re-triggerable monostable will begin a new timing cycle if the input triggers again during the duration of the output pulse. The output pulse will be longer than usual if it is retriggered during the pulse, finally terminating one pulse width after the last trigger [55].

This property of the re-triggerable monostable multi-vibrator is used to test when the measured signal turns to zero. The monostable is used to test when the signal is switched on or off. The pulse created by the comparator, illustrated in Figure 4.32, is used to trigger the monostable. If the measured signal becomes smaller than $V_{REF}$ for longer than a specified time, the monostable will trigger the oscilloscopes.

The SN74LS122, re-triggerable monostable multi-vibrator is used in the triggering system [56]. The comparator creates a pulse every 10ms, thus the output pulse duration only requires to be set longer than 10ms. Figure 4.33 shows the circuit diagram of the re-triggerable monostable multi-vibrator that is implemented into the triggering system. A complete description of the re-triggerable monostable multi-vibrator and of the calculations done to design the circuit is given in Appendix F.4.

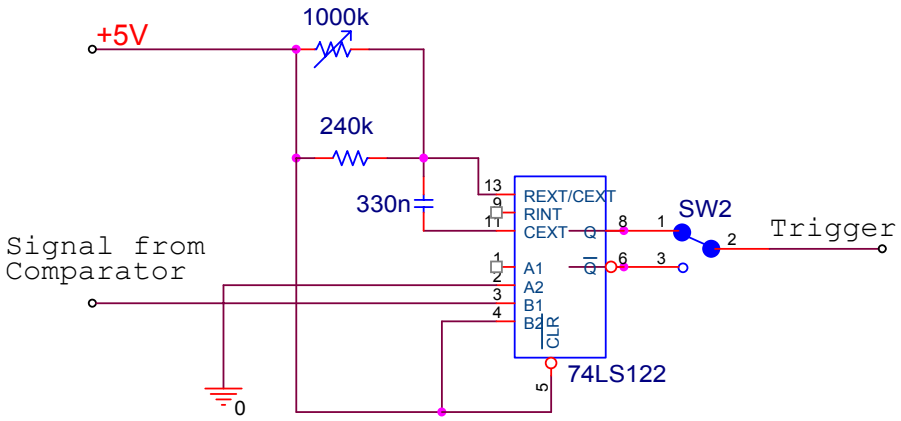


**Figure 4.33 : Circuit diagram of the re-triggerable monostable multi-vibrator.**

A two way switch is inserted between pins 6 and 8 of the monostable to enable triggering when the transmission line is either switched off or on. Figure 4.34 illustrates the input and output waveforms when the comparator stopped supplying pulses (three-phase line is switched off) to the monostable multi-vibrator. Figure 4.35 illustrates the input and output waveforms when the comparator started supplying pulses (three-phase line is switched on) to the monostable multi-vibrator. Figure F.7 (Appendix F) illustrates how the output of the monostable multi-vibrator operates.

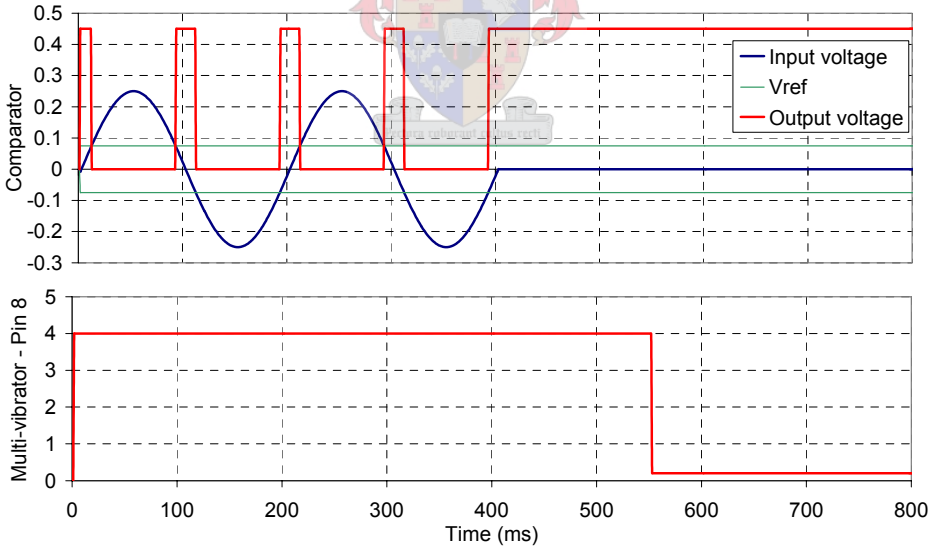


**Figure 4.34 : Input and output waveforms of the monostable multi-vibrator when the input voltage switches off.**

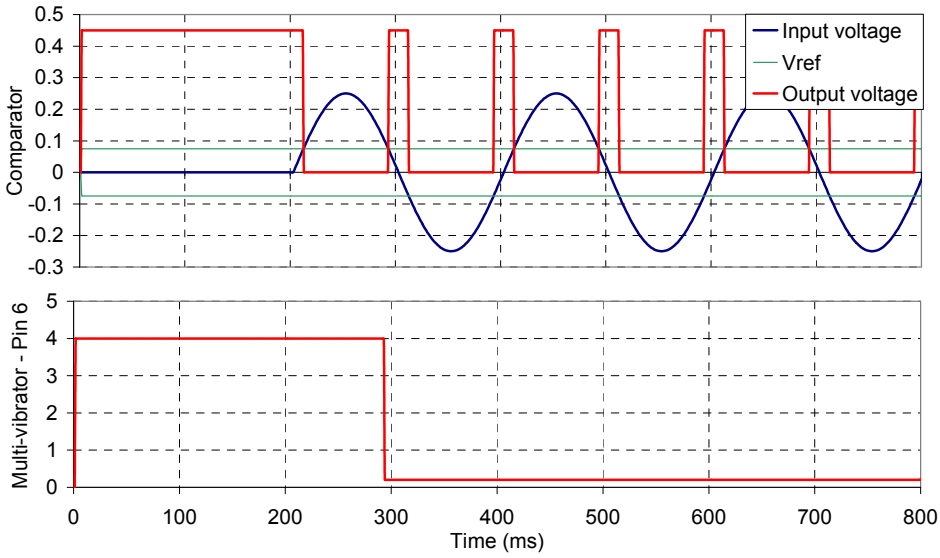


**Figure 4.35 : Input and output waveforms of the monostable multi-vibrator when the input voltage switches on.**

### 4.4.5.5. Complete trigger system

Figure 4.37 shows the circuit diagram of the complete triggering system consisting of the lowpass filter, gain stage, comparator and monostable multi-vibrator. Figure 4.36 shows a photograph of the complete triggering system

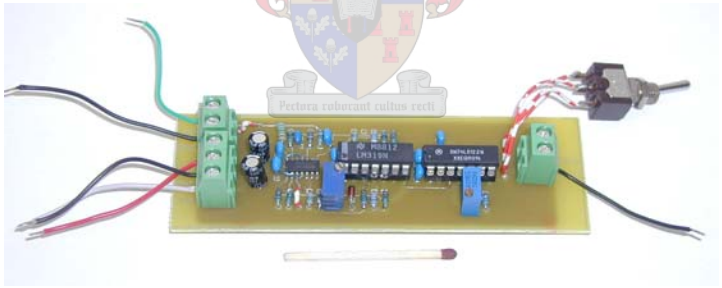

**Figure 4.36 : Photograph of the complete triggering system.**

Section 4.4.4 discussed the assembly of the measuring system. Figure 4.38 shows this assembly and illustrates the location of the triggering system. The triggering system's output is split and connected to the two optocouplers which in turn is connected to the two oscilloscopes' external trigger-in ports.

The cables that are used to connect the two oscilloscopes via the optocouplers have to be very long (at least 8m), in order for the two measuring stations to be placed on opposite sides of the transmission line. The two measuring stations are electrically isolated from each other by optocouplers in order to eliminate a floating ground through induction on the long wires.

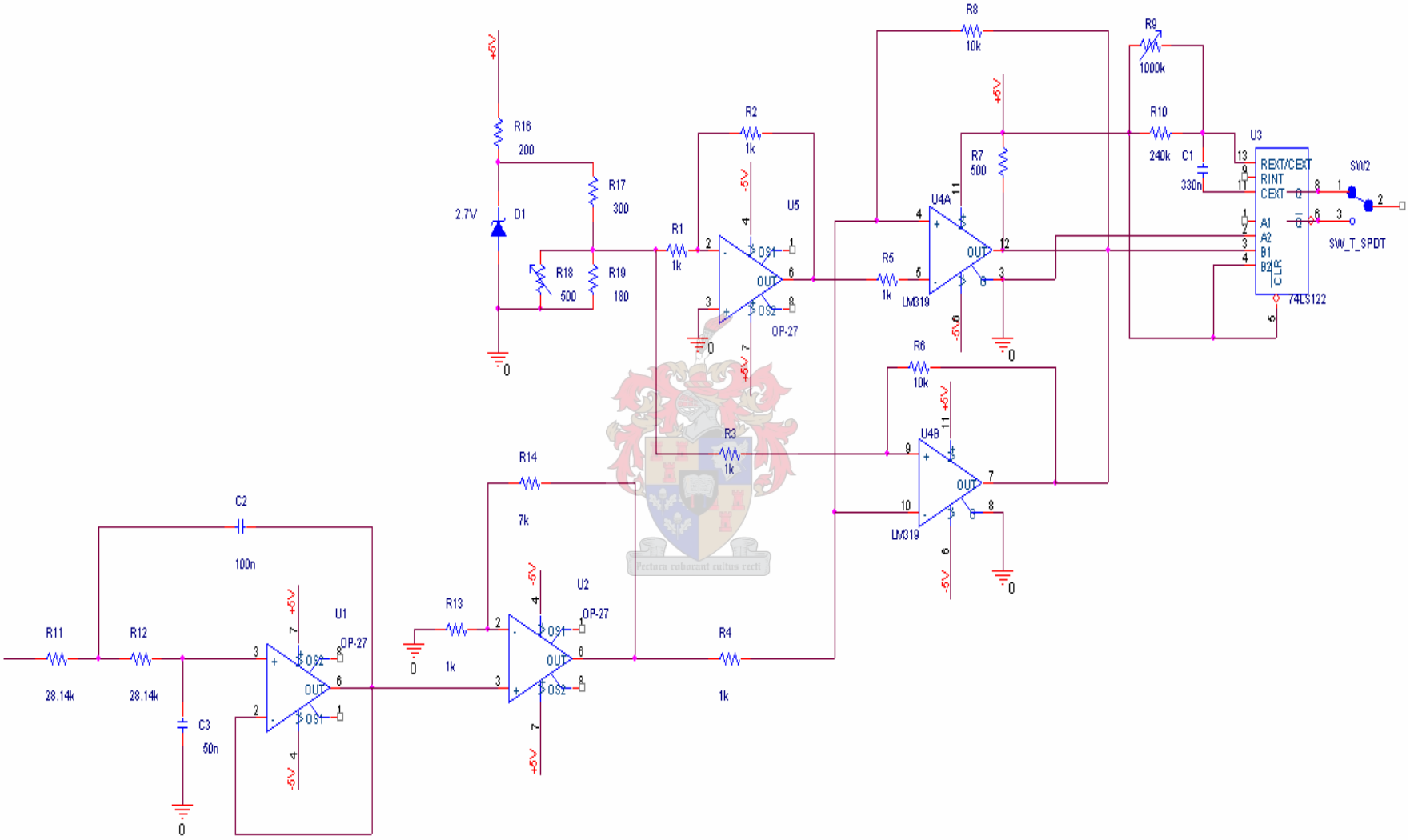


**Figure 4.37 : Circuit diagram of the complete triggering system.**

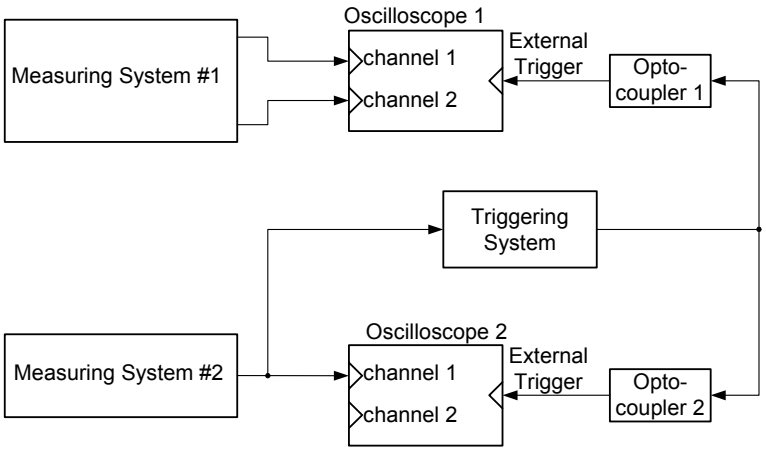


**Figure 4.38: Block diagram of measurement system #1 and #2, connected to the two HandyScope oscilloscopes as well as the triggering system with the two optocouplers.**

## Description of the Optocoupler

The 6N137 optocoupler is used in this project. It is an optical gate that combines a GaAsP light emitting diode and an integrated high gain photo detector. An enable input allows the detector to be strobed. Appendix F.5 gives a detailed description of the optocoupler. Figure 4.39 shows the circuit diagram of the optocoupler. A VN10KM, n-channel, enhancement-mode MOSFET is used. The MOSFET's gate is connected to the output of the triggering system. Pin 6 is connected to the External Trigger In (pin 8) of the HandyScope.

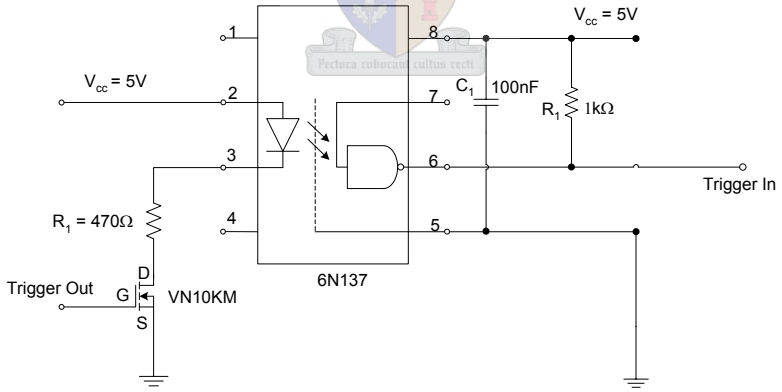


**Figure 4.39: Circuit diagram of the optocoupler connected to the oscilloscopes.**

## Description of the oscilloscope

A 25 pin female Sub-D connector is available if required to connect to the HandyScope 3. The pins used in this project were the following:

5 5 V out, 10mA max
7 Ground

8 External trigger in (TTL)

The trigger source of the HandyScope's oscilloscope can be set to different sources to determine when measuring has to start. In this project the two HandyScope's triggering are set to the digital external trigger.

#### 4.4.5.6. Laboratory evaluation of the triggering system

The complete triggering system was tested under laboratory conditions to verify that the system work correctly without excessive time delays. The triggering system was connected to two oscilloscopes, via the optocouplers and fibre optic cable, and measured a sinusoidal wave supplied by a normal signal generator. Figure 4.34 and Figure 4.35 show that the system triggers about one wave-length after the input signal turns on or off.

Figure 4.40 shows the waveforms recorded by the two oscilloscopes when the system is triggered by switching OFF the measured sinusoidal wave. Figure 4.41 shows the waveform recorded by the two oscilloscopes when the system is triggered by switching ON the measured sinusoidal wave.

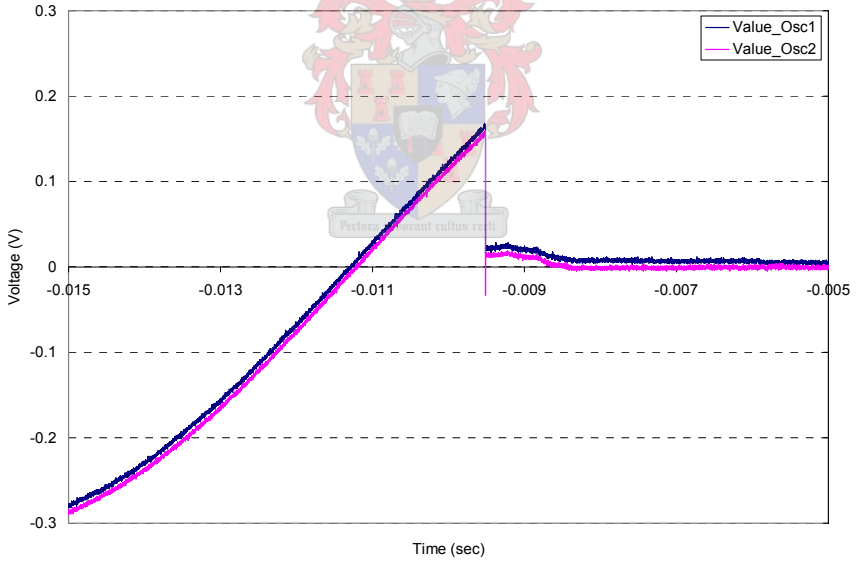


**Figure 4.40 : Comparing the values measured by the two oscilloscopes if triggered by the external triggering system. The system was set to trigger when a sinusoidal wave was switched off. Sample frequency = 1M/sec; Samples = 50000.**

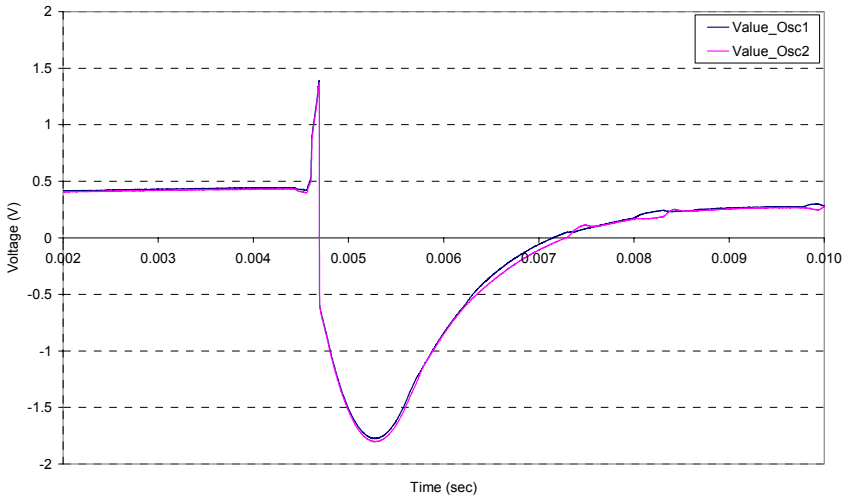


**Figure 4.41 : Comparing the values measured by the two oscilloscopes if triggered by the external triggering system. The system was set to trigger when a sinusoidal wave was switched on. Sample frequency = 500kS/sec; Samples = 20000.**

## 4.5. Conclusions

The Thévenin equivalent impedances of the three redesigned sensors were measured and compared. These tests show good comparison between the three sensors after the termination capacitances are corrected. Frequency tests are done with different termination capacitors illustrating good frequency response at the power frequency of 50Hz. Due to availability 10nF capacitors are used for the termination capacitors of the new sensors.

Experimental evaluation of the triggering system is performed and provided good results for triggering on switching transients. The system works fast and accurately and is inexpensive.

# 5. Open-air capacitive voltage sensor topologies for three-phase transmission configurations

## 5.1. Introduction

The main objective of this research project is the development of a methodology to measure three-phase transmission line voltages using an array of three open-air capacitive voltage sensors. This chapter contributes toward this objective by analysing the voltage coupling relationships for a three-phase transmission line configuration with multiple capacitive sensors located near the earth plane. A typical 400 kV transmission line configuration is used, namely a three-phase, flat, single circuit line configuration. Single-plate sensors are used in the initial investigations in order to simplify the overall line and sensor topologies and the associated voltage equations.

Various sensor positions are considered and the implications of increasing the number of sensors to five are investigated. Determination of the voltage transfer functions between the various phase conductors and sensors from the measured phase voltages and sensor voltages are investigated. This is supported by simulations of the capacitive coupling matrix of the configurations using ELECTRO.

## 5.2. Single-element plate capacitive sensor arrangement with three sensors

### 5.2.1. Physical configuration

Figure 5.1 shows the geometric arrangement of three floating single-element plate sensors located symmetrically between a three-phase, flat, single-circuit, transmission line configuration and an infinite ground plane. Each phase is represented by a single overhead conductor. The notations, i.e. $p_1$, $p_2$, $p_3$, $s_1$, $s_2$, $s_3$ and $g$, denote the various elements, namely the three phases, three sensors and the ground plane respectively. The dimension parameters shown in Figure 5.1 are defined as follows:

| | |
|---|---|
| $r_l$ | Phase conductor radius [m] |
| $h_l$ | Phase conductor height above ground [m] |
| $h_s$ | Sensor height above ground [m] |
| $w_s$ | Sensor width [m] |
| $p_l$ | Distance between the phase conductors [m] |

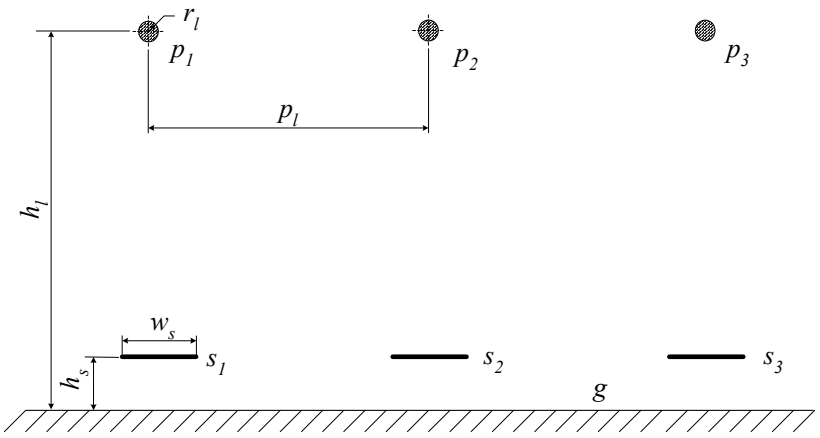


**Figure 5.1: Topology of three single-element plate sensors underneath a flat, three-phase single circuit line configuration.**

### 5.2.2. Voltage relationships

It is shown in Appendix J.3 that the voltage induced on a capacitive sensor underneath a three-phase transmission line is proportional to the electric field strength at that position. Equations (J.25), (J.26) and (J.27) (Appendix J) prove that the electric field strength, at a specific point in space, due to the charge of an overhead conductor is linearly proportional to the magnitude of the charge as well as the geometry of the point in reference to that conductor. The charge is linearly proportional to the voltage on the conductor as well as the capacitive matrix of the transmission line configuration. The electric field strength, at a specific point in space, is thus linearly proportional to the capacitive matrix of the line.

The three phase voltages, i.e. $v_{p1}$, $v_{p2}$ and $v_{p3}$, induce voltages $v_{s1}$, $v_{s2}$ and $v_{s3}$ respectively on the three sensors through capacitive coupling. The voltage transfer functions between the various phases and the sensors are thus determined by the capacitive coupling matrix between these elements. Figure 5.2 shows the relevant phase and sensor voltages and defines a set of voltage transfer functions, namely $G_{s1p1}$, $G_{s1p2}$, $G_{s1p3}$, $G_{s2p1}$, $G_{s2p2}$, $G_{s2p3}$, $G_{s3p1}$, $G_{s3p2}$ and $G_{s3p3}$, to assist in defining the capacitive coupling elements between phase conductors and sensors. For instance, $G_{sipj}$ denotes the voltage transfer function between phase conductor $p_i$ and sensor $s_i$.

The voltages induced on the sensors for the topology shown in Figure 5.1 are given by the system of linear equations

$$\left[v_s\right] = \left[G\right]\left[v_p\right] \tag{5.1}$$

where

$$\left[v_s\right] = \left[v_{s1} \quad v_{s2} \quad v_{s3}\right]^T, \tag{5.2}$$

$$\left[v_p\right] = \left[v_{p1} \quad v_{p2} \quad v_{p3}\right]^T, \tag{5.3}$$

and

$$\left[G\right] = \begin{bmatrix} G_{s1p1} & G_{s1p2} & G_{s1p3} \\ G_{s2p1} & G_{s2p2} & G_{s2p3} \\ G_{s3p1} & G_{s3p2} & G_{s3p3} \end{bmatrix}. \tag{5.4}$$

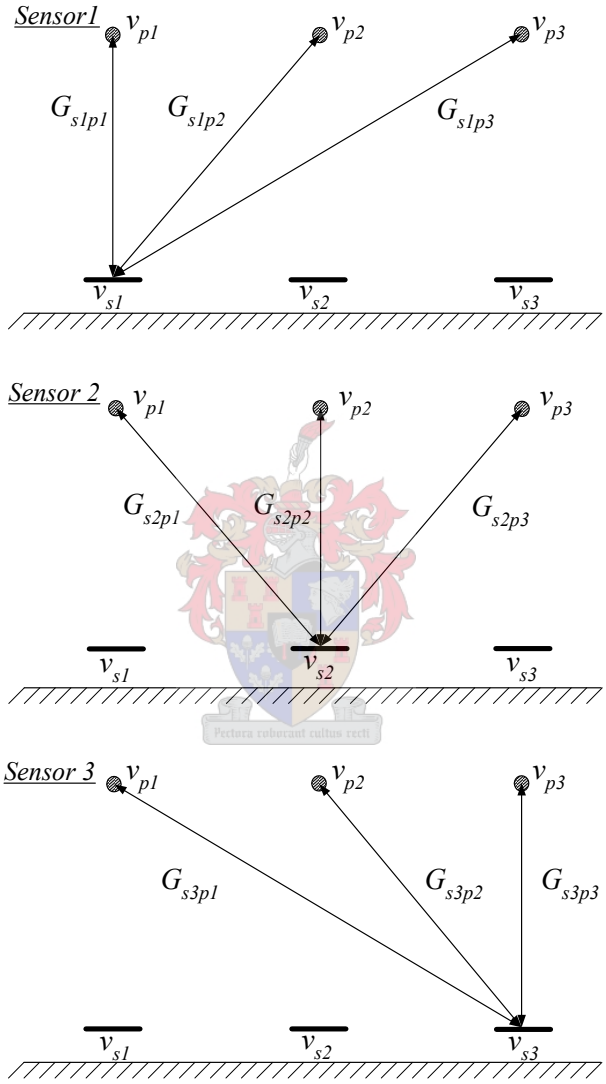


**Figure 5.2: Voltage transfer function definitions for a three single-plate sensor topology.**

Based on the assumption that leakage conductances are neglected in this investigation, the voltage transfer functions are determined by the capacitive matrix elements of the transmission line and sensor topology. Due to symmetry, some of the capacitive matrix elements and the associated voltage transfer functions are equal. This property can be used to simplify the voltage equations. If the voltage transfer functions and measured sensor voltages

references in equation (5.1) are known, the unknown phase voltages can be calculated by solving the linear system.

The symmetry of the topology shown in Figure 5.1 gives rise to the following simplifying relationships:

$$G_1 = G_{s1p1} = G_{s3p3} \tag{5.5}$$

$$G_2 = G_{s1p2} = G_{s3p2} \tag{5.6}$$

$$G_3 = G_{s1p3} = G_{s3p1} \tag{5.7}$$

$$G_4 = G_{s2p1} = G_{s2p3} \tag{5.8}$$

$$G_5 = G_{s2p2}. \tag{5.9}$$

The transfer function matrix **G** is then given by the relationship

$$\boldsymbol{G} = \begin{bmatrix} G_1 & G_2 & G_3 \\ G_4 & G_5 & G_4 \\ G_3 & G_2 & G_1 \end{bmatrix}. \tag{5.10}$$

Since the voltage transfer functions are determined by the capacitive coupling elements between the conductor and sensor elements in the topology, the capacitive coupling matrix of the topology, i.e.

$$[C] = \begin{bmatrix} C_{s1p1} & C_{s1p2} & C_{s1p3} \\ C_{s2p1} & C_{s2p2} & C_{s2p3} \\ C_{s3p1} & C_{s3p2} & C_{s3p3} \end{bmatrix}, \tag{5.11}$$

was determined using the ELECTRO software package. This yields the result

$$[C] = \begin{bmatrix} -38.5 & -27.1 & -15.5 \\ -27.3 & -34.2 & -27.3 \\ -15.5 & -27.1 & -38.5 \end{bmatrix} pF \tag{5.12}$$

for a line configuration shown in Figure 5.1 and with the dimensions given in Table 5.1. This matrix exhibit the same symmetry relationships reflected in equation (5.10). The capacitive coupling elements given in equation (5.12) show a difference of 10.98% between coupling factors $C_{s1p1}$ and $C_{s2p2}$ and a difference of 0.9% between coupling factors $C_{s1p2}$ and $C_{s2p1}$.

**Table 5.1: Dimensions parameters for the line configuration shown in Figure 5.1.**

| Parameter | Value | Parameter | Value |
|---|---|---|---|
| $r_l$ | 0.01 m | $h_l$ | 18 m |
| $h_s$ | 0.3 m | $w_s$ | 0.05 m |
| $p_l$ | 8.5 m | | |

This knowledge can be used to obtain an approximate simplified solution by introducing the simplifying relationships

$$G_1 = G_{s1p1} = G_{s2p2} = G_{s3p3} \tag{5.13}$$

$$G_2 = G_{s1p2} = G_{s2p1} = G_{s2p3} = G_{s3p2} \tag{5.14}$$

and

$$G_3 = G_{s1p3} = G_{s3p1}. \tag{5.15}$$

This yields the voltage transfer function matrix

$$\boldsymbol{G} = \begin{bmatrix} G_1 & G_2 & G_3 \\ G_2 & G_1 & G_2 \\ G_3 & G_2 & G_1 \end{bmatrix}. \tag{5.16}$$

Appendix C discusses the different approaches that are formulated to calculate the capacitive coupling factors due to this assumption.

### 5.2.3. Sensors located off-centre under the outer phases

In practice, i.e. under field conditions, aligning the sensors directly under the transmission line conductors poses a cumbersome task due to the height of the conductors. This task can be simplified by positioning the centre sensor $s_2$ directly under the centre conductor $p_2$, and position sensor $s_1$ and $s_2$ symmetrically relative to sensor $s_2$ as illustrated in Figure 5.3 and Figure 5.4. This causes that the symmetry relationships in the voltage transfer function matrix and the capacitive coupling matrix are maintained, thereby yielding the same voltage transfer function matrix given in equation (5.10).

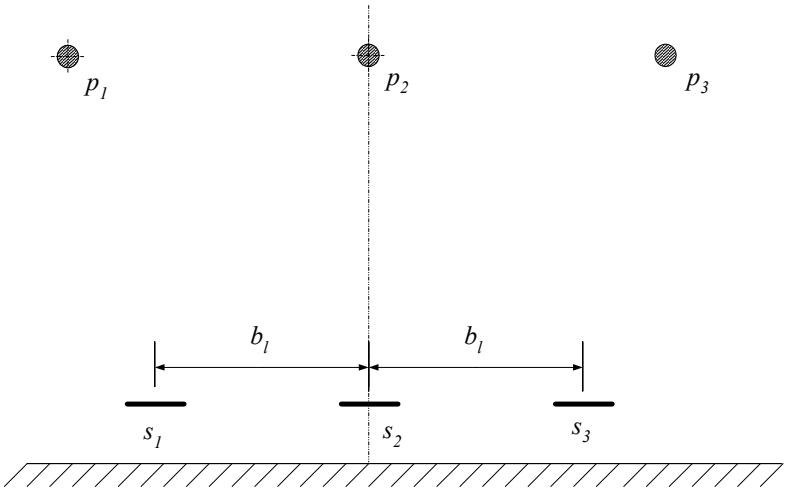


**Figure 5.3: Topology of three single-element plate sensors with a flat, three-phase single circuit line configuration with offset sensor positions.**

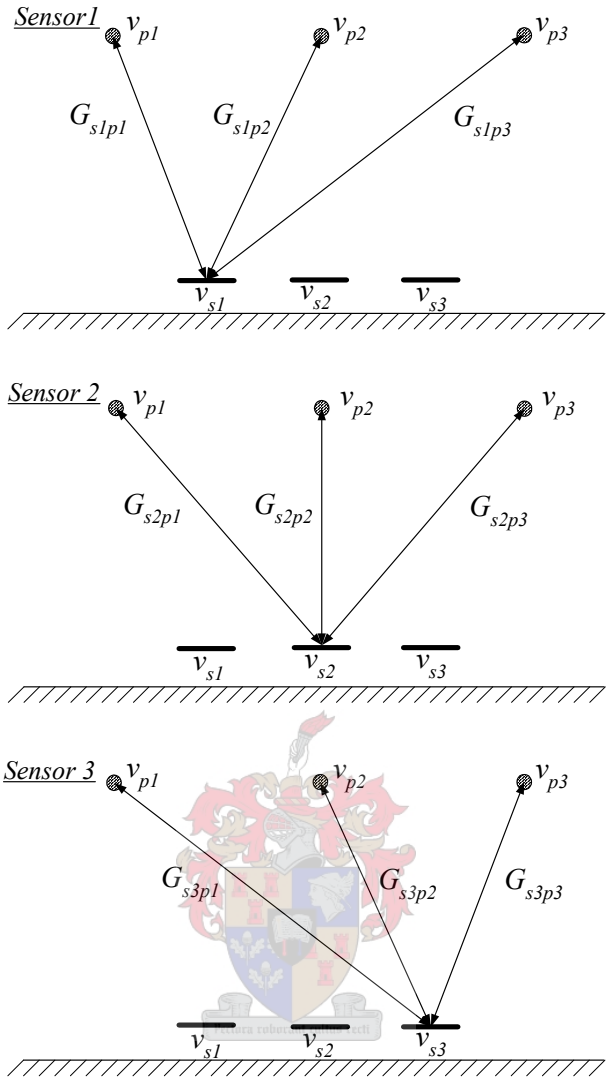


**Figure 5.4: Voltage transfer function definitions for three single-plate sensor topology with offset sensor positions.**

## 5.3. Single-element plate capacitive sensor arrangement with five sensors

In the previous sections three sensors are used to evaluate the capacitive coupling matrix. It is of interest to consider the case where more than three sensors are employed. This introduces redundancy into the set of equations, and can be used for checking and possible calibration purposes. Figure 5.5 shows a topology with five floating sensors arranged symmetrically with respect to the centre phase conductor. The letters in circles, i.e. *1, 2, 3,* $s_1$, $s_2$, $s_3$, $s_4$, $s_5$ and *g,* denote the various elements, namely the three phases, the five sensors and the ground plane respectively. Figure 5.6 shows the relevant phase and sensor voltages and defines a set of voltage transfer functions, namely $G_{s1p1}$, $G_{s1p2}$, $G_{s1p3}$, $G_{s2p1}$, $G_{s2p2}$, $G_{s2p3}$, $G_{s3p1}$, $G_{s3p2}$, $G_{s3p3}$, $G_{s4p1}$, $G_{s4p2}$, $G_{s4p3}$, $G_{s5p1}$, $G_{s5p2}$ and $G_{s5p3.}$, to assist in defining the capacitive coupling elements

between phase conductors and sensors. For instance, $G_{sipj}$ denotes the voltage transfer function between phase conductor $p_i$ and sensor $s_i$.

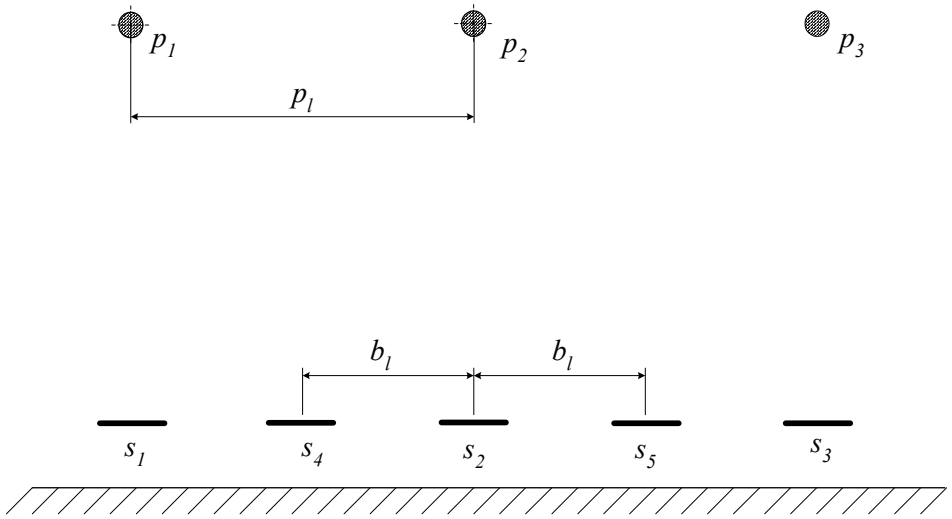


**Figure 5.5: Topology of five single-element plate sensors with a flat, three-phase single circuit line configuration.**

The symmetry of the topology gives rise to the following simplifying relationships:

$$G_1 = G_{s1p1} = G_{s3p3} \tag{5.17}$$

$$G_2 = G_{s1p2} = G_{s3p2} \tag{5.18}$$

$$G_3 = G_{s1p3} = G_{s3p1} \tag{5.19}$$

$$G_4 = G_{s2p1} = G_{s2p3} \tag{5.20}$$

$$G_5 = G_{s2p2} \tag{5.21}$$

$$G_6 = G_{s4p1} = G_{s5p3} \tag{5.22}$$

$$G_7 = G_{s4p2} = G_{s5p2} \tag{5.23}$$

$$G_8 = G_{s4p3} = G_{s5p1} \tag{5.24}$$

The voltage transfer function matrix **G** is then given by

$$\boldsymbol{G} = \begin{bmatrix} G_1 & G_2 & G_3 \\ G_4 & G_5 & G_4 \\ G_3 & G_2 & G_1 \\ G_6 & G_7 & G_8 \\ G_8 & G_7 & G_6 \end{bmatrix}. \tag{5.25}$$

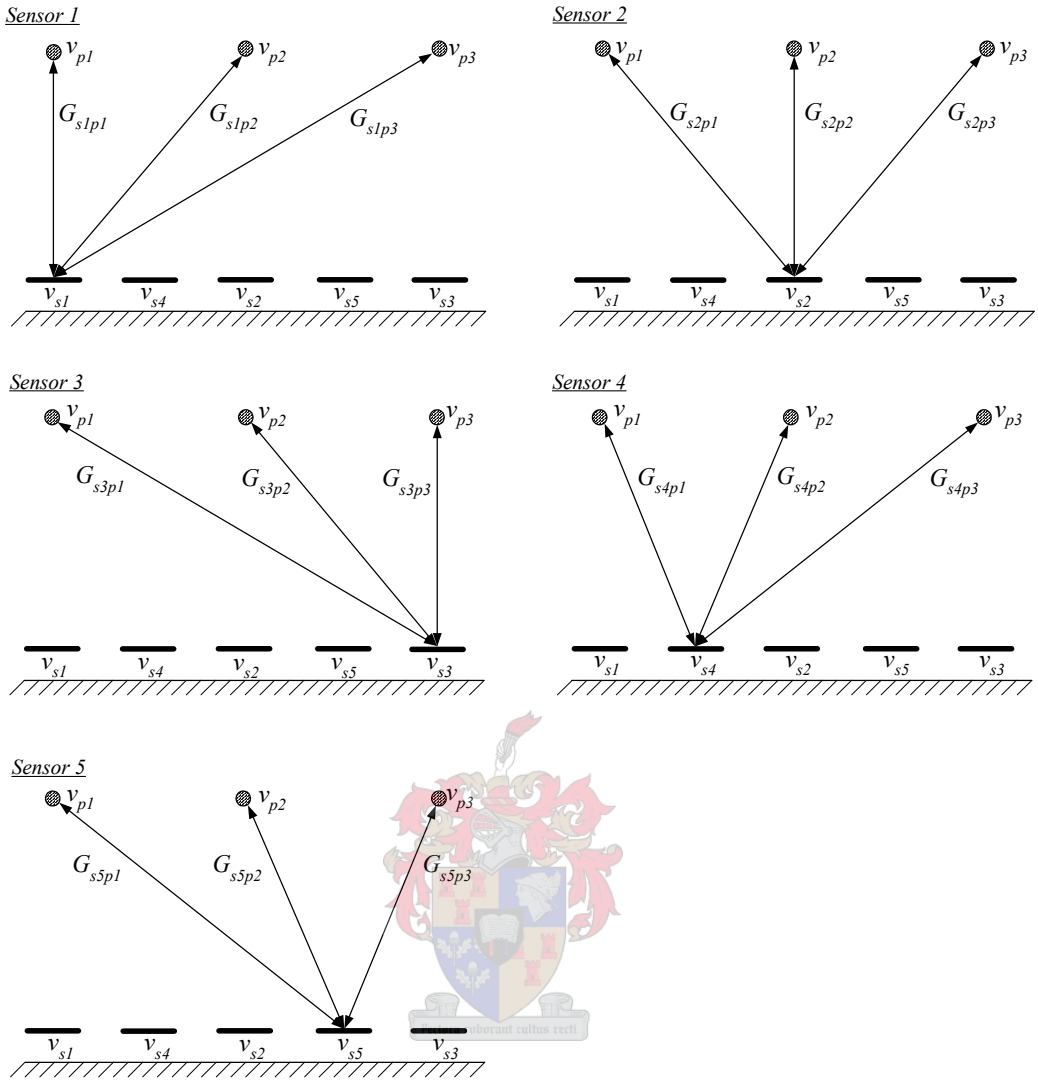


**Figure 5.6: Voltage transfer function definitions for five single-element plate sensor.**

## 5.4. Experimental determination of the voltage transfer functions

The voltage equations presented in the previous sections relate the voltages induced on the sensors to the phase conductor voltages through the voltage transfer function matrix G. The elements of G can be determined by calculating the capacitive couplings between the sensors and conductors in the topology with software packages such as ELECTRO, as is done in this research. However, the voltage transfer functions can also be measured if circumstances allow, e.g. for an experimental test arrangement such as developed in this project. It is therefore of interest to investigate the possibilities for calculating the elements of the G matrix from measured sensor voltages and phase conductor voltages. The evaluations presented in this section apply for the topologies defined in Figure 5.1 and Figure 5.3, as represented by the G matrix given in (5.10).

### 5.4.1. Evaluation of voltage transfer functions for arbitrary phase conductor voltages

The objective of the relationships considered in this section is to review the relationships for determining the elements of the voltage transfer function matrix from measurements of the sensors voltage waveforms and conductor voltage waveforms for a typical three-phase system. Such measurements can be readily conducted for the case where the sensors are located close to a substation.

It follows from equations (5.1) and (5.10) that the sensor voltages for the topologies shown in Figure 5.1 and Figure 5.3 can be expressed in the form

$$v_{s1}(t) = G_1 v_{p1}(t) + G_2 v_{p2}(t) + G_3 v_{p3}(t) \tag{5.26}$$

$$v_{s2}(t) = G_4 v_{p1}(t) + G_5 v_{p2}(t) + G_4 v_{p3}(t) \tag{5.27}$$

and

$$v_{s3}(t) = G_3 v_{p1}(t) + G_2 v_{p2}(t) + G_1 v_{p3}(t). \tag{5.28}$$

The voltage equation for sensor 2 references two transfer functions, namely $G_4$ and $G_5$. If one of these is known, the other one can be calculated. Also, the voltage equations for sensors 1 and 3 references three transfer functions, namely $G_1$, $G_2$ and $G_3$. If one of these is known, the others can be calculated from the pair of simultaneous equations.

The voltage transfer functions can be readily determined from measured phase conductor and sensor voltages by forcing some phase voltages to zero. If conductor $p_1$ is energised and conductors $p_2$ and $p_3$ are grounded, $G_1$, $G_4$ and $G_3$ can be obtained from the relationships

$$v_{s1}(t) = G_1 v_{p1}(t) \ , \tag{5.29}$$

$$v_{s2}(t) = G_4 v_{p1}(t) \tag{5.30}$$

and

$$v_{s3}(t) = G_3 v_{p1}(t) \ . \tag{5.31}$$

Similarly, for $p_2$ energised and $p_1$ and $p_3$ grounded, $G_4$ and $G_5$ can be obtained from the relationships

$$v_{s1}(t) = G_4 v_{p2}(t) \ , \tag{5.32}$$

$$v_{s2}(t) = G_5 v_{p2}(t) \tag{5.33}$$

and

$$v_{s3}(t) = G_4 v_{p2}(t) \ . \tag{5.34}$$

The above methodology can also be applied for the general unsymmetrical configuration with a total of nine independent voltage transfer functions as shown in equation (5.4), by including the measurements with $p_3$ energised and $p_1$ and $p_2$ grounded.

It is also possible to determine the voltage transfer functions from measurements with two phase conductors energised and only one phase conductor grounded. If conductor $p_2$ is grounded equations (5.26), (5.27) and (5.28) reduce to

$$v_{s1}(t) = G_1 v_{p1}(t) + G_3 v_{p3}(t) \ , \tag{5.35}$$

$$v_{s2}(t) = G_4 v_{p1}(t) + G_4 v_{p3}(t) \tag{5.36}$$

and

$$v_{s3}(t) = G_3 v_{p1}(t) + G_1 v_{p3}(t) \ . \tag{5.37}$$

Solving equation (5.36) for $G_4$ yields

$$G_4 = \frac{v_{s2}(t)}{v_{p1}(t) + v_{p3}(t)} \ . \tag{5.38}$$

Solving equations (5.35) and (5.37) for $G_1$ and $G_3$ yields

$$G_1 = \frac{v_{s1}(t) v_{p1}(t) - v_{s3}(t) v_{p3}(t)}{{v_{p1}}^2(t) - {v_{p3}}^2(t)} \tag{5.39}$$

and

$$G_3 = \frac{v_{s3}(t) v_{p1}(t) - v_{s1}(t) v_{p3}(t)}{{v_{p1}}^2(t) - {v_{p3}}^2(t)} \ . \tag{5.40}$$

Transfer functions $G_2$ and $G_5$ can then be obtained from a set of measurements with all three phase conductors energised. This methodology is suitable for experimental measurements in the laboratory where it is easy to energise or ground individual phases.

### 5.4.2. Evaluation of voltage transfer functions for sinusoidal conductor voltages

For sinusoidal phase conductor voltages, equations (5.26) to (5.28) can be expressed in the format

$$v_{s1}(t) = G_1 V_{p1} \cos(wt + \theta_1) + G_2 V_{p2} \cos(wt + \theta_2) + G_3 V_{p3} \cos(wt + \theta_3) \ , \tag{5.41}$$

$$v_{s2}(t) = G_4 V_{p1} \cos(wt + \theta_1) + G_5 V_{p2} \cos(wt + \theta_2) + G_4 V_{p3} \cos(wt + \theta_3) \tag{5.42}$$

and

$$v_{s3}(t) = G_3 V_{p1} \cos(wt + \theta_1) + G_2 V_{p2} \cos(wt + \theta_2) + G_1 V_{p3} \cos(wt + \theta_3) \tag{5.43}$$

where $v_{s1}(t)$, $v_{s2}(t)$ and $v_{s3}(t)$ denote the induced sensor voltages, $V_{p1}$, $V_{p2}$ and $V_{p3}$ denote the peak amplitudes of the phase conductor voltages, $\theta_1$, $\theta_2$ and $\theta_3$ denote the phase angles of the phase conductor voltages and $G_1$ *to* $G_5$ denote the voltage transfer functions between the conductors and sensors.

For a balanced unsymmetrical system the same equations are derived as presented in section 5.4.1. The voltage transfer functions can then be determined from the measured phase conductor and sensor voltages at a specific instant in time.

For a balanced, symmetrical system certain constraints are placed on the methods of deriving the equations discussed in section 5.4.1. Firstly the question arises whether the zero-crossings of the conductor voltages can be used to derive equations from which the G-values can be determined. In order to investigate this aspect, consider the balanced, symmetrical system of the phase conductor voltages $v_{p1}(t)$, $v_{p2}(t)$ and $v_{p3}(t)$ given by the relationships

$$v_{p1}(t) = V_m \cos(wt + \theta) \ , \tag{5.44}$$

$$v_{p2}(t) = V_m \cos(wt + \theta + 120°) \tag{5.45}$$

and

$$v_{p3}(t) = V_m \cos(wt + \theta - 120°) \tag{5.46}$$

where $V_m$ and $\theta$ denote the maximum value and phase angle respectively of the phase conductor voltages. For a balanced three-phase system the sum of the voltages equals 0, i.e.

$$v_{p1}(t) + v_{p2}(t) + v_{p3}(t) = 0 \ . \tag{5.47}$$

Equation (5.42) can be reduced to the form

$$v_{s2}(t) = V_m \left[ \frac{1}{2}\cos(wt) + \frac{\sqrt{3}}{2}\sin(wt) \right](G_4 - G_5) \ . \tag{5.48}$$

Consider the time instant when the voltage waveform of the middle conductor, i.e. $v_{p2}(t)$, goes through a zero-crossing, thus no voltage is induced on the sensors by this phase conductor. This yields the relationship

$$0 = G_5 V_{p2} \cos(wt + 120°)$$

from which

$$wt = -30° \ .$$

Thus, for $wt$ = -30˚, equation (5.42) yields

$$\begin{aligned} v_{s2}(t) &= V_m \left[ \frac{1}{2}\cos(-30) + \frac{\sqrt{3}}{2}\sin(-30) \right](G_4 - G_5) \\ &= 0. \end{aligned} \tag{5.49}$$

Therefore $G_4$ and $G_5$ cannot be evaluated by this approach. Evaluating equations (5.41) and (5.43) for $wt$ = -30˚ yields

$$v_{s1}(t) = V_{\max}\frac{\sqrt{3}}{2}(G_1 - G_3) \tag{5.50}$$

and

$$v_{s3}(t) = -V_{\max}\frac{\sqrt{3}}{2}(G_1 - G_3)\,. \tag{5.51}$$

The above equations are not independent, thus $G_1$ and $G_3$ cannot be determined from these relationships. Similar results are obtained for the zero-crossings associated with phase conductors 1 and 3.

### 5.4.3. Applying different phase voltages

If different phase voltage magnitudes, with the same phase differences, are applied to the three-phase system, different sets of equations are obtained from the measured waveforms. In the case of two different magnitudes of phase voltages two set of equations are obtained. The first set is expressed by equations (5.26), (5.27) and (5.28) and the second set is expressed by

$$v_{sx}(t) = G_1 v_{px}(t) + G_2 v_{py}(t) + G_3 v_{pz}(t)\,, \tag{5.52}$$

$$v_{sy}(t) = G_4 v_{px}(t) + G_5 v_{py}(t) + G_4 v_{pz}(t) \tag{5.53}$$

and

$$v_{sz}(t) = G_3 v_{px}(t) + G_2 v_{py}(t) + G_1 v_{pz}(t) \tag{5.54}$$

Solving equation (5.27) for $G_4$ yields

$$G_4 = \frac{v_{s2}(t) - G_5 v_{p2}(t)}{v_{p1}(t) + v_{p3}(t)}\,. \tag{5.55}$$

From equations (5.53) and (5.55) $G_5$ can be expressed by the relationship

$$G_5 = \frac{v_{s2}(t)\left[v_{px}(t) + v_{pz}(t)\right] - v_{sy}(t)\left[v_{p1}(t) + v_{p3}(t)\right]}{v_{p2}(t)\left[v_{px}(t) + v_{pz}(t)\right] - v_{py}(t)\left[v_{p1}(t) + v_{p3}(t)\right]}\,. \tag{5.56}$$

For a balanced-three-phase system, equation (5.56) reduce to

$$G_5 = \frac{v_{s2}(t)v_{py}(t) - v_{sy}(t)v_{p2}(t)}{v_{p2}(t)v_{py}(t) - v_{py}(t)v_{p2}(t)} \tag{5.57}$$

Equation (5.57) is not solvable due to the fact that the numerator equals 0. If different phase voltages are applied to the power system, the coupling factors cannot be calculated for a symmetrical balanced three-phase system. The electric field that induces the voltage on the

three sensors is proportional to the overhead voltage. If the overhead voltage is increased by a factor $g$, the electric field will increase by a factor $g$ and thus the induced voltage also increases with a factor $g$.

### 5.4.4. Using the difference factor between different transfer functions

If two of the transfer functions in equations (5.26), (5.27) and (5.28) can be expressed in terms of the remaining unknown functions the three equations can be solved simultaneously. Let transfer functions $G_5 = kG_1$ and $G_4 = pG_2$, where $k$ and $p$ are constant factors for a specific power system geometry, then equations (5.26), (5.27) and (5.28) reduce to

$$v_{s1} = G_1 v_{p1} + G_2 v_{p2} + G_3 v_{p3} \ , \tag{5.58}$$

$$v_{s2} = pG_2 v_{p1} + kG_1 v_{p2} + pG_2 v_{p3} \tag{5.59}$$

and

$$v_{s3} = G_3 v_{p1} + G_2 v_{p2} + G_1 v_{p3} \ . \tag{5.60}$$

These three equations are then solved with *Mathematica* for $G_1$, $G_2$ and $G_3$ and are denoted by

$$G_1 = \frac{v_{s2}v_{p2}\left(-v_{p1}+v_{p3}\right)+v_{s1}pv_{p1}\left(v_{p1}+v_{p3}\right)-v_{s3}pv_{p3}\left(v_{p1}+v_{p3}\right)}{\left(v_{p1}-v_{p3}\right)\left(-kv_{p2}^2+p\left(v_{p1}+v_{p3}\right)^2\right)}, \tag{5.61}$$

$$G_2 = \frac{kv_{p2}\left(-v_{s1}v_{p1}+v_{s3}v_{p3}\right)+v_{s2}\left(v_{p1}^2-v_{p3}^2\right)}{\left(v_{p1}-v_{p3}\right)\left(-kv_{p2}^2+p\left(v_{p1}+v_{p3}\right)^2\right)} \tag{5.62}$$

and

$$G_3 = \frac{v_{s2}v_{p2}\left(-v_{p1}+v_{p3}\right)+v_{s3}\left(-kv_{p2}^2+pv_{p1}\left(v_{p1}+v_{p3}\right)\right)+v_{s1}\left(kv_{p2}^2-pv_{p3}\left(v_{p1}+v_{p3}\right)\right)}{\left(v_{p1}-v_{p3}\right)\left(-kv_{p2}^2+p\left(v_{p1}+v_{p3}\right)^2\right)}. \tag{5.63}$$

Different methods are used for determining the values of $k$ and $p$, i.e. numerical and analytical methods.

## 5.5. Numerical determination of the capacitance coupling matrix

In this section the capacitance matrix of a flat, three-phase line configuration with three sensors located beneath it is simulated with ELECTRO. Since the voltage transfer functions are determined by the capacitive coupling elements between the conductor and sensor elements in the topology, the capacitive coupling matrix of the topology are used to calculate the difference between different transfer function elements. The transfer function elements are linearly proportional to the corresponding capacitive coupling components.

Single-element plate sensors beneath the line configuration are evaluated at first to obtain a preliminary estimate of the difference between the various transfer functions. Thereafter the sensor model is changed to incorporate the three-element parallel plate sensor topology.

### 5.5.1. Capacitance matrix for a single-element plate sensor topology

Figure 5.7 illustrates the line configuration that is simulated with ELECTRO. This section uses the notations of the capacitive coupling elements declared in section 5.2.2. The transfer functions are obtained from the capacitive matrix where $G_1$ and $G_5$ are compared as well as $G_2$ and $G_4$.

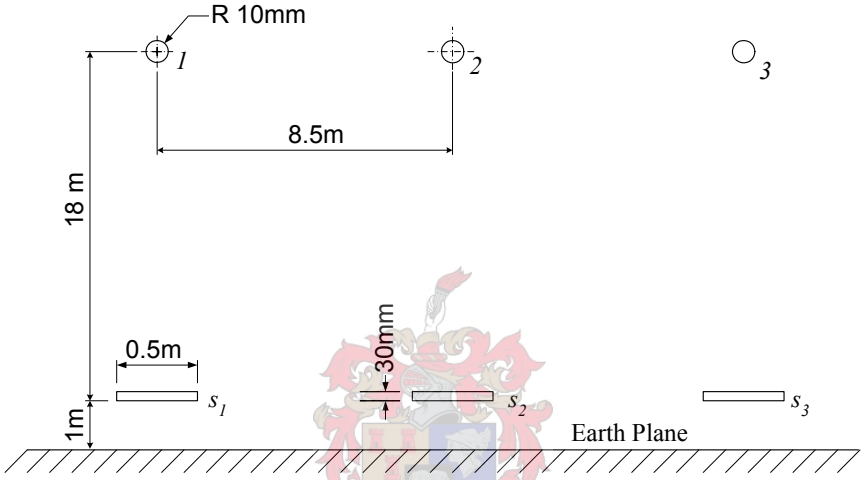


**Figure 5.7: Single element parallel plate sensors underneath a three-phase transmission line.**

From the ELECTRO simulation of the capacitance matrix it is estimated that transfer function $G_5$ is 10.98% larger than transfer function $G_1$. Transfer function $G_4$ is estimated to be 0.9% larger than transfer function $G_2$. Table A.3 (Appendix A) tabulates the capacitance matrix obtained from ELECTRO.

### 5.5.2. Capacitance matrix for a three-element parallel plate sensor topology

Figure 5.8 illustrates three three-element parallel plate sensors underneath the line configuration. This sensor and line configuration simulated with ELECTRO is similar to the sensor and line configuration for measurements done in the field underneath 400kV three-phase transmission lines. The neutral wires are omitted for this simulation. As in the previous section, the different capacitive coupling components must be compared with each other to obtain the percentage difference between different transfer function elements. Figure 5.9 shows that in this simulation the sensors consist out of a bottom plate, a top plate and a faraday cage. This complicates the simulation as there are more capacitive elements that must be evaluated.

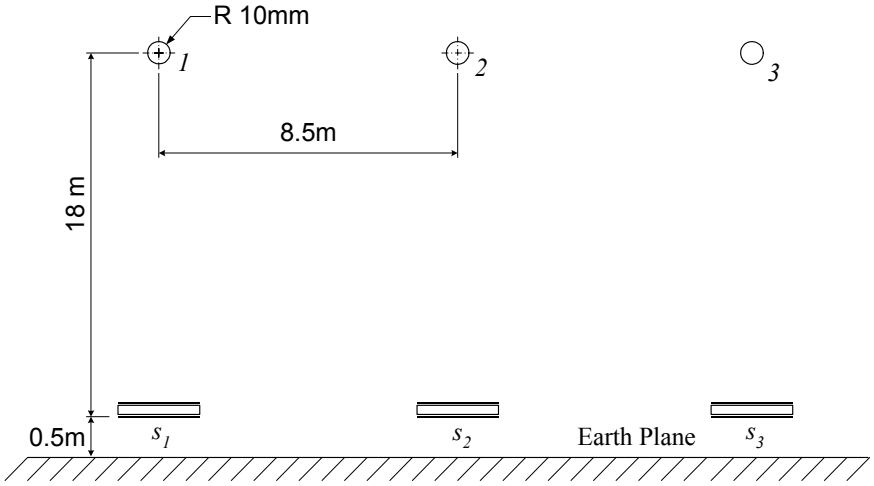


**Figure 5.8: Three element parallel plate sensors underneath a three-phase transmission line.**

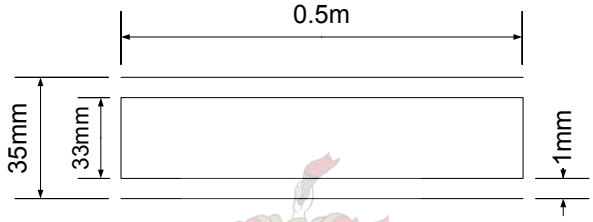


**Figure 5.9: Dimensions of the parallel plate sensor.**

The percentage difference between the transfer functions associated with the top plates, the bottom plates and the faraday cages, of sensors $s_1$, $s_2$ and $s_3$, have to be calculated. Table 5.2 compares the different transfer functions. If the results from Table 5.2 are compared with the results obtained with the single-element sensor it is estimated that the percentage difference evaluated by each table differed by 3.1% for *G5 vs. G1* and 11% for *G4 vs. G2* from each other. The difference between the coupling factors for the top plate, the faraday cage and the bottom plate can be taken as the same.

These simulations are done to calculate a constant scaling factor, *k*, to compare coupling factors *G5* to *G1* and coupling factors *G4* to *G2*. For instance, if coupling factor *G1* is known for the top plate of the sensor, coupling factor *G5* can be estimated as *G5* = (100%-10.98%) x *G1*. The same principle applied to coupling factors *G4* and *G2*.

**Table 5.2: Difference between the transfer functions of the three-element sensors various sections.**

| Plate | Transfer functions | Difference (%) | Transfer functions | Difference (%) |
|---|---|---|---|---|
| **Top** | G5 vs G1 | 10.57 | G4 vs G2 | 1.18 |
| **Cage** | G5 vs G1 | 10.59 | G4 vs G2 | 1.23 |
| **Bottom** | G5 vs G1 | 10.46 | G4 vs G2 | 1.14 |

## 5.6. Electric field profile underneath three-phase transmission line

The electric field strength underneath three-phase line configurations can be calculated with the equations reviewed in Appendix J.4. Chapter 3 compares the simulated and measured values of the electric field strength underneath three-phase line configurations and good comparison is found. The deviation between calculated and measured values of the electric field can be assigned to the numerous assumptions that are made for calculating the electric field. Software programs, EMFP and ELECTRO, thus prove to be adequate for evaluating the electric field strength underneath various line configurations.

The electric field strength is used to construct the electric field profile underneath a transmission line. This section uses the electric field profile to obtain the optimal positions for placing the sensors underneath the HV transmission line.

The electric field strength underneath a three-phase line is also used to determine the relationship between various capacitive coupling factors.

### 5.6.1. Evaluating the electric field

From Appendix J the electric field $\tilde{E}_{a1}$ due to the charge of an overhead sub-conductor *a1* and its image conductor *a1'* is denoted by [40]

$$\bar{E}_{a1} = \left(\tilde{E}_{x,a1} + \tilde{E}_{x,a1'}\right)\bar{i}_x + \left(\tilde{E}_{y,a1} + \tilde{E}_{y,a1'}\right)\bar{i}_y = \tilde{E}_{x,a1}\,\bar{i}_x + \tilde{E}_{y,a1}\,\bar{i}_y \tag{5.64}$$

where $\bar{i}_x$ and $\bar{i}_y$ are the unit vectors along the horizontal and vertical axes. $\tilde{E}_{x,a1}$ and $\tilde{E}_{y,a1}$ represent the electric field vector components due to both *a1* and its image conductor *a1'*. Equation (5.64) shows that the electric field strength consists out of a vertical and a horizontal component. The vertical component under a transmission line is the quantity that is used to characterize induction effects in objects close to ground level.

The vertical component can be used to evaluate the electric field profile at height $y_s$ above the ground plane. The vertical component is denoted by [40]

$$\tilde{E}_{y,a1} = \frac{\left(Q_{r,a1} + jQ_{i,a1}\right)}{2\pi\varepsilon_0}\left[\frac{-\left(y_{a1} - y_s\right)}{\left[\left(x_{a1} - x_s\right)^2 + \left(y_{a1} - y_s\right)^2\right]} - \frac{\left(y_{a1} + y_s\right)}{\left[\left(x_{a1} - x_s\right)^2 + \left(y_{a1} + y_s\right)^2\right]}\right]. \tag{5.65}$$

where $\left(Q_{r,a1} + jQ_{i,a1}\right)$ denotes the real and imaginary components of the charge present on the sub-conductor *a1*, $x_s$ and $y_s$ denotes the coordinates of point *s* in space and $x_{a1}$ and $y_{a1}$ denotes the coordinates of conductor *a1* in space.

For a power line with more than one phase conductor, i.e. a three-phase line, superposition is used to calculate the total horizontal component $\tilde{E}_x$ and the total vertical component $\tilde{E}_y$ of the electric field vector at point *s* due to all the charge carrying conductors in the power line. The total electric field is denoted by equations (J.28) to (J.34) (Appendix J).

### 5.6.2. Electric field profile

A typical 132kV transmission line used in the Western Cape is simulated with EMFP to obtain a common electric field profile underneath a three-phase transmission line. Figure 5.10 shows the dimensions of the tower type used for the transmission line. The conductor that is used is the Kingbird conductor which has an overall diameter of 23.8mm and a GMR of 9.27mm. The electric field profile at a height of 0.3m is simulated. This is the height of the sensor on top of the support structure. The electric field profile is dependant on the height of the conductor above the ground plane and thus the sag of the overhead transmission line must always be taken into account.

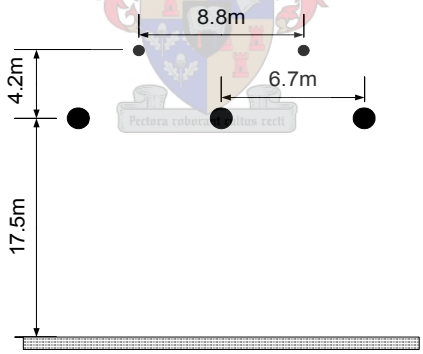


**Figure 5.10: Typical tower structure dimensions for a 132kV power line.**

Figure 5.11 shows the horizontal component, vertical component and resultant value of the electric and magnetic field strength for sag of 0m. These profiles were simulated with EMFP. The vertical component of the electric field is the magnitude used for the measurements discussed in the rest of the section. The horizontal component has minimal contribution to the resultant electric field value. The electric field profile is simulated for different values of sag from 0m to 6.5m.

Table 5.3 tabulates the y-component values of the electric field for different sag values. The line configuration and dimensions illustrated in Figure 5.10 are used for these evaluations.

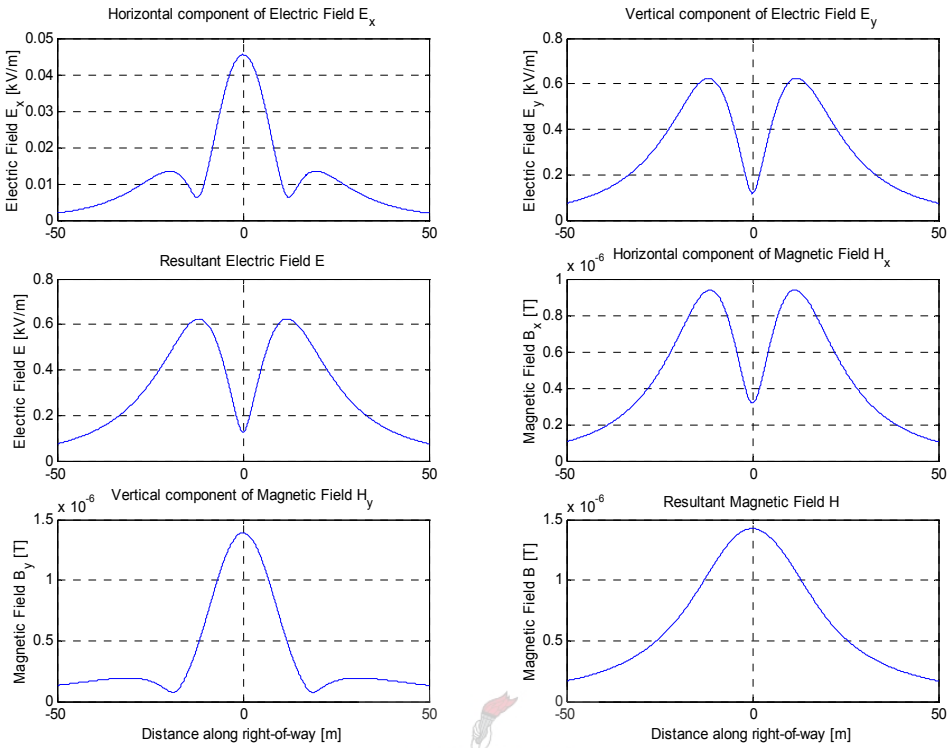


**Figure 5.11 : Electric and Magnetic Fields for 0m sag**

**Table 5.3: Comparing y-components of the electric field strength for different sag values**

| sag | conductor height | horizontal value at peak [m] | peak value [kV/m] | value beneath conductor [kV/m] |
|---|---|---|---|---|
| 5 | 12.5 | 9.456 | 1.163 | 1.06 |
| 5.5 | 12 | 9.259 | 1.251 | 1.15 |
| 6 | 11.5 | 9.059 | 1.348 | 1.25 |
| 6.5 | 11 | 8.859 | 1.456 | 1.36 |

The electric field increased with an increase in conductor sag. Table 5.3 shows that the electric field underneath the transmission line has an increase in peak value of about 0.1kV/m for an increase of 0.5m in the conductor sag. The electric field thus has an increase of 8.5% for an increase of 0.5m in sag. As the voltage measured by the sensors is linear to the electric field the sensors can be used underneath the overhead transmission line to calculate the sag of the overhead conductors.

### 5.6.3. Optimal placement of sensors underneath transmission line

Positioning the sensors such that sensor $s_2$ is directly underneath the centre conductor and sensor $s_1$ and $s_3$ symmetrical relative to sensor $s_2$ causes that the symmetry relationship in the

voltage transfer function matrix and the capacitive coupling matrix are maintained. The optimal positions for sensors $s_1$ and $s_3$ must thus be found.

Figure 5.12 shows the y-component of the electric field underneath the line configuration shown in Figure 5.10 for a sag of 5m. Figure 5.12 and Table 5.3 show that the peak values of the electric field y-component is 9.456m from the centre phase and thus not centralised beneath the two outer phases. ELECTRO or EMFP can be used for calculating the horizontal position where the y-component will have its peak value.

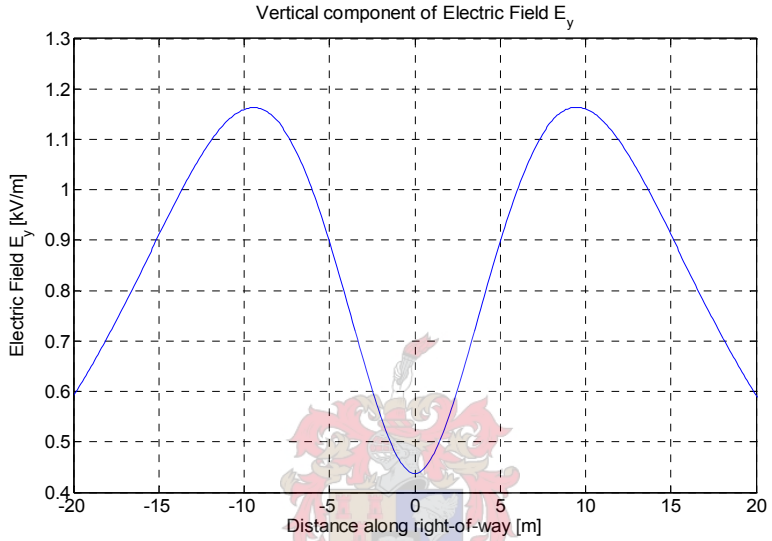


**Figure 5.12 : Vertical component of the electric field for a 5m sag (Right-of-way = 40m)**

Figure 5.12 shows that the electric field profile has three zero-slope points, two maximal turning points and one minimal turning point. The rate of change is minimal at these three points. If the three sensors are placed at the stationary points the voltage induced on the sensors respectively will be less sensitive to positional variations. At the three stationary points the derivative of the function for electric field's y-component is equal to 0, i.e. $\frac{dE(x)}{dx} = 0$. The horizontal position, underneath the transmission line, at which the y-component has stationary points, can thus be obtained.

### 5.6.4. Determining the factor of difference between various transfer functions

Section 5.4.4 shows that if two of the transfer functions in equations (5.26), (5.27) and (5.28) can be expressed in terms of the remaining unknown functions the three equations can be solved simultaneously. One method of determining the factor of difference between the transfer functions is with a numerical software program, i.e. ELECTRO. An analytical

method for determining the factor of difference is developed. This method is faster than the numerical program and provides an easy method for determining the factor of difference.

Figure 5.13 shows the electric field profile underneath a flat three-phase line configuration due to the voltage on the centre conductor. The other two conductors are grounded and located at -3.5m and 3.5m from the centre conductor. The middle sensor is placed beneath the centre conductor and the other two sensors are placed 4m from the centre. The voltage induced on the sensor is linearly proportional to the y-component of the electric field strength at the positions of the sensors. To obtain the electric field strength at the positions of the sensors form the electric field profile in Figure 5.13 the average value of the electric field strength over the width of the sensors are evaluated. To determine the average value equation (5.65) is integrated over the width of the sensor and then the value obtained is divided with the distance of the sensor's width.

For the middle sensor equation (5.65) is integrated between 0.25 and -0.25 m, due to the fact that the sensor has a width of 0.5m and the sensor is located at position 0m. For the centre located at -4m equation (5.65) is integrated between -4.75 and -4.25 m.

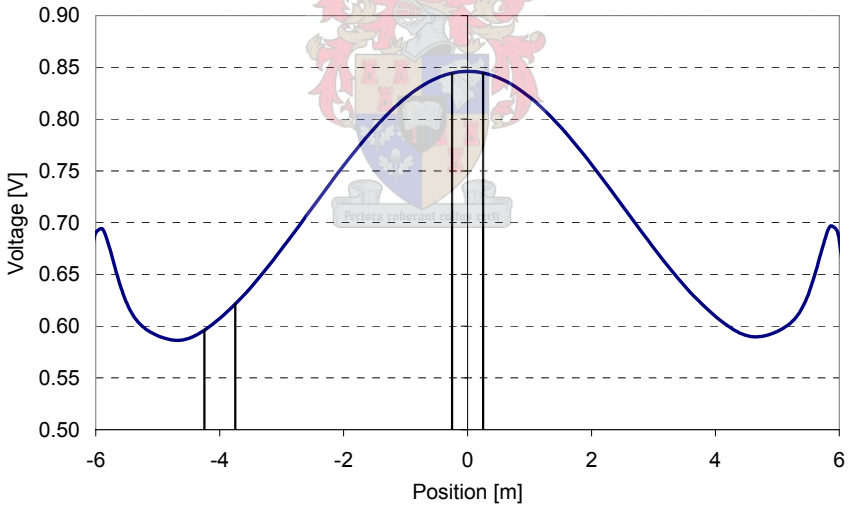


**Figure 5.13: Electric field profile if only the centre conductor is energised.**

The voltage induced on sensor $s_1$ due to the voltage of overhead HV conductor $p_1$ is given by

$$v_{s1} = G_{s1p1} v_{p1} \tag{5.66}$$

where $G_{s1p1}$ denotes the transfer function between sensor $s_1$ and the overhead conductor. The voltage induced on sensor $s_1$ due to the voltage of overhead HV conductor $p_1$ is given by

$$v_{s2} = G_{s2p1} v_{p1} \tag{5.67}$$

where $G_{s2p1}$ denotes the transfer function between sensor $s_2$ and the overhead conductor. Dividing equation (5.66) with equation (5.67) obtain the relationship between the two transfer functions given by

$$\frac{v_{s1}}{v_{s2}} = \frac{G_{s1p1}v_{p1}}{G_{s2p1}v_{p1}} = \frac{G_{s1p1}}{G_{s2p1}} \tag{5.68}$$

The factor of difference equals the difference between the induced voltages on the sensors. From equation (J.39) (Appendix J) the voltages induced on the sensors are linearly proportional to the electric field strength at the position of the sensor. Implementing equation (J.39) (Appendix J) into equation (5.68) the ratio between the two transfer functions is reduced to

$$\frac{G_{s1p1}}{G_{s2p1}} = \frac{v_{s1}}{v_{s2}} = \frac{akE_{s1}(x)}{akE_{s2}(x)} = \frac{E_{s1}(x)}{E_{s2}(x)} \tag{5.69}$$

Only the y-component is used for these evaluations. Substituting equation (5.65) into equation (5.69) the relationship between the two transfer functions is given by

$$\begin{aligned}\frac{G_{s1p1}}{G_{s2p1}} &= \frac{\frac{(Q_{r,a1}+jQ_{i,a1})}{2\pi\varepsilon_0}\left[\frac{-(y_{a1}-y_{s1})}{\left[(x_{a1}-x_{s1})^2+(y_{a1}-y_{s1})^2\right]}-\frac{(y_{a1}+y_{s1})}{\left[(x_{a1}-x_{s1})^2+(y_{a1}+y_{s1})^2\right]}\right]}{\frac{(Q_{r,a1}+jQ_{i,a1})}{2\pi\varepsilon_0}\left[\frac{-(y_{a1}-y_{s2})}{\left[(x_{a1}-x_{s2})^2+(y_{a1}-y_{s2})^2\right]}-\frac{(y_{a1}+y_{s2})}{\left[(x_{a1}-x_{s2})^2+(y_{a1}+y_{s2})^2\right]}\right]} \\ &= \frac{\left[\frac{-(y_{a1}-y_{s1})}{\left[(x_{a1}-x_{s1})^2+(y_{a1}-y_{s1})^2\right]}-\frac{(y_{a1}+y_{s1})}{\left[(x_{a1}-x_{s1})^2+(y_{a1}+y_{s1})^2\right]}\right]}{\left[\frac{-(y_{a1}-y_{s2})}{\left[(x_{a1}-x_{s2})^2+(y_{a1}-y_{s2})^2\right]}-\frac{(y_{a1}+y_{s2})}{\left[(x_{a1}-x_{s2})^2+(y_{a1}+y_{s2})^2\right]}\right]}\end{aligned} \tag{5.70}$$

Equation (5.70) only consists of geometrical values, i.e. the dimensions of the three-phase line configuration and the $x$ and $y$ values of the sensors. These values are easily obtainable for a certain tower structure and line configuration. The difference between the two transfer functions can thus be calculated from the dimensions of the line configuration and provide a fast and easier way to evaluate the difference between various transfer functions.

The equations that must be used for substituting into equation (5.69) is the average value of the electric field strength at the various sensor positions for which the transfer functions must

be calculated. However these equations will still have the same form as that of equation (5.65).

## 5.7. Conclusion

In this chapter various methods are developed to obtain the transfer functions between the transmission lines and the sensors. In the original methods it was assumed that $G_2 = G_4$ and $G_1 = G_5$, however it is shown that this assumption is incorrect.

The best way of determining the transfer functions is by energising one conductor at a time and grounding the other two. For a symmetrical unbalanced three-phase system the transfer functions can be determined by measuring two of the waveforms at the instant that the third waveform has a zero crossing. For a symmetrical balanced three-phase system the transfer functions cannot be evaluated from checking the zero crossing.

The software program ELECTRO is used to obtain the differences between the different capacitive coupling components and hence the transfer functions. The percentage differences that are obtained in section 5.5 are used to relate the transfer functions $G_2$ and $G_4$ and transfer functions $G_1$ and $G_5$ respectively. A new set of equations are then obtained from which the transfer functions can be calculated.

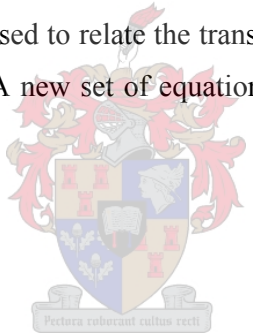

# 6. Equivalent circuit models for three-phase line topologies

## 6.1. Introduction

Equivalent circuit models must be derived to calculate the Thévenin equivalent voltage and impedance of the three-element sensor topology. This is required to clarify the relationship between the transfer function characteristics of the sensors and the individual parameters defining the sensor topology [1].

As was performed by Botha, a two-dimensional approximation of the sensor topology is made and only the resistive and capacitive components are included in these models. All inductive coupling is ignored as it is assumed that the sensor dimensions are electrically small.

Thévenin's theorem is used throughout to determine the equivalent voltage source and impedance to characterise the sensor topologies. The Thévenin equivalent voltage and impedance are both functions of frequency because of the capacitive elements in the equivalent circuit models.

The Thévenin equivalent impedance and voltage derived for the equivalent circuit models are very complex. Different methods are thus required to simplify these equations. Section 6.3 discusses the various methods for simplifying the Thévenin equivalent equations.

## 6.2. Equivalent circuit models for the three-phase capacitive sensor topologies.

This section expands the single-phase capacitive sensor topologies developed by Botha [1] for three-phase transmission line topology. For the sake of completeness, equivalent circuits and the associated Thévenin equivalent impedance and voltage relationships are developed for all three sensors, i.e. single-element, two-element and three-element sensors, in three-phase topologies. The experimental results focus on the three-element parallel plate sensor.

The three-phase topology features three capacitive sensors located underneath a three-phase transmission line. Note that, although the individual sensors are typically shown directly below the phase conductors, the locations of the sensors only affect the values of coupling capacitances and not the circuit topologies.

### 6.2.1. Equivalent circuit for the single element plate sensor

Figure 6.1 shows the physical geometry of a three-phase topology with single-element sensors located directly below each of the phase conductors. The notations *a, b, c,* $s_a$, $s_b$, $s_c$ and *g* denote the three phase conductors, plate elements of each of the three sensors and the ground plane respectively.

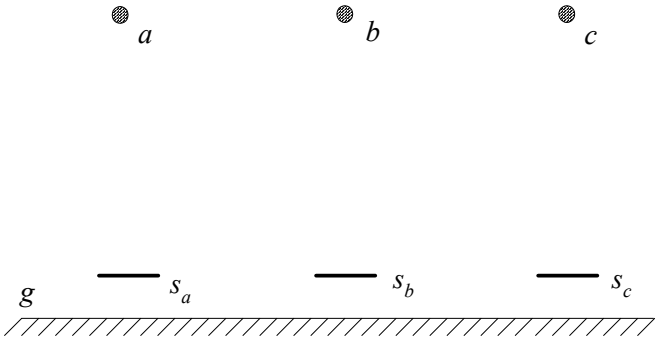


**Figure 6.1: Three-phase topology with single-element sensors.**

Figure 6.2 shows the coupling capacitances for the sensor located below the centre conductor. Figure 6.3 presents an equivalent circuit for a single-element sensor in a three-phase topology. The phase conductor coupling capacitances to ground, i.e. $C_{ag}$, $C_{bg}$ and $C_{cg}$, are not included as these do not affect the Thévenin equivalent circuit model of the topology. The parameters shown in Figure 6.3 are defined as follows:

| | |
|---|---|
| $C_{as}$, $C_{bs}$, $C_{cs}$ | Coupling capacitances between the phase conductors and sensor. |
| $R_{as}$, $R_{bs}$, $R_{cs}$ | Resistances between the phase conductors and sensor. |
| $C_{sg}$, $R_{sg}$ | Capacitance and resistance between the sensor element and ground plane respectively. |

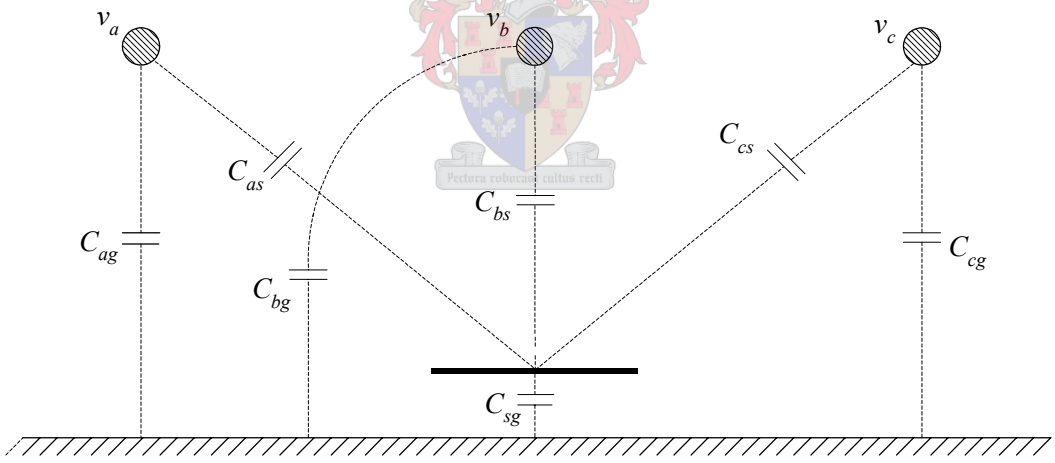


**Figure 6.2: Coupling capacitances for a single-element sensor in a three-phase topology.**

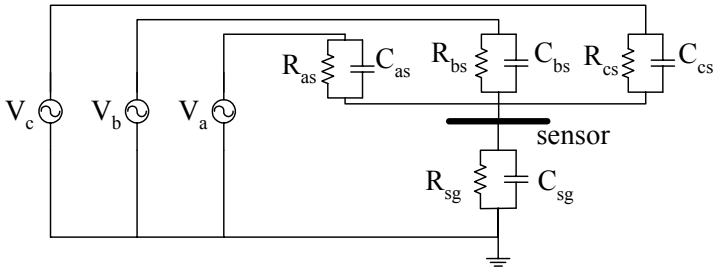


**Figure 6.3: Equivalent circuit for a single-element sensor in a three-phase topology.**

Resistances $R_{as}$, $R_{bs}$ and $R_{cs}$ represent losses in air and can be omitted. However, the sensor support structure cannot be regarded as a perfect insulator. Therefore $R_{sg}$ must be included in the model. The resulting equivalent circuit is show in Figure 6.4

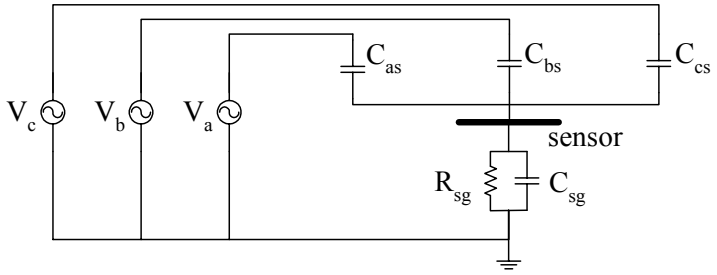


**Figure 6.4: Simplified equivalent circuit for a single-element sensor in a three-phase topology.**

It is shown in Appendix B that the Thévenin equivalent impedance and voltage of the circuit topology are then given by the relationships

$$Z_{TH} = \frac{R_{sg}}{sR_{sg}\left(C_{as}+C_{bs}+C_{cs}+C_{sg}\right)+1} \tag{6.1}$$

and

$$\begin{aligned} V_{TH} &= \frac{sR_{sg}\left(V_aC_{as}+V_bC_{bs}+V_cC_{cs}\right)}{sR_{sg}\left(C_{as}+C_{bs}+C_{cs}+C_{sg}\right)+1} \\ &= Z_{TH}\left(V_aC_{as}+V_bC_{bs}+V_cC_{cs}\right) \end{aligned} . \tag{6.2}$$

Because the principle of superposition applies, the equations for the Thévenin equivalent voltages and impedances for the three-phase topology can be obtained from equations (6.1) and (6.2) by introducing appropriate notational changes. This yields the following relationships:

$$Z_{TH1} = \frac{R_{s1g}}{sR_{s1g}\left(C_{as1}+C_{bs1}+C_{cs1}+C_{s1g}\right)+1} \tag{6.3}$$

$$V_{TH1} = Z_{TH1}\left(V_aC_{as1}+V_bC_{bs1}+V_cC_{cs1}\right) . \tag{6.4}$$

$$Z_{TH2} = \frac{R_{s2g}}{sR_{s2g}\left(C_{as2}+C_{bs2}+C_{cs2}+C_{s2g}\right)+1} \tag{6.5}$$

$$V_{TH2} = Z_{TH2}\left(V_aC_{as2}+V_bC_{bs2}+V_cC_{cs2}\right) . \tag{6.6}$$

$$Z_{TH3} = \frac{R_{s3g}}{sR_{s3g}\left(C_{as3}+C_{bs3}+C_{cs3}+C_{s3g}\right)+1} \tag{6.7}$$

and

$$V_{TH3} = Z_{TH3}\left(V_aC_{as3}+V_bC_{bs3}+V_cC_{cs3}\right). \tag{6.8}$$

where $Z_{TH1}$, $Z_{TH2}$ and $Z_{TH3}$ denote the Thévenin equivalent impedances for sensors $s_1$, $s_2$ and $s_3$ respectively while $V_{TH1}$, $V_{TH2}$ and $V_{TH3}$ denote the Thévenin equivalent voltages for sensors $s_1$, $s_2$ and $s_3$ respectively.

#### 6.2.1.1. High frequency model

For high frequencies the equivalent circuit shown in Figure 6.3 can be simplified by omitting all of the loss terms. This yields the equivalent circuit shown in Figure 6.5. The associated Thévenin equivalent impedance $Z_{TH}$ and voltage $V_{TH}$ are then given by the relationships

$$Z_{TH} = \frac{1}{sC_{TH}} \tag{6.9}$$

where

$$C_{TH} = C_{as} + C_{bs} + C_{cs} + C_{sg}\,. \tag{6.10}$$

and

$$V_{TH} = Z_{TH}\left(V_a C_{as} + V_b C_{bs} + V_c C_{cs}\right)\,. \tag{6.11}$$

This circuit also applies for high frequencies where the capacitances dominate the transfer function response.

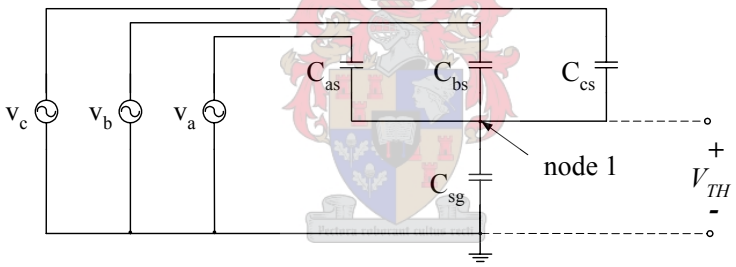


**Figure 6.5:High frequency equivalent circuit topology for a single-element sensor in a three-phase topology.**

With appropriate notational changes equations (6.9) to (6.11) give rise to the following relationships:

$$Z_{TH1} = \frac{1}{s\left(C_{as1} + C_{bs1} + C_{cs1} + C_{s1g}\right)} \tag{6.12}$$

$$\begin{aligned} V_{TH1} &= Z_{TH1}\left(V_a C_{as1} + V_b C_{bs1} + V_c C_{cs1}\right) \\ &= V_a\left(C_{as1} Z_{TH1}\right) + V_b\left(C_{bs1} Z_{TH1}\right) + V_c\left(C_{cs1} Z_{TH1}\right) \end{aligned}\,. \tag{6.13}$$

$$Z_{TH2} = \frac{1}{s\left(C_{as2} + C_{bs2} + C_{cs2} + C_{s2g}\right)} \tag{6.14}$$

$$V_{TH2} = Z_{TH2}\left(V_a C_{as2} + V_b C_{bs2} + V_c C_{cs2}\right) = V_a\left(C_{as2} Z_{TH2}\right) + V_b\left(C_{bs2} Z_{TH2}\right) + V_c\left(C_{cs2} Z_{TH2}\right) \quad (6.15)$$

$$Z_{TH3} = \frac{1}{s\left(C_{as3} + C_{bs3} + C_{cs3} + C_{s3g}\right)} \quad (6.16)$$

and

$$V_{TH3} = Z_{TH3}\left(V_a C_{as3} + V_b C_{bs3} + V_c C_{cs3}\right) = V_a\left(C_{as3} Z_{TH3}\right) + V_b\left(C_{bs3} Z_{TH3}\right) + V_c\left(C_{cs3} Z_{TH3}\right) \quad (6.17)$$

### 6.2.2. Equivalent circuit for the two element parallel plate sensor

Botha [1] concluded that the single-plate sensor is very sensitive to ground level variations and proposed that a two-element differential topology can be used to overcome this problem. The equivalent circuit representations for the two-element sensor topology are evaluated in this section.

Figure 6.6 shows the physical geometry of a three-phase topology with two-element sensors located directly below each of the phase conductors. The notations *a, b, c,* $s_{a1}$, $s_{a2}$, $s_{b1}$, $s_{b2}$, $s_{c1}$, $s_{c2}$ and *g* denote the three phase conductors, parallel plate elements of each of the three sensors and the ground plane respectively.

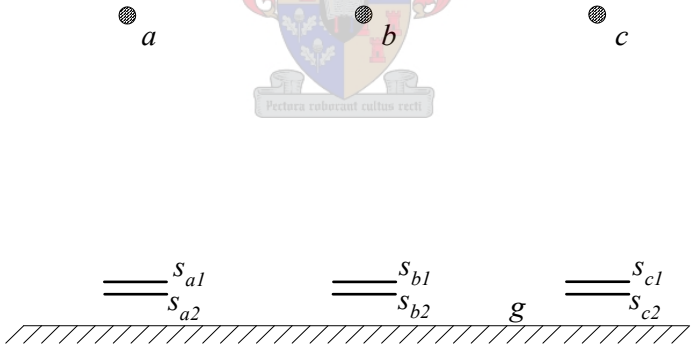


**Figure 6.6: Three-phase topology with two-element sensors.**

Figure 6.7 shows the coupling capacitances for the sensor located below the centre conductor. Figure 6.8 presents an equivalent circuit for a two-element parallel plate sensor in a three-phase topology. The phase conductor coupling capacitances to ground, i.e. $C_{ag}$, $C_{bg}$ and $C_{cg}$, are not included as these do not affect the Thévenin equivalent circuit model of the topology. The parameters shown in Figure 6.8 are defined as follows:

| | |
|---|---|
| $C_{as1}$, $C_{bs1}$, $C_{cs1}$ | Coupling capacitances between the phase conductors and top sensor plate. |

| | |
|---|---|
| $C_{as2}$, $C_{bs2}$, $C_{cs2}$ | Coupling capacitances between the phase conductors and bottom sensor plate. |
| $R_{as1}$, $R_{bs1}$, $R_{cs1}$ | Resistances between the phase conductors and top sensor plate. |
| $R_{as2}$, $R_{bs2}$, $R_{cs2}$ | Resistances between the phase conductors and bottom sensor plate. |
| $C_{s1g}$, $R_{s1g}$ | Capacitance and resistance respectively between the top sensor plate and ground. |
| $C_{s2g}$, $R_{s2g}$ | Capacitance and resistance respectively between the bottom sensor plate and ground. |
| $C_{s1s2}$, $R_{s1s2}$ | Capacitance and resistance respectively between the top and bottom sensor plates. |

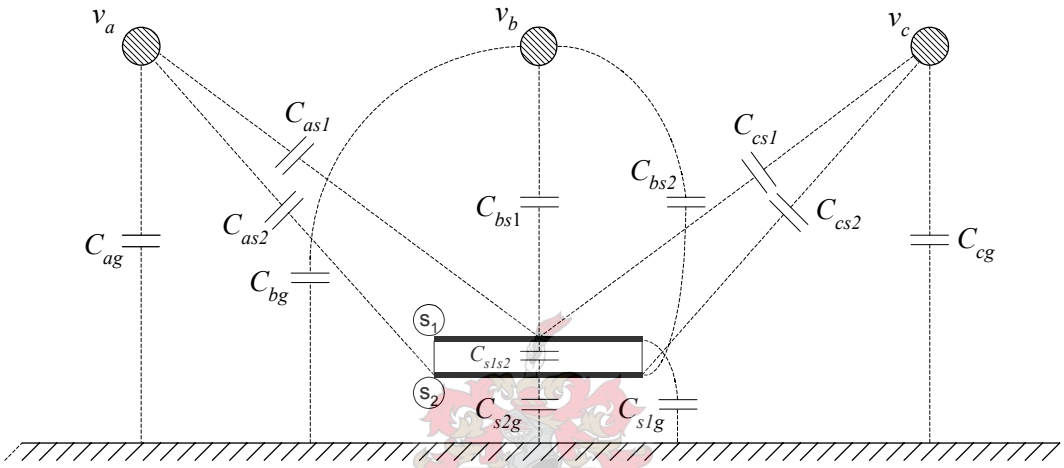


**Figure 6.7: Coupling capacitances for a two-element sensor in a three-phase topology.**

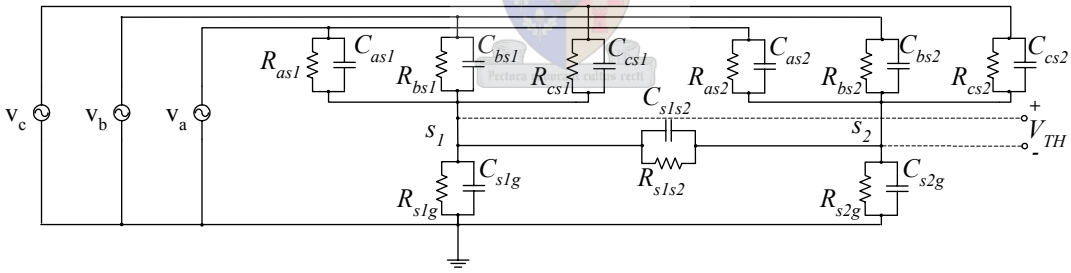


**Figure 6.8: Equivalent circuit for a two-element sensor in a three-phase topology.**

Resistances $R_{as1}$, $R_{bs1}$, $R_{cs1}$, $R_{as2}$, $R_{bs2}$ and $R_{cs2}$ represent losses in air and can be omitted. However, the dielectric substrate separating the sensor plates and the sensor support structure cannot be regarded as perfect insulators. Therefore $R_{s1s2}$, $R_{s1g}$ and $R_{s2g}$ must be included in the model. The resulting equivalent circuit model is shown in Figure 6.9.

The equivalent circuit shown in Figure 6.9 gives rise to complex equations for the Thévenin equivalent impedance and voltage. Since no experimental results are given in this thesis for the two-element sensor topology, the Thévenin equivalent model will only be developed for a simplified case with all loss terms omitted.

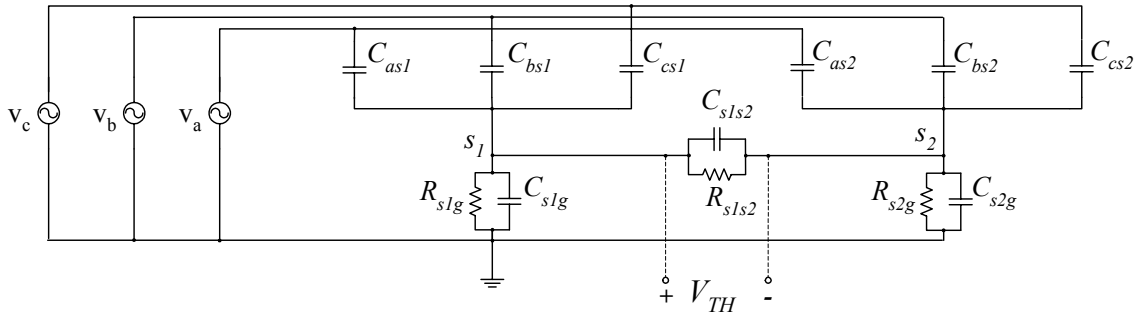


**Figure 6.9: Simplified equivalent circuit for a two-element sensor in a three-phase topology.**

### 6.2.2.1. High frequency model

For high frequencies the equivalent circuit shown in Figure 6.8 can be simplified by omitting all of the loss terms.

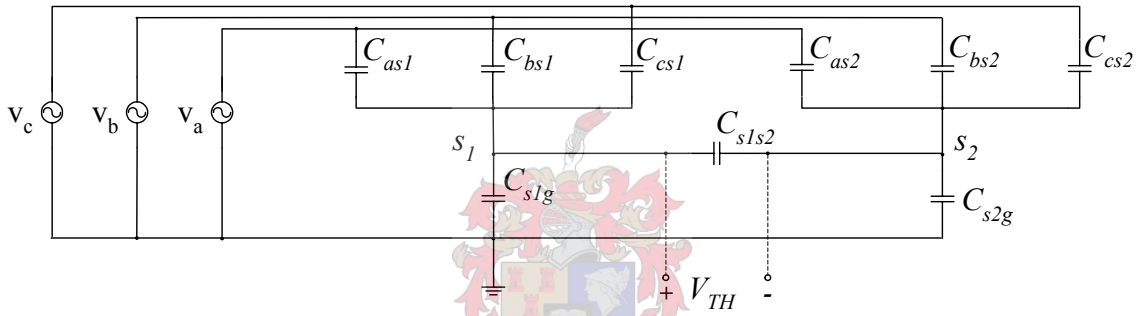


**Figure 6.10: High frequency equivalent circuit for a two-element sensor in a three-phase topology.**

It shown in Appendix B that the Thévenin equivalent impedance $Z_{TH}$ and voltage $V_{TH}$ of the equivalent circuit shown in Figure 6.10 are given by the following relationships:

$$Z_{TH} = \frac{1}{sC_{TH}} \tag{6.18}$$

where

$$C_{TH} = C_{s1s2} + \frac{C_{s1}C_{s2}}{C_{s1} + C_{s2}},$$

$$C_{s1} = C_{as1} + C_{bs1} + C_{cs1} + C_{s1g}$$

$$C_{s2} = C_{as2} + C_{bs2} + C_{cs2} + C_{s2g}$$

and

$$V_{TH} = \frac{C_{s2}\left(v_a C_{as1} + v_b C_{bs1} + v_c C_{cs1}\right) - C_{s2}\left(v_a C_{as2} + v_b C_{bs2} + v_c C_{cs2}\right)}{\left(C_{s1} + C_{s2}\right)C_{TH}}. \tag{6.19}$$

Similar relationships, with appropriate notational changes, apply for sensors $s_1$ and $s_2$.

### 6.2.3. Equivalent circuit for the three-element parallel plate sensor

Botha [1] developed a three-element parallel plate sensor and investigated the advantages of a three-element sensor compared to the single-element and two-element parallel plate sensor configurations for a single-phase topology. The main focus of the investigation detailed in this thesis is the application of the three-element sensor for three-phase topologies. Therefore detailed modelling of this sensor for a three-phase topology is undertaken. Figure 6.11 shows the physical geometry of a three-phase topology with three-element sensors located directly below each of the phase conductors. The notations *a, b, c,* $s_{a1}$, $s_{a2}$, $s_{a3}$, $s_{b1}$, $s_{b2}$, $s_{b3}$, $s_{c1}$, $s_{c2}$, $s_{c3}$ and *g* denote the three phase conductors, plate elements of each of the three sensors and the ground plane respectively.

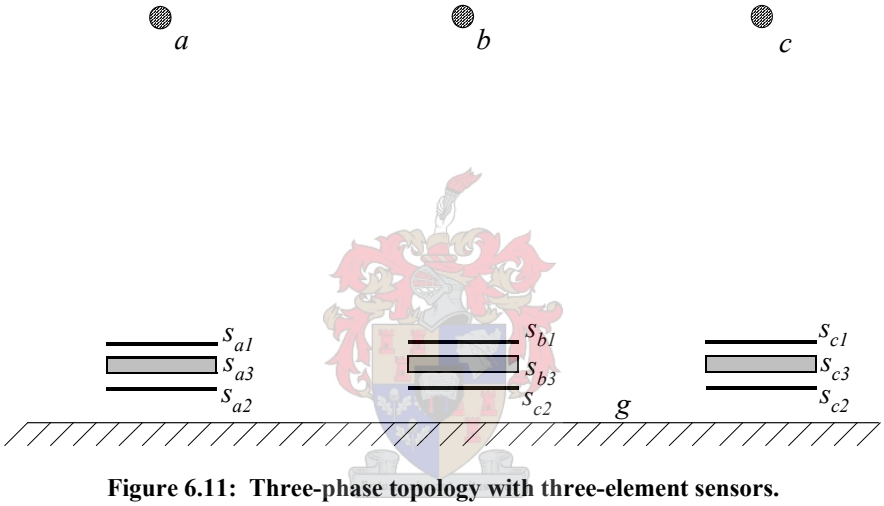


**Figure 6.11: Three-phase topology with three-element sensors.**

#### 6.2.3.1. General model

Figure 6.12 shows the coupling capacitances for the sensor located below the centre conductor. The phase conductor coupling capacitances to ground, i.e. $C_{ag}$, $C_{bg}$ and $C_{cg}$, are not included as these do not affect the Thévenin equivalent circuit model of the topology. Figure 6.13 presents a general equivalent circuit for a three-element parallel plate sensor in a three-phase topology.

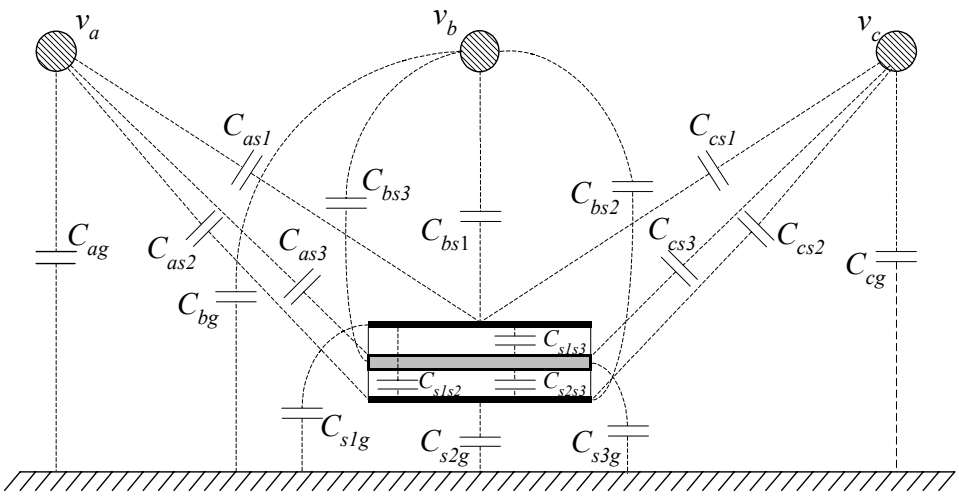


**Figure 6.12: Coupling capacitances for a three-element sensor in a three-phase topology.**

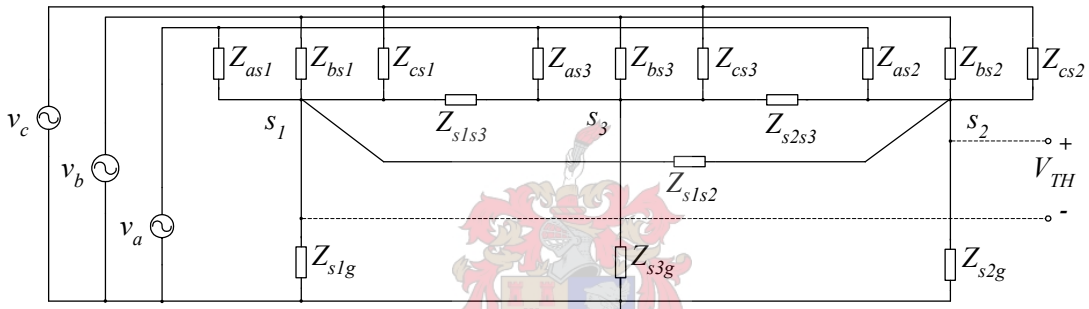


**Figure 6.13: General equivalent circuit for a single three-element sensor in a three-phase topology.**

It shown in Appendix B that the Thévenin equivalent impedance and voltage of the equivalent circuit shown in Figure 6.13 are given by the following relationships:

$$Z_{TH} = Z_t \,||\, Z_{s1s2} = \frac{Z_{s1s2}\left[Z_f Z_g + Z_3\left(Z_f + Z_g\right)\right]}{\left(Z_{s1s2} + Z_3\right)\left(Z_f + Z_g\right) + Z_f Z_g} \tag{6.20}$$

where

$$Z_a = Z_{as1} \,||\, Z_{bs1} \,||\, Z_{cs1} \,||\, Z_{s1g} \ , \tag{6.21}$$

$$Z_b = Z_{as2} \,||\, Z_{bs2} \,||\, Z_{cs2} \,||\, Z_{s2g} \ , \tag{6.22}$$

$$Z_c = Z_{as3} \,||\, Z_{bs3} \,||\, Z_{cs3} \,||\, Z_{s3g} \ , \tag{6.23}$$

$$Z_1 = \frac{Z_{s1s3} Z_c}{Z_a + Z_c + Z_{s1s3}} \ , \tag{6.24}$$

$$Z_2 = \frac{Z_a Z_c}{Z_a + Z_c + Z_{s1s3}} \ , \tag{6.25}$$

$$Z_3 = \frac{Z_{s1s3} Z_a}{Z_a + Z_c + Z_{s1s3}} \ , \tag{6.26}$$

$$Z_f = Z_1 + Z_{s2s3} \ , \tag{6.27}$$

$$Z_g = Z_2 + Z_b \tag{6.28}$$

$$Z_t = Z_f \,||\, Z_g + Z_3 \tag{6.29}$$

and

$$V_{TH} = V_z Z_{s1s3} - \left( \frac{Z_{s1s3}}{Z_{s2s3}} + 1 \right) \left( \frac{1}{Z_B} \right) \left[ \frac{V_z}{Z_{s1s2}} - \frac{V_y}{Z_{s1s3}} + Z_C \left( \frac{G_2 - V_y Z_a}{G_1} \right) \right] + \frac{Z_3 Z_{s1s3} \left( G_2 + V_y Z_a \right)}{G_1} \tag{6.30}$$

where

$$G_1 = \frac{Z_a}{Z_{s2s3}} + \frac{Z_b}{Z_{s1s3}} + \frac{Z_3}{Z_{s1s2}^2} - Z_1 Z_2 Z_3 \ , \tag{6.31}$$

$$G_2 = V_x Z_b + V_z \left( Z_1 Z_2 - \frac{1}{Z_{s1s2}^2} \right) \ , \tag{6.32}$$

$$\begin{aligned} V_x &= -\frac{V_a}{Z_{as1}} - \frac{V_b}{Z_{bs1}} - \frac{V_c}{Z_{cs1}} \\ V_y &= -\frac{V_a}{Z_{as2}} - \frac{V_b}{Z_{bs2}} - \frac{V_c}{Z_{cs2}} \\ V_z &= -\frac{V_a}{Z_{as3}} - \frac{V_b}{Z_{bs3}} - \frac{V_c}{Z_{cs3}} \end{aligned} \tag{6.33}$$

$$\begin{aligned} Z_a &= \frac{Z_1}{Z_{s2s3}} + \frac{1}{Z_{s1s2} Z_{s1s3}} \\ Z_b &= \frac{Z_2}{Z_{s1s3}} + \frac{1}{Z_{s1s2} Z_{s2s3}} \\ Z_c &= \frac{Z_3}{Z_{s1s2}} + \frac{1}{Z_{s1s3} Z_{s2s3}} \end{aligned} \tag{6.34}$$

and

$$\begin{aligned} Z_1 &= \frac{1}{Z_{as1}} + \frac{1}{Z_{bs1}} + \frac{1}{Z_{cs1}} + \frac{1}{Z_{s1s2}} + \frac{1}{Z_{s1s3}} + \frac{1}{Z_{s1g}} \\ Z_2 &= \frac{1}{Z_{as2}} + \frac{1}{Z_{bs2}} + \frac{1}{Z_{cs2}} + \frac{1}{Z_{s1s2}} + \frac{1}{Z_{s2s3}} + \frac{1}{Z_{s2g}} \\ Z_3 &= \frac{1}{Z_{as3}} + \frac{1}{Z_{bs3}} + \frac{1}{Z_{cs3}} + \frac{1}{Z_{s1s3}} + \frac{1}{Z_{s2s3}} + \frac{1}{Z_{s3g}} \ . \end{aligned} \tag{6.35}$$

#### 6.2.3.2. Detailed model

The impedances shown in Figure 6.13 can be replaced with appropriate combinations of resistance and capacitive elements to derive a more detailed equivalent circuit representation for the sensor. This equivalent circuit is shown in Figure 6.14, where the loss terms between the three phase conductors and the sensing elements, i.e. $R_{as1}$, $R_{bs1}$, $R_{cs1}$, $R_{as2}$, $R_{bs2}$, $R_{cs2}$, $R_{as3}$, $R_{bs3}$ and $R_{cs3}$, have been omitted. The parameters shown in Figure 6.14 are defined as follows:

| | |
|---|---|
| $C_{as1}$, $C_{bs1}$, $C_{cs1}$ | Coupling capacitance between the phase conductors and top sensor plate. |
| $C_{as2}$, $C_{bs2}$, $C_{cs2}$ | Coupling capacitance between the phase conductors and bottom sensor plate. |
| $C_{as3}$, $C_{bs3}$, $C_{cs3}$ | Coupling capacitance between the phase conductors and sensor faraday cage. |
| $C_{s1g}$, $R_{s1g}$ | Capacitance and resistance respectively between the top sensor plate and ground. |
| $C_{s2g}$, $R_{s2g}$ | Capacitance and resistance respectively between the bottom sensor plate and ground. |
| $C_{s3g}$, $R_{s3g}$ | Capacitance and resistance respectively between the sensor faraday cage and ground. |
| $C_{s1s2}$, $R_{s1s2}$ | Capacitance and resistance respectively between the top and bottom sensor plates. |
| $C_{s1s3}$, $R_{s1s3}$ | Capacitance and resistance respectively between the top sensor plate and sensor faraday cage. |
| $C_{s2s3}$, $R_{s2s3}$ | Capacitance and resistance respectively between the bottom sensor plate and sensor faraday cage. |

Only one element of the three-element sensor is connected to the support structure and the sensor support structure cannot be regarded as a perfect insulator. Therefore the resistive value between the element, connected to the support structure, and ground must be included in the model, i.e. if the support structure is connected to element $s_1$ resistive value $R_{s1g}$ must be included in the model. The other two resistive values between the elements and ground plane can be omitted. For the evaluations done in this section all three resistive values are however included. The specific resistive values that can be omitted for a certain method of support structure connection can thus be eliminated in the final equivalent equations.

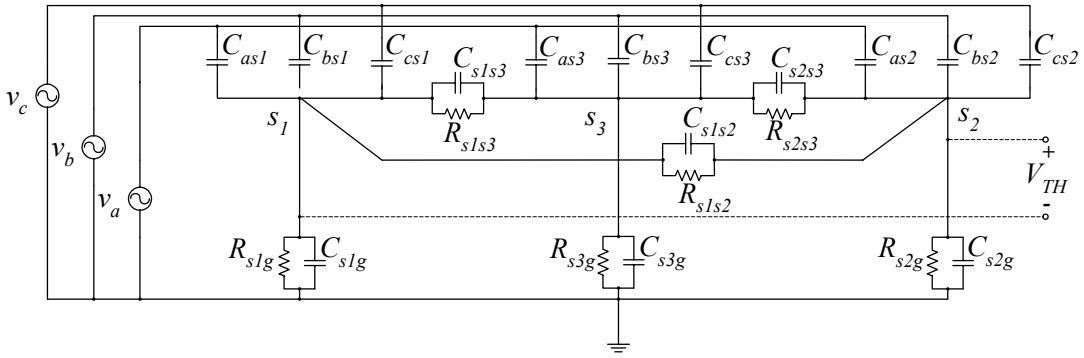


**Figure 6.14: Detailed equivalent circuit for a three-element sensor in a three-phase topology.**

It is shown in appendix B that the Thévenin equivalent impedance and voltage of the equivalent circuit given in Figure 6.14 can be derived from equations (6.20) to (6.35) by substituting the impedances with the following relationships:

$$
\begin{aligned}
Z_{as1} &= 1/(sC_{as1}) \\
Z_{bs1} &= 1/(sC_{bs1}) \\
Z_{cs1} &= 1/(sC_{cs1}) \\
Z_{s1g} &= R_{s1g}/(sR_{s1g}C_{s1g}+1) \\
\\
Z_{as2} &= 1/(sC_{as2}) \\
Z_{bs2} &= 1/(sC_{bs2}) \\
Z_{cs2} &= 1/(sC_{cs2}) \\
Z_{s2g} &= R_{s2g}/(sR_{s2g}C_{s2g}+1) \\
\\
Z_{as3} &= 1/(sC_{as3}) \\
Z_{bs3} &= 1/(sC_{bs3}) \\
Z_{cs3} &= 1/(sC_{cs3}) \\
Z_{s3g} &= R_{s3g}/(sR_{s3g}C_{s3g}+1) \\
\\
Z_{s1s2} &= R_{s1s2}/(sR_{s1s2}C_{s1s2}+1) \\
Z_{s1s3} &= R_{s1s3}/(sR_{s1s3}C_{s1s3}+1) \\
Z_{s2s3} &= R_{s2s3}/(sR_{s2s3}C_{s2s3}+1)
\end{aligned}
\qquad (6.36)
$$

### 6.2.3.3. High frequency model

For high frequencies the equivalent circuit shown in Figure 6.14 can be simplified by omitting all of the loss terms. This yields the equivalent circuit shown in Figure 6.15.

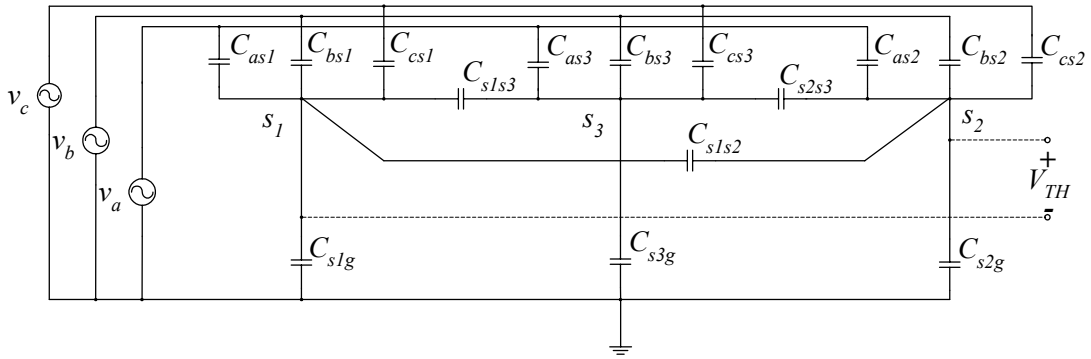


**Figure 6.15: High frequency equivalent circuit for a three-element sensor in a three-phase topology.**

It is shown in appendix B that the Thévenin equivalent impedance and voltage of the equivalent circuit given in Figure 6.15 can be derived from equations (6.20) to (6.35) by substituting the impedances with the following relationships:

$$
\begin{aligned}
Z_{as1} &= 1/(sC_{as1}) \\
Z_{bs1} &= 1/(sC_{bs1}) \\
Z_{cs1} &= 1/(sC_{cs1}) \\
Z_{s1g} &= 1/(sC_{s1g}) \\
\\
Z_{as2} &= 1/(sC_{as2}) \\
Z_{bs2} &= 1/(sC_{bs2}) \\
Z_{cs2} &= 1/(sC_{cs2}) \\
Z_{s2g} &= 1/(sC_{s2g}) \\
\\
Z_{as3} &= 1/(sC_{as3}) \\
Z_{bs3} &= 1/(sC_{bs3}) \\
Z_{cs3} &= 1/(sC_{cs3}) \\
Z_{s3g} &= 1/(sC_{s3g}) \\
\\
Z_{s1s2} &= 1/(sC_{s1s2}) \\
Z_{s1s3} &= 1/(sC_{s1s3}) \\
Z_{s2s3} &= 1/(sC_{s2s3})
\end{aligned}
\qquad (6.37)
$$

### 6.3. Simplification

The equations presented in section 6.2.3 for the Thévenin voltages and impedances are too expansive for the scope of this thesis and must be simplified. Redundant terms that can be omitted in the equations are identified.

This section simplifies the equations of the ideal model to demonstrate the various methods that can be used. To identify the redundant terms in the ideal model the capacitive values of the different terms must be known and compared with each other. A simulation of a three-element parallel plate sensor underneath a three-phase transmission line is done in ELECTRO to evaluate the capacitive matrix. Table 6.1 tabulates the values of the capacitive matrix where *va, vb, vc* denotes the three overhead conductors and *m2_s1, m2_s2, m2_s3* denotes respectively the top plate, faraday cage and bottom plate of the sensor placed beneath the centre conductor.

**Table 6.1 : Capacitive matrix of a three-element parallel plate sensor underneath a three-phase transmission line. The values are specified in Farad [F].**

| | p1 | p2 | p3 | m2_s1 | m2_s3 | m2_s2 |
|---|---|---|---|---|---|---|
| **p1** | 1.05E-09 | -1.86E-10 | -9.01E-11 | -1.28E-11 | -3.01E-12 | -2.94E-12 |
| **p2** | -1.86E-10 | 1.07E-09 | -1.86E-10 | -1.59E-11 | -3.75E-12 | -3.66E-12 |
| **p3** | -9.01E-11 | -1.86E-10 | 1.05E-09 | -1.28E-11 | -3.01E-12 | -2.94E-12 |
| **m2_s1** | -1.28E-11 | -1.59E-11 | -1.28E-11 | 6.69E-07 | -6.67E-07 | -4.96E-10 |
| **m2_s3** | -3.00E-12 | -3.75E-12 | -3.01E-12 | -6.67E-07 | 1.34E-06 | -6.67E-07 |
| **m2_s2** | -2.94E-12 | -3.67E-12 | -2.94E-12 | -4.96E-10 | -6.67E-07 | 6.70E-07 |

It is noticed that the difference between some of the values have magnitudes of 4 orders or more. This fact was used in this section to create several guidelines to simplify the equations. For two capacitors $C_A$ and $C_B$, where $C_A << C_B$, the impedances are denoted by

$$Z_A = \frac{1}{sC_A} \quad \text{and} \quad Z_B = \frac{1}{sC_B} \quad ,$$

thus $Z_A >> Z_B$.

From this statement the following guidelines can be made if $C_A << C_B$:

Guideline 1: Capacitors in series

$$Z_A + Z_B = Z_A \approx 1/C_A \tag{6.38}$$

Guideline 2: Capacitors in parallel

$$1/Z_p = 1/Z_A + 1/Z_B \approx C_A + C_B \approx C_B \tag{6.39}$$

The two guidelines declare that for two capacitances in series the capacitance with the greater value can be ignored and for two capacitors in parallel the smaller capacitance can be ignored.

The magnitude of the difference between two capacitors must be defined for which values it will be large for the two guidelines to be implemented. Two instances, namely *Method 1* and *Method 2* are created for this purpose. Each method uses a different value of when the difference between capacitors is large enough.

*Method 1*: When two line-to-sensor capacitances are multiplied with each other and added to a capacitance that consisted of two sensor-to-ground capacitances or two sensor-to-sensor capacitances, the term of the two line-to-sensor capacitances can be left out. This is due to the fact that the order of magnitude difference is so large that the smaller term can be left out if the order of magnitude difference between the line-to-sensor capacitance and the sensor-to-ground capacitance are doubled. For instance:

$$C_{as1} * C_{bs1} = \left(-1.53E^{-11}\right)\left(-1.95E^{-11}\right) = 2.9835E^{-22}$$

*and*

$$C_{s1g} * C_{s2g} = \left(6.69E^{-7}\right)\left(1.34E^{-7}\right) = 8.9646E^{-13}$$

The two equations have an order of magnitude difference of 9 between them. Thus, if these two terms are added together, the term $C_{as1} * C_{bs1}$ can be left out.

*Method 2*: All the terms left out in *Method 1* are again omitted. Terms which have an order of magnitude difference of three or more are also left out, as explained below:

(line-to-sensor)*(line-to-sensor) + (line-to-sensor)*(sensor-to-ground)
≈ (line-to-sensor)*(sensor-to-ground)

(line-to-sensor)*(sensor-to-ground) + (sensor-to-ground)*(sensor-to-ground)
≈ (sensor-to-ground)*(sensor-to-ground)

Using these two methods the Thévenin voltage and impedance of the ideal circuit are simplified as defined in the following sections.

### 6.3.1. Simplifying the Thévenin Impedance

#### 6.3.1.1. Method 1

Implementing *method 1* does not reduce the equation for the Thévenin equation by much and is thus discarded.

#### 6.3.1.2. Method 2

To simplify the ideal model's Thévenin impedance the capacitance of Table 6.1 and the simplifying guidelines are implemented into equations (6.21) to (6.23). The equations obtained are:

$$Z_a = \frac{1}{s\left(C_{as1} + C_{bs1} + C_{cs1} + C_{s1g}\right)} \approx \frac{1}{sC_{s1g}}, \tag{6.40}$$

$$Z_b = \frac{1}{s\left(C_{as2} + C_{bs2} + C_{cs2} + C_{s2g}\right)} \approx \frac{1}{sC_{s2g}} \tag{6.41}$$

and

$$Z_c = \frac{1}{s\left(C_{as3} + C_{bs3} + C_{cs3} + C_{s3g}\right)} \approx \frac{1}{sC_{s3g}}. \tag{6.42}$$

By implementing equations (6.40), (6.41) and (6.42) into equations (6.24) to (6.29) the Thévenin impedance of (6.20) can be simplified to

$Z_{TH} =$

$$\left( \frac{\left( \frac{1}{Cs1g\,Cs3g\left(\frac{1}{Cs1g\,s}+\frac{1}{Cs1s3\,s}+\frac{1}{Cs3g\,s}\right)s^2} + \frac{1}{Cs2g\,s} \right)\left( \frac{1}{Cs1s3\,Cs3g\left(\frac{1}{Cs1g\,s}+\frac{1}{Cs1s3\,s}+\frac{1}{Cs3g\,s}\right)s^2} + \frac{1}{Cs2s3\,s} \right)}{\frac{1}{Cs1g\,Cs3g\left(\frac{1}{Cs1g\,s}+\frac{1}{Cs1s3\,s}+\frac{1}{Cs3g\,s}\right)s^2} + \frac{1}{Cs1s3\,Cs3g\left(\frac{1}{Cs1g\,s}+\frac{1}{Cs1s3\,s}+\frac{1}{Cs3g\,s}\right)s^2} + \frac{1}{Cs2g\,s} + \frac{1}{Cs2s3\,s}} + \right.$$

$$\left. \frac{1}{Cs1g\,Cs1s3\left(\frac{1}{Cs1g\,s}+\frac{1}{Cs1s3\,s}+\frac{1}{Cs3g\,s}\right)s^2} \right) /$$

$$\left( Cs1s2 \left( \frac{\left( \frac{1}{Cs1g\,Cs3g\left(\frac{1}{Cs1g\,s}+\frac{1}{Cs1s3\,s}+\frac{1}{Cs3g\,s}\right)s^2} + \frac{1}{Cs2g\,s} \right)\left( \frac{1}{Cs1s3\,Cs3g\left(\frac{1}{Cs1g\,s}+\frac{1}{Cs1s3\,s}+\frac{1}{Cs3g\,s}\right)s^2} + \frac{1}{Cs2s3\,s} \right)}{\frac{1}{Cs1g\,Cs3g\left(\frac{1}{Cs1g\,s}+\frac{1}{Cs1s3\,s}+\frac{1}{Cs3g\,s}\right)s^2} + \frac{1}{Cs1s3\,Cs3g\left(\frac{1}{Cs1g\,s}+\frac{1}{Cs1s3\,s}+\frac{1}{Cs3g\,s}\right)s^2} + \frac{1}{Cs2g\,s} + \frac{1}{Cs2s3\,s}} + \right.\right.\right.$$

$$\left.\left.\left. \frac{1}{Cs1g\,Cs1s3\left(\frac{1}{Cs1g\,s}+\frac{1}{Cs1s3\,s}+\frac{1}{Cs3g\,s}\right)s^2} + \frac{1}{Cs1s2\,s} \right) s \right) \right).$$

This equation is not as complex as equation (B.32) (Appendix B), but the Thévenin impedance can be simplified even more. From equation (6.20) it is seen that the Thévenin impedance is equal to the parallel combination of impedances $Z_t$ and $Z_{s1s2}$. The capacitance between the top and bottom plate, $Z_{s1s2}$, are 3 orders of magnitude smaller than the sensor-to-

ground capacitances (i.e. $C_{s1s2} << C_{as1}$). From *guideline 2* the capacitance of $Z_{s1s2}$ can therefore be ignored obtaining the Thévenin impedance as

$$\frac{\left(\frac{1}{Cs1g^2\left(\frac{2}{Cs1g\,s}+\frac{1}{Cs1s3\,s}\right)s^2}+\frac{1}{Cs2g\,s}\right)\left(\frac{1}{Cs1g\,Cs1s3\left(\frac{2}{Cs1g\,s}+\frac{1}{Cs1s3\,s}\right)s^2}+\frac{1}{Cs2s3\,s}\right)}{\frac{1}{Cs1g^2\left(\frac{2}{Cs1g\,s}+\frac{1}{Cs1s3\,s}\right)s^2}+\frac{1}{Cs1g\,Cs1s3\left(\frac{2}{Cs1g\,s}+\frac{1}{Cs1s3\,s}\right)s^2}+\frac{1}{Cs2g\,s}+\frac{1}{Cs2s3\,s}}+$$

$$\frac{1}{Cs1g\,Cs1s3\left(\frac{2}{Cs1g\,s}+\frac{1}{Cs1s3\,s}\right)s^2} \quad . \qquad (6.43)$$

This simplified method greatly reduced the complexity of equation (B.32) (Appendix B) to the above equation.

### 6.3.2. Simplifying the Thévenin voltage

#### 6.3.2.1. Method 1

As with the Thévenin impedance, implementing *method 1* does not reduce the equation for the Thévenin equation by much and is thus discarded.

#### 6.3.2.2. Method 2

To simplify the ideal model's Thévenin voltage the capacitances of Table 6.1 and the simplifying guidelines are implemented into equations (6.30) to (6.35). The equation obtained for the Thévenin voltage is denoted by

$$\frac{-Cas3\,s\,va-Cbs3\,s\,vb-Ccs3\,s\,vc}{Cs1s3\,s}+((Cs1s3+Cs2s3+Cs3g)$$
$$((Cs1s2\,Cs2s3\,s^2+Cs1s3\,(Cs1s2+Cs2g+Cs2s3)\,s^2)\,(-Cas1\,s\,va-Cbs1\,s\,vb-Ccs1\,s\,vc)+$$
$$(Cs1s2\,Cs1s3\,s^2+(Cs1g+Cs1s2+Cs1s3)\,Cs2s3\,s^2)\,(-Cas2\,s\,va-Cbs2\,s\,vb-Ccs2\,s\,vc)+$$
$$(-Cs1s2^2\,s^2+(Cs1g+Cs1s2+Cs1s3)\,(Cs1s2+Cs2g+Cs2s3)\,s^2)$$
$$(-Cas3\,s\,va-Cbs3\,s\,vb-Ccs3\,s\,vc)))\Big/$$
$$(Cs1s3\,(Cs1s2^2\,(Cs1s3+Cs2s3+Cs3g)\,s^3-(Cs1g+Cs1s2+Cs1s3)\,(Cs1s2+Cs2g+Cs2s3)$$
$$(Cs1s3+Cs2s3+Cs3g)\,s^3+Cs2s3\,s\,(Cs1s2\,Cs1s3\,s^2+(Cs1g+Cs1s2+Cs1s3)\,Cs2s3\,s^2)+$$
$$Cs1s3\,s\,(Cs1s2\,Cs2s3\,s^2+Cs1s3\,(Cs1s2+Cs2g+Cs2s3)\,s^2)))-$$
$$\left(\left(1+\frac{Cs2s3}{Cs1s3}\right)(-Cs1s3\,s\,(-Cas2\,s\,va-Cbs2\,s\,vb-Ccs2\,s\,vc)+\right.$$
$$Cs1s2\,s\,(-Cas3\,s\,va-Cbs3\,s\,vb-Ccs3\,s\,vc)+((Cs1s3\,Cs2s3\,s^2+Cs1s2\,(Cs1s3+Cs2s3+Cs3g)\,s^2)$$
$$((Cs1s2\,Cs2s3\,s^2+Cs1s3\,(Cs1s2+Cs2g+Cs2s3)\,s^2)\,(-Cas1\,s\,va-Cbs1\,s\,vb-Ccs1\,s\,vc)-$$
$$(Cs1s2\,Cs1s3\,s^2+(Cs1g+Cs1s2+Cs1s3)\,Cs2s3\,s^2)\,(-Cas2\,s\,va-Cbs2\,s\,vb-Ccs2\,s\,vc)+$$
$$(-Cs1s2^2\,s^2+(Cs1g+Cs1s2+Cs1s3)\,(Cs1s2+Cs2g+Cs2s3)\,s^2)$$
$$(-Cas3\,s\,va-Cbs3\,s\,vb-Ccs3\,s\,vc)))\Big/$$
$$(Cs1s2^2\,(Cs1s3+Cs2s3+Cs3g)\,s^3-(Cs1g+Cs1s2+Cs1s3)\,(Cs1s2+Cs2g+Cs2s3)$$
$$(Cs1s3+Cs2s3+Cs3g)\,s^3+Cs2s3\,s\,(Cs1s2\,Cs1s3\,s^2+(Cs1g+Cs1s2+Cs1s3)\,Cs2s3\,s^2)+$$
$$\left.Cs1s3\,s\,(Cs1s2\,Cs2s3\,s^2+Cs1s3\,(Cs1s2+Cs2g+Cs2s3)\,s^2)))\right)\Big/$$
$$(Cs1s2\,Cs2s3\,s^2+Cs1s3\,(Cs1s2+Cs2g+Cs2s3)\,s^2)$$

Even though this equation is somewhat simplified compared to equation B33 it will be helpful if the equation can be simplified even further. As with the Thévenin impedance *Method 2* is repeated, using the fact that $C_{s1s2} << C_{as1}$. By implementing this fact into the simplification of the Thévenin impedance, equations (6.31) to (6.35) are rewritten as

$$\begin{aligned} Z_1 &= s\left(C_{s1s3}+C_{s1g}\right) \\ Z_2 &= s\left(C_{s2s3}+C_{s2g}\right) \\ Z_3 &= s\left(C_{s1s3}+C_{s2s3}+C_{s3g}\right) \end{aligned} \quad , \tag{6.44}$$

$$\begin{aligned} Z_a &= s^2\left(C_{s1s3}+C_{s1g}\right)C_{s2s3} \\ Z_b &= s^2\left(C_{s2s3}+C_{s2g}\right)C_{s1s3} \\ Z_c &= s^2 C_{s1s3}C_{s2s3} \end{aligned} \quad , \tag{6.45}$$

$$\begin{aligned} V_x &= s\left(-v_a C_{as1}-v_b C_{bs1}-v_c C_{cs1}\right) \\ V_y &= s\left(-v_a C_{as2}-v_b C_{bs2}-v_c C_{cs2}\right) \\ V_z &= s\left(-v_a C_{as3}-v_b C_{bs3}-v_c C_{cs3}\right) \end{aligned} \quad , \tag{6.46}$$

$$\begin{aligned} G_1 = &-s^3\left(C_{s1g}+C_{s1s3}\right)\left(C_{s2g}C_{s2s3}+C_{s3g}C_{s2s3}+C_{s2g}C_{s3g}\right) \\ &-s^3 C_{s1g}C_{s1s3}\left(C_{s2g}+C_{s2s3}\right) \end{aligned} \tag{6.47}$$

and

$$G_2 = -s^3\left(v_a C_{as3}C_T + v_b C_{bs3}C_T + v_c C_{cs3}C_T\right)$$

where

$$C_T = \left(C_{s1g}+C_{s1s3}\right)\left(C_{s2s3}+C_{s1s3}+C_{s3g}\right) . \tag{6.48}$$

The Thévenin voltage is then reduced to

$$\begin{aligned} &-\frac{1}{Cs1s3\ s} \\ &\Big(s\ (Cas3\ va + Cbs3\ vb + Ccs3\ vc) + \\ &\quad ((Cs1g + Cs1s3)\ (Cs1s3 + Cs2s3 + Cs3g) \\ &\qquad (-Cs2s3\ s\ (Cas2\ va + Cbs2\ vb + Ccs2\ vc) - \\ &\qquad\quad (Cs1s3 + Cs2s3 + Cs3g)\ s\ (Cas3\ va + Cbs3\ vb + Ccs3\ vc))) / \\ &\quad (Cs1g\ Cs1s3\ (Cs2g + Cs2s3) + (Cs1g + Cs1s3)\ (Cs2s3\ Cs3g + Cs2g\ (Cs2s3 + Cs3g))) + \\ &\frac{1}{Cs1s3\ (Cs2g + Cs2s3)} \\ &((Cs1s3 + Cs2s3) \\ &\quad (Cs1s3\ s\ (Cas2\ va + Cbs2\ vb + Ccs2\ vc) - \\ &\qquad (Cs1s3\ (Cs1g + Cs1s3)\ Cs2s3 \\ &\qquad\quad (Cs2s3\ s\ (Cas2\ va + Cbs2\ vb + Ccs2\ vc) - \\ &\qquad\qquad (Cs1s3 + Cs2s3 + Cs3g)\ s\ (Cas3\ va + Cbs3\ vb + Ccs3\ vc))) / \\ &\qquad (Cs1g\ Cs1s3\ (Cs2g + Cs2s3) + \\ &\qquad\quad (Cs1g + Cs1s3)\ (Cs2s3\ Cs3g + Cs2g\ (Cs2s3 + Cs3g)))))\Big) \end{aligned} \tag{6.49}$$

It was thus possible to simplify the equation significantly, from equation B.33 (Appendix B) to equation (6.49). This section showed that by using the two guidelines the Thévenin impedance and voltage can be greatly reduced to a form that can be easily used for calculations.

## 6.4. Conclusion

This chapter derived the equivalent circuit models for a three-element parallel plate sensor based on the work done by Botha [1]. Due to the complexity of the equations Mathematical software programs (Mathematica) are used, to calculate the Thévenin voltage and impedance of the three-element parallel plate sensor. If the capacitive coupling and resistivity between the different elements of a specific power system and measurement system are known, the Thévenin impedance and voltage can be easily calculated with mathematical programs such as Mathematica or Matlab.

# 7. Experimental evaluation of the capacitive sensor assembly

## 7.1. Introduction

Laboratory tests were conducted to compare the results obtained by the three sensors and to calibrate the associated voltage transfer functions. This was achieved using the arrangement shown in Figure 7.1.

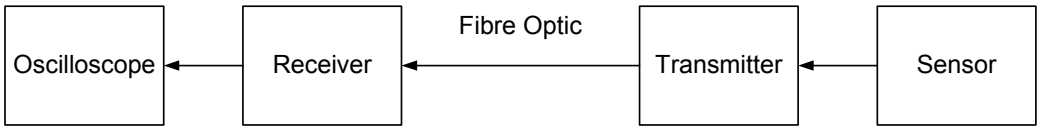


**Figure 7.1: Block diagram of the measuring arrangement.**

The performance of the HandyScope oscilloscope, used to measure the analog output of the receiver circuit, was first evaluated. The three transmitters were tested and the voltage gains were compared and calibrated. The effects of sensor orientation and the linearity of the sensors with input voltage magnitude were tested in the HV Lab. Figure 7.2 presents a block diagram illustrating the different steps in testing all the elements of the measurement process.

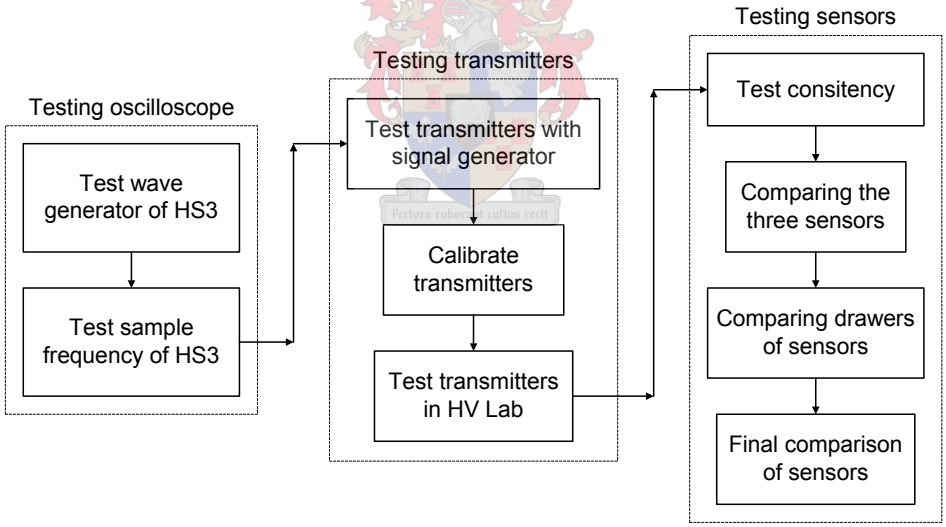


**Figure 7.2: Block diagram illustrating the steps of testing all the elements used in the measurement process.**

## 7.2. Calibration and evaluation of optical link instrumentation

The transfer gain of the optical link between the sensors and the oscilloscope were evaluated and calibrated. The different characteristics of the oscilloscopes must to be tested in conjunction with the transmitters and sensors i.e. to evaluate if the sampling frequencies of the oscilloscope have an effect on the consistency and validity of the measurements.

At sampling frequencies greater that 100KS/sec data loss was found to occur because the time axis data is rounded off to the 5th decimal. The data can be corrected using MATLAB. Figure 7.3 illustrates the difference between the HandyScope3 data log (Measurement1) and the corrected time data log obtained from Matlab (Measurement2).

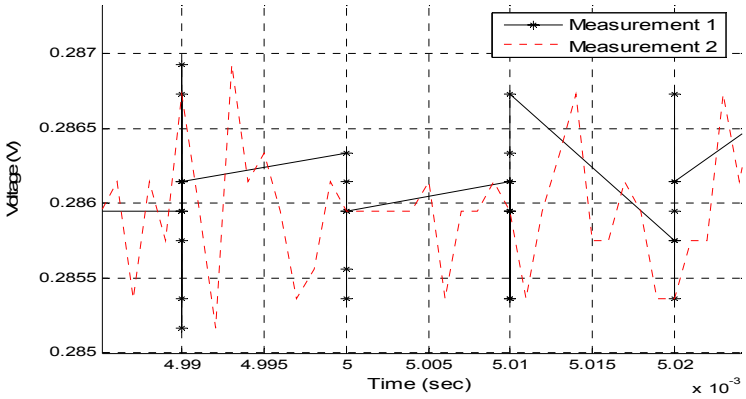


**Figure 7.3: The sinusoidal waveform (Measurement 1) measured by the Handyscope3 and the sinusoidal waveform (Measurement 2) after the time axis was correct by Matlab.**

### 7.2.1. Calibrating the transmitters

The outputs of the three transmitters were compared using a signal generator as a source. The signal generator is connected to the transmitter using a BNC connector and coaxial cable; the transmitter connected to the receiver via optic fibre and the receiver connected to the oscilloscope with a BNC connector and coaxial cable. The same sinusoidal, 50Hz signal with an amplitude of 0.28V, is applied onto the input of each of the three transmitters. A value of 0.28V is used as that is the value of the voltage levels measured underneath HV transmission lines in the field.

The three transmitters are calibrated with an internal adjustable capacitor. The transmitters are calibrated with the 5V 1 kHz square wave test probe of a Tektronics oscilloscope and a 10x probe. Figure 7.4 shows the transmitters' waveform after calibration. The input is the square wave generated by the test probe and the output is the signal obtained from the transmitter. The transmitters' input and output are accurate replicas of each other except in the vicinity of the rising and falling edges.

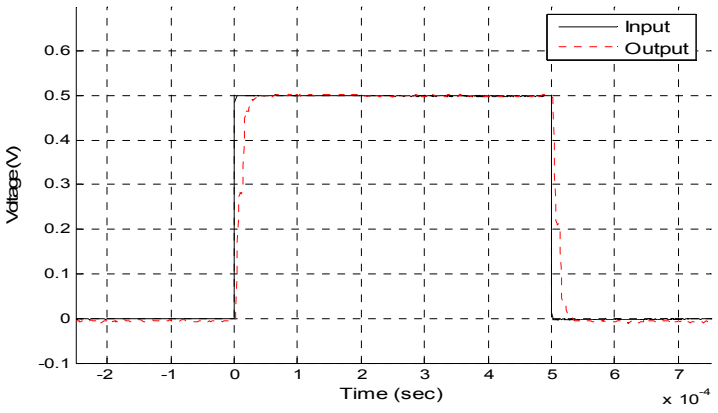


**Figure 7.4: Measured square wave after calibration of transmitters.**

### 7.2.2. Evaluating transmitters in the HV Lab in conjunction with capacitive sensors

To determine if the three transmitters give the same results under laboratory conditions all three transmitters were consecutively tested under the same test conditions. Figure 7.5 illustrates the test arrangement used. An HV busbar was constructed above a copper ground plane. The test sensor was placed on top of the glass/PVC support structure under the busbar and the busbar was energised to 18 kV using a single phase transformer.

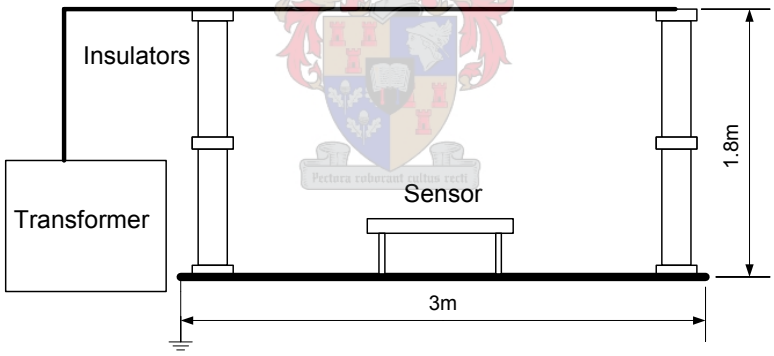


**Figure 7.5: Illustrating the construction and composition of the sensors underneath the bus bar in the HV Lab.**

*Sensor A* was used in conjunction with the three different transmitters to measure the electric field underneath the bus bar. Figure 7.6 and Figure 7.7 compare the waveforms obtained with *transmitter 1* and *2*. The waveforms exhibit a small difference in amplitude, while Figure 7.6 shows that *transmitter1* has a small negative DC-offset. This gain discrepancy disappeared after the transmitters are calibrated. The above procedure was repeated with *Sensor B* and *Sensor C*. All three sensors delivered consistent results.

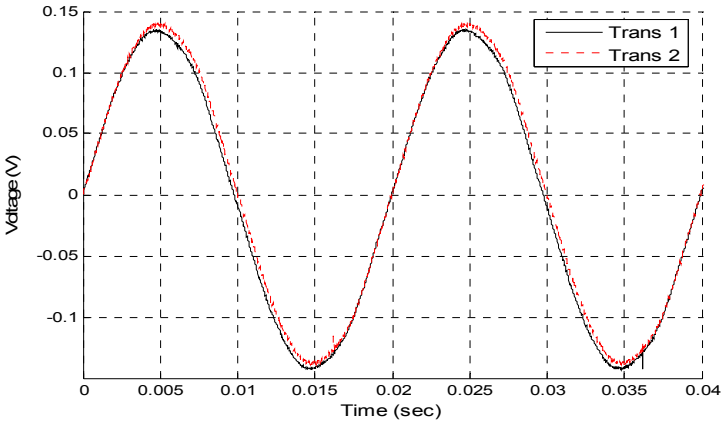


**Figure 7.6: Comparing the measurements between *Transmitter 1* and *Transmitter 2*.**

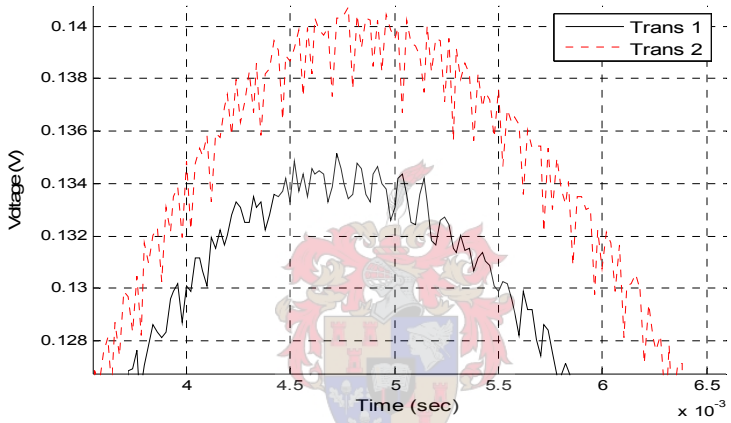


**Figure 7.7: Illustrating the difference in sampling between *Transmitter 1* and *Transmitter 2*.**

## 7.3. Indoor calibration and evaluation of capacitive sensors

### 7.3.1. Comparison of three sensors

The individual sensors used for the first two field measurements were tested in the HV Lab using the test configuration illustrated in Figure 7.5, with the same HV excitation voltage level for each measurement. For calibration purposes the waveforms measured by the individual sensors are compared with each other. Figure 7.8 presents waveforms initially measured with the three. It is seen that a discrepancy of about 8.2% exists between the measurement obtained with *Sensor C* and the measurements obtained with *sensor A and B*.

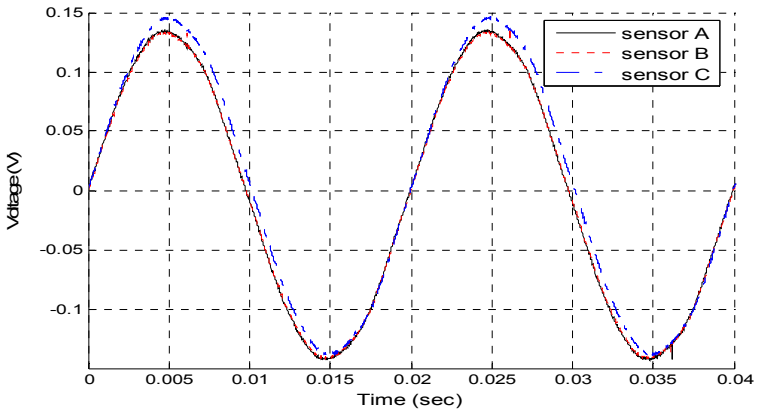


**Figure 7.8: Comparing the waveforms of the three sensors with each other.**

The sensors were cleaned thoroughly with alcohol to improve the galvanic isolation of the sensor elements from each other and the support structure. The comparative tests were repeated. Figure 7.9 presents the results and shows a major improvement compared to the results of Figure 7.8. Figure 7.10 shows that the biggest discrepancy, i.e. between *sensor C* and *sensor B,* is 4.2 % and the difference between *sensor A* and *sensor C* is 3%.

The discrepancies between the waveforms in Figure 7.10 were regarded as excessive and further investigations were conducted, including an investigation to determine whether calibration is effected by interchanging the instrumentation drawers. This was shown to have no effect.

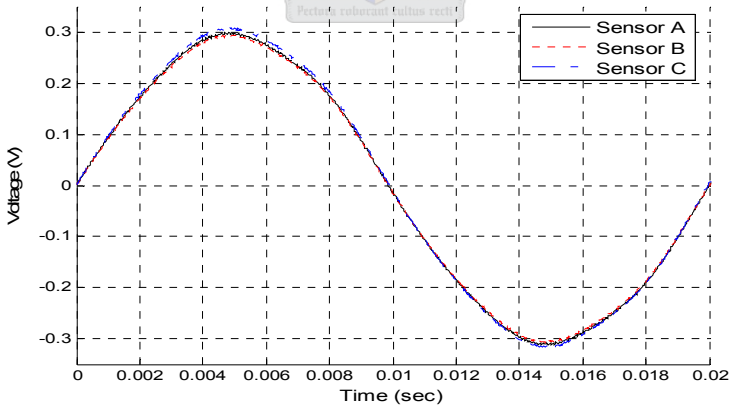


**Figure 7.9: Comparing the three different sensors after the support structure was thoroughly cleaned.**

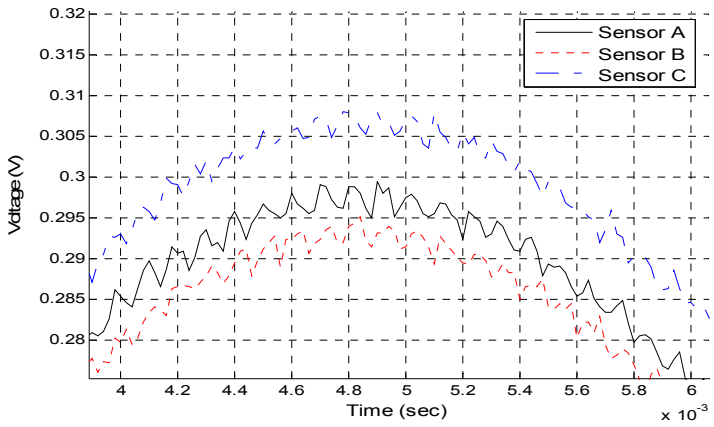


**Figure 7.10: Zoomed view of the comparison between the three sensors in Figure 7.9.**

The effects of tolerances in the values of the termination capacitances used with the sensors were discussed in section 4.3.3. The above investigations were conducted before the capacitance values of the termination capacitances were matched. After matching the termination capacitances, the tests were repeated. This yielded the results shown in Figure 7.11, where the difference between *sensor C* and *sensor A* is now only 1.17%.

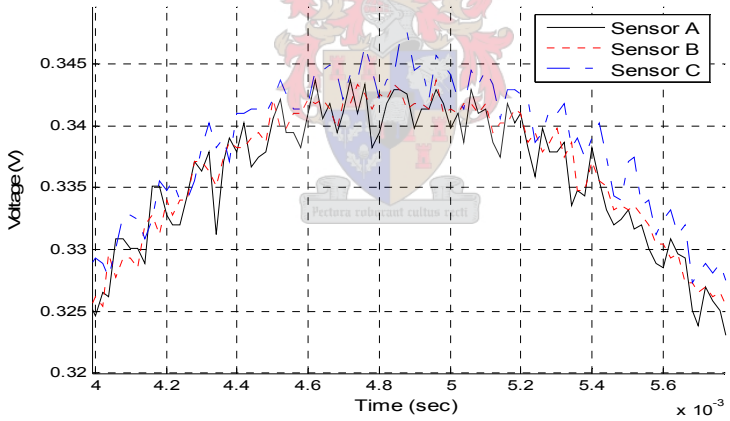


**Figure 7.11: The three sensors compared to each other, illustrating the effect of implementation of the new WIMA capacitors.**

### 7.3.2. Testing the characteristics of the three-element parallel sensors

Further measurements were conducted to evaluate the linearity of a sensor with voltage magnitude and to determine the effects of sensor orientation on the output voltage. These measurements were conducted for one of the sensors only.

### 7.3.2.1. Linearity

The voltage of the HV conductor was varied between 5kV and 20kV to determine if the sensor has a linear response with voltage magnitude. Table 7.1 tabulates the voltages measured by the sensor as well as the percentage increase in the measured voltages. Figure 7.12 and Figure 7.13 graphs the results presented in Table 7.1.

**Table 7.1: The percentage difference between the increased voltages.**

| Measure-ment | Condcutor voltage | Measured voltage | V dif | % dif |
|---|---|---|---|---|
| 1 | 5 | 0.071 | | |
| 2 | 10 | 0.191 | 0.12 | 169.0141 |
| 3 | 15 | 0.253 | 0.062 | 87.32394 |
| 4 | 20 | 0.338 | 0.085 | 119.7183 |

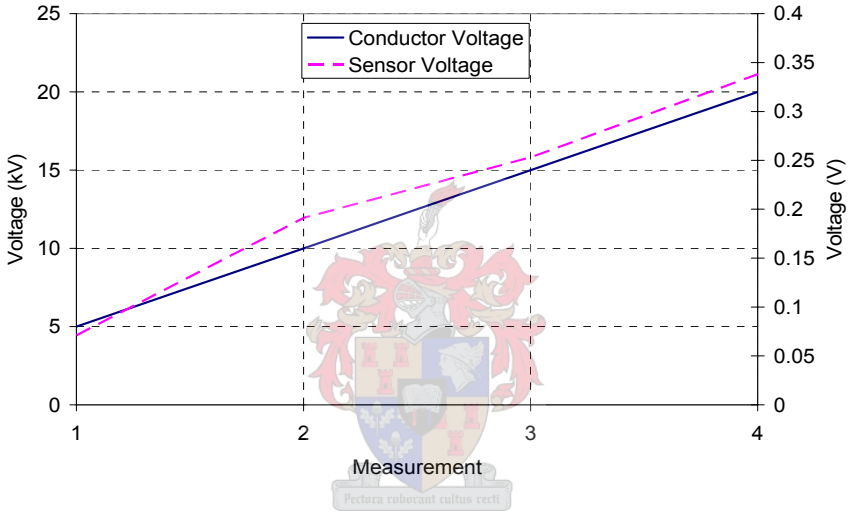


**Figure 7.12: Comparison of the linearity of the conductor and measured voltages.**

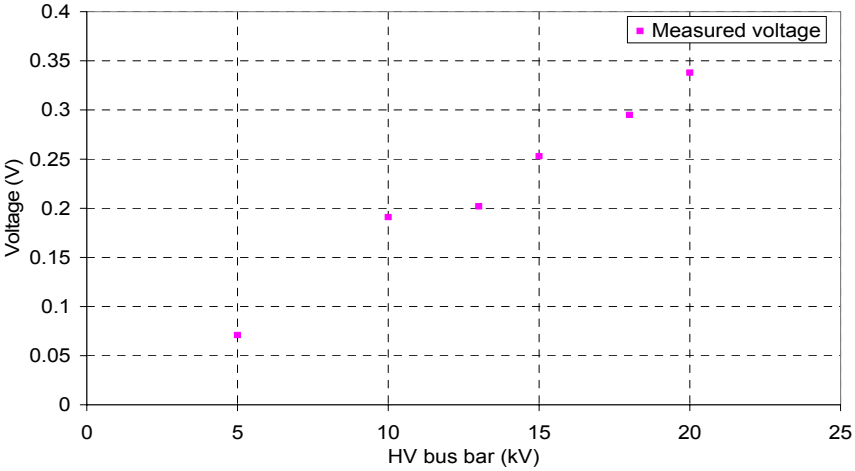


**Figure 7.13: Sensor voltage magnitude versus busbar voltage magnitude.**

### 7.3.3. Effects of sensor orientation

The effects of the orientation of the sensor underneath the HV busbar were also evaluated. Figure 7.14 shows the different orientations that were considered. The measured voltages for the different orientations were compared with *position 1* as the reference position.

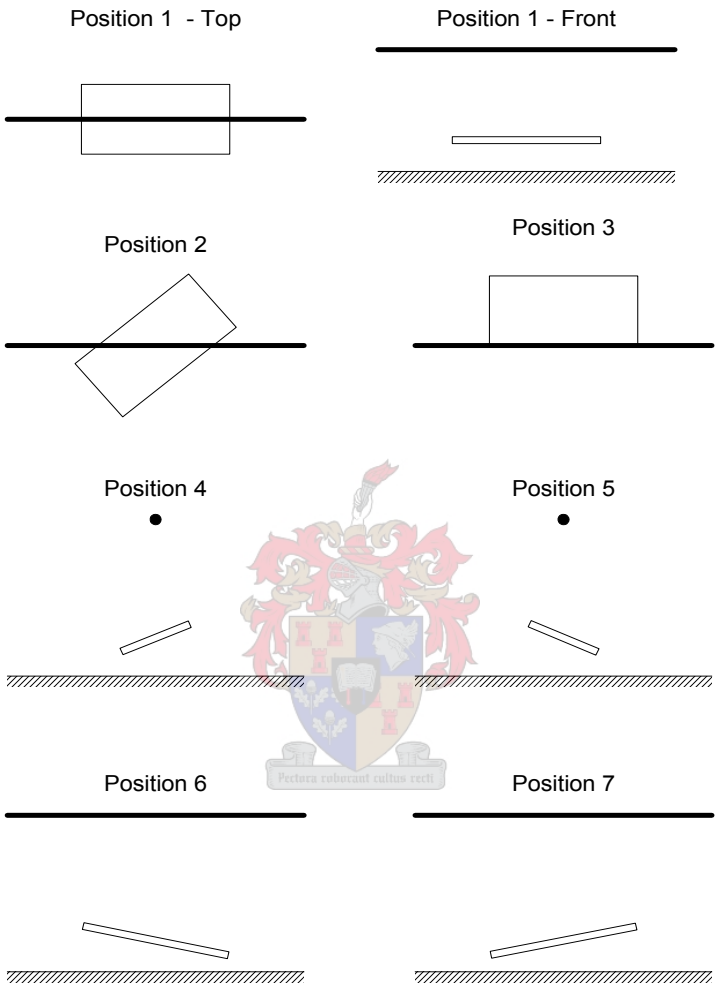


**Figure 7.14: Different orientations underneath the HV conductor.**

Figure 7.15 compares the measured voltages for orientations *1*, *2* and *3*. The measured voltage for *orientation 3* is smaller than for *orientation 1 and 2* due to the fact that less electric field couples with the sensor. Figure 7.16 and Figure 7.17 shows the voltages measured for the other orientations. As expected, the measured voltage is clearly dependent on the orientation of the sensor underneath the conductor.

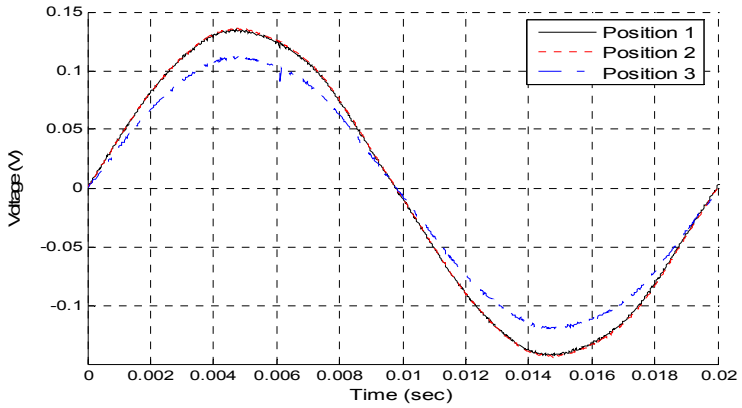


**Figure 7.15: Waveforms obtained when the sensor are placed at positions 1, 2 and 3.**

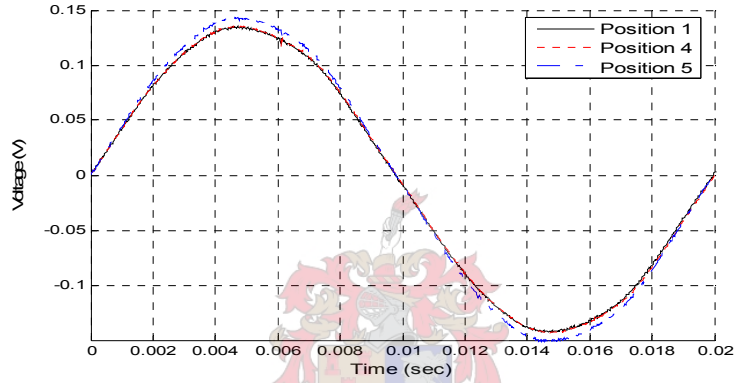


**Figure 7.16: Waveforms obtained when the sensor are placed at positions 1, 4 and 5.**

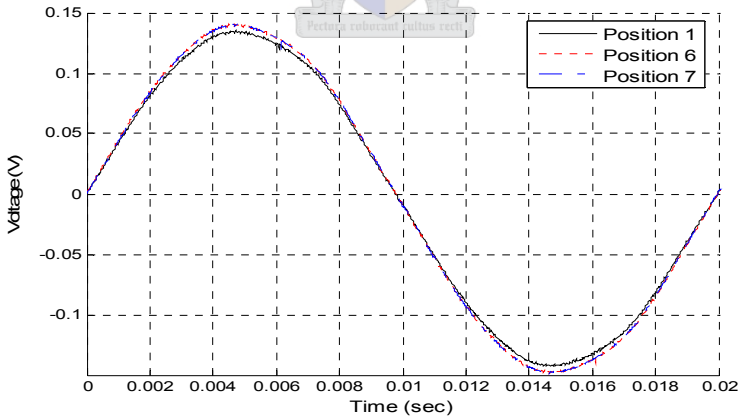


**Figure 7.17: Waveforms obtained when the sensor are placed at positions 1, 6 and 7.**

### 7.3.4. Evaluation of the triggering circuit with the capacitive sensor

The performance of the triggering circuit was evaluated with the three-element parallel sensor in the HV Lab. The following five different types of triggering tests were performed:

- The voltage is switched off abruptly, i.e. the voltage drops to zero immediately. Triggering circuit is switched to OFF.
- The voltage is switched off gradually, i.e. the voltage is decreased until the circuit triggers. Triggering circuit is switched to OFF.
- The voltage is switched on abruptly, i.e. the voltage jumps immediately to the final voltage level. Triggering circuit is switched to ON.
- The voltage is switched on gradually, i.e. the voltage is increased until the circuit triggers. Triggering circuit is switched to ON.
- The trigger is generated manually, i.e. the trigger switch is turned from OFF to ON, or from ON to OFF.

Figure 7.18 and Figure 7.19 illustrates the waveforms measured for the different triggering methods. Figure 7.18 shows the triggering test when the voltage is switched off abruptly. Figure 7.19 shows the triggering test if the voltage is switched on abruptly. Figure 7.20 shows that the circuit triggers at 0.202V if the voltage is gradually increased, or gradually decreased. The voltage at which the circuit triggers can be adjusted manually on the triggering circuit. The results show that the trigger circuit performed as intended for all cases.

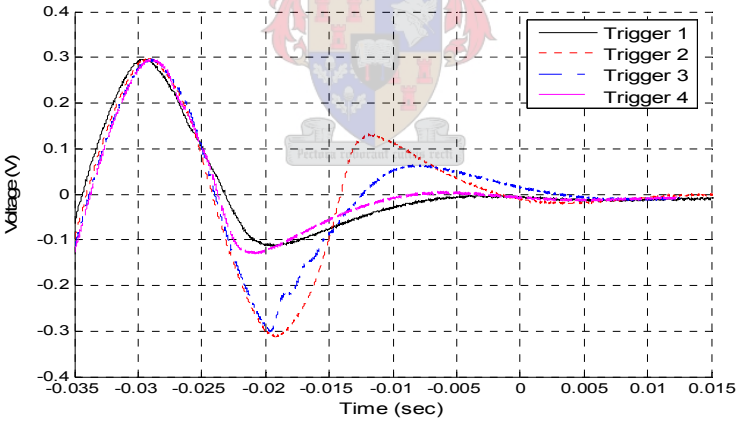


**Figure 7.18: Four different waveforms if triggered when the voltage is suddenly switched off.**

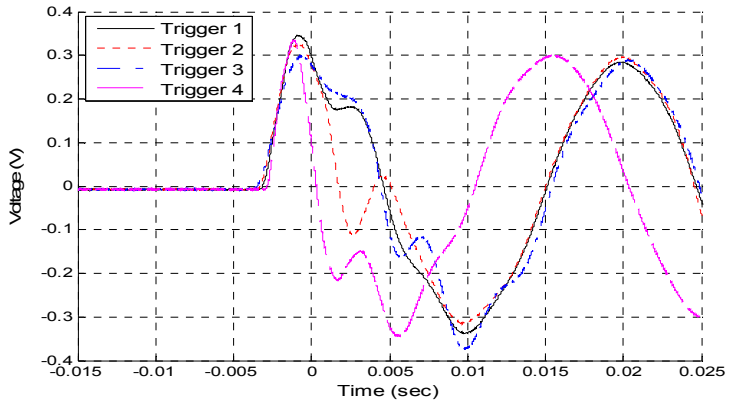


**Figure 7.19: Four different waveforms if triggered when the voltage is suddenly switched on (voltage step).**

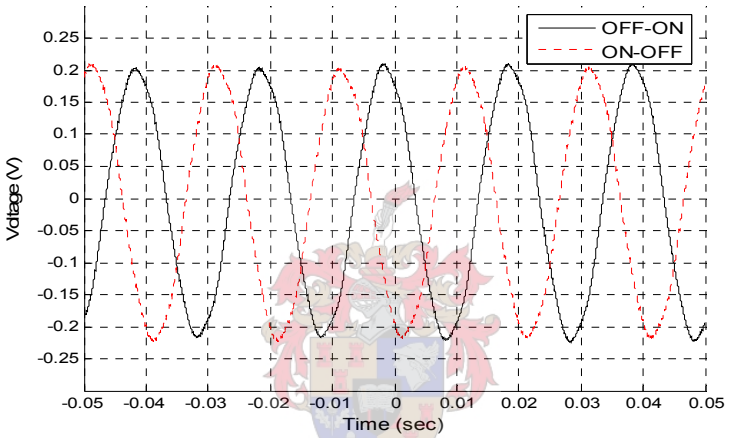


**Figure 7.20: The measured waveforms if the circuit is triggered by gradually increasing ot decreasing the voltage.**

## 7.4. Field evaluation of the new sensors

### 7.4.1. Capacitive voltage measurements in the field

After construction of the new three-element parallel plate sensors, these sensors were briefly tested in the field underneath a 400kV, three-phase transmission line. The same interface instrumentation, i.e. three optical links and two oscilloscopes, each connected to a Laptop, used in conjunction with the original sensors were used for this field test. This topology thus consisted of two separate stations, namely *Station 1* comprised of *Sensor A* and *Sensor B* connected to *Oscilloscope 1* and *Station 2* comprised of *Sensor C* connected to *oscilloscope 2*. *Oscilloscope 2* was used to trigger the other oscilloscope via an optocoupler-link. There was a slight time delay through the optocoupler (Appendix F.5), which required correction when the measurements from the two oscilloscopes were compared. A brief explanation of some of the tests is given below.

The three sensors were each positioned underneath each of the phase conductors. The voltages induced on the sensors were measured and the waveforms compared. Figure 7.21 illustrates the amplitude and phase differences between the three measured signals. Figure 7.22 illustrates the two waveforms measured by *sensor A* and *sensor B* if both sensors were placed underneath the centre phase (*phase B*). As expected, the measured waveforms correlate closely.

The field measurements gave rise to the following practical conclusions:

- A safe and easy to use container is required to transport the glass tubes.
- A digital camera will be helpful so that the arrangement of the field measurements can be photographed.
- A table or some platform will help to make the setup of the equipment easier.
- The ground level was not flat, so it was difficult to align the sensors 100%.
- The three sensors were not placed perpendicular to the transmission lines due to the topography of the site at which the field measurements were done.
- Further research is required to determine the optimal termination impedance of the sensor.
- A methodology is required to measure the dimensions of the line configuration.

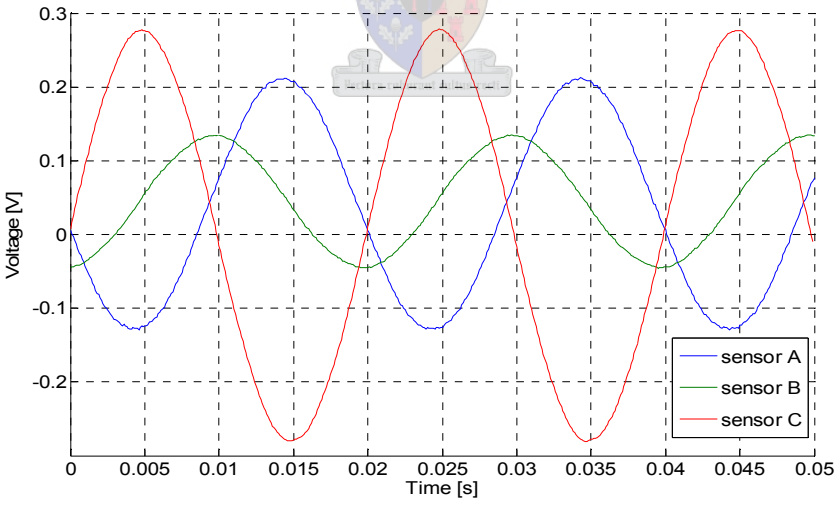


**Figure 7.21: Comparison of the measured phase voltages.**

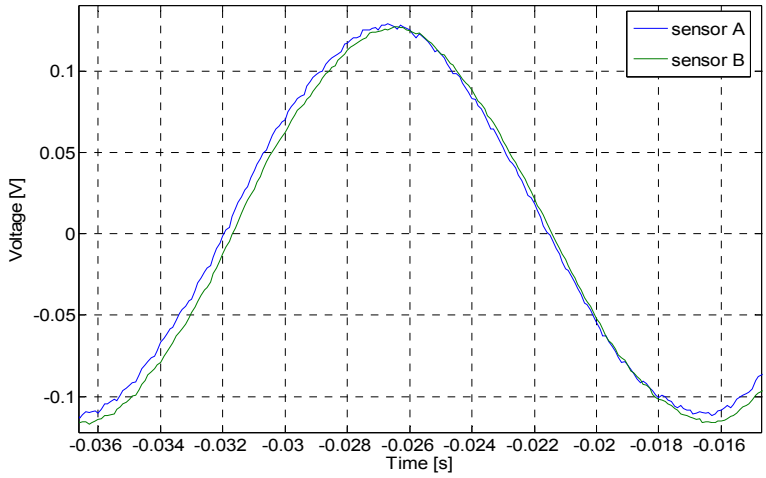


**Figure 7.22: Measured voltages with sensor A and sensor B positioned underneath the middle phase.**

### 7.4.2. Survey of test site for HV measurements

Future field tests require accurate measurement of the transmission line geometry for calculation of the capacitive coupling between the overhead conductors and the sensors. The shape of the terrain, tower construction and conductor sag affect the geometry of the test topology. Although most of the geometrical information can be obtained from the tower, and conductor data (Appendix E and F), the distance between the ground and the overhead conductors is varies with time, temperature and tension.

Land survey equipment can be used to calculate the distance to the overhead conductors and other geometrical quantities of interest. This is reviewed in Appendix I. Field tests were conducted where a 400kV power line from Muldersvlei passes the Joostenberg Primary School on the Hoopenberg road. The photograph in Figure 7.23 shows the test location.

**Figure 7.23: Location where experiment survey measurements are done.**

Figure 7.24 illustrates the measurements taken with the theodolite near the HV towers, where:

| | |
|---|---|
| *Point 1* | Position on ground underneath centre of conductor span. |
| *Point 2* | Position 1m above *Point 1*. |
| *Point 3* | Centre spot where theodolite is centred above. |
| *Point 4* | Height of theodolite. |
| *Point 5* | Position on HV conductor at the centre of conductor span. |
| *Point 6 & 7* | Attachment position between conductor and insulators. |

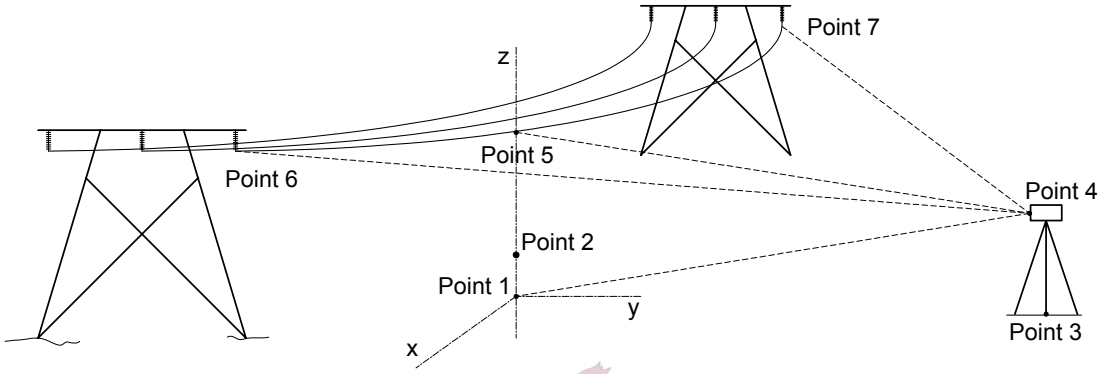


**Figure 7.24: Survey geometry at high voltage transmission line.**

The coordinates of the above five points are used to calculate the distance between the two successive towers, the distance between the conductor and ground at the measuring point and the degree of sag of the transmission line. Figure 7.25 shows how the arrangement in Figure 7.24 can be represented trigonometrically where:

| | |
|---|---|
| *s* | Height of theodolite = 1.6m |
| *k* | Vertical distance between *point 1* and *point 3* = 3.765m |
| *g* | Resultant distance between *point 1* and *point 3* = 83.0m |
| *p* | Horizontal distance between *point 1* and *point 3* = 82.915m |
| *t* | Distance between *point 2* and *point 4* = 83.088m |
| *α* | Angle between horizontal plane and ground = 2.956° |
| *θ* | Angle between horizontal plane and HV conductor = 7.133° |

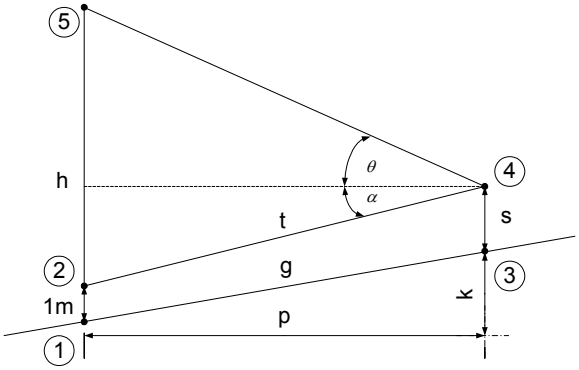


**Figure 7.25: Trigonometrical representation of survey setup underneath power system.**

From the measured data, the distance between the overhead conductor and ground was calculated as 15.668m. The overhead conductor sag is calculated with the information obtained from Figure 7.24. Figure 7.26 illustrates the trigonometrical representation for calculating the conductor sag. The sag was calculated as 3.546m.

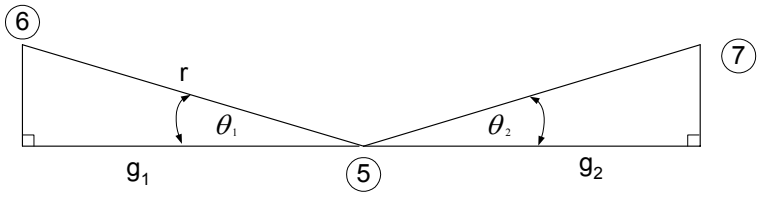


**Figure 7.26: Trigonometrical representation of calculating the conductor sag.**

The survey method described above was successfully used to calculate the conductor height above ground, as well as all the other geometrical parameters concerning the transmission line. The following measurements are required for a complete survey of the tower and transmission line geometry:

- Measure distance between *point 1* and *point 3*.
- Measure angle 1; angle 2; angle 5; angle 6; angle 7.
- Measure the horizontal difference between *point1* and *point 3*.
- Measure distance between *point1* and *point 3* with the measuring stick.
- Measure distance between *point 3* and the bottom point of the two towers.
- Measure the distance between the two towers.
- Measure the angle of the two towers at the insulators.
- Measure height of Theodolite on tripod.

## 7.5. Conclusion

For reliable field measurements it is important to clean the sensors and the support structure thoroughly, to calibrate the transmitters before any measurements are done and to scale the results transmitted by each optical line with the correct value. The sensors were found to exhibit good calibration properties as well as consistency. The field measurements proved that adequate output voltage levels are obtained with the new three-element parallel plate sensors for a practical 400 kV transmission line. Various practical problems experienced during the field measurements were identified for future consideration.

A software program was developed to process survey data to determine the geometrical properties of a specific transmission line.

# 8. Development of outdoor HV test facility

## 8.1. Introduction

This chapter presents a purpose built three-phase line topology as well as the implementation of three-element parallel plate sensors underneath it. Experimental evaluation of these sensors underneath an ESKOM three-phase transmission line is impractical. A test facility with controlled conditions is necessary for experimental evaluation of the three-element sensors. A three-phase power system is designed, developed and constructed on the roof of the machine laboratory at the University of Stellenbosch electrical department. The advantages of this facility are the following:

- The ease of taking measurements with the sensors.
- The amount of time saved.
- The controllability of the energising voltage.
- Measurement of coupling factors with single-phase energising.
- Easy testing of different characteristics of sensors underneath power systems.
- The exact measurement of the power geometry.

The size of the constructed three-phase transmission line is dependent on the topography of the roof and on the limitations created by electric fields. As it is not possible to construct a full size model of a transmission line, the geometry of the power system has to be scaled down. Appendix J.4 illustrates that if the system geometry and voltage are scaled by the same factor, the absolute magnitudes and directions of the fields at equivalent points in a full size system will be identical to that of a scaled system. The constructed line configuration is scaled replicas of typical ESKOM transmission line dimensions. Thus, the exact dimensions of ESKOM three-phase power systems have to be known. This chapter covers the development of the test facility.

A review is given on span calculations to compensate for the sag of overhead conductors. This knowledge is used for estimating which scaled tower types will be suitable for testing in the test facility.

The various aspects that must be taken into account for the construction of the test facility are discussed. A discussion is provided on the power sources used for energising the overhead conductors. Section 8.6 illustrates the construction of the test facility.

The block diagrams for the different segments of the test facility are provided as well as the test procedures for the different HV tests.

Single-phase and three-phase capacitive voltage measurements are done. Switching transients are also measured with the sensors. The performance of the sensor assembly developed in this thesis is evaluated in these tests.

## 8.2. Span calculations for Transmission lines

Overhead conductors elongate (sag) over time, temperature and tension thereby changing their original positions after installation. The required prediction of the future behaviour of the conductor is determined through calculations commonly referred to as sag-tension calculations [60].

### 8.2.1. Methods of calculating sag

The calculations done to estimate the sag on overhead conductors are complex and different characteristics of the conductor must be taken into account. The characteristics which mainly affect a conductor's sag and tension are: it's mechanical strength; its own weight; its change of length due to temperature change; its elastic stretch under load and its non-elastic stretch under load. Other factors affecting sags and tensions are: wind, ice loading, span length, and factors of safety [62].

Different methods for measuring the sag are used, namely:

- Sag and tension calculations (reviewed in section 8.2.4).
- Sag checking by stop watch; sag check by slope measurement
- Sag check by production of conductor tangent.

The capacitive sensors supply an easier method of measuring the sag. When the sensors are placed underneath the transmission line, the charge induced on the sensors is dependant on the geometry of the overhead conductors, i.e. dependant on the height of the conductors. When the height of the conductor changes (due to sag) the charge induced on the parallel plates changes.

### 8.2.2. Conductors

Aluminium has replaced copper as the most common conductor metal for overhead transmission. Although a larger aluminium cross-sectional area is required to obtain the same loss as in a copper conductor, aluminium has a lower cost and lighter weight. One of the most common conductor types is aluminium conductor, steel-reinforced (ACSR), which consist of layers of aluminium strands surrounding a central core of steel strands. The use of steel strands gives ACSR conductors a high strength-to-weight ratio. Sag-tension calculations for

ACSR conductors are more complex than calculations for ACC, AAAC, or ACAR, conductors. The complexity results from the different behaviour of steel and aluminium strands in response to tension and temperature [60]. The sizes of ACSR conductors can be specified by taking the major parameters which are: the ratio of the aluminium to steel diameters and the total cross sectional area and using these to derive an internationally uniform code. Appendix D.2 tabulates these codes for British, South-African, and Canadian standards.

### 8.2.3. Conductor Creep

Most solid materials, when tensioned momentarily by a moderate part of their breaking loads, will extend in proportion to the tension. They will return to their original lengths when the tension is removed. However, if the load is maintained for a period, additional non-elastic extension or 'creep' will remain after the tension is removed. Because of the *creep* elongation, the resulting final sags are greater and the conductor tension is less than the initial values. The prediction of the creep of a stranded conductor from first principals is not easy and permanent increase in conductor length due to heavy load occurrences cannot be predicted at the time the line is built.

### 8.2.4. Single span calculations

A span of tensioned conductor of uniform mass per unit length supported only at its ends, almost exactly takes the shape of a catenary curve. For typical lines across non-mountainous country, the catenary curve is almost a parabola. Hyperbolic methods should be considered for long river-crossing spans, mountainous sloping spans or heavy cables, such as submarine cable, being lifted from the sea bed. For the purpose of tower design for normal types of line, a level 'normal span' is selected [61]. The sag is derived as [61]

$$S = \frac{T}{w}\left[\cosh\left(\frac{Lw}{2T}\right) - 1\right] \qquad \text{(catenary)}$$

or [61]

$$S = \frac{wL^2}{8T} \qquad \text{(parabola)}$$

where the tension calculation symbols are as follows:

L = span (horizontal distance between supports) [m]

T = horizontal component of tension [N]

w = vertical force or resultant force per unit length of conductor in the span [N/m]

S = sag of the conductor at mid-span, measured vertically [m]

Appendix H presents typical sag and tension data of different conductors. Appendix H.1 reviews the calculations for measuring the changes of tension in the conductors.

### 8.3. Research for construction of test facility

Before construction of the test facility can begin, research is required to estimate the dimensions of the power system. The test facility is required to be a scaled model of typical ESKOM transmission lines. The dimensions of the roof determine the dimensions of the scaled power systems. Figure 8.1 illustrates the dimensions of one side of the Machine Lab's roof.

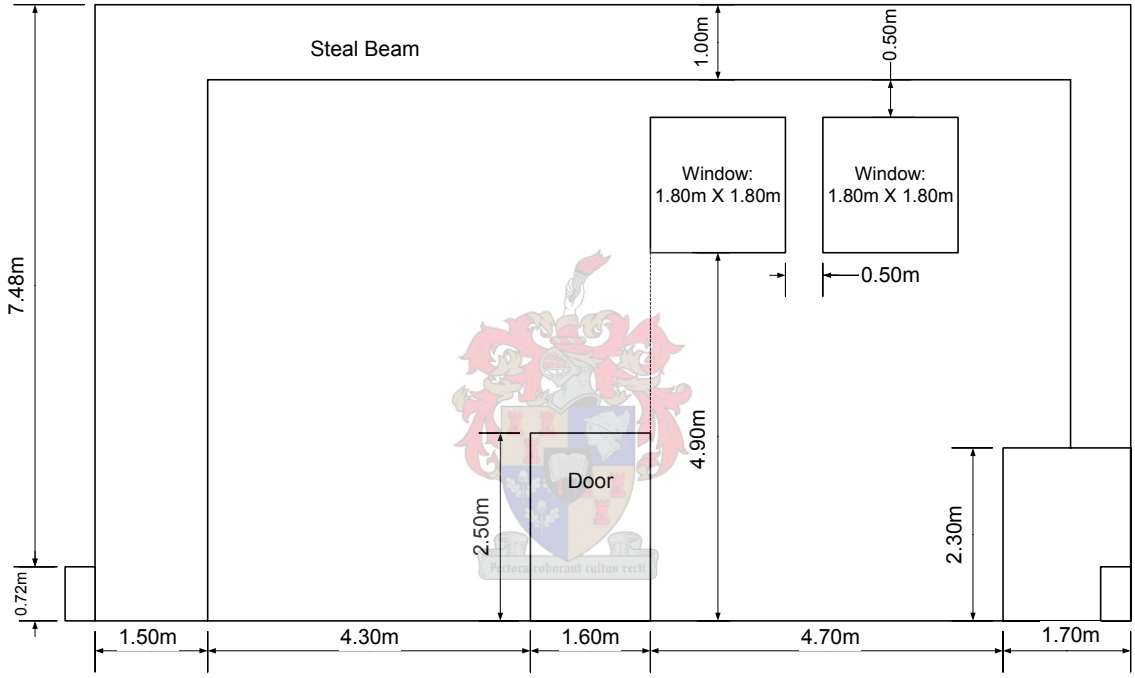


**Figure 8.1: Dimensions of Machine Lab roof where test facility are constructed.**

Only flat, three-phase, single circuit transmission line configurations can be represented on the roof. If the three overhead conductors can be adjusted horizontally and vertically, different line configurations can be represented in the test facility. Figure 8.2 shows the bracket that is designed for allowing the overhead conductors to be adjusted horizontally. A tension bolt is used to adjust the conductors vertically. By adjusting the tension of the conductors, the sag of the conductor is in effect varied. Figure 8.3 shows the dimensions of the bracket. The centre phase's bracket has a length of 0.75m as the position of the centre does not require adjustment under normal circumstances. The brackets used for the two side phases have a length of 1.5m. The phase distance between the outer conductors and the centre conductor can thus be varied by 1.5m. Research is done to locate the positions where

the two outer brackets must be fixed. The types of tower configurations (transmission line configurations) that have to be scaled down in the test facility determine the position of the two outer brackets.

**Figure 8.2: Bracket used for adjusting overhead conductors.**

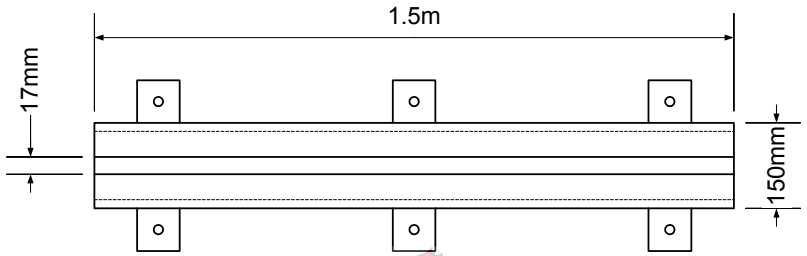


**Figure 8.3: Dimensions of bracket illustrated in Figure 8.2.**

## 8.4. Research on tower types for implementation in test facility

Appendix E illustrates different tower types for 132kV power systems. In order to determine which tower types can be scaled down for the test facility, three 132kV tower types and three 400kV tower types were evaluated. As the height of the conductor in the test facility is the determining factor, this value is compared to the height, including the sag, of the different tower types' conductors. By comparing these two quantities a scale factor can be calculated. This scale factor is used to estimate the phase distance between the conductors in the test facility in accordance to the accompanying tower type's phase distance. As the value of the transmission line conductors' distance from the ground plane is required for these calculations, the sag of overhead conductors for different tower types have to be calculated. By using the calculations described in section 8.2, the average sag for 132kV transmission lines are determined as 5m and for 400kV transmission lines as 6m.

As the conductors can be adjusted in the test facility, via the brackets and tension bolts, transmission lines with different sag values can be represented. The brackets are fitted to the wall at a height of 6.9m. If a sag of 0.9m is determined for the conductor, the height of the test facility's conductors can be taken as 6m. Table 8.1 and Table 8.2 tabulate the characteristics of 132kV and 400kV transmission lines as well as the dimensions of these

power systems if it is scaled down for implementation in the test facility. The tables include the following information:

- *Tower type:* The name of the tower type.
- *Conductor type:* Conductors used in accordance with the tower type.
- *Phase separation:* Distance between two adjacent phases.
- *Max phase attachment:* The height above ground that the phase conductors are attached to the tower. Distance between conductor and ground before any sag.
- *Earth separation:* Distance between the two earth conductors.
- *Max earth attachment:* The height above ground that the earth conductors are attached to the tower. Distance between earth conductor and ground before any sag.
- *Conductor height:* The height above ground of the transmission line conductors after sag has been taken into consideration.
- *Factor between line and roof:* Factor between height of transmission line conductors and height of test facility conductors.
- *Phase separation on roof:* The distance between the phases of the test facility. This distance is obtained by dividing the *phase separation* of the transmission line with the *factor between line and roof*.

From these tables it is noted that if the brackets are fitted to facilitate phase separation adjustment of between 3m and 4.5m, most of the tower types for the different sags can be scaled for the test facility except the 240 SC tower type.

**Table 8.1: 132kV Power systems tested for implementation in test facility.**

**132kV Power System**

| Tower Type | Conductor type | Phase separation | Max phase attachment | Earth separation | Max earth attachment |
|---|---|---|---|---|---|
| 16 | | 6.7 | 17.5 | 4.4 | 21.7 |
| 224 SC | 2xWolf | 6 | 14.738 | 4.51 | 19.85 |
| 240 SC | Bear | 5.5 | 17.575 | 4.85 | 20.277 |

**Measurements for roof**

| | Tower type 16 | | | Tower type 224 SC | | | Tower type 240 SC | | |
|---|---|---|---|---|---|---|---|---|---|
| Sag | Conductor height | Factor between line and roof | Phase separation on roof | Conductor height | Factor between line and roof | Phase separation on roof | Conductor height | Factor between Line and Roof | Phase separation on roof |
| 3.5 | 14 | 2.33 | 2.871 | 11.238 | 1.87 | 3.203 | 14.075 | 2.35 | 2.345 |
| 4.5 | 13 | 2.17 | 3.092 | 10.238 | 1.71 | 3.516 | 13.075 | 2.18 | 2.524 |
| 5.5 | 12 | 2.00 | 3.350 | 9.238 | 1.54 | 3.897 | 12.075 | 2.01 | 2.733 |
| 6.5 | 11 | 1.83 | 3.655 | 8.238 | 1.37 | 4.370 | 11.075 | 1.85 | 2.980 |

**Table 8.2: 400kV Power systems tested for implementation in test facility.**

**400kV Power System**

| Tower Type | Conductor type | Phase separation | Max phase attachment | Earth separation | Max earth attachment |
|---|---|---|---|---|---|
| 1 | | 7.9 | 19.932 | 6.95 | 25.398 |
| 506A | | 9.45 | 20.87 | 8.3 | 25 |
| 506B | | 8 | 19.37 | 8.429 | 25 |

**Measurements for roof**

| | Tower Type 1 | | | Tower Type 506A | | | Tower Type 506B | | |
|---|---|---|---|---|---|---|---|---|---|
| Sag | Conductor height | Factor between line and roof | Phase separation on roof | Conductor height | Factor between line and roof | Phase separation on roof | Conductor height | Factor between Line and Roof | Phase separation on roof |
| 5 | 14.932 | 2.49 | 3.174 | 15.87 | 2.65 | 3.573 | 14.37 | 2.40 | 3.340 |
| 6 | 13.932 | 2.32 | 3.402 | 14.87 | 2.48 | 3.813 | 13.37 | 2.23 | 3.590 |
| 7 | 12.932 | 2.16 | 3.665 | 13.87 | 2.31 | 4.088 | 12.37 | 2.06 | 3.880 |
| 8 | 11.932 | 1.99 | 3.973 | 12.87 | 2.15 | 4.406 | 11.37 | 1.90 | 4.222 |

## 8.5. Power Supply for test facility

In the test facility, the down-scaling factors for the different tower types are between 2 and 2.5. The power supply required for the test facility would ideally be 66kV for the 132kV tower types and 160kV for the 400kV. Obtaining transformers with such capacity is however very difficult, especially a 160kV:220V transformer. The voltage for the overhead conductors of the test facility must be transformed from 220V. Emphasis is thus given to the 132kV tower types.

### Three-phase

A three phase high voltage test transformer (110V:22000V) is obtained from ESKOM. If the voltage of the test facility must be scaled by the same amount, this transformer will not be adequate. However, sufficient tests can be done with this 22kV transformer. For future research 66kV transformers will be very useful. The low voltage side of the transformer is connected to the following:

- A 15A mini circuit breaker.
- A 15A three-phase ganged regulating autotransformer.
- Three voltmeters - measurement of input voltage to high voltage transformer.
- Three rheostats - additional impedance for LV circuit to limit HV short circuit current.

A capacitive divider with indicating instrumentation for the measurement of the HV output is connected to one of the HV phases. A three-phase 400V 50Hz wall outlet is used to energise the low voltage side of the autotransformer.

**Single-phase**

A single-phase, high voltage test transformer (220V:35000V) is obtained for energising the test facility. This proved helpful for measuring the coupling factors between the three overhead conductors and the three sensors. A control desk, with overload protection, for the control of the low voltage side of the transformer, is used. The output voltage of the control desk can be varied between 0V and 220V. Thus, the HV side of the transformer can be varied between 0V and 35000V.

It is required to measure the single-phase transformer's output to ensure that the control desk's Voltage Transformer (VT) is calibrated correctly. The single-phase transformer is energised through the control desk and the output of the transformer is measured by the KVM-100 (reference voltage divider calibrated with international standards). These measurements are used to create a calibration table for use of the control desk's VT. The VT has two scales namely, a 17.5kV scale and a 30kV scale. Table 8.3 compares the values between the control desk 17.5kV scale and those measured by the KVM-100. Table 8.4 compares the values between the control desk 30kV scale and those measured by the KVM-100.

Figure 8.4 and Figure 8.5 plots the values of the KVM-100 against the values from the two scales of the control desk VT. These two figures illustrate the linearity of each scale. A small difference is found between the measured values and the values given by the two scales, especially for voltages less than 12kV. The two tables are used whenever the single-phase transformer is used to calibrate the VT's values.

**Table 8.3: 17.5kV scale compared with the real values measured by the KVM-100**

| 17.5 kV Scale | KVM-100 | % difference |
|---|---|---|
| 7.5 | 7.72 | 2.85 |
| 8 | 8.36 | 4.31 |
| 8.5 | 8.8 | 3.41 |
| 9 | 9.35 | 3.74 |
| 9.5 | 9.84 | 3.46 |
| 10 | 10.34 | 3.29 |
| 10.5 | 10.8 | 2.78 |
| 11 | 11.3 | 2.65 |
| 12 | 12.24 | 1.96 |
| 13 | 13.2 | 1.52 |
| 14 | 14.1 | 0.71 |
| 15 | 15.1 | 0.66 |
| 16 | 16.2 | 1.23 |
| 17 | 17.3 | 1.73 |
| 17.5 | 17.8 | 1.69 |

**Table 8.4: 30kV scale compared with the real values measured by the KVM-100**

| 30kV Scale | KVM-100 | % difference |
|---|---|---|
| 10 | 11 | 9.09 |
| 11 | 11.7 | 5.98 |
| 12 | 12 | 0.00 |
| 13 | 13.3 | 2.26 |
| 14 | 14.2 | 1.41 |
| 15 | 15.1 | 0.66 |
| 16 | 16.2 | 1.23 |
| 17 | 17.2 | 1.16 |
| 18 | 18.5 | 2.70 |
| 19 | 19.3 | 1.55 |
| 20 | 20.5 | 2.44 |
| 21 | 21.3 | 1.41 |
| 22 | 22.2 | 0.90 |
| 23 | 23.4 | 1.71 |
| 24 | 24.4 | 1.64 |
| 25 | 25.2 | 0.79 |
| 26 | 26 | 0.00 |
| 27 | 27.1 | 0.37 |
| 28 | 28.1 | 0.36 |

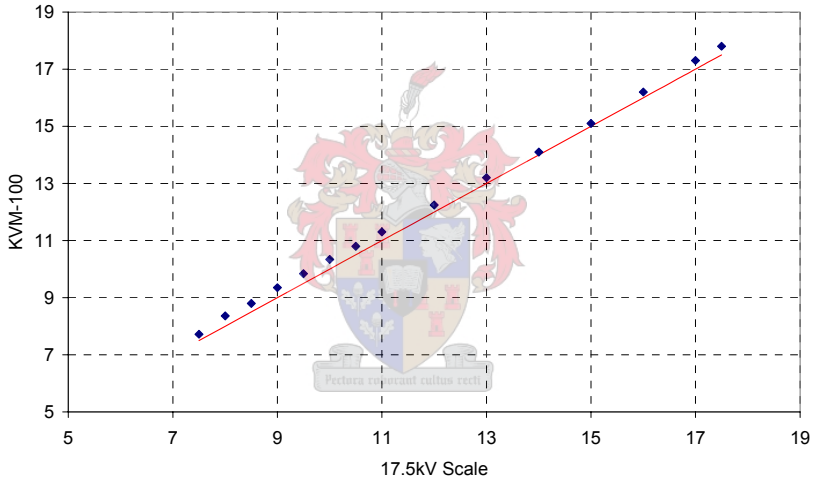


**Figure 8.4: KVM-100 measurements versus the 17.5kV, illustrating the linearity of the VT.**

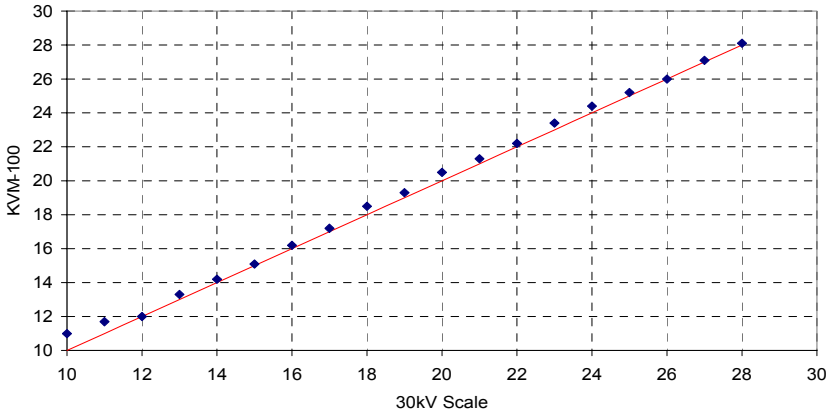


**Figure 8.5: KVM-100 measurements versus the 30kV, illustrating the linearity of the VT.**

## 8.6. Construction of the test facility

Construction of the HV test facility started at the beginning of February 2006. The construction of the overhead conductors was finished end of February 2006. The transformers were connected middle March and final constructions of the test facility was finished at the end of March 2006.

The workshop of the electrical department manufactured the brackets that were used to suspend the high voltage cables of the test facility. The workshop personnel were tasked with the suspension of the conductors. This was a very cumbersome process as everything had to be done on scaffolding. Figure 8.6 shows a photograph of the scaffolding used in bolting one of the brackets to the wall. From this photograph the difficulty of constructing the cables, due to the height of the conductors, are clearly evident. MINK cables were used for the high voltage conductors. Appendix D.2 presents all necessary information for MINK cables.

**Figure 8.6: Workshop personnel busy securing a bracket against the wall.**

Figure 8.7 illustrates the chain and the 33kV silicon insulator used to connect each cable to the bracket. The cable was then suspended and the tension bolt in Figure 8.7 adjusted until the tension in the cable was correct. Figure 8.8(a) shows the workshop personnel suspending the cables and Figure 8.8(b) shows the cable, chain and insulator after it was suspended.

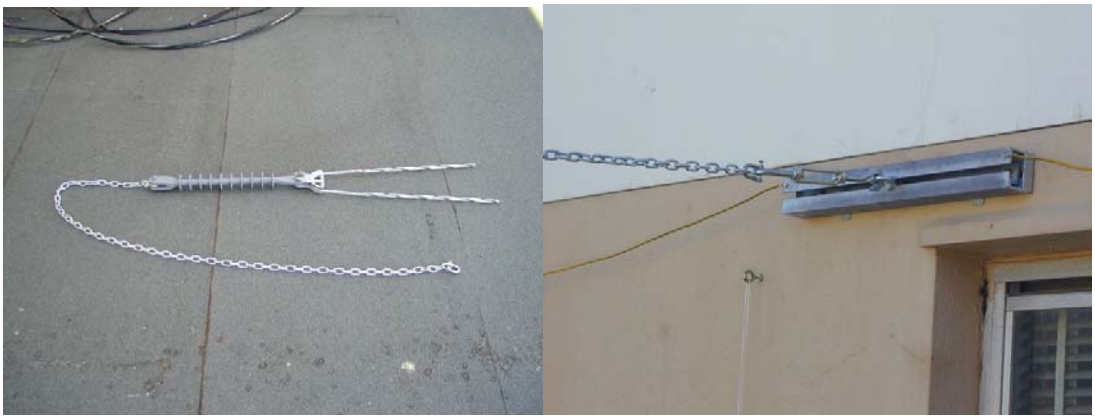

**Figure 8.7: Chain and insulator used to connect HV cable to bracket.**

**Figure 8.8: (a) Adjustment of cables and (b) cables after suspension.**

Adequate safety precautions were made for fault conditions during energisation of the conductors. Copper 16mm$^2$ earth cables were connected to each bracket in case of a flashover from one of the HV cables. These earth cables are connected to the earth in the HV Lab

After all the HV cables and earth cables were suspended, the three-phase transformer was connected to the HV and earth cable. Figure 8.9(a) shows the three-phase transformer, placed next to the HV cables' connections. Figure 8.9(b) shows the wiring of the transformer. The primary (LV) and secondary (HV) side of the transformer are connected in Y. The star point of the secondary side is connected to the earth wire. The current transformer's secondary windings were shorted out. The primary side's three-phases were connected to the three-phase autotransformer in room E360.

An ideal test facility would be a system where all three conductors had the same catenary curve and conductor height, the phases had the same distances between each other and the ground plane was a perfect flat conducting plane. The constructed test facility however had a few short comings as the ground plane was not a perfectly flat area, with a perfect conducting

surface and some of the conductor heights differed by 1%. The conductor heights can however be adjusted to a point where the ground clearance of the three conductors are the same. The parapet of the roof is 0.72m high and can interfere with the electric field lines from the overhead conductors, causing a discrepancy in the measurements.


**Figure 8.9: (a) Three-phase transformer used at test facility and (b) wiring of the transformer.**

## 8.7. Block diagrams of test facility

The following section illustrates the block diagrams of the single-phase setup and the three-phase setup. The previous sections present a description of the different components of the test facility. All the equipment on the low-voltage side of the experiment was placed in Room E360. It included all the equipment illustrated in Figure 8.10 and Figure 8.12. The computer, USB oscilloscopes and receiver cards were also placed inside Room E360.

### 8.7.1. Single-phase diagrams

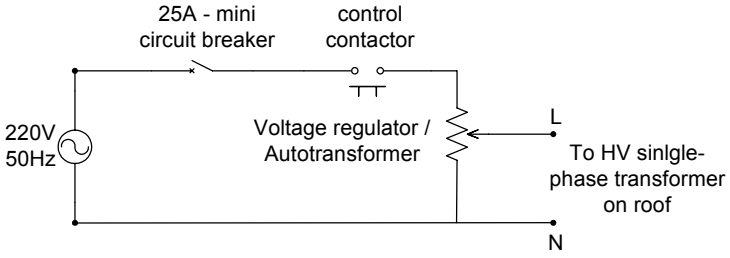


**Figure 8.10: Control desk with overload protection for the control of the high voltage transformer (output voltage could be varied between 0V and 220V).**

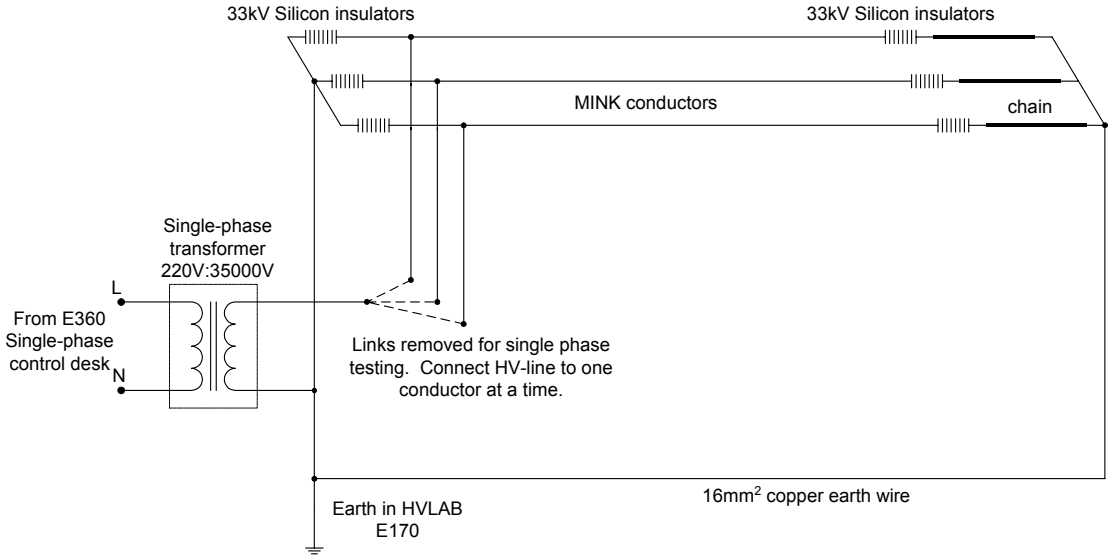


**Figure 8.11: Line diagram of conductors, earth wires and single-phase HV test transformer, for single-phase testing.**

## 8.7.2. Three-phase diagrams

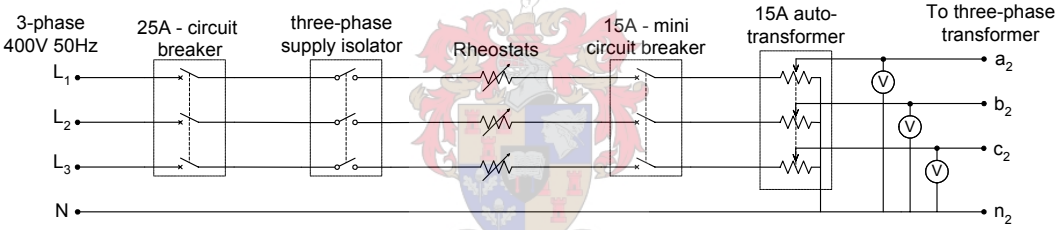


**Figure 8.12: Low-voltage control system in E360, used to energise the three-phase, high-voltage, transformer.**

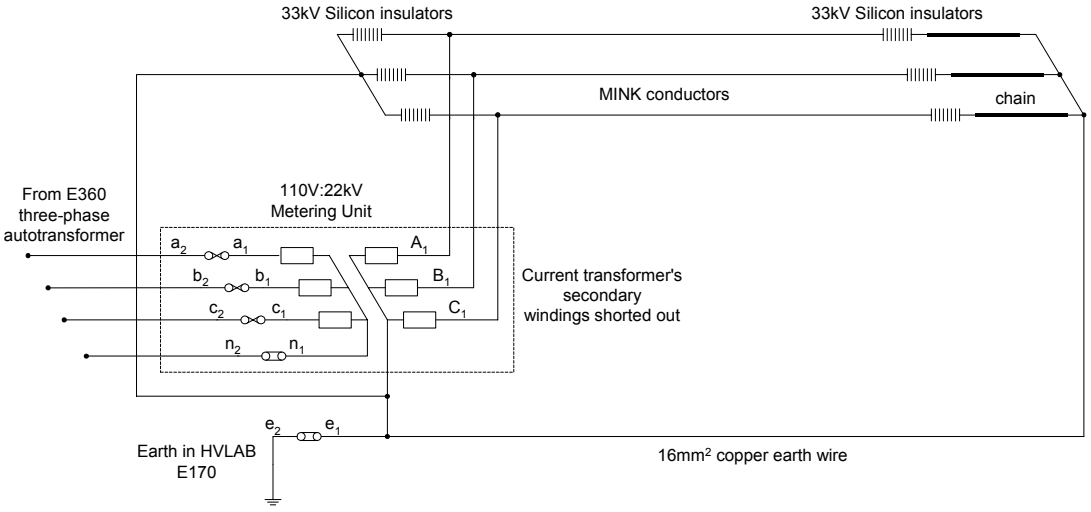


**Figure 8.13: Line diagram of conductors, earth wires and three-phase HV transformer (metering unit) for three-phase testing.**

### 8.8. Operating procedures for measurements in test facility

Before any HV tests could be done in the test facility, safety tests and procedures must be created in conjunction with the safety officer (Petrus Pieterse). In the following section the test procedures for the single-phase and the three-phase test are stated.

#### 8.8.1. Operating procedure for single phase tests

**Energising of overhead conductors:**

1. Ensure that three-phase transformer is disconnected from overhead lines.
2. Ensure that both entrance doors to open roof area have visible warning signs.
3. Lock the east entrance door of the roof and close the sliding latch to prevent all access to roof area from the eastern part of the building.
4. Connect high voltage terminal of test transformer to the required overhead conductor.
5. Prepare test equipment for trials (Computer, capacitive sensor etc.)
6. Remove earth conductors from overhead lines.
7. Close and lock west entrance door. Ensure that no person can obtain entrance to roof area, either by guarding entrance or any other means.
8. Connect control desk to AC mains socket.
9. Ensure autotransformer to be in the 0 position.
10. Switch main Circuit breaker (on control panel) to the ON position.
11. Press push-button, labelled "ON".
12. Set Autotransformer dial to the required output voltage by monitoring the output voltage on the Kilo-Volt meter on the panel.

**De-energising of system:**

This procedure had to be followed whenever access to the open area was required.

1. Reduce output voltage to 0V by means of turning the autotransformer dial fully anticlockwise.
2. Press push-button, labelled "OFF".
3. Switch main circuit breaker (on control panel) to the "OFF" position.
4. Unlock west entrance door.
5. Connect visible earth conductors to all overhead conductors.
6. Access to roof area is now safe. Adjustments and any other work may now be conducted on the area.

7. Remove High Voltage transformer from open (roof) area and lock entrance door after completion of experiment.

### 8.8.2. Operating procedure for three-phase tests

**Energising of overhead conductors:**

1. Ensure that both entrance doors to open roof area have visible warning signs.
2. Lock the east entrance door of the roof and close the sliding latch to prevent all access to roof area from the east part of the building.
3. Connect three-phase transformer to overhead lines.
4. Prepare test equipment for trials (Computer, capacitive sensor etc.)
5. Remove earth conductors from overhead lines.
6. Close and lock west entrance door. Ensure that no person can obtain entrance to roof area, either by guarding entrance or any other means.
7. Switch on three phase supply Isolator switch (south wall).
8. Ensure autotransformer to be in the 0 position.
9. Switch 15A Circuit breaker to the ON position.
10. Set Autotransformer dial to the required output voltage by monitoring the transformer primary voltage and the output voltage on the Kilo-Volt display (on indicating instrument of High Voltage measuring set comprising a capacitive divider and an indicating instrument). Ensure that the primary voltage does not exceed a **Phase voltage of 63.5V** and that the secondary voltage does not exceed a value of **12.7 kV.**

**De-energising of system:**

This procedure had to be followed whenever access to the open area was required.

1. Reduce output voltage to 0V by means of turning the autotransformer dial fully anticlockwise.
2. Switch 15A circuit breaker to the “OFF” position.
3. Switch three phase supply isolator switch (south wall) to the “OFF” position.
4. Unlock west entrance door.
5. Connect visible earth conductors to all overhead conductors.
6. Access to roof area is now safe. Adjustments and any other work may now be conducted on the area.

7. Remove supply connections to High Voltage transformer and lock entrance door after completion of experiment.

### 8.9. High Voltage tests in test facility

After the safety operating procedure, described in the previous section, is completed the measurements, necessary for the specific test, are done. For the three-element parallel plate sensor the measurements are done in a number of steps. All of these steps are written up in the following test procedure.

**Test procedure for three-element parallel plate sensors in test facility**

1. Take all necessary safety precautions
2. Note position of sensors underneath overhead conductors
3. Measure conductor height
4. Measure atmosphere temperature
5. Measure temperature inside Faraday cage of sensor
6. Switch on all measuring instrumentation
7. Take all necessary safety precautions
8. Energise system
9. Conduct all measurements necessary and save these measurements
10. Measure high voltage
11. De-energise system
12. Take all necessary safety precautions
13. Measure conductor height
14. Measure atmosphere temperature
15. Measure temperature inside Faraday cage of sensor

A weather station is provided by ESKOM for all necessary atmospheric measurements. All of these steps, described above, are necessary for relating all the different measurements to each other. Table 8.5 presents a wish-list of the measurements that are intended to be done in the HV test facility. It is not possible to do all of these tests within the scope of this thesis due to weather and time constraints. All the tests that are not done in this thesis are recommended for future evaluation of the three-element parallel plate sensors underneath a three-phase transmission line.

**Table 8.5: check-list of intended measurements for the three-element parallel plate sensors.**

| | | | | | | | |
|---|---|---|---|---|---|---|---|
| **Single-phase Test** | Measure calibration factors | Measure difference between grounded and ungrounded phases | Different positions underneath overhead conductor | Determine calibration factors that will be used for the three-phae test | Non-ideal ground plane | Determine calibration factors after optimal ground plane has been determined | Sag calculations |
| | | | Determine maximum electric field | | Ideal ground plane - not grounded | | Effect of earthed objects |
| | | | Different angle of sensor | | Ideal ground plane - grounded | | Clean waveform |
| | | | | | | | Conformal coating |
| | Triggering test - ON/OFF | | | | | | |
| **Three-phase Test** | Implement calibration factors | Test to determine overhead voltages | Balanched three-phase | | | | |
| | | | Unbalanced three-phase | | | | |
| | | Sag calculations | | | | | |

## 8.10. Single-phase HV tests in Test Facility

### 8.10.1. Overview

The test facility is designed in order to test capacitive voltage sensors. The concept of calculating the phase voltages by measuring induced voltages on the three-element parallel plate sensors is evaluated. These tests are simplified in the test facility due to the fact that the dimensions of the three-phase line configuration geometry are known as well as are the phase voltages. To determine the phase voltages with the sensors, the coupling factors between each phase and sensor must be known. Chapter 5 discusses the coupling factors between the different phases and sensors. The problem with determining the capacitive coupling factors are that all three phases induce a voltage on each sensor making it very difficult to discriminate between the different phase voltages via the induced voltages. The coupling factors can be determined by only energising a single conductor at a time and measuring the induced voltages on each sensor. The coupling factors evaluated in the single-phase tests are then implemented in the three-phase tests for determining the phase voltages.

### 8.10.2. Capacitive coupling components of line and sensor configuration

The single-phase transformer is used to energise each phase separately with a known voltage. The voltages induced on each sensor are measured and these quantities are used to determine the capacitive coupling factors. Figure 8.14 illustrates the different capacitive coupling

factors between the three-phases and the three sensors. The vectors in Figure 8.14 are not the actual coupling factors, but only a representation of the coupling factors in this discussion.

The induced voltages on each sensor $v_{sA}$, $v_{sB}$ and $v_{sC}$ are denoted by the relationships

$$v_{sA} = G_{pAsA}v_{pA} + G_{pBsA}v_{pB} + G_{pCsA}v_{pC} \quad , \tag{8.1}$$

$$v_{sB} = G_{pAsB}v_{pA} + G_{pBsB}v_{pB} + G_{pCsB}v_{pC} \tag{8.2}$$

and

$$v_{sC} = G_{pAsC}v_{pA} + G_{pBsC}v_{pB} + G_{pCsC}v_{pC} \tag{8.3}$$

where $v_{pA}$, $v_{pB}$ and $v_{pC}$ denote the phase voltages and $G$ denotes the different coupling factors. The subscript values of $G$ denote the phase and sensor whose coupling factor is determined. The phase voltages are solved from the above linear system. The three phase voltages are now denoted by

$$\begin{bmatrix} v_{pA} \\ v_{pB} \\ v_{pC} \end{bmatrix} = \begin{bmatrix} G_{pAsA} & G_{pBsA} & G_{pCsA} \\ G_{pAsB} & G_{pBsB} & G_{pCsB} \\ G_{pAsC} & G_{pBsC} & G_{pCsC} \end{bmatrix} \begin{bmatrix} v_{sA} \\ v_{sB} \\ v_{sC} \end{bmatrix} . \tag{8.4}$$

This linear system is used to evaluate the phase voltages of the three-phase line configuration in the test facility by means of the three capacitive voltage sensors. The coupling matrix of equation (8.4) will be diagonally symmetrical if the line configuration is symmetrical around the centre phase and if it is a balanced three-phase system.

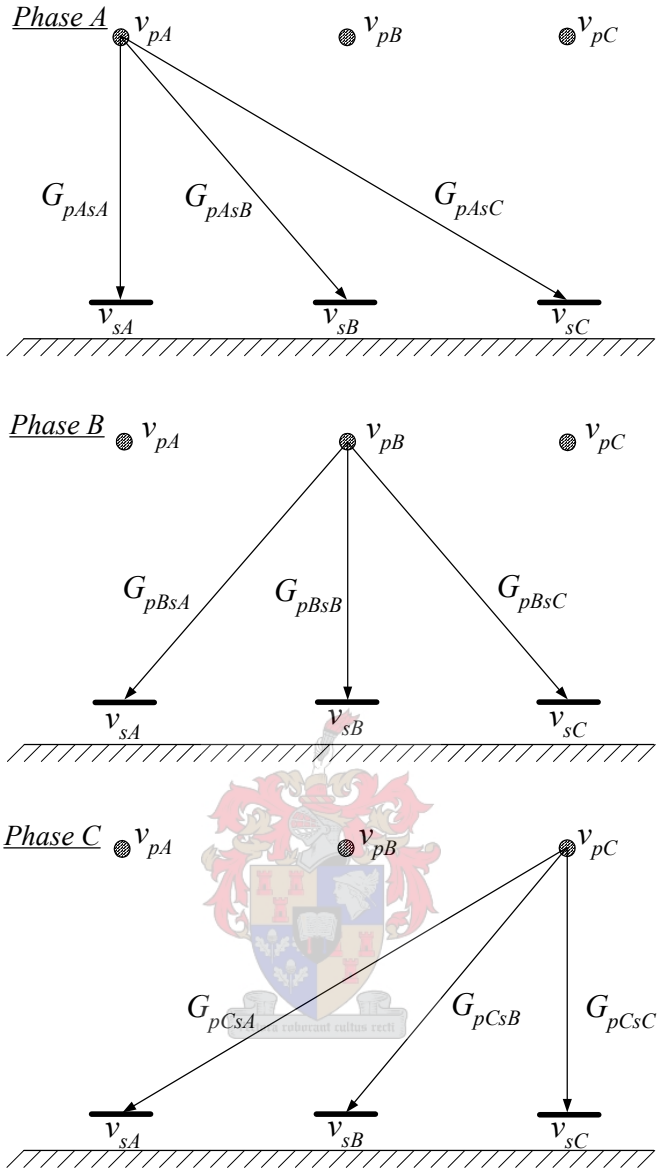


**Figure 8.14: Capacitive coupling factors between the phases and the sensors.**

### 8.10.3. Assembly of test facility for single-phase test

Figure 8.15 illustrates the geometry of the line configuration in the test facility. The geometry stays the same for all the tests done in this project. The line configuration is not symmetrical around the centre phase as the distance between *phase A* and *B* differs from the distance between *phase B* and *C* due to construction constraints. The distance between the ground plane and the conductor's position at the centre of the span length are measured. These suspension heights for the three conductors are the following:

*Phase A* = 5.118m

*Phase B* = 5.178m

*Phase C* = 5.181m

A discrepancy of 1.21% exists between the heights of *phase A* and *C* and a discrepancy of 1.16% exists between the *phase A* and *B*. The discrepancies in the symmetry of the line geometry can be corrected for future measurements. Due to time and labour constraints these discrepancies are not eliminated for the test done in this project. Although these discrepancies are not an ideal scenario, adequate capacitive coupling tests can be performed.

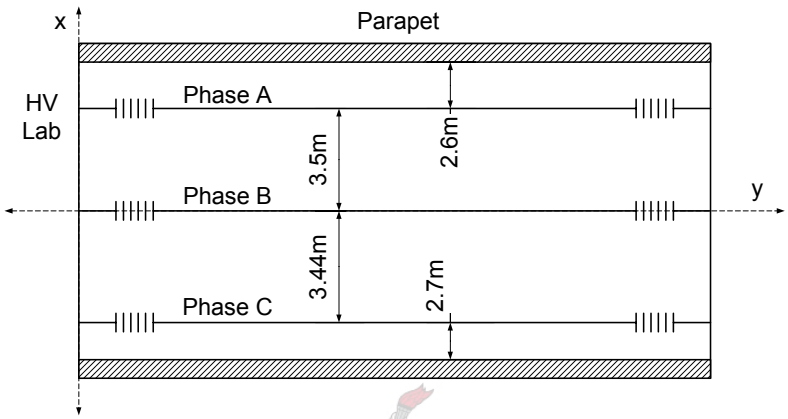


**Figure 8.15: Geometry of overhead conductors for single phase tests (not to scale).**

The equipment for the single-phase tests must be assembled and connected. Next the *Operating Procedure* document has to be completed where after the test procedure must be performed in the steps explained in section 8.9. Figure 8.16(a) shows the control desk of the single-phase transformer. Figure 8.16(b) shows the single-phase transformer connected to one of the overhead conductors while the other two conductors are earthed.

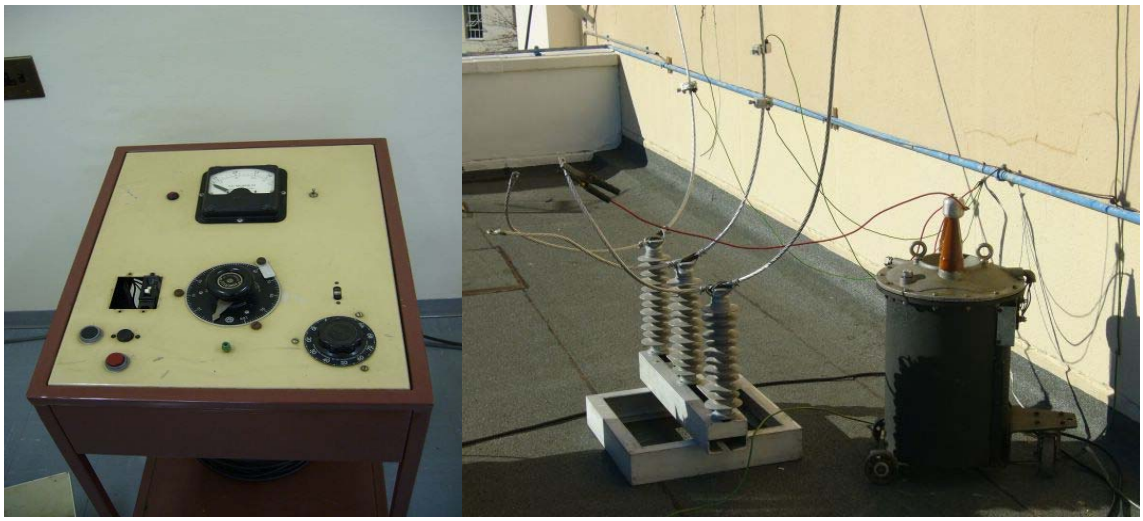

**Figure 8.16: (a) Control desk for single-phase transformer and (b) single-phase transformer connected to overhead conductor.**

Figure 8.17 shows the test facility with the three sensors centralised underneath the three overhead conductors. The parapet on either side of the ground plane, the extractor fans from Machines Laboratory as well as the transformer can be seen. Care must be taken not to place the sensors in the vicinity of objects that can influence the voltage induced on the sensors.

**Figure 8.17: HV Test facility with the three sensors centralised underneath the conductors.**

Figure 8.18(a) shows the three sensors placed upon the support structures. The fibre optic cables connect the transmitters, inside the sensors' faraday cages, with the receivers. Figure 8.18(b) show the receiver cards connected to the oscilloscope. The measuring assembly illustrated in Figure 8.17 and Figure 8.18 is used to do the capacitive coupling evaluations.

**Figure 8.18: (a) Sensors with transmitters inside Faraday cage and (b) receivers inside Room E360.**

### 8.10.4. Capacitive voltage measurements

#### 8.10.4.1. Filtering of measured waveforms

The three waveforms that are measured with the sensors exhibited too much noise. The high frequency noise must thus be filtered out. The waveforms can be filtered before measurement with the oscilloscope, but instead the measured data is filtered digitally with MATLAB. Appendix H presents all MATLAB codes used for processing the measured waveforms. A $2^{nd}$ order lowpass Butterworth filter, with a cut-off frequency of 500Hz, is implemented in MATLAB to filter the waveforms. Figure 8.19 shows the frequency response of this filter. The phase response has a phase-shift of 8 degrees at 50Hz. This phase-shift is however of no concern because if all three waveforms have the same phase-shift the three filtered waveforms stay the same relative to each other. No error in calculating the coupling factors will thus be created. The only concern is that the magnitudes of the waveforms stay the same. Figure 8.20 shows the three measured waveforms and the three filtered waveforms. The phase shifts between the original filtered waveforms are clearly noticeable.

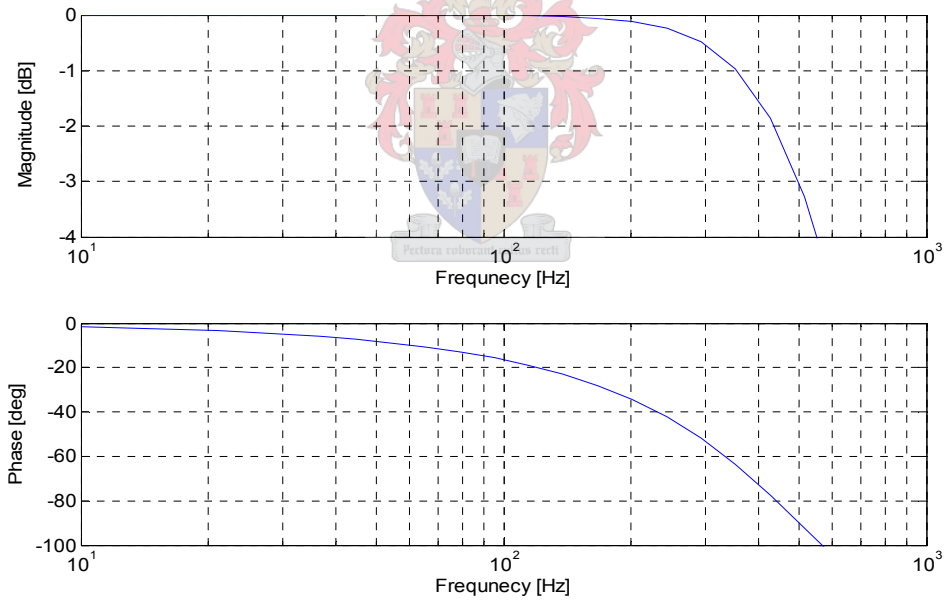


**Figure 8.19: Frequency response of Butterworth filter.**

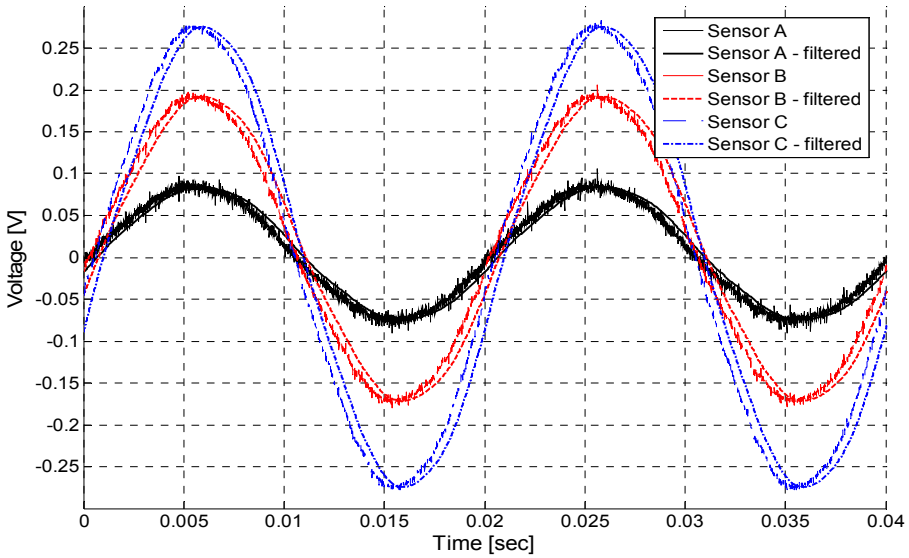


**Figure 8.20: Original and filtered waveforms.**

### 8.10.4.2. Overview of single-phase test

An overview is presented of the different single-phase tests performed. The same procedures for each test are followed. Section 8.10.4.3 is the only section that discusses the test in detail. The other sections duplicate the test done in section 8.10.4.3 on other line configurations. The following tests are performed with the single-phase transformer:

*Section 8.10.4.3*: Only one phase is energised with a voltage of 20.5kV (measured on the calibrated scale) while the other two phases are connected to ground. The three waveforms measured for each phase energisation are then compared to one another. These waveforms are then used to calculate the different coupling factors between the energised phase and sensors. The evaluations done in section 8.10.4.3 are repeated for the tests to follow. The coupling factors are evaluated for each test sequence as well as the difference between the coupling factors. The results from the different tests are then compared with each other to make a final conclusion of the single-phase measurements done in the test facility.

*Section 8.10.4.4*: The energisation voltage is set at 20.5kV and the non-energised conductors are left floating. The waveforms obtained by this test are compared with those measured in section 8.10.4.3 to evaluate the effect of grounded conductors vs. floating conductors.

*Section 8.10.4.5*: The energisation voltage is set at 25.2kV. The coupling factors are measured for the conditions of grounded non-energised conductors and floating non-energised conductors. To test the linearity of the coupling factors, the coupling factors are compared with those calculated in the two previous sections.

*Section 8.10.4.6*: Phase B is energised with 20.5kV. The electric field profile is compared with the measured voltage profile underneath the overhead conductors. The electric field profile is simulated in ELECTRO.

*Section 8.10.4.7*: The sensors are tested for consistency

*Section 8.10.4.8*: The coupling factor discrepancies for simulated and measured values are compared.

Table 8.6 tabulates the weather conditions during the measurements as well as the energisation of each phase. The weather was overcast while the wind was blowing between 4 and 8 km/h. The barometer had a value of 1020.6mB.

**Table 8.6: Weather and energising conditions at test facility during measurements.**

| Test # | Phase A []kV] | Phase B [kV] | Phase C [kV] | Temp [°C] | Humidity [%] |
|---|---|---|---|---|---|
| 1 | 20.5 | 0 | 0 | 16 | 64 |
| 2 | 0 | 20.5 | 0 | 16 | 64 |
| 3 | 0 | 0 | 20.5 | 16 | 58 |
| 4 | 20.5 | Floating | Floating | 16 | 64 |
| 5 | Floating | 20.5 | Floating | 16 | 62 |
| 6 | Floating | Floating | 20.5 | 16 | 58 |
| 7 | 25.2 | 0 | 0 | 16 | 63 |
| 8 | 0 | 25.2 | 0 | 16 | 64 |
| 9 | 0 | 0 | 25.2 | 16 | 63 |
| 10 | 25.2 | Floating | Floating | 16 | 63 |
| 11 | Floating | 25.2 | Floating | 16 | 63 |
| 12 | Floating | Floating | 25.2 | 16 | 66 |
| 13 | 0 | 20.5 | 0 | 15 | 65 |
| 14 | 0 | 20.5 | 0 | 15 | 65 |
| 15 | 0 | 20.5 | 0 | 15 | 68 |
| 17 | 0 | 20.5 | 0 | 15 | 68 |
| 18 | 0 | 20.5 | 0 | 15 | 67 |
| 19 | 0 | 20.5 | 0 | 15 | 67 |
| 20 | 0 | 20.5 | 0 | 15 | 67 |
| 21 | 0 | 20.5 | 0 | 15 | 69 |

### 8.10.4.3. Non-energised phases connected to ground

The three-phases energised with 20kV respectively. From the 30kV calibration table, Table 8.4, the actual voltage on the overhead conductor is obtained as 20.5kV. Figure 8.21, Figure 8.22 and Figure 8.23 presents the voltage waveforms measured by the three capacitive sensors.

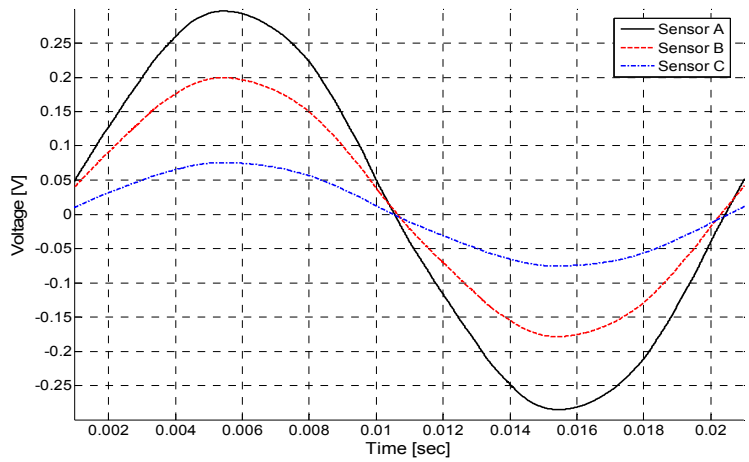


**Figure 8.21: Phase A = 20.5kV; Phase B = 0kV; Phase C = 0kV.**

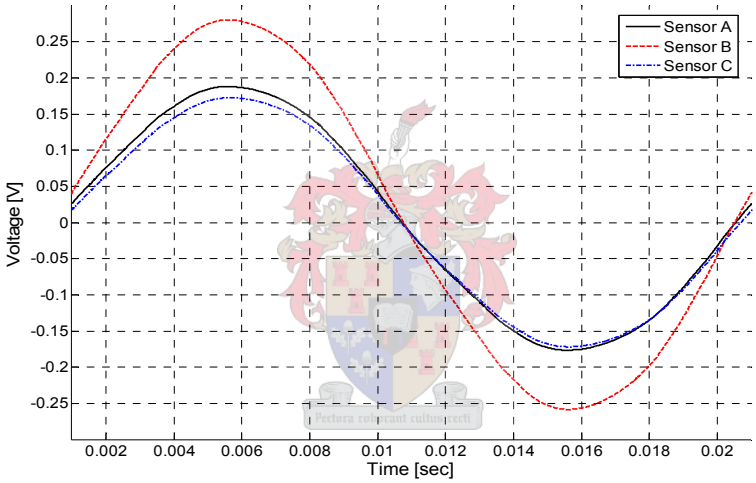


**Figure 8.22: Phase A = 0kV; Phase B = 20.5kV; Phase C = 0kV.**

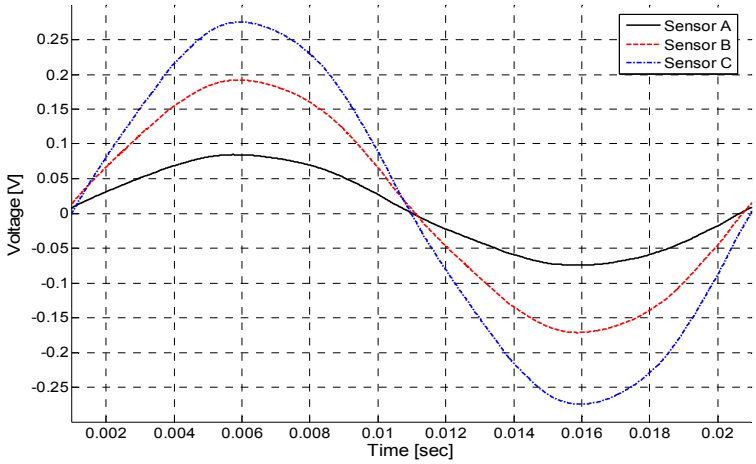


**Figure 8.23: Phase A = 0kV; Phase B = 0kV; Phase C = 20.5kV.**

In an ideal system, where the line configuration is symmetrical, *sensor A* and *sensor C* will have identical waveforms if *phase B* is energised. The test facility is however not an ideal symmetrical system and thus are not exactly the same. Figure 8.22 shows the difference between the two waveforms if *phase B* is energised. This is not a problem for measuring the capacitive coupling factors as the same conditions that hold for the single-phase tests also hold for the three-phase test. As long as the test constraints stay the same for all the different tests the capacitive coupling factors will stay the same. The two coupling factors $G_{pBsA}$ and $G_{pBsC}$ in Figure 8.14 have different values. The difference between these two waveforms is 9.11% for the positive peak values and 2.62% for the negative peak values. The signal measured by *sensor A* has a small DC offset of 5.8mV.

For an ideal, symmetrical system the waveforms of Figure 8.21 and Figure 8.23 will be the same due to the fact that the coupling factor matrix will be diagonally symmetrical. Figure 8.24 compares the waveforms from Figure 8.21 and Figure 8.23. Although the system is not completely symmetrical the waveforms are still very similar due to the symmetry in the line configuration. The phase difference between the two set of waveforms are due to different triggering instants. The biggest discrepancy between the two sets of waveforms is between *phase A - sensor A* and *phase C - sensor C*. These two waveforms represent coupling factors $G_{pAsA}$ and $G_{pCsC}$.

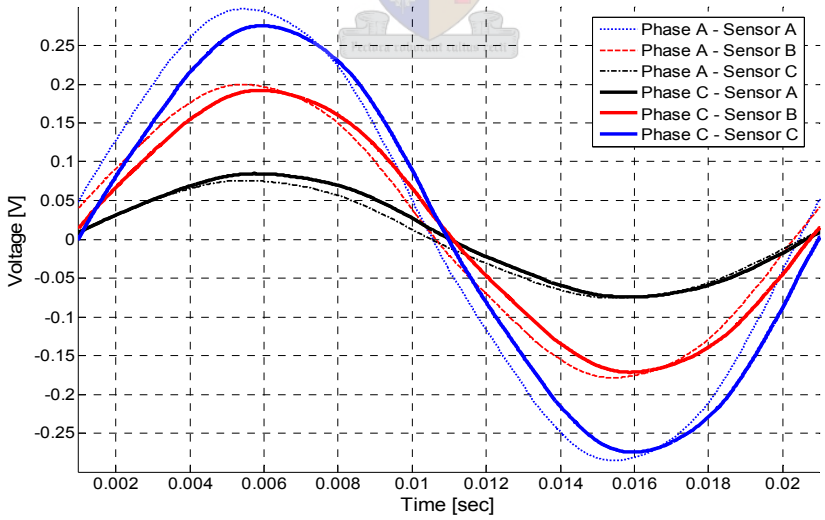


**Figure 8.24: Illustrating the fact that when *phase A* and *phase C* are energised the measured waveforms are mirror images of each other.**

The coupling factors are calculated from the waveforms presented in Figure 8.21, Figure 8.22 and Figure 8.23. Table 8.7 tabulates the values of the coupling factors. The coupling factors

are evaluated by dividing the phase voltage (20.5kV) with the voltage induced on the sensor. For an ideal system coupling factors $G_{pAsA}$ and $G_{pCsC}$, $G_{pAsB}$ and $G_{pCsB}$, $G_{pAsC}$ and $G_{pCsA}$, and $G_{pBsA}$ and $G_{pBsC}$, will have the same values. Table 8.8 tabulated the differences between the various coupling factors. The coupling factor matrix must ideally be diagonally symmetrical, the same as the capacitive matrix of a three-phase power line configuration.

**Table 8.7: Calculated values for the coupling factors if the non-energised phases are grounded and the energised voltage equals 20.5kV.**

| | Peak voltages measured on sensors | | | Coupling factors | | | | | |
|---|---|---|---|---|---|---|---|---|---|
| | Sensor A [V] | Sensor B [V] | Sensor C [V] | Sensor A | | Sensor B | | Sensor C | |
| **Phase A** | 0.2969 | 0.1994 | 0.07573 | $G_{pAsA}$ | 69.047 | $G_{pAsB}$ | 102.808 | $G_{pAsC}$ | 270.699 |
| **Phase B** | 0.1881 | 0.2802 | 0.1724 | $G_{pBsA}$ | 108.985 | $G_{pBsB}$ | 73.162 | $G_{pBsC}$ | 118.910 |
| **Phase C** | 0.08462 | 0.1919 | 0.2751 | $G_{pCsA}$ | 242.260 | $G_{pCsB}$ | 106.826 | $G_{pCsC}$ | 74.518 |

**Table 8.8: Comparison between the different coupling factors.**

| Factors | % dif |
|---|---|
| $G_{pAsA}$ vs $G_{pCsC}$ | 7.34 |
| $G_{pAsB}$ vs $G_{pCsB}$ | 3.76 |
| $G_{pAsC}$ vs $G_{pCsA}$ | 10.51 |
| $G_{pBsA}$ vs $G_{pBsC}$ | 8.35 |

From the above measurements the non-idealness of the test facility is prominent. It is however proved that adequate measurements and evaluations of the coupling factors can be made in the test facility. The evaluations that are done in this section are repeated for the remaining tests.

### 8.10.4.4. Non-energised phases floating

Each phase is energised respectively with 20.5kV while the non-energised conductors are left floating (no ground connected to it). The induced waveforms on the sensors are again used to evaluate the coupling factors between the different conductors and the different sensors. Table 8.9 tabulates these coupling factors. Table 8.10 tabulates the percentage differences between the different coupling factors.

**Table 8.9: Calculated values for the coupling factors if the non-energised phases are floating and the energised voltage equals 20.5kV.**

| | Peak voltages measured on sensors | | | Coupling factors | | | | | |
|---|---|---|---|---|---|---|---|---|---|
| | Sensor A [V] | Sensor B [V] | Sensor C [V] | Sensor A | | Sensor B | | Sensor C | |
| **Phase A** | 0.3252 | 0.2457 | 0.1135 | $G_{pAsA}$ | 63.038 | $G_{pAsB}$ | 83.435 | $G_{pAsC}$ | 180.617 |
| **Phase B** | 0.2331 | 0.3251 | 0.2151 | $G_{pBsA}$ | 87.945 | $G_{pBsB}$ | 63.058 | $G_{pBsC}$ | 95.305 |
| **Phase C** | 0.1236 | 0.2366 | 0.3021 | $G_{pCsA}$ | 165.858 | $G_{pCsB}$ | 86.644 | $G_{pCsC}$ | 67.858 |

**Table 8.10: Comparison between the different coupling factors if the non-energised phases are floating.**

| Factors | % dif |
|---|---|
| $G_{pAsA}$ vs $G_{pCsC}$ | 7.10 |
| $G_{pAsB}$ vs $G_{pCsB}$ | 3.70 |
| $G_{pAsC}$ vs $G_{pCsA}$ | 8.17 |
| $G_{pBsA}$ vs $G_{pBsC}$ | 7.72 |

The waveforms obtained by the floating conductor tests are compared with the waveforms obtained when the non-energised conductors are grounded. Figure 8.25, Figure 8.26 and Figure 8.27 illustrates these comparisons.

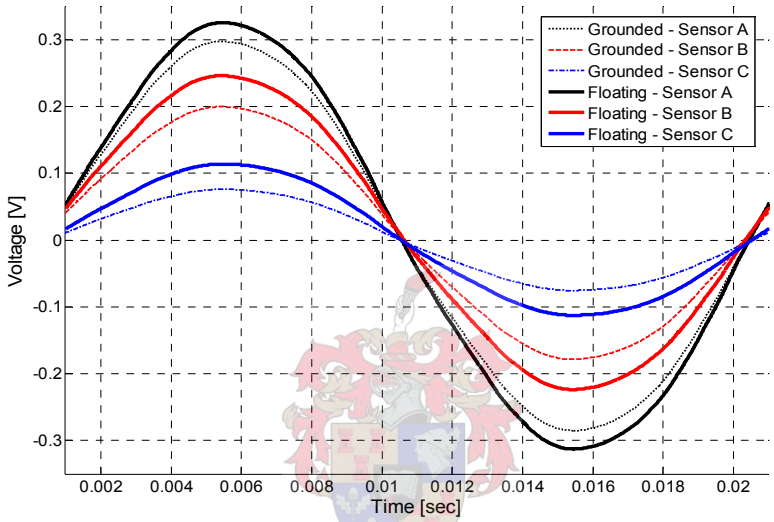


**Figure 8.25: Comparison between waveforms of grounded conductor and floating conductors. Phase A = 20.5kV; Phase B = 0kV; Phase C = 0kV.**

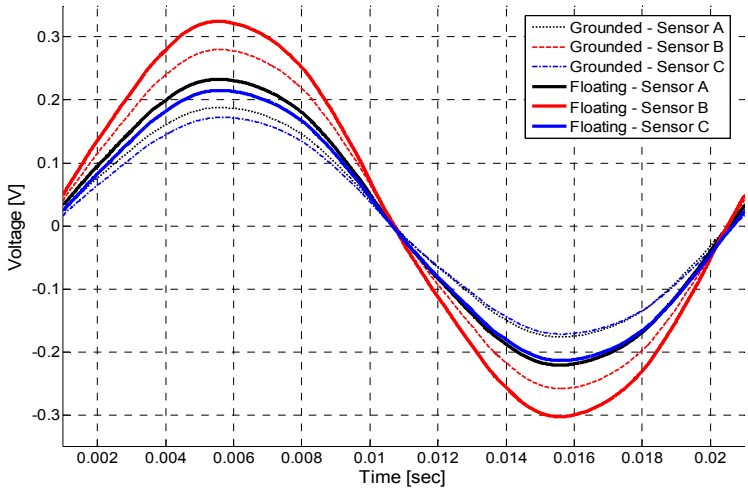


**Figure 8.26: Comparison between waveforms of grounded conductor and floating conductors. Phase A = 0kV; Phase B = 20.5kV; Phase C = 0kV.**

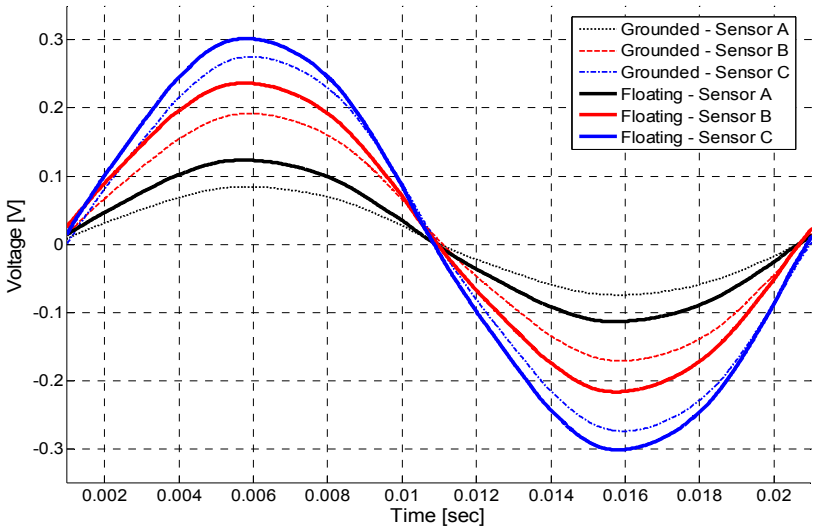


**Figure 8.27: Comparison between waveforms of grounded conductor and floating conductors. Phase A = 0kV; Phase B = 0kV; Phase C = 20.5kV.**

The differences between the two sets of waveforms are evident each time. Grounding or not grounding the non-energised conductors will thus play an important role in calculating the coupling factors. Grounding the non-energised conductors is the preferred method for calculating the coupling factors, as this is similar to the method of evaluating the coupling factors described in section 5.4. A known voltage of 0V is used for the voltage of grounded conductors during calculation of the capacitive coupling components. The voltage on a floating conductor is unknown and thus not able to be represented by a mathematical quantity in analytical calculations. Floating boundary conditions can be used in ELECTRO.

Figure 8.25, Figure 8.26 and Figure 8.27 compares the peak voltages with each other to evaluate the difference between the voltages induced on the sensors if the non energised conductors are grounded and floating. Table 8.11 presents the differences between these values. The waveforms of the floating phases are taken as the reference values. Table 8.11 shows that the matrix is diagonally symmetrical, indicating that the difference between the peak values is a factor of the power systems geometry. Table 8.12 compares the coupling factors for these two circumstances.

**Table 8.11: Comparing peak values of waveforms for grounded and floating phases if only one phase is energised at a time.**

| | difference [%] | | | difference [V] | | |
|---|---|---|---|---|---|---|
| | **Sensor A** | **Sensor B** | **Sensor C** | **Sensor A** | **Sensor B** | **Sensor C** |
| **Phase A** | 8.70 | 18.84 | 33.28 | 0.028 | 0.046 | 0.038 |
| **Phase B** | 19.31 | 13.81 | 19.85 | 0.045 | 0.045 | 0.043 |
| **Phase C** | 31.54 | 18.89 | 8.94 | 0.039 | 0.045 | 0.027 |

**Table 8.12: Comparing coupling factors of waveforms for grounded and floating phases if only one phase is energised at a time.**

| Factors | Grounded | Floating | % difference |
|---|---|---|---|
| $G_{pAsA}$ vs $G_{pCsC}$ | 7.34 | 7.65 | 3.97 |
| $G_{pAsB}$ vs $G_{pCsB}$ | 3.76 | 3.85 | 2.21 |
| $G_{pAsC}$ vs $G_{pCsA}$ | 10.51 | 8.17 | -28.57 |
| $G_{pBsA}$ vs $G_{pBsC}$ | 8.35 | 8.37 | 0.26 |

### 8.10.4.5. Different energisation voltages

The energisation voltage is increased to 25.2kV. This section repeats the tests done in sections 8.10.4.3 and 8.10.4.4. By comparing the coupling factors evaluated in this section with the coupling factors in the previous two sections the linearity of the voltage induced on the sensors can be evaluated. The coupling factors between the different overhead conductors and the three sensors must stay the same for different energisation voltages. Table 8.13 tabulates the coupling factors when the non-energised conductors are grounded. Table 8.14 tabulates the coupling factors when the non-energised conductors are floating.

**Table 8.13: Calculated values for the coupling factors if the non-energised phases are grounded and the energised voltage equals 25.2kV.**

| | Peak voltages measured on sensors | | | Coupling factors | | | | | |
|---|---|---|---|---|---|---|---|---|---|
| | Sensor A [V] | Sensor B [V] | Sensor C [V] | Sensor A | | Sensor B | | Sensor C | |
| **Phase A** | 0.3615 | 0.2417 | 0.09253 | $G_{pAsA}$ | 69.710 | $G_{pAsB}$ | 104.261 | $G_{pAsC}$ | 272.344 |
| **Phase B** | 0.2288 | 0.341 | 0.2115 | $G_{pBsA}$ | 110.140 | $G_{pBsB}$ | 73.900 | $G_{pBsC}$ | 119.149 |
| **Phase C** | 0.1029 | 0.2348 | 0.3394 | $G_{pCsA}$ | 244.898 | $G_{pCsB}$ | 107.325 | $G_{pCsC}$ | 74.249 |

**Table 8.14: Calculated values for the coupling factors if the non-energised phases are floating and the energised voltage equals 25.2kV.**

| | Peak voltages measured on sensors | | | Coupling factors | | | | | |
|---|---|---|---|---|---|---|---|---|---|
| | Sensor A [V] | Sensor B [V] | Sensor C [V] | Sensor A | | Sensor B | | Sensor C | |
| **Phase A** | 0.396 | 0.2985 | 0.1394 | $G_{pAsA}$ | 63.636 | $G_{pAsB}$ | 84.422 | $G_{pAsC}$ | 180.775 |
| **Phase B** | 0.2845 | 0.3965 | 0.2639 | $G_{pBsA}$ | 88.576 | $G_{pBsB}$ | 63.556 | $G_{pBsC}$ | 95.491 |
| **Phase C** | 0.1513 | 0.2913 | 0.3713 | $G_{pCsA}$ | 166.557 | $G_{pCsB}$ | 86.509 | $G_{pCsC}$ | 67.870 |

Table 8.15 compares the coupling factors for the 20.5kV energisation with the coupling factors for the 25.2kV energisation. The differences between the different coupling factors have a median of 0.95 and 0.42 for the grounded and floating conductors respectively. These results prove the linearity of the coupling factors.

**Table 8.15: Comparing the different coupling factors for the different energisation values.**

| Coupling factor | Grounded | | | Floating | | |
|---|---|---|---|---|---|---|
| | 20.5kV | 25.2kV | % dif | 20.5kV | 25.2kV | % dif |
| $G_{pAsA}$ | 69.0468 | 69.7095 | **0.95** | 63.0381 | 63.6364 | **0.94** |
| $G_{pAsB}$ | 102.808 | 104.261 | **1.39** | 83.4351 | 84.4221 | **1.17** |
| $G_{pAsC}$ | 270.699 | 272.344 | **0.60** | 180.617 | 180.775 | **0.09** |
| $G_{pBsA}$ | 108.985 | 110.14 | **1.05** | 87.9451 | 88.5764 | **0.71** |
| $G_{pBsB}$ | 73.162 | 73.9003 | **1.00** | 63.0575 | 63.5561 | **0.78** |
| $G_{pBsC}$ | 118.91 | 119.149 | **0.20** | 95.3045 | 95.4907 | **0.19** |
| $G_{pCsA}$ | 242.26 | 244.898 | **1.08** | 165.858 | 166.557 | **0.42** |
| $G_{pCsB}$ | 106.826 | 107.325 | **0.46** | 86.6441 | 86.5088 | **-0.16** |
| $G_{pCsC}$ | 74.5184 | 74.2487 | **-0.36** | 67.8583 | 67.8696 | **0.02** |

### 8.10.4.6. Horizontal electric field profile

The electric field profile underneath the three conductors is investigated if only the middle conductor (*phase B*) is energised with 20.5kV. Only the electric profile in the vicinity directly underneath the three conductors is tested.

As it is the electric field underneath the overhead conductors that induce a voltage on the sensors, the electric field profile for the power system of the test facility has to be evaluated. The electric field profiles of the test facility are simulated in ELECTRO for grounded and floating conductors. Figure 8.28 presents the electric field profile of the single-phase test with the non-energised conductors grounded. Figure 8.29 shows the electric field profile of the single-phase test with the non-energised conductors floating. Figure 8.30 compares the electric field profile, for a balanced three-phase energisation of the test facility, between simulations done with a wide ground plane and a normal ground plane. The non-symmetry of the electric field profiles is illustrated with these simulations.

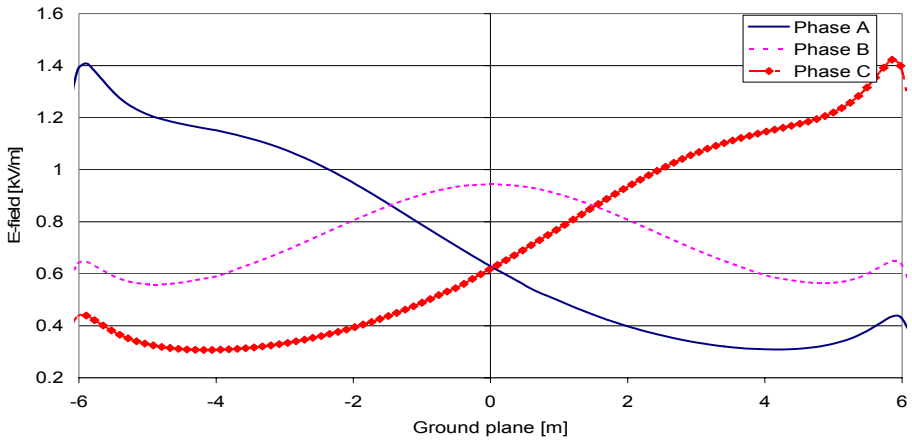


**Figure 8.28: Electric field profile, simulated in ELECTRO, of the single-phase test if the non-energised conductors are grounded.**

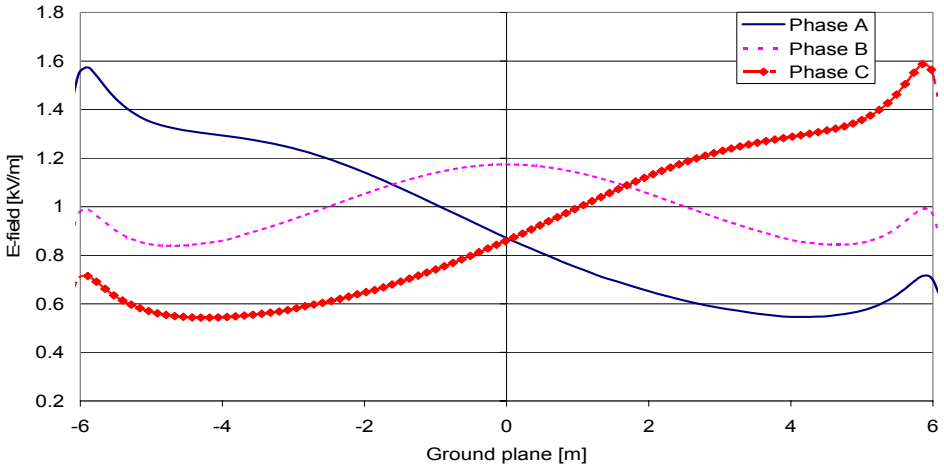


**Figure 8.29: Electric field profile, simulated in ELECTRO, of the single-phase test if the non-energised conductors float.**

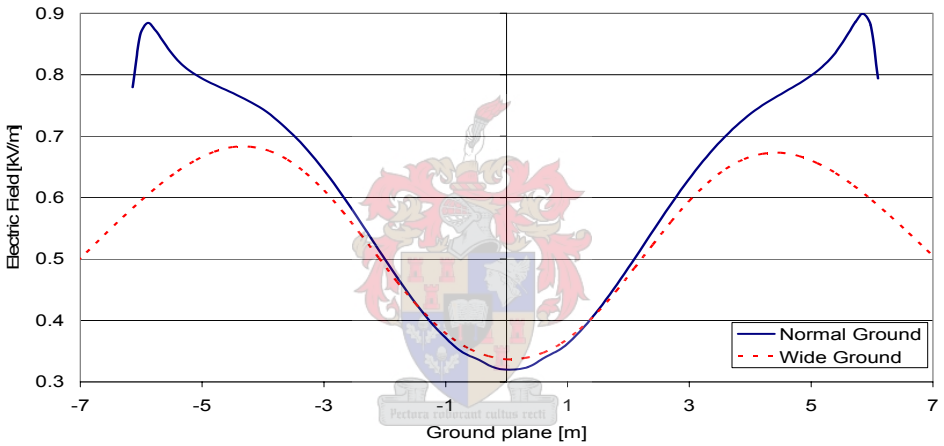


**Figure 8.30: Electric field profile, simulated in ELECTRO, of a three-phase test for a normal ground plane and a wide ground plane.**

The sensors are used to construct a measured horizontal electric field profile underneath the overhead conductors for a single-phase energised voltage of 20.5kV. The centre conductor was energised while the non-energised conductors were grounded. The values of the voltages measured by the three sensors are used to construct the profile. Thus instead of an electric field profile an induced voltage profile is constructed. Table 8.16 tabulates the measured voltages and Figure 8.31 graphs the voltage profile. The peak voltage value at each position is graphed. The parapets on the roof restrict the measurement of a complete voltage profile as the sensors cannot be brought in close proximity of the parapets. The parapets have a significant influence on the voltages induced on the sensors.

This section clearly illustrates the importance of the position of the sensors underneath the overhead conductors. Whenever coupling factors are evaluated for a specific power system

geometry, great care must be taken in positioning the sensors. Each time the position of the sensors change, the coupling factors will change.

**Table 8.16: Voltages measured by the three sensors for different horizontal positions.**

| | Position underneath conductors [cm] | | | | | |
|---|---|---|---|---|---|---|
| | -30 | -20 | -10 | 10 | 20 | 30 |
| Sensor A | 0.174 | 0.1782 | 0.1818 | 0.1895 | 0.1943 | 0.1976 |
| Sensor B | 0.2781 | 0.2787 | 0.2775 | 0.2778 | 0.2779 | 0.2766 |
| Sensor C | 0.1828 | 0.1777 | 0.174 | 0.1665 | 0.1634 | 0.1597 |

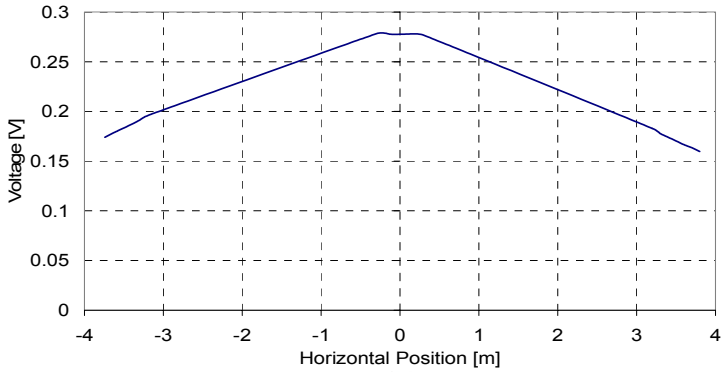


**Figure 8.31: Voltage profile underneath conductors if centre phase is energised with 20.5kV while the other two conductors are grounded.**

### 8.10.4.7. Testing all three sensors underneath one phase

The three sensors can be tested for consistency by placing all three sensors underneath the same phase as illustrated in Figure 8.32. Figure 8.33 compares the three waveforms to each other. Only the centre phase is energised with the non-energised phases grounded.

**Figure 8.32: All three sensors placed underneath phase B in the test facility.**

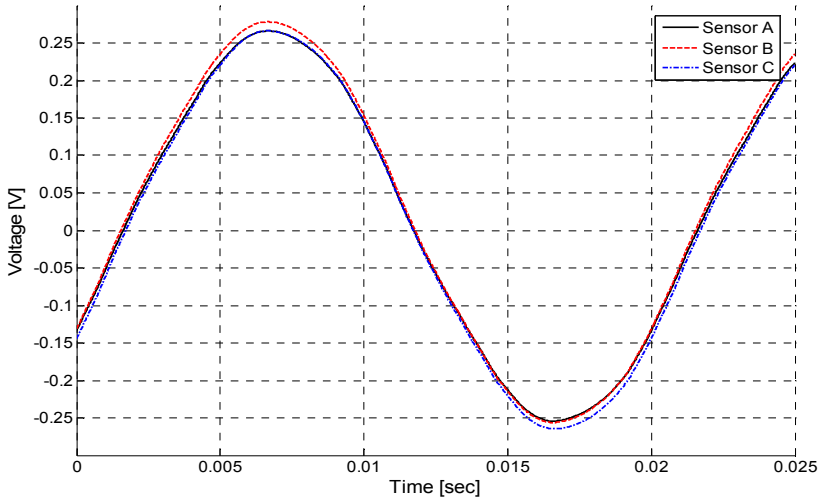


**Figure 8.33: Waveforms measured if all three sensors are placed underneath phase B with only phase B energised while the other two phases are grounded.**

Figure 8.32 shows the sensors placed underneath the same phase, but at different positions in the test facility. At different locations on the roof, the roof's geometry is different (i.e. near gas room or near extractor fan) which will cause small differences between the induced voltages on each sensor.

A small DC offset is noticeable on each waveform. If the different offsets are removed, the discrepancy between the waveforms of *sensor A* and *B* is 2.67% and between *sensor A* and *C* only 1.98%.

It is necessary to test the consistency of the capacitive voltage measurements on the roof. This is performed by energising the same conductor numerous times and testing if the same results are obtained by the different sensors. *Sensor A* and *Sensor B* are swapped in one of the measurements to test if the sensors have an effect on the measurements. Table 8.17 compares the peak values of the different waveforms to each other. *Measurement 1* is taken as the reference measurement. In the 2nd measurement *sensors A* and *B* are swapped around. Discrepancies of less than 1% are obtained proving the consistency of the sensors and the energising voltage.

**Table 8.17: Discrepancies between different measurements at the same positions and same energisation voltage.**

| Positions | Measurements | | | | |
|---|---|---|---|---|---|
| | 1 | 2 | | 3 | |
| | Voltage | Voltage | % dif | Voltage | % dif |
| Position 1 | 0.2661 | 0.2679 | 0.68 | 0.2656 | -0.19 |
| Position 2 | 0.2781 | 0.2761 | -0.72 | 0.2801 | 0.72 |
| Position 3 | 0.2661 | 0.2658 | -0.11 | 0.2666 | 0.19 |

### 8.10.4.8. Comparison of the coupling factors

Chapter 6 showed that for three-phase measurements in the field it is necessary to estimate a factor of difference between some capacitive coupling factors. The capacitive coupling factors estimated in the above sections must thus be compared to each other in order to evaluate these factors for the test facilities' line configuration. These factors must then be compared with the factors derived from the ELECTRO simulations presented in Chapter 6. The estimation of these differences is a crucial step in calculating the coupling factors for three-phase line configurations.

The coupling factors which are compared with each other are factors $G_{pBsB}$ and $G_{pAsA}$ and factors $G_{pAsB}$ and $G_{pBsA}$. Figure 8.14 illustrates these coupling factors. Table 8.18 tabulates the differences between the coupling factors of the different situations. The differences between the different factors did not correspond, especially when the non-energised conductors are floating. Research in evaluating the factors between the different coupling factors is essential for future field tests with the three-element parallel plate sensors.

**Table 8.18: Different coupling factors for measured and simulated values.**

| Factors | % difference | | |
|---|---|---|---|
| | Electro | Grounded | Floating |
| $G_{pBsB}$ vs $G_{pAsA}$ | 13.69 | 5.96 | 0.03 |
| $G_{pAsB}$ vs $G_{pBsA}$ | 1.62 | 5.67 | 5.13 |

### 8.10.4.9. Varying the sensor height above the ground plane

The effect that the height of the sensor above the ground has on the induced voltage measured by the sensor is tested. The sensor is placed 0.4m, 0.6m and 0.8m above the ground plane. Only *phase B* is energised with 22kV while the other two phases are grounded. Only *sensor B* is used in these measurements. *Sensor B* is centralised underneath *phase B*. Figure 8.34 shows the measured waveforms at the three different heights. No noticeable differences between the peak voltages of the three waveforms are observed.

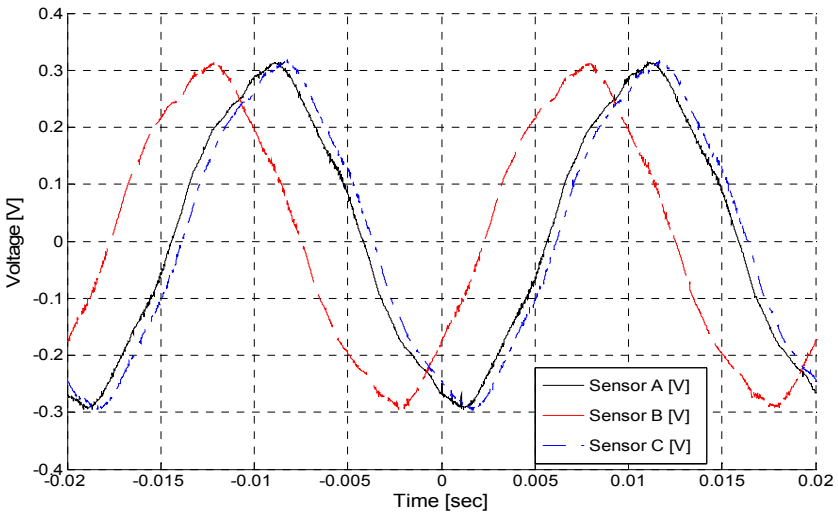


**Figure 8.34: Comparing the voltages induced on the sensors at different heights above the ground plane.**

### 8.10.4.10. Transient tests

Single-phase switching transient test are performed with the three phases respectively. Measurements are performed where the phase voltage is switched from 0V to 22kV (ON) and from 22kV to 0V (OFF). The non-energised phases are grounded. The transients formed with the on- and off-switching of the power supply are measured. The high-voltage values of the overhead conductors are measured with HV probes in these measurements.

The sample frequency of the transmitter cards is 100 kHz. Any high frequency noise above the Nyquist frequency can thus be filtered. A 2$^{nd}$ order lowpass Butterworth filter, with a cut-off frequency of 10 kHz is implemented in MATLAB to filter the waveforms. Figure 8.35 shows the unfiltered waveforms of the voltages induced on the sensors. A lot of noise is observed on the waveforms. This noise can be ascribed to the interface instrumentation used. For future evaluation of the three-element sensor, investigation must be done into the exact source of the noise, i.e. receiver card, termination capacitance, etc. Only high-frequency noise generated in the HV system must be measured. Figure 8.36 shows the filtered waveforms of the voltages induced on the sensors. Figure 8.37 compares the filtered three measured waveforms to the HV waveform measured with a HV probe if *phase A* is switched on. Only *phase A* was energised. Figure 8.38 compares the filtered three measured waveforms to the HV waveform measured with HV probes if *phase A* was switched off.

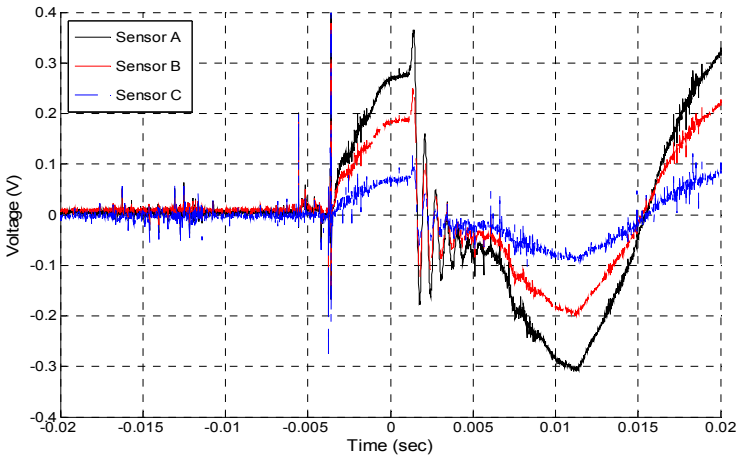


**Figure 8.35: Unfiltered transient waveforms measured by the three sensors if Phase A is switched on.**

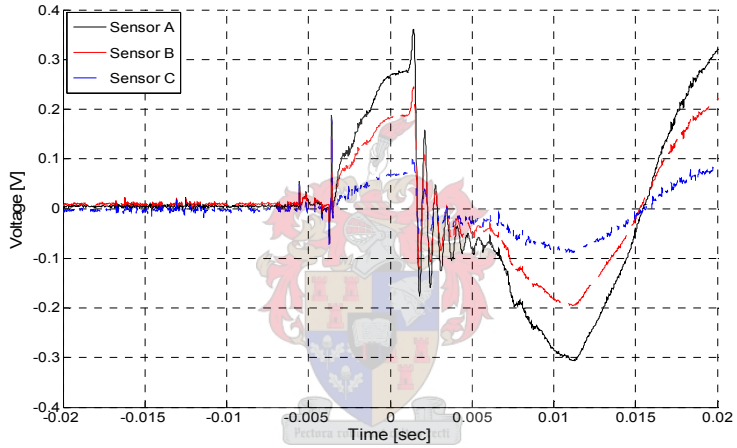


**Figure 8.36: Filtered transient waveforms (cut-off frequency = 10 kHz) measured by the three sensors if Phase A is switched on.**

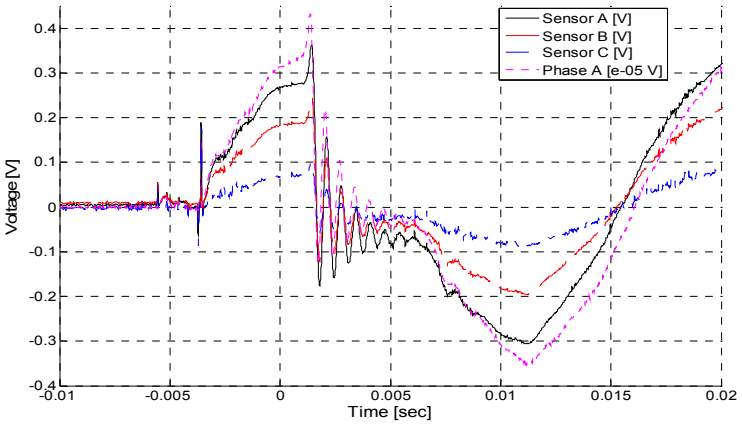


**Figure 8.37: Comparing the phase voltage of *phase A* with the three sensor voltage waveforms if phase A is switched on.**

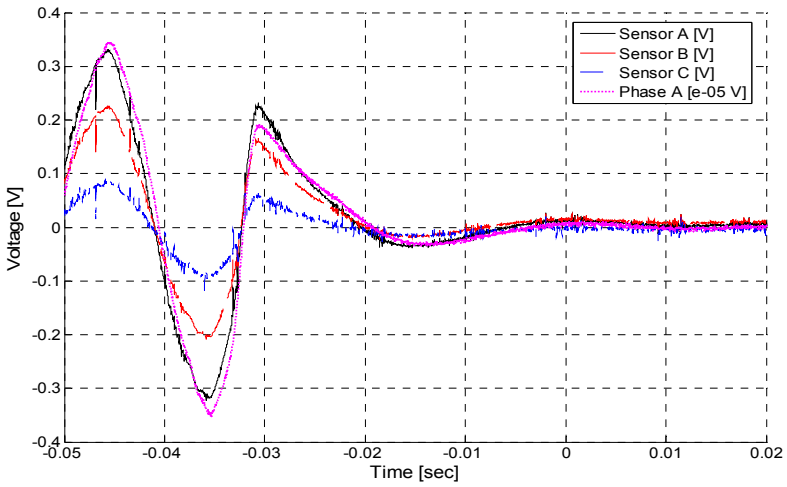


**Figure 8.38: Comparing the phase voltage of *phase A* with the three sensor voltage waveforms if phase A is switched off.**

### 8.10.5. Evaluation of phase voltages from capacitive coupling components derived from the single-phase tests

The capacitive coupling components of the linear system, denoted by equation (8.4), are evaluated in the capacitive voltage measurements of section 8.10.4 . The capacitive coupling components evaluated from the measurements when the non-energised phases are grounded are taken as the preferred values. The phase voltages are evaluated from equation (8.4) as

$$v_{pA} = 136.828v_{sA} - 115.552v_{sB} + 38.5171v_{sC}, \tag{8.5}$$

$$v_{pB} = -125.394v_{sA} + 234.068v_{sB} - 124.707v_{sC} \tag{8.6}$$

and

$$v_{pC} = 40.9151v_{sA} - 114.876v_{sB} + 142.066v_{sC} \tag{8.7}$$

where $v_{sA}$, $v_{sB}$ and $v_{sC}$ denote the voltages measured with the three-element parallel plate sensors. Care must be taken when the capacitive coupling factors are evaluated. If the geometry of the line configuration or if the ground conductivity in the test facility are altered the coupling factors will change.

## 8.11. Three-phase tests

Balanced three-phase tests are performed in order to evaluate if the measuring system developed in this project can effectively be used to measure the phase voltages of a three-phase transmission line accurately. The dimensions of the test facility's line configuration stay the same as that of Figure 8.15.

Equations (8.5), (8.6) and (8.7) are used to evaluate the phase voltages from the voltages induced on the three capacitive voltage sensors. The three phase voltages are measured with HV probes. Figure 8.39 shows the test setup for measuring the HV waveforms. These measured phase voltages are then compared with the phase voltages evaluated from the equations.


**Figure 8.39: Test setup for measuring HV waveforms**

The three-phase line configuration is energised as a balanced 22kV three-phase system. Figure 8.40 shows the measured voltage waveforms induced on the sensors. These three waveforms are used to evaluate the HV phase voltages. Figure 8.41 compares the waveform evaluated from the equations and the measured waveform of *phase A*. Good comparison is found between these two waveforms with a discrepancy of 4.24% between the peak values.

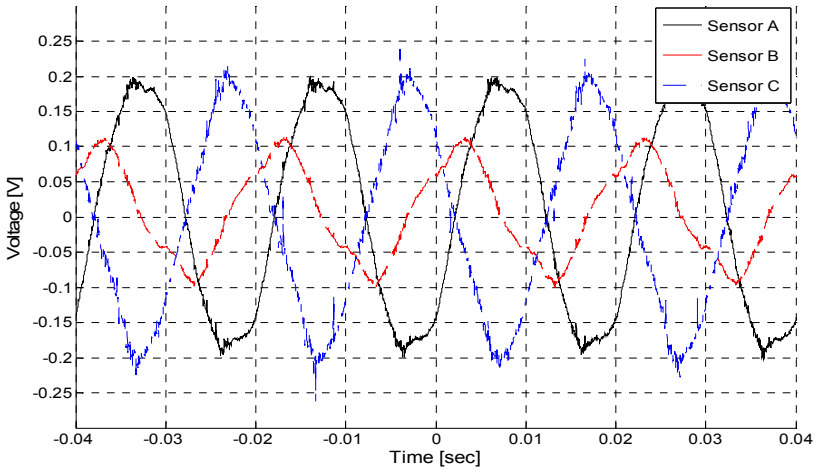


**Figure 8.40: Measured capacitive voltage waveforms.**

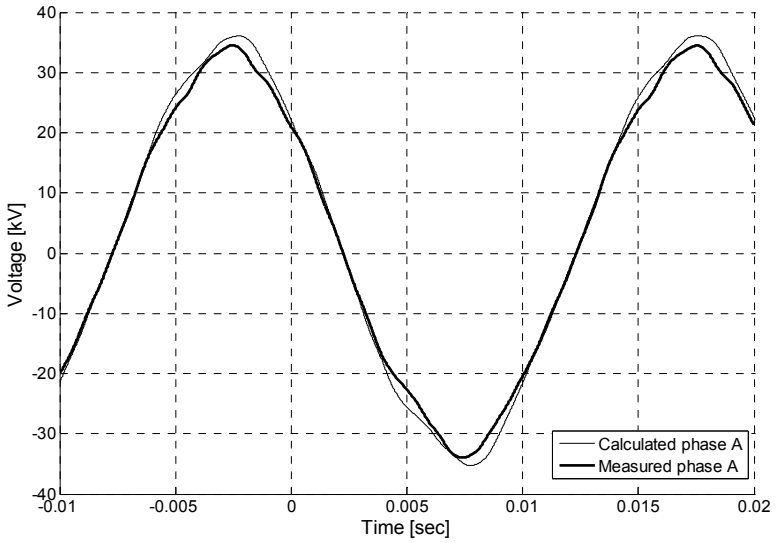


**Figure 8.41: Comparison of evaluated and measured waveform for *phase A*.**

Three-phase transient tests are performed to evaluate the capacitive sensors as well as the method of determining the overhead HV phase values. Figure 8.42 shows the three voltage waveforms measured with the sensors if the HV three-phase system is switched on. There is a lot of high frequency noise on the waveforms, especially at the peak values of the waveforms. For proper evaluation of the decoupling method used for reconstructing the HV waveforms the waveforms measured with the sensors would ideally not have noise that is not induced via the HV phases.

The three waveforms measured with the sensors are filtered and then used to reconstruct the HV waveforms. Equations (8.5), (8.6) and (8.7) are used to decouple the three phase voltages and then reconstruct the HV waveforms. Figure 8.45 compares the evaluated waveforms with the measured HV waveforms. Very good correlation between the calculated and the measured HV waveforms are obtained except at the peak values. The discrepancies at the peak values can be ascribed to the excessive noise on the peak values of the measured waveforms, illustrated in Figure 8.42. The single-phase transient tests used to determine the capacitive coupling components are also not optimal, especially for when *phase C* was energised separately. Waveform distortion occurred with the energisation of *phase C*.

At the zero crossing excellent correlation is found between the different waveforms.

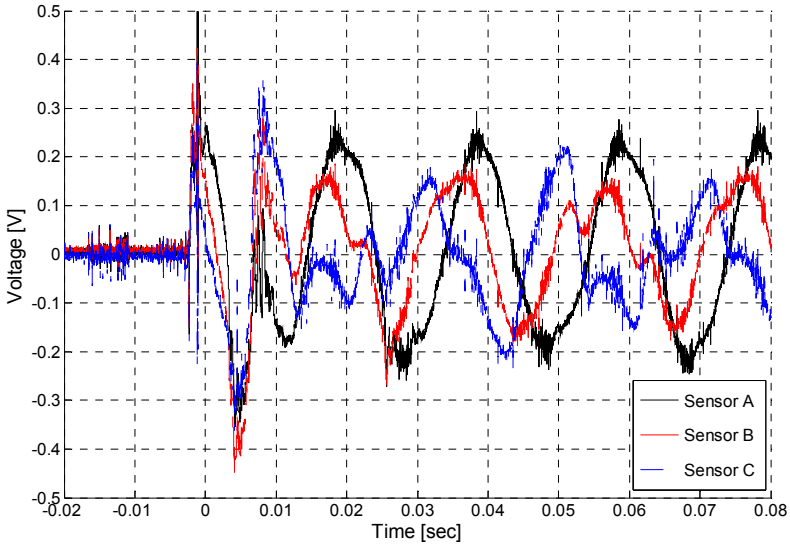


**Figure 8.42: Measured capacitive voltage waveforms if the HV three-phase system is switched on.**

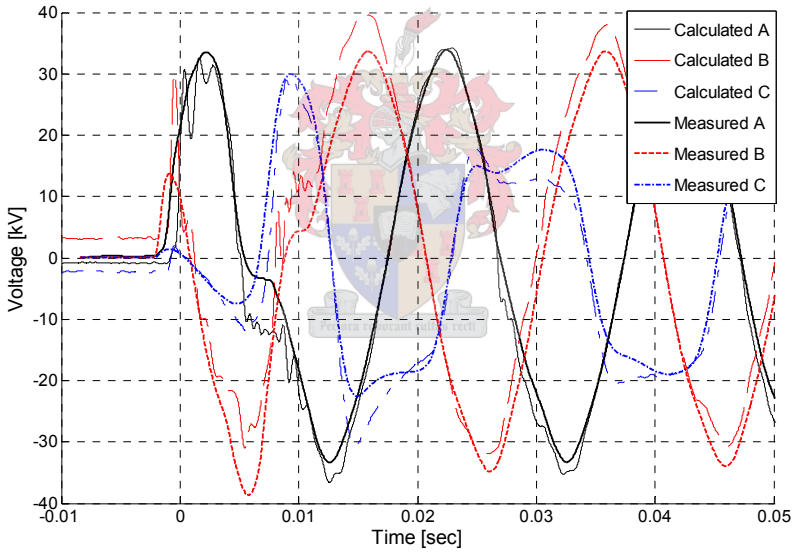


**Figure 8.43: Comparison between evaluated and measured waveform if the HV three-phase system is switched on.**

Figure 8.44 shows the unfiltered voltages measured with the sensors if the HV three-phase system is switched off. The same procedure as above is used to reconstruct the HV waveforms. Equations (8.5), (8.6) and (8.7) are again used to evaluate the HV phase voltages from the three measured waveforms. Figure 8.45 compares the evaluated waveforms with the measured HV waveforms. The discrepancies at the peak values of the waveforms are evident but excellent correlation is found at the zero crossings.

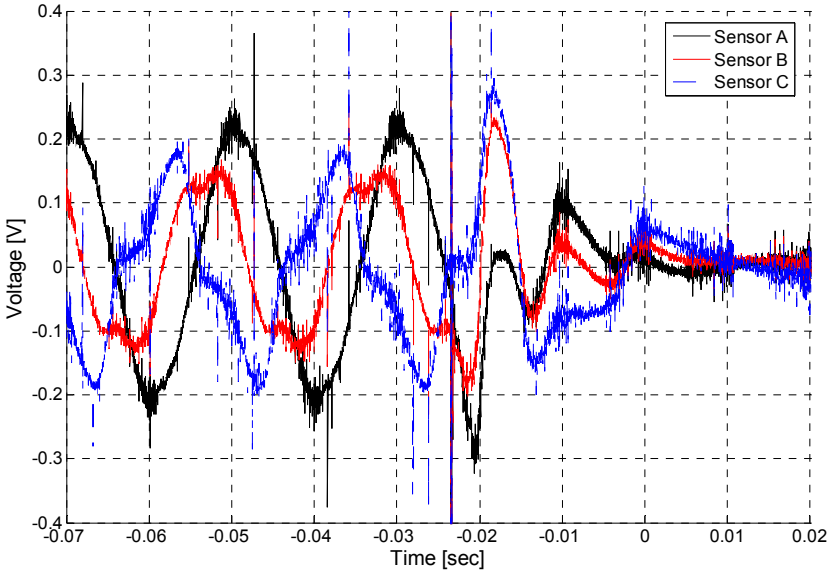


**Figure 8.44: Measured capacitive voltage waveforms if the HV three-phase system is switched off.**

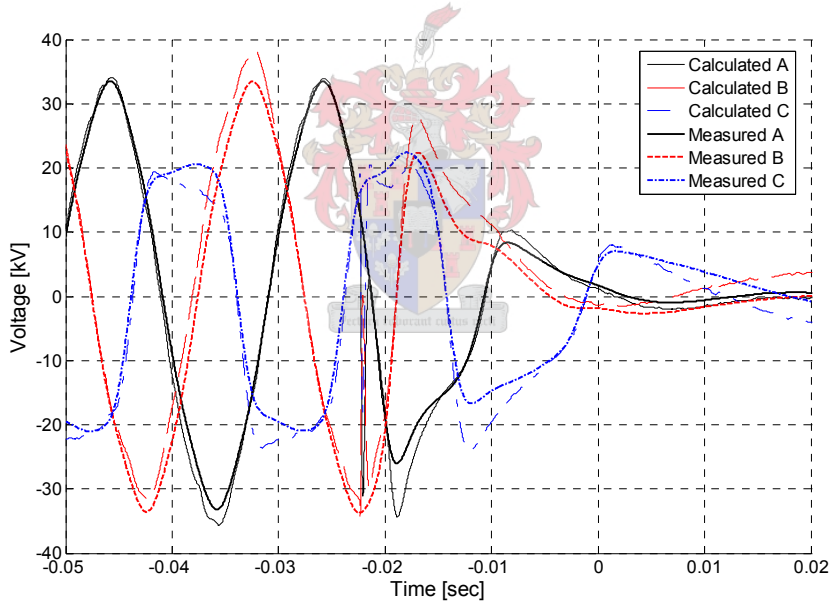


**Figure 8.45: Comparison between evaluated and measured waveform if the HV three-phase system is switched off.**

The transients tests show that the sensor and method developed in this project for measuring HV phases underneath transmission lines provide adequate results. The capacitive three-element sensors can thus be used for future evaluation of capacitive voltage measurements underneath three-phase transmission lines.

## 8.12. Conclusion

This chapter presents the design, development and construction of a high-voltage test facility, where single-phase and three-phase capacitive coupling tests can be performed. The test facility proves to be adequate for capacitive coupling measurements. Different single-phase tests are done to calculate the coupling factors between the different overhead conductors and the three sensors. The tests prove the linearity of the coupling factors and the consistency of the sensors. The geometry of the overhead conductors for the test done in this chapter is not optimal. The distance between the conductors and the heights of the conductors are not the same and must be changed for future measurements. However the test facility still proves to provide excellent possibilities for high voltage open-air capacitive voltage measurements.

There is a large amount of high frequency noise on the waveforms, especially at the peak values of the waveform. This noise can be ascribed to the interface instrumentation used. For future evaluation of the three-element sensor, the exact source of the noise, i.e. receiver card, termination capacitance, must be determined.

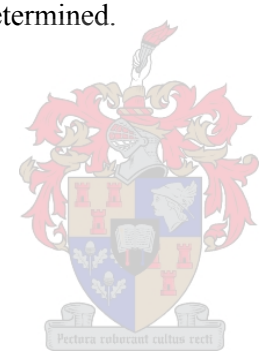

# 9. Conclusion and recommendations

This chapter summarizes the research results presented in this thesis and presents conclusions and recommendations for further work.

## 9.1. Literature review

### 9.1.1. Introduction – capacitive voltage sensors

The objective of this thesis is the research and development of an open-air capacitive high voltage measuring device. As a precursor to this research a background study is done on high voltage and traditional voltage measurement techniques. Although most of the capacitive voltage measurements as well as the decoupling of the phase voltages from the measured sensor voltages is done at the power frequency, 50 Hz, future research will centre on wideband measuring. It is thus necessary to critically evaluate the existing high voltage transducer principles and equipment in the context of wideband HV measuring applications. This evaluation is done in the literature review.

In the literature review the recent gain in popularity of using open-air, capacitive voltage measurements on high voltage transmission lines are showed. This is due to the small size, reliability, safety, good EMC properties and low cost of these methods versus traditional methods.



**Traditional HV measuring methods**

A review is provided on traditional high voltage measuring methods. A description of the available technology, its advantages and disadvantages are given. The shortcomings of the traditional voltage transducers are the high cost, large equipment, limited voltage levels and limited bandwidth. Most of these transducers operate well at their designed operating frequency but if the frequency changes the response of the device normally changes. It is concluded that alternative methods have to be found for wideband measuring.

**Optical sensing**

Optical sensing is an alternative form for measuring HV. This provides a convenient method of transmitting signals from high voltage to ground and vice versa. The size and cost of the fibre increase as insulators have to be fitted to the fibre to guard against surface tracking on the fibre resulting in a flash over. The drawback of optical sensing is an increase in equipment size, not being maintenance free and the measured capacitance requires calibration.

**AC voltage sensors**

AC voltage sensors that work on the principles of electric field strength and capacitive coupling measurements are discussed.

Fixed electrode sensors work on these principles. These sensors are used to measure high voltage and can either be constructed as an integral part of high voltage equipment or as separate units. The fixed electrode sensors are subdivided into three types, namely the GIS voltmeters, open-air voltage sensors and open-air electric field strength meters. Gas-insulated switchgear (GIS) overcomes many of the limitations of the conventional open-type HV switchgear. Many of the GIS sensors are designed to have very high bandwidths.

The capacitive sensors designed and tested for GIS offer reduced size, are unaffected by atmospheric conditions, possesses a high degree of operational reliability and safety to personnel, are easier to install, have good EMC properties and have low cost.

Different open air applications are described by Van Heesch [15] and Feldman *et al* [35]. These applications have low cost, simple installation, large bandwidths, are linear and have excellent EMC qualities.

Gerrard [10] implemented a multiple point electric field measurement system for monitoring voltage changes on three-phase power systems. The electric fields generated can be measured accurately at distances from conductors and is a function of the instantaneous voltages on all conductors; it depends on the geometry of both the power system and its environment.

Botha [1] described the wideband modelling of capacitive voltage sensors for open air transmission line applications. She concluded that the interface instrumentation must have high input impedance and that galvanic isolation be maintained. Botha designed capacitive sensors consisting of a differential parallel plate sensor with a floating faraday cage in between. The termination and interface instrumentation (fibre optic link) was placed inside the faraday cage. Botha however used a digitising topology which offers an improved accuracy and versatility but is more complex and has a high power supply requirement.

The conclusion reached is that capacitive sensors can be applied effectively in power system applications. This equipment is smaller, cheaper and has wider bandwidth than traditional transducers.

A spherical potential-free sensor was developed by Feser, Pfaff and co workers [3]. This instrument was used to measure the localised electric field, but the voltage on a nearby HV electrode could also be determined.

**Capacitive sensors**

Development of full contact systems has been limited by the insulation burden. For AC or transient excitation, stray capacitances exist between the resistor/capacitor terminals and ground. The capacitive and resistive dividers are sensitive to objects in close proximity, which will increase the stray capacitances. Capacitive voltage transformers have limited bandwidth. The bandwidth of the measuring systems may be increased, with limited success, by proper compensation or by using alternative configurations.

Non-electrical contact systems is physically connected to the high voltage line, but is electrically isolated from both the ground and the instrumentation. The installation burden is reduced by this system because the instrumentation is not connected to a ground reference, but limits the accuracy with which voltage measurements may be made. Most developments of optical systems have been for current measurements. Development of hybrid voltage sensors has been limited by the absence of a ground reference and a suitable power supply. Development of passive sensors has been limited by the temperature coefficients of the materials used.

With open-air sensors and electric field sensors, no physical contact is made to the high voltage system and the instrumentation is at ground potential. The sensor may be at ground potential or at the potential of the location at which it is placed. The absence of a connection to the high voltage line limits the accuracy with which the measurements are made but the insulation burden of all other methods is removed completely which can result in smaller and potentially cheaper systems.

It is concluded that capacitive sensors may be applied effectively in power system applications. These sensors fulfil the requirements for smaller and cheaper equipment with wider bandwidths and the sensors can usually be implemented to be non-intrusive. Conventional voltage measuring sensors work well for their intended functions, but require large amounts of insulation to ensure safe operation and are usually large and costly. The literature review clearly shows the relevance of using an open air capacitive voltage sensor, for measurements done in high voltage environments on AC power lines.

### 9.1.2. Electrostatic theory of capacitive sensor design

The scope of this thesis is the development of a capacitive sensor for implementation in an AC environment. The constraints for the design of capacitive voltage sensors are investigated in the literature review. A brief discussion of analytical methods and the use of software packages for calculating capacitive coupling are also done.

It is concluded that correct circuit design will play a very important role in developing a capacitive sensor. The predicted working environment of the sensors should also be taken into account when designing the sensor system. The principles of superposition and charge images are important techniques used for calculation of electric fields underneath power systems. Measurement of the capacitance between the different sensor plates plays an important role.

From Botha's [1] work the necessity to calculate the capacitive coupling between the overhead transmission lines and the sensors are stated. Botha's [1] method are expanded to three-phase AC measurements and therefore the capacitive coupling matrix is more complex.

By calculating the capacitive coupling matrix, the electric field underneath the transmission lines, at specific locations can also be determined. Analytical methods and software packages are used to calculate the various coupling factors. The analytical methods provide an understanding of how the capacitive coupling between the transmission lines and the capacitive sensors can be calculated. It is however shown that for more complex examples of transmission line parameters, as used in this project, the calculations are not adequate because of the geometrical complexity. The BEM software program (ELECTRO) is used for this purpose.

### 9.1.3. Capacitive sensor and data acquisition instrumentation developed by Botha

A review is presented on the capacitive plate sensor topologies developed by Botha. Botha concluded that the three-element parallel plate sensor topology is the superior sensor topology of the different open-air plate topologies.

## 9.2. Software Packages

The transmission line parameters of HV transmission lines are used to test and evaluate different software packages. Software packages are required to simulate electric fields and the capacitive matrix of three-phase power systems, as analytical methods will not always be adequate for complex simulation models. For complex cases numerical methods (ELECTRO) should be used. The BEM program, ELECTRO, gives accurate results, when compared to actual measurements done by ESKOM, for the calculation of electric field values beneath various transmission lines.

The deviation between calculated and measured values is due to numerous assumptions made in simplifying the process of calculating the electric field. The deviation between the calculated and measured values is however insignificant. It is proved that ELECTRO is an

adequate method for calculating the capacitance matrixes and electric fields of three-phase power systems.

### 9.3. Development of three-element parallel plate sensors

A complete new measuring system is required to measure voltages underneath a three-phase transmission line. The measuring assembly that is developed consists out of three three-element parallel plate sensors, transmitter and receiver units, optocouplers, triggering system and oscilloscopes.

The block diagrams of the measurement assembly as well as the design of the new three-element parallel plate sensor are presented. The sensors are tested in the field to prove proper working condition. The new smaller sensors proved to be better than the original sensors. The capacitance of the three sensors are measured, compared and corrected with each other where after good comparison between the three sensors are found.

The termination impedance of the sensors is investigated. The termination impedance of the sensors is developed according to the input impedance of the transmitting equipment. Frequency tests are done with different terminations illustrating good frequency response at the working frequency of 50Hz. If the sensors can be constructed with more precision and the termination capacitors have smaller (1pF) tolerances, even more accuracy between the different sensors can be achieved. The termination of the sensors must be changed for an increase in bandwidth.



**Support Structure**

In this project the sensors are placed on top of the support structure. For future research the support structure must rather be connected to the Faraday cage [1]. The leakage between the floating Faraday cage and ground will then have a negligible effect on the frequency response of the sensor. The support structure's height must also be adjustable so that the sensors can be placed at the same level.

**Triggering System**

A triggering system is developed for switching transient measurements. The difficulty in designing the triggering system arose from the fact that the normal waveforms measured by the sensors are three sinusoidal waves. The triggering system of the oscilloscope can therefore not be used and a purpose built triggering system has to be designed to trigger the

two oscilloscopes when measuring the transients and voltage waveforms of the overhead, high voltage lines.

The triggering system that is designed is tested in the laboratory and demonstrated adequate triggering. The system works fast and accurately and is inexpensive. It is easy to assemble. The system is tested in conjunction with the three-element parallel plate sensors and illustrates adequate working condition. For future measurements a four channel oscilloscope will be available. Only one oscilloscope and trigger cable will then be required, thus making the optocouplers unnecessary.

### 9.4. Capacitive Coupling

To determining the voltage on the overhead conductors by using the capacitive coupling sensors, the coupling factors between the different conductors and the sensors must be calculated. Different methods of calculating the capacitive coupling factors are evaluated. All the methods evaluated are for sensors placed underneath a flat three-phase single-circuit power line. It is necessary to discriminate between the different phase voltages.

ELECTRO is used to obtain the differences between the different coupling factors in a three-phase power system. This is necessary to solve the capacitive coupling equations. To derive the capacitive coupling factors of a three-phase system is not a very straight forward solution. For future research numerical modelling of the line topologies must be performed in a 3D simulation package, e.g. COULOMB.

Methods for placing the sensors at the optimal positions underneath the three-phase transmission line are also discussed.

### 9.5. Equivalent circuit models

After it has been proven that open-air, low-frequency capacitive coupling measurements can be successfully achieved by the three-element parallel plate sensors, future development must be done to improve the bandwidth of the instrumentation.

Equivalent circuit models are derived to calculate the Thévenin equivalent voltage and impedance of the sensor topology. This is done to clarify the relationship between the transfer function characteristics of the sensors and the individual parameters defining the sensor topology [1]. The equivalent circuit models formulated are directly derived from the sensor topologies, model approximations and mathematics developed by Botha [1].

The single-phase sensor topologies created by Botha are extended to three-phase transmission lines. The single-element plate sensor, differential two-element parallel plate sensor and differential three-element parallel plate sensors topologies are analysed. Different methods for simplifying the Thévenin equivalent impedance and voltage equations are developed.

Due to the complexity of the equations, mathematical software programs are used (Mathematica), to calculate the Thévenin voltage and impedance of the three-element parallel plate sensor. Thus if the capacitive coupling and resistance between the different elements of a specific power system and measurement system are known, the Thévenin impedance and voltage can easily be calculated with mathematical programs such as Mathematica or Matlab. These equations prove to be very important for future research in capacitive coupling measurements.

### 9.6. Comparing capacitive voltage sensors

The three capacitive voltage sensors are tested in the HV Lab. The results obtained by all sensors have to be comparable and the sensors have to be consistent, accurate and linear. The HandyScope oscilloscope, the three transmitters and the sensors are tested in the HV Lab under the same test conditions to ensure that consistent results are obtained. The tests prove that the sensors are consistent, linear, accurate, comparable and easily manageable. It proves that the sensors will be adequate for capacitive coupling measurements in the field.

The importance of cleaning the sensors and support structure thoroughly, prove the importance of galvanic isolation. Calibration of the transmitters is a necessity.

For future research in high frequency measurements the transmitters must be replaced as it can only sample at 100 kS/sec.

It will be very helpful if the sensors can be calibrated properly. Most electric field sensors are calibrated inside parallel plate capacitors where uniform fields can be produced. Such a facility can easily be constructed in the HV Lab.

**Land Survey**

During the field measurements it is concluded that future field tests require accurate measurement of the power system's geometry. The geometry of the power system has to be known to accurately calculate the capacitive coupling between the overhead conductors and the sensors. The shape of the terrain, the tower construction and the sag of the conductors greatly affect the geometry of the test site.

The described survey method successfully calculates the conductor height above ground, as well as all necessary geometrical information concerning the power system.

**Field Test**

For future field test a proper site must be found under which adequate capacitive sensor measurements can be preformed. A level site, underneath a 132kV or 400kV transmission line, is required. The transmission line must stand alone, thus no other high voltage lines must be in the vicinity. Equipment is required to locate the exact position underneath the overhead conductors.

For future research in capacitive voltage measurements extensive tests must be performed underneath three-phase HV line configurations.

### 9.7. HV Test Facility

A test facility is required in which single-phase and three-phase capacitive coupling test can be performed under controlled conditions. To implement the developed sensors, for experimental purposes underneath an ESKOM three-phase power system proves to be impractical. A three-phase power system is designed, developed and constructed on the roof of the machine laboratory at the University of Stellenbosch electrical department. The advantages of this facility are: the ease of taking measurements, the controllability of the energising voltage, single-phase energising, easy testing of different characteristics of the sensors and the exact measurement of the power geometry.

A scale model of different power systems can therefore be constructed in the test facility. Thorough knowledge of tower types, conductor sizes and conductor sag is required for this purpose. The power systems that can be constructed are scaled representations of typical ESKOM power system dimensions. A single-phase 33kV transformer and a three-phase 22kV transformer are implemented in the HV Test Facility. A 132kV power system is scaled down for the first test.

Different aspects are taken into account for the construction of the test facility. The different test procedures and safety precautions are stated. The line diagrams for the different segments of the test facility are illustrated.

The test facility proves to be an adequate environment for capacitive voltage measurements. Different single-phase tests are done to calculate the coupling factors between the different overhead conductors and the three sensors. The tests prove the linearity of the coupling factors and the consistency of the sensors. The geometry of the overhead conductors for the

tests was however not optimal. For future research the geometry can be corrected and changed to the scale of the power system required.

The test facility proves to provide excellent opportunity for high voltage open-air capacitive voltage measurements.

## References:


1. M. Botha, *Wideband modelling of capacitive voltage sensors for open-air transmission line applications*, PhD thesis, University of Stellenbosch, February 2002.

2. H.I. Bassen and G.S. Smith, "*Electric field probes – a review*", IEEE Transactions on Antennas and Propagation, vol. AP-31, pp. 710 – 718, September 1983.

3. K. Feser, W.R. Pfaff, G. Weyreter and E. Gockenbach, "*Distortion-free measurement of high impulse voltages*", IEEE Transactions on Power Delivery, vol. 3, pp. 857-866, July 1988.

4. K. Feser and W.R. Pfaff, "*A potential free spherical sensor for the measurement of transient electric fields*", IEEE Transactions on Power Apparatus and Systems, vol. 103, pp. 2904-2911, October 1984.

5. W.R. Pfaff, "*Accuracy of a spherical sensor for the measurement of three-dimensional electric fields*", 5th International Symposium on High Voltage Engineering, no. 32.05, Braunschweig, Germany, August 1987.

6. T. Krauß, W. Köhler and K. Feser, "*High bandwidth potential-free electric field probe for the measurement of three-dimensional fields*", 10th International Symposium on High Voltage Engineering, Montreal, Canada, August l997.

7. M.S. Naidu and V. Kamaraju, *High Voltage Engineering – 1st Edition,* McGraw-Hill, New Delhi, 1982.

8. E. Kuffel and W.S Zaengl, *High Voltage Engineering - Fundamentals*, Pergamon Press, Oxford UK, first edition, 1984.

9. T. Wildi, *Electrical Power Technology*, Wiley, New York, 1981.

10. C.A. Gerrard, *Remote monitoring of Power System Conductor Voltages*, PhD thesis University of Liverpool, 1996.

11. J.D. Glover and M.S. Sarma, *Power System: Analysis and Design*, 3rd Edition, Brooks/Cole, Thomson Learning, 2002.

12. L.K. Baxter, *Capacitive Sensors: Design and Applications*, IEEE Press Series on Electronics Technology, Piscataway, NJ, 1997.

13. H.A. Haus and J.R. Melcher, *Electromagnetic Fields and Energy*, Prentice-Hall, Englewood Cliffs, NJ, 1989.

14. C.A. Gerrard, J.R. Gibson, G.R. Jones, L. Holt and D. Simkin, "*Measurements of power system voltages using remote electric field monitoring*", IEE Proceedings: Generation, Transmission and Distribution, vol. 145, pp. 217-224, May 1998.

15. E.J.M. van Heesch, R. Caspers, P.F.M. Gulickx, G.A.P. Jacobs, W.F.J. Kersten and P.C.T. van der Laan, "*Three-phase voltage measurements with simple open-air sensor*", 7th International Symposium on High voltage Engineering, no. 63.08, pp 165-169, Dresden, Germany, August, 1991.

16. A.J. Schwab, *High Voltage Measurement Techniques*, English translation edition, Springer-Verlag, Berlin – Heidelberg - New York, 1972.

17. T.J. Gallagher and A.J. Pearmain, *High Voltage: Measurement and Testing Design*, 1st Edition, John Wiley & Sons, New York, NY, 1983.

18. T.J. Blalock, D.F. Bullock, W.S. Zaengl and T. Liao, "*A Capacitive Voltage Divider for UHV Outdoor Testing*", IEEE Transactions on Power Apparatus & Systems", vol. 89, pp 1404-1412.

19. E.J.M. van Heesch, et al, "*Field test and response of the D/I High Voltage measuring system*", Proceedings 6th International Symposium on High Voltage Engineering, vol.3, no. 42.23, New Orleans, USA, 1989.

20. A.J. Schwab and J.H.W. Pagel, "*Precision capacitive voltage divider for impulse voltage measurements*", IEEE Transactions on Power Apparatus and Systems, vol. PAS-91, pp. 2376-2382, November/December 1972.

21. R.T. Lythall, *The J&P Switchgear Book*, Newnes-Butterworth, London, 1972.

22. *Voltage Transformers,* BS 7625, British Standards Institution, 1993.

23. M. Moghsi, *Optical Fibre Voltage and Current Sensors*, PhD thesis, University of Liverpool, 1989

24. N.A. Pilling, *Optical Fibre Measurements in Power Systems*, PhD thesis, University of Liverpool, 1992.

25. C. Moulton, "*Light Pulse System Shrinks High Voltage Protection Device*", Industrial Electronics, pp71-75, 1965.

26. F. Caspers and E. Neuman, "*Optical Power Supply for Measuring or Communication Devices at High Voltage Levels*", IEEE Transactions on Instrumentation and Measurements, vol. 29, pp73-74, 1980.

27. P.P. Banjaree and T. Poon, *Principles of Applied Optics*, Asken Associates Inc, Irwin, Boston USA, 1991.

28. E.A. Ballik and D.W. Liu, "*Measurements of High-Voltage Pulses Employing a Quartz Pockels Cell*", IEEE Journal of Quantum Electronics, vol. 19, pp. 1166-1168, 1983.

29. H.M. Hertz, "*Capacitively Coupled KDP Pockels Cell for High Voltage Pulse Measurements*", Journals of Physics E, Scientific Instruments. Vol. 18, pp. 522-525, 1985.

30. K. Tokoro, Y. Harumoto, H. Yamamoto, Y. Yoshida, H. Mukae, Y. Ohno, M. Shimada and Y. Ida, "*Development of Electronic Potential and Current Transducers suitable for Gas Insulated Switchgear and adequate for the application of Substation Digital Control*", IEEE Transactions on Power Apparatus and Systems, vol. 101, pp. 3967-3976, 1982.

31. W. Hall, *Personal Communication*, Reyrolle Switchgear, Newcastle Upon Tyne, UK, 1993.

32. A.P.J. van Deursen, P.F.M. Gulickx and P.C.T. van der Laan, "*A current and voltage sensor combined in one unit*", 8th International Symposium on High Voltage Engineering, no. 56.02, pp. 463-466, Yokohama, Japan, 1993.

33. P. Osmokrovic, D. Petrokovic, O. Markovic, N. Kartalovic and D. Vukic, "*Measuring system for fast transients monitoring in gas-insulated substations*", European Transactions on Electrical Power Engineering, vol. 7, pp. 165-172, 1997.

34. Nitech, *Plus-1 The Portable Line Monitoring System That Lets You Read Between the Lines*, Advertising Literature, Nitec Inc., Fairfield, CT, USA, 1987.

35. J.M. Feldman, N. Reinhardt and K. Kuehn, "*A Hotstick instrument for the Estimation of the Potential of an HVDC conductor*", IEEE Transactions on Power Delivery, vol. 7, pp. 1533-1541, 1992.

36. H. Shimada, T. Furukawa and M. Ohchi, "*Electric field analysis for a static induction type of voltage sensor in three-phase power distribution systems*", IEE Proceedings: Generation, Transmission and Distribution, vol. 145, pp. 437-443, 1998.

37. Y. Yamagata, K. Tanaka, S. Nishiwaki, N. Takahashi, T. Kokumai, I. Miwa, T. Komukai and K. "*Imai, Suppression of VFT in 1100kV GIS by adopting resistor-fitted disconnector*", IEEE Transactions on Power Delivery, vol. 11, pp. 872-879, 1996.

38. B. Coetzee, *Power-frequency Electric and Magnetic fields of Power Lines*, Department of Electrical and Electronics Engineering, University of Stellenbosch, June, 2003

39. Institution of Electrical Engineers, *Report of a Working Group – The Possible Biological Effects of Low Frequency Electromagnetic Fields*, July 1991.

40. D.W. Deno and L.E. Zaffanella, *Transmission Line Reference Book- 345kV and above*, pp340 – 358. 2nd Edition, Electric Power Research Institution, Palo Alto, California, USA, 1982.

41. M. Abdel-Salam; H. Anis, A. El-Morshedy and R. Radwan, *High Voltage Engineering: Theory and Practice*, 2nd Edition, Revised and Expanded, Marcel Dekker Inc, New York, 2000.

42. R. Malewski, A. De Champlain, "*Digital Impulse Recorder. for HV Laboratories*" IEEE Transactions, vol. PAS-99, pp636-649, 1980

43. N. Hylten-Cavallius, *High Voltage Laboratory Planning*, E. Haefly & Co, Basel Switzerland, 1988.

44. K. Toda, M. Ikeda, T. Teranishi, T. Inoue, T. Yanari, *9th International Symposium on High Voltage Engineering (ISH'95)*, Graz, Austria, Paper 2296, 1995.

45. P. Högg, D. Fuchsle, A. Kara, *Pass for retrofitting, extending and constructing new high - voltage substations*, ABB Rev 2, pp. 12-20, 1998.

46. WINSOFT, *User Manual*, Windows software for HANDYSCOPE 3, TiePie Engineering.

47. N. Braithwaite and G. Weaver, *Electronic Materials: Inside Electronic Devices*, 2nd edition, Butterworth-Heinemann, 1998.

48. P.H. Pretorius, *Electric and magnetic fields (EMF): Potential effect on O/H line designs*, Electron, February 1996.

49. F.B. Siebrits, *Field implementation of a transient voltage measurement facility using current transformers,* MSc thesis, University of Stellenbosch, 2003.

50. J.W. Nilsson and S.A. Riedel, *Electric Circuits*, Sixth Edition, Prentice Hall, 2001.

51. D.E. Johnson, *Introduction to Filter Theory*, Electrical Engineering Series, Prentice Hall, 1976.

52. D.A. Neaman, *Electronic Circuit Analysis and Design, Second Edition*, McGraw-Hill, 2001.

53. T. Cipri, *Absolute-value comparator touts accuracy, size*, Engineering Expressions Consulting, page 124-126, Sunnyvale, CA, www.ednmag.com, 7 March 2002.

54. National Semiconductor Corporation, *LM119/LM219/LM319 High Speed Dual Comaparator*, www.national.com, August 2000.

55. P. Horowitz and W. Hill, *The Art of Electronics*, Second Edition, Cambridge Cambridge University Press, 1995.

56. Texas Instruments, *Data Sheet: SN74LS122, Retriggerable Monostable Multivibrators*, SDLS043-December 1983 – revised March 1988.

57. *Maps and compasses – Surveying*, Department of education and the Arts, http://education.qld.gov.au/curriculum/area/maths, 2006.

58. *Theodolites,* The department of Geomatics, www.sli.unimelb.edu.au/planesurvey, 1999.

59. *Theodolite*, Wikipedia, the free encyclopedia, http://en.wikipedia.org/wiki, 2006.

60. Southwire Company, *Sag and Tension of conductors*, Overhead Conductor Manual, 2005.

61. P. Nefzger, J.F. Nolasco, *Overhead power lines*, Springer, 2003.

62. *Appropriate Technology for electrical reticulation in developing countries*, General Manager Distribution and marketing, ESKOM.

63. *A vital link in Power Transmission*, Oman Cable Inventory, www.omancables.com, 2006.

64. *High Voltage Test Technique Part 3: Measuring Devices*, IEC-Publications 60-3, 1976.

65. *IEEE Standard Techniques for High Voltage Testing*, IEEE std. 4-1978, Clause 2.4.2.2, Tolerances, 1978.

66. *Electric Fields and Superposition*, Physics at Pennstate, http://class.phys.psu.edu, 4 August 2006.

67. Thomson W (Lord Kelvin), *Papers on Electrostatics and Magnetism*, Macmillan: London, 1882.

68. *Force, field and superposition,* Georgia Tech Physics Lab, www.physlab.gatech.edu, August 2006.

69. *Induced charge in a conductor,* Web Physics, http://webphysics.davidson.edu, August 2006.

70. *Induced charge*, Richard Fitzpatrick, Associate Professor of Physics, The University of Texas at Austin, http://farside.ph.utexas.edu, 4 August 2006.

71. *Electrostatics*, Encyclopedia Britannica, www.briatannica.com, August 2006

72. J.J. Grainger and W.D. Stevenson, *Power System Analysis*, McGraw-Hill, 1994.

73. *Boundary Element Method,* Integrated Engineering Software, www.integratedsoft.com, August 2006.

74. C.A. Harper, ed., *Handbook of Materials and Processes for Electronics*. McGraw-Hill, 1970.

75. Datasheet, *KEMET Capacitor*, www.kemet.com/page/celead, July 2006.

76. *Dissipation factor – Electrical*, About, http://composite.about.com, September 2006.

# Appendix A. Capacitance matrices of power systems

## A.1. Capacitance matrixes for three-phase power line configurations

Section 3.2.4 and section 3.2.5 compare the results between analytical and numerical (ELECTRO) methods for different line topologies. Table A.1 tabulates the capacitive phase matrixes for a three-phase line configuration without neutral conductors, developed by the analytical and numerical method. The discrepancies between the values obtained by the two methods are also given. Table A.2 tabulates the capacitive phase matrixes for a three-phase line configuration with one neutral conductor, developed by the analytical and numerical method. The discrepancies between the values obtained by the two methods are also given.

**Table A.1 : Capacitance phase matrix for a three-phase line without any neutral conductors.**

**Analytical results**

| | phase-A | phase-B | phase-C |
|---|---|---|---|
| **phase-A** | 8.60E-12 | -1.84E-12 | -8.00E-13 |
| **phase-B** | -1.84E-12 | 8.92E-12 | -1.84E-12 |
| **phase-C** | -8.00E-13 | -1.84E-12 | 8.60E-12 |

**ELECTRO results**

| | phase-A | phase-B | phase-C |
|---|---|---|---|
| **phase-A** | 8.58E-12 | -1.86E-12 | -8.19E-13 |
| **phase-B** | -1.86E-12 | 8.91E-12 | -1.86E-12 |
| **phase-C** | -8.19E-13 | -1.86E-12 | 8.58E-12 |

**Table A.2 : Capacitance phase matrix for a three-phase line with one neutral conductor.**

**Analytical results**

| | phase-A | phase-B | phase-C |
|---|---|---|---|
| **phase-A** | 8.787E-12 | -1.490E-12 | -6.150E-13 |
| **phase-B** | -1.490E-12 | 9.587E-12 | -1.490E-12 |
| **phase-C** | -6.150E-13 | -1.490E-12 | 8.787E-12 |

**ELECTRO Results**

| | phase-A | phase-B | phase-C |
|---|---|---|---|
| **phase-A** | 8.772E-12 | -1.500E-12 | -6.296E-13 |
| **phase-B** | -1.500E-12 | 9.580E-12 | -1.500E-12 |
| **phase-C** | -6.296E-13 | -1.500E-12 | 8.772E-12 |



Table A.3 tabulates the capacitance matrix of a flat, three-phase single-circuit line configuration with three single-element plate sensors located underneath the phase centres. The discrepancies between the various transfer function elements can be determined from this table as the transfer function elements are linearly proportional to the capacitive coupling components.

The symmetry of the topology shown in Figure 5.1 gives rise to the following simplifying relationships:

$$G_1 = G_{s1p1} = G_{s3p3} \quad (A.1)$$

$$G_2 = G_{s1p2} = G_{s3p2} \quad (A.2)$$

$$G_3 = G_{s1p3} = G_{s3p1} \quad (A.3)$$

$$G_4 = G_{s2p1} = G_{s2p3} \quad (A.4)$$

$$G_5 = G_{s2p2} \quad (A.5)$$

The discrepancy between transfer functions $G_1$ and $G_5$ is given as 10.98% and the discrepancy between transfer functions $G_2$ and $G_4$ is given as 0.9%.

Table A.4 tabulates the capacitive matrix of a flat, three-phase single-circuit line configuration with three three-element plate sensors located underneath the phase centres.

**Table A.3 : Capacitance matrix for a single-element plate sensor located underneath a three-phase transmission line.**

| | $v_{p1}$ | $v_{p2}$ | $v_{p3}$ | $v_{s1}$ | $v_{s2}$ | $v_{s3}$ |
|---|---|---|---|---|---|---|
| $v_{p1}$ | 1.05E-09 | -1.86E-10 | -8.96E-11 | -3.85E-11 | -2.74E-11 | -1.58E-11 |
| $v_{p2}$ | -1.86E-10 | 1.07E-09 | -1.86E-10 | -2.71E-11 | -3.43E-11 | -2.72E-11 |
| $v_{p3}$ | -8.96E-11 | -1.86E-10 | 1.05E-09 | -1.56E-11 | -2.74E-11 | -3.85E-11 |
| $v_{s1}$ | -3.85E-11 | -2.71E-11 | -1.55E-11 | 3.12E-09 | -2.98E-11 | -5.80E-12 |
| $v_{s2}$ | -2.73E-11 | -3.42E-11 | -2.73E-11 | -2.96E-11 | 3.12E-09 | -2.96E-11 |
| $v_{s3}$ | -1.55E-11 | -2.71E-11 | -3.85E-11 | -5.99E-12 | -2.97E-11 | 3.12E-09 |

**Table A.4: Capacitance matrix for a three-element parallel sensor underneath a flat, three-phase, single circuit line configuration.**

| | p1 | p2 | p3 | m1_bo | m1_boks | m1_onder | m2_bo | m2_boks | m2_onder | m3_bo | m3_boks | m3_onder |
|---|---|---|---|---|---|---|---|---|---|---|---|---|
| p1 | 1.05E-09 | -1.86E-10 | -9.01E-11 | -1.78E-11 | -4.20E-12 | -4.10E-12 | -1.28E-11 | -3.01E-12 | -2.94E-12 | -7.27E-12 | -1.72E-12 | -1.67E-12 |
| p2 | -1.86E-10 | 1.07E-09 | -1.86E-10 | -1.26E-11 | -2.97E-12 | -2.91E-12 | -1.59E-11 | -3.75E-12 | -3.66E-12 | -1.26E-11 | -2.99E-12 | -2.90E-12 |
| p3 | -9.01E-11 | -1.86E-10 | 1.05E-09 | -7.27E-12 | -1.71E-12 | -1.68E-12 | -1.28E-11 | -3.01E-12 | -2.94E-12 | -1.78E-11 | -4.22E-12 | -4.09E-12 |
| m1_bo | -1.78E-11 | -1.26E-11 | -7.27E-12 | 6.69E-07 | -6.67E-07 | -4.96E-10 | -6.38E-12 | -1.52E-12 | -1.49E-12 | -1.30E-12 | -2.88E-13 | -2.95E-13 |
| m1_boks | -4.19E-12 | -2.97E-12 | -1.71E-12 | -6.67E-07 | 1.34E-06 | -6.67E-07 | -1.49E-12 | -3.43E-13 | -3.03E-13 | -3.03E-13 | -6.43E-14 | -6.52E-14 |
| m1_onder | -4.09E-12 | -2.91E-12 | -1.67E-12 | -4.96E-10 | -6.67E-07 | 6.70E-07 | -1.54E-12 | -3.68E-13 | -4.00E-13 | -3.17E-13 | -6.37E-14 | -6.62E-14 |
| m2_bo | -1.28E-11 | -1.59E-11 | -1.28E-11 | -6.38E-12 | -1.50E-12 | -1.54E-12 | 6.69E-07 | -6.67E-07 | -4.96E-10 | -6.44E-12 | -1.44E-12 | -1.53E-12 |
| m2_boks | -3.00E-12 | -3.75E-12 | -3.01E-12 | -1.51E-12 | -3.46E-13 | -3.66E-13 | -6.67E-07 | 1.34E-06 | -6.67E-07 | -1.55E-12 | -3.23E-13 | -3.75E-13 |
| m2_onder | -2.94E-12 | -3.67E-12 | -2.94E-12 | -1.49E-12 | -3.22E-13 | -4.02E-13 | -4.96E-10 | -6.67E-07 | 6.70E-07 | -1.59E-12 | -2.30E-13 | -3.90E-13 |
| m3_bo | -7.27E-12 | -1.26E-11 | -1.78E-11 | -1.30E-12 | -3.07E-13 | -3.19E-13 | -6.44E-12 | -1.55E-12 | -1.59E-12 | 6.69E-07 | -6.67E-07 | -4.96E-10 |
| m3_boks | -1.71E-12 | -2.98E-12 | -4.22E-12 | -2.83E-13 | -6.31E-14 | -5.95E-14 | -1.43E-12 | -3.19E-13 | -2.16E-13 | -6.67E-07 | 1.34E-06 | -6.67E-07 |
| m3_onder | -1.68E-12 | -2.90E-12 | -4.10E-12 | -2.96E-13 | -6.81E-14 | -7.12E-14 | -1.53E-12 | -3.73E-13 | -3.93E-13 | -4.96E-10 | -6.67E-07 | 6.70E-07 |

## A.2. Power lines simulated in ELECTRO and EMFP for comparison with ESKOM measured electric field strengths.

The following data was obtained from Coetzee [38] and presents the power line data for the simulations done in EMFP and ELCTRO for comparison with ESKOM [48] measured values.

**Table A.5: Simulation data for an 88kV power line.**

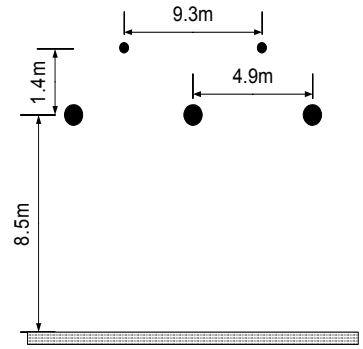


**Conductor data**

**Neutral conductors:**
1-Rabbit (ACSR)
Outside radius: 5.025mm
GMR : 3.646mm

**Phase Conductors:**
1-Wolf (ACSR)
Outside radius: 9.065mm
GMR : 6.69mm

**Voltage & Current**

**Voltage:**
Line-to-line voltage:
88kV

**Typical Current:**
Line current: 60A

**Other data**
Frequency: 50Hz
Right-of-way width: 15.5m

**Table A.6: Simulation data for a 132kV power line.**

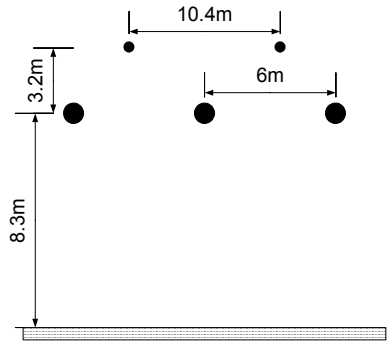


**Conductor data**

**Neutral conductors:**
1-Rabbit (ACSR)
Outside radius: 5.025mm
GMR : 3.646mm

**Phase Conductors:**
1-Bear (ACSR)
Outside radius: 11.725mm
GMR : 9.002mm

**Voltage & Current**

**Voltage:**
Line-to-line voltage: 132kV

**Typical Current:**
Line current: 150A

**Other data**
Frequency: 50Hz
Right-of-way width: 15.5m

**Table A.7: Simulation data for a 275kV power line.**

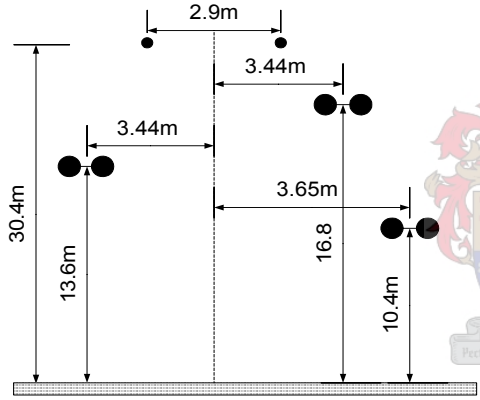


**Conductor data**

**Neutral conductors:**
1-Rabbit (ACSR)
Outside radius: 5.025mm
GMR : 3.646mm

**Phase Conductors:**
2_Zebra (ACSR)
Outside radius: 14.31mm
GMR : 11.049mm
Bundle Spacing: 380mm

**Voltage & Current**

**Voltage:**
Line-to-line voltage: 275kV

**Typical Current:**
Line current: 350A

**Other data**
Frequency: 50Hz
Right-of-way width: 23.5m

**Table A.8: Simulation data for a 400kV power line.**

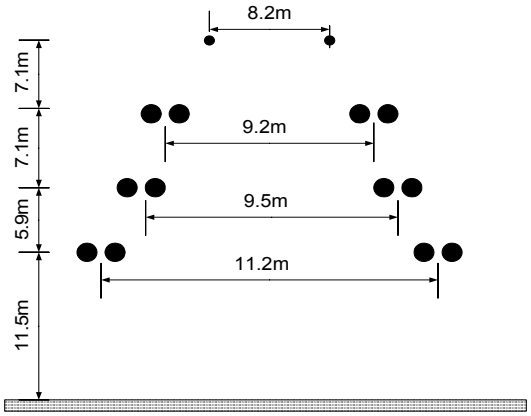


**Conductor data**

**Neutral conductors:**
1-Rabbit (ACSR)
Outside radius: 5.025mm
GMR : 3.646mm

**Phase Conductors:**
2-Dinossaur (ACSR)
Outside radius: 17.97mm
GMR : 10.959mm
Bundle Spacing: 380mm

**Voltage & Current**

**Voltage:**
Line-to-line voltage: 400kV

**Typical Current:**
Line current: 650A

**Other data**
Frequency: 50Hz
Right-of-way width: 23.5m

**Table A.9: Simulation data for a 765kV power line.**

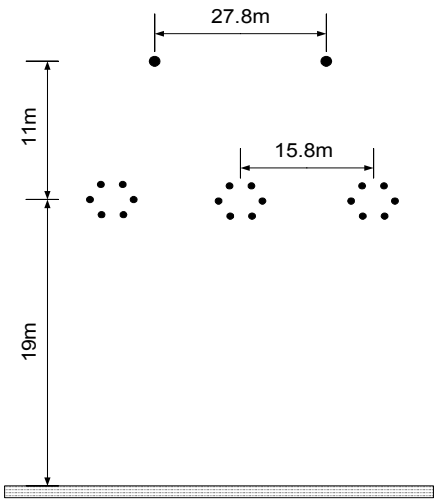


**Conductor data**

**Neutral conductors:**
1-Hare (ACSR)
Outside radius: 7.08mm
GMR : 5.137mm

**Phase Conductors:**
6-Zebra (ACSR)
Outside radius: 14.31mm
GMR : 11.049mm
Bundle Spacing: 320mm

**Voltage & Current**

**Voltage:**
Line-to-line voltage: 765kV

**Typical Current:**
Line current: 560A

**Other data**
Frequency: 50Hz
Right-of-way width: 40m

# Appendix B. Equivalent circuits models for three-phase capacitive sensor topologies

## B.1. Introduction

This appendix deduces Thévenin equivalent models for single-element, two-element and three-element parallel plate capacitive sensors in three-phase transmission line topologies.

## B.2. Single-element sensor

Figure B.1 shows the equivalent circuit for a single-element capacitive sensor in a three-phase transmission line topology.

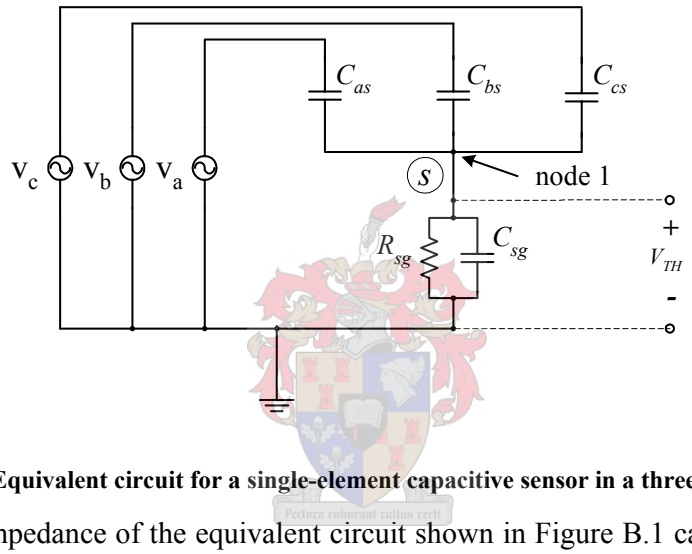


**Figure B.1: Equivalent circuit for a single-element capacitive sensor in a three-phase topology.**

The Thévenin impedance of the equivalent circuit shown in Figure B.1 can be determined by short-circuiting the phase voltage sources to yield the circuit shown in Figure B.2. This gives rise to the following relationship for Thévenin impedance:

$$Z_{TH} = \frac{R_{sg}}{sR_{sg}\left(C_{as}+C_{bs}+C_{cs}+C_{sg}\right)+1} \tag{B.1}$$

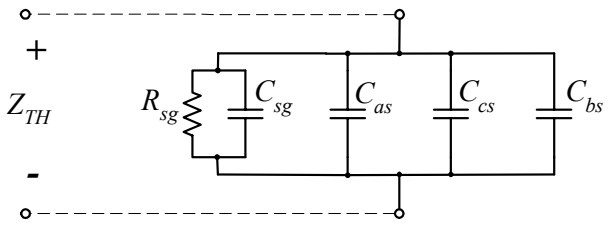


**Figure B.2: Equivalent circuit model for the single-element sensor for calculating the Thévenin impedance.**

Nodal analysis can be applied to deduce the Thévenin equivalent voltage for the equivalent circuit shown in Figure B.1. This yields

$$\frac{V_{TH}}{Z_a}+\frac{V_{TH}-V_{as}}{1/sC_{as}}+\frac{V_{TH}-V_{bs}}{1/sC_{bs}}+\frac{V_{TH}-V_{cs}}{1/sC_{cs}}=0 \tag{B.2}$$

where

$$Z_a=\frac{R_{sg}}{sR_{sg}C_{sg}+1} \tag{B.3}$$

Equations (B.2) and (B.3) give rise to the following expressions for the Thévenin equivalent voltage $V_{TH}$

$$\begin{aligned} V_{TH} &= \frac{sR_{sg}\left(V_aC_{as}+V_bC_{bs}+V_cC_{cs}\right)}{sR_{sg}\left(C_{as}+C_{bs}+C_{cs}+C_{sg}\right)+1} \\ &= Z_{TH}\left(V_aC_{as}+V_bC_{bs}+V_cC_{cs}\right) \end{aligned} \tag{B.4}$$

## B.3. Two-element parallel plate sensor

Figure B.3 shows the high frequency equivalent circuit diagram for a two-element capacitive sensor in a three-phase transmission line topology.

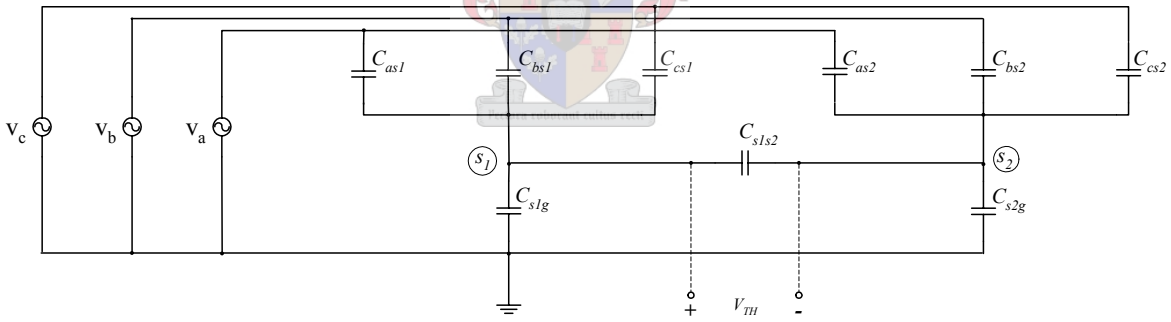


**Figure B.3: High frequency equivalent circuit for a two-element capacitive sensor in a three-phase topology.**

The Thévenin impedance of the equivalent circuit shown in Figure B.3 can be determined by short-circuiting the phase voltage sources to yield the circuit shown in Figure B.4.

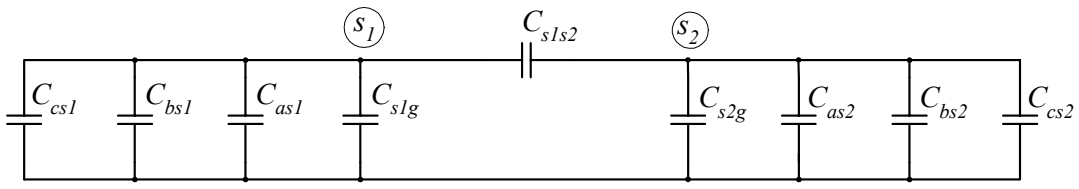


**Figure B.4: Equivalent circuit of the two-element sensor for calculating the Thévenin impedance.**

Nodal analysis can be applied to deduce the Thévenin equivalent voltage for the equivalent circuit shown in Figure B.3. Figure B.3 gives rise to the following voltage equations for nodes 1 and 2 respectively:

$$0 = sv_1 C_{s1g} + s(v_1 - v_c) C_{cs1} + s(v_1 - v_b) C_{bs1} + s(v_1 - v_a) C_{as1} + s(v_1 - v_2) C_{s1s2} \tag{B.5}$$

$$0 = sv_2 C_{s2g} + s(v_2 - v_c) C_{cs2} + s(v_2 - v_b) C_{bs2} + s(v_2 - v_a) C_{as2} + s(v_2 - v_1) C_{s1s2} \tag{B.6}$$

Solving equations (B.5) and (B.6) for $v_1$ and $v_2$ yields

$$v_1 = \frac{v_a C_{as1} + v_b C_{bs1} + v_c C_{cs1} + v_2 C_{s1s2}}{C_{as1} + C_{bs1} + C_{cs1} + C_{s1g} + C_{s1s2}} \tag{B.7}$$

and

$$v_2 = \frac{v_a C_{as2} + v_b C_{bs2} + v_c C_{cs2} + v_1 C_{s1s2}}{C_{as2} + C_{bs2} + C_{cs2} + C_{s2g} + C_{s1s2}} \quad . \tag{B.8}$$

The Thévenin equivalent voltage is the potential difference between $v_1$ and $v_2$ and is given by the relationships

$$V_{TH} = \frac{C_{s2}\left(v_a C_{as1} + v_b C_{bs1} + v_c C_{cs1}\right) - C_{s2}\left(v_a C_{as2} + v_b C_{bs2} + v_c C_{cs2}\right)}{\left(C_{s1} + C_{s2}\right) C_{TH}} \tag{B.9}$$

and

$$Z_{TH} = \frac{1}{sC_{TH}} \tag{B.10}$$

where

$$C_{s1} = C_{as1} + C_{bs1} + C_{cs1} + C_{s1g}$$

$$C_{s2} = C_{as2} + C_{bs2} + C_{cs2} + C_{s2g} \quad .$$

$$C_{TH} = C_{s1s2} + \frac{C_{s1} C_{s2}}{C_{s1} + C_{s2}}$$

## B.4. Three-element capacitive sensor

### B.4.1. General equivalent circuit

Figure B.5 shows the equivalent circuit diagram for a three-element capacitive sensor in a three-phase transmission line topology. The circuit parameters are shown as impedances, typically consisting of parallel resistive and capacitive elements in order to simplify the expressions for the associated Thévenin equivalent model.

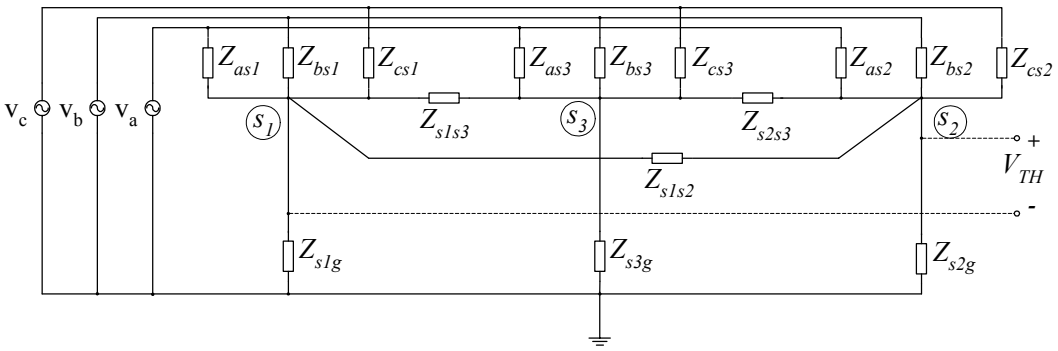


**Figure B.5: Equivalent circuit for a three-element capacitive sensor in a three-phase topology.**

The Thévenin impedance of the equivalent circuit shown in Figure B.5 can be determined by short-circuiting the phase voltage sources to yield the circuit shown in Figure B.6. This circuit can be reduced by combining some of the impedances to yield the simplified equivalent circuit shown in Figure B.7, where

$$Z_a = Z_{as1} \| Z_{bs1} \| Z_{cs1} \| Z_{s1g} = \frac{1}{\frac{1}{Z_{as1}} + \frac{1}{Z_{bs1}} + \frac{1}{Z_{cs1}} + \frac{1}{Z_{s1g}}}, \quad \text{(B.11)}$$

$$Z_b = Z_{as2} \| Z_{bs2} \| Z_{cs2} \| Z_{s2g} = \frac{1}{\frac{1}{Z_{as2}} + \frac{1}{Z_{bs2}} + \frac{1}{Z_{cs2}} + \frac{1}{Z_{s2g}}} \quad \text{(B.12)}$$

and

$$Z_c = Z_{as3} \| Z_{bs3} \| Z_{cs3} \| Z_{s3g} = \frac{1}{\frac{1}{Z_{as3}} + \frac{1}{Z_{bs3}} + \frac{1}{Z_{cs3}} + \frac{1}{Z_{s3g}}}. \quad \text{(B.13)}$$

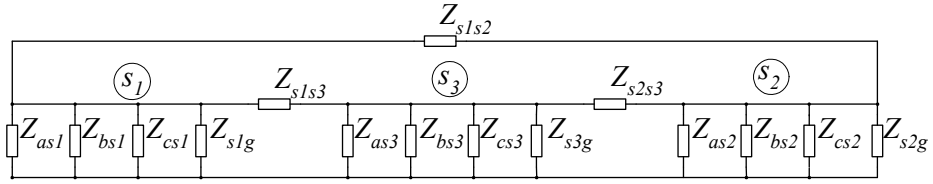


**Figure B.6: Equivalent circuit for the Thévenin impedance of a three-element capacitive sensor in a three-phase topology.**

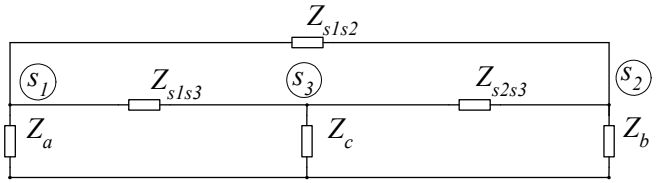


**Figure B.7: Reduced Equivalent circuit for the Thévenin impedance of a three-element capacitive sensor in a three-phase topology.**

The delta configuration consisting of $Z_a$, $Z_{s1s3}$ and $Z_c$ in Figure B.7 can be transformed to an equivalent wye configuration represented in Figure B.8 by $Z_1$, $Z_2$ and $Z_3$, where

$$Z_1 = \frac{Z_{s1s3} Z_c}{Z_a + Z_c + Z_{s1s3}} \quad , \tag{B.14}$$

$$Z_2 = \frac{Z_a Z_c}{Z_a + Z_c + Z_{s1s3}} \tag{B.15}$$

and

$$Z_3 = \frac{Z_{s1s3} Z_a}{Z_a + Z_c + Z_{s1s3}} \quad . \tag{B.16}$$

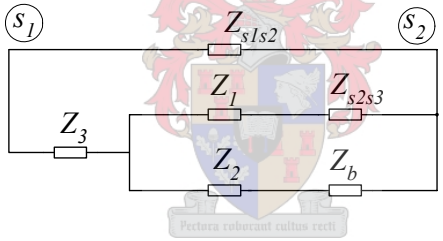


**Figure B.8: Circuit model if lower Δ impedance is replaced by its equivalent Y impedance.**

The Thévenin impedance is then given by the relationship

$$\begin{aligned} Z_{TH} &= Z_t \,||\, Z_{s1s2} \\ &= \frac{Z_{s1s2}\left[ Z_f Z_g + Z_3 \left( Z_f + Z_g \right) \right]}{\left( Z_{s1s2} + Z_3 \right)\left( Z_f + Z_g \right) + Z_f Z_g} \end{aligned} \tag{B.17}$$

where

$$\begin{aligned} Z_t &= Z_f \,||\, Z_g + Z_3 \\ &= \frac{Z_f Z_g}{Z_f + Z_g} + Z_3 \end{aligned} \quad . \tag{B.18}$$

$$\begin{aligned} Z_f &= Z_1 + Z_{s2s3} \\ Z_g &= Z_2 + Z_b \end{aligned} \quad . \tag{B.19}$$

The Thévenin voltage of the equivalent circuit shown in Figure B.5 can be obtained by nodal analysis. The node voltage equations for the three sensor element nodes are given by the relationships

$$\frac{V_1-V_a}{Z_{as1}}+\frac{V_1-V_b}{Z_{bs1}}+\frac{V_1-V_c}{Z_{cs1}}+\frac{V_1-V_3}{Z_{s1s3}}+\frac{V_1-V_2}{Z_{s1s2}}+\frac{V_1}{Z_{s1g}}=0 \quad , \tag{B.20}$$

$$\frac{V_2-V_a}{Z_{as2}}+\frac{V_2-V_b}{Z_{bs2}}+\frac{V_2-V_c}{Z_{cs2}}+\frac{V_2-V_3}{Z_{s2s3}}+\frac{V_2-V_1}{Z_{s1s2}}+\frac{V_2}{Z_{s2g}}=0 \tag{B.21}$$

and

$$\frac{V_3-V_a}{Z_{as3}}+\frac{V_3-V_b}{Z_{bs3}}+\frac{V_3-V_c}{Z_{cs3}}+\frac{V_3-V_1}{Z_{s1s3}}+\frac{V_3-V_2}{Z_{s2s3}}+\frac{V_3}{Z_{s3g}}=0 \quad . \tag{B.22}$$

Equations (B.20) to (B.22) can be solved for $v_1$ and $v_2$, from which the Thévenin voltage is obtained as $v_1$-$v_2$, yielding

$$V_{TH}=V_zZ_{s1s3}-\left(\frac{Z_{s1s3}}{Z_{s2s3}}+1\right)\left(\frac{1}{Z_B}\right)\left[\frac{V_z}{Z_{s1s2}}-\frac{V_y}{Z_{s1s3}}+Z_C\left(\frac{G_2-V_yZ_a}{G_1}\right)\right] + \frac{Z_3Z_{s1s3}\left(G_2+V_yZ_a\right)}{G_1} \tag{B.23}$$

where

$$G_2=V_xZ_b+V_z\left(Z_1Z_2-\frac{1}{Z_{s1s2}^2}\right) \quad . \tag{B.24}$$

Then

$$V_{TH}=V_zZ_{s1s3} -\left(\frac{Z_{s1s3}}{Z_{s2s3}}+1\right)\left(\frac{1}{Z_B}\right)\left[\frac{V_z}{Z_{s1s2}}-\frac{V_y}{Z_{s1s3}}+Z_C\left(\frac{V_xZ_b+V_z\left(Z_1Z_2-\frac{1}{Z_{s1s2}^2}\right)-V_yZ_a}{G_1}\right)\right] + \frac{Z_3Z_{s1s3}\left(V_xZ_b+V_z\left(Z_1Z_2-\frac{1}{Z_{s1s2}^2}\right)+V_yZ_a\right)}{G_1} \tag{B.25}$$

where

$$G_1=\frac{Z_a}{Z_{s2s3}}+\frac{Z_b}{Z_{s1s3}}+\frac{Z_3}{Z_{s1s2}^2}-Z_1Z_2Z_3 \quad , \tag{B.26}$$

$$V_x = -\frac{V_a}{Z_{as1}} - \frac{V_b}{Z_{bs1}} - \frac{V_c}{Z_{cs1}}$$
$$V_y = -\frac{V_a}{Z_{as2}} - \frac{V_b}{Z_{bs2}} - \frac{V_c}{Z_{cs2}} \quad , \tag{B.27}$$
$$V_z = -\frac{V_a}{Z_{as3}} - \frac{V_b}{Z_{bs3}} - \frac{V_c}{Z_{cs3}}$$

$$Z_a = \frac{Z_1}{Z_{s2s3}} + \frac{1}{Z_{s1s2}Z_{s1s3}}$$
$$Z_b = \frac{Z_2}{Z_{s1s3}} + \frac{1}{Z_{s1s2}Z_{s2s3}} \tag{B.28}$$
$$Z_c = \frac{Z_1}{Z_{s1s2}} + \frac{1}{Z_{s1s3}Z_{s2s3}}$$

and

$$Z_1 = \frac{1}{Z_{as1}} + \frac{1}{Z_{bs1}} + \frac{1}{Z_{cs1}} + \frac{1}{Z_{s1s2}} + \frac{1}{Z_{s1s3}} + \frac{1}{Z_{s1g}}$$
$$Z_2 = \frac{1}{Z_{as2}} + \frac{1}{Z_{bs2}} + \frac{1}{Z_{cs2}} + \frac{1}{Z_{s1s2}} + \frac{1}{Z_{s2s3}} + \frac{1}{Z_{s2g}} \quad . \tag{B.29}$$
$$Z_3 = \frac{1}{Z_{as3}} + \frac{1}{Z_{bs3}} + \frac{1}{Z_{cs3}} + \frac{1}{Z_{s1s3}} + \frac{1}{Z_{s2s3}} + \frac{1}{Z_{s3g}}$$

### B.4.2. Full equivalent circuit

Figure B.5 shows the high frequency equivalent circuit for the three-element sensor in a three-phase configuration. The Thévenin voltage and impedance of this circuit can be derived from equations (B.11) to (B.29) by substituting the impedances with appropriate shunt combinations of capacitances and resistances.

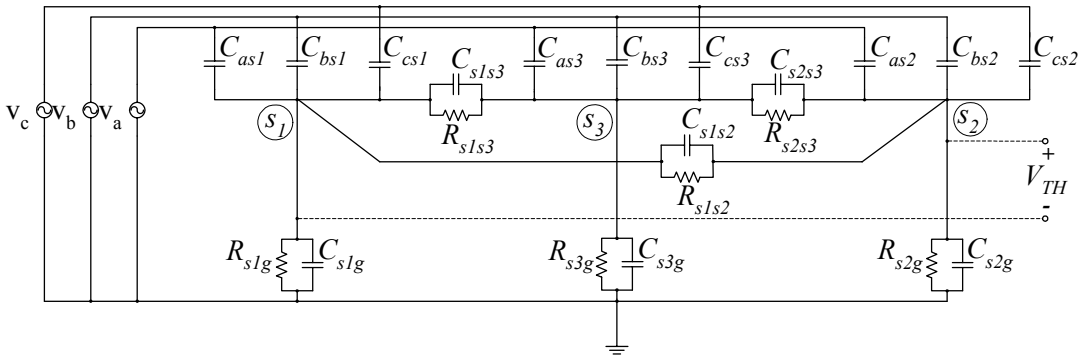


**Figure B.9: Equivalent circuit model if the shunt loss terms are included for a three-element parallel plate sensor underneath a three-phase transmission line.**

The Thévenin impedance is evaluated in Mathematica by using the following program:

```
Zas1 = 1 / (s * Cas1)
Zbs1 = 1 / (s * Cbs1)
Zcs1 = 1 / (s * Ccs1)
Zs1g = Rs1g / (s * Rs1g * Cs1g + 1)

Zas2 = 1 / (s * Cas2)
Zbs2 = 1 / (s * Cbs2)
Zcs2 = 1 / (s * Ccs2)
Zs2g = Rs2g / (s * Rs2g * Cs2g + 1)

Zas3 = 1 / (s * Cas3)
Zbs3 = 1 / (s * Cbs3)
Zcs3 = 1 / (s * Ccs3)
Zs3g = Rs3g / (s * Rs3g * Cs3g + 1)

Zs1s2 = Rs1s2 / (s * Rs1s2 * Cs1s2 + 1)
Zs1s3 = Rs1s3 / (s * Rs1s3 * Cs1s3 + 1)
Zs2s3 = Rs2s3 / (s * Rs2s3 * Cs2s3 + 1)

Za = 1 / (1 / Zas1 + 1 / Zbs1 + 1 / Zcs1 + 1 / Zs1g)
Zb = 1 / (1 / Zas2 + 1 / Zbs2 + 1 / Zcs2 + 1 / Zs2g)
Zc = 1 / (1 / Zas3 + 1 / Zbs3 + 1 / Zcs3 + 1 / Zs3g)

Z1 = (Zs1s3 * Zc) / (Za + Zc + Zs1s3)
Z2 = (Za * Zc) / (Za + Zc + Zs1s3)
Z3 = (Zs1s3 * Za) / (Za + Zc + Zs1s3)

Zf = Z1 + Zs2s3
Zg = Z2 + Zb


Zt = (Zf * Zg) / (Zf + Zg) + Z3
Zth = (Zt * Zs1s2) / (Zt + Zs1s2)
```

The Thévenin impedance is then presented by the relationship

$$\left(Rs1s2\left(Rs1s3\Big/\left((1+Cs1s3\,Rs1s3\,s)\left(Cas1\,s+Cbs1\,s+Ccs1\,s+\frac{1+Cs1g\,Rs1g\,s}{Rs1g}\right)\right.\right.\right.$$
$$\left.\left.\left.\left(\frac{Rs1s3}{1+Cs1s3\,Rs1s3\,s}+\frac{1}{Cas1\,s+Cbs1\,s+Ccs1\,s+\frac{1+Cs1g\,Rs1g\,s}{Rs1g}}+\frac{1}{Cas3\,s+Cbs3\,s+Ccs3\,s+\frac{1+Cs3g\,Rs3g\,s}{Rs3g}}\right)\right)\right)+$$
$$\left(\left(\left(\frac{Rs2s3}{1+Cs2s3\,Rs2s3\,s}+Rs1s3\Big/\left((1+Cs1s3\,Rs1s3\,s)\left(Cas3\,s+Cbs3\,s+Ccs3\,s+\frac{1+Cs3g\,Rs3g\,s}{Rs3g}\right)\right.\right.\right.\right.$$
$$\left.\left.\left.\left.\left(\frac{Rs1s3}{1+Cs1s3\,Rs1s3\,s}+\frac{1}{Cas1\,s+Cbs1\,s+Ccs1\,s+\frac{1+Cs1g\,Rs1g\,s}{Rs1g}}+\frac{1}{Cas3\,s+Cbs3\,s+Ccs3\,s+\frac{1+Cs3g\,Rs3g\,s}{Rs3g}}\right)\right)\right)\right)$$
$$\left(\frac{1}{Cas2\,s+Cbs2\,s+Ccs2\,s+\frac{1+Cs2g\,Rs2g\,s}{Rs2g}}+1\Big/\left(\left(Cas1\,s+Cbs1\,s+Ccs1\,s+\frac{1+Cs1g\,Rs1g\,s}{Rs1g}\right)\left(Cas3\,s+Cbs3\,s+Ccs3\,s+\right.\right.\right.$$
$$\left.\left.\left.\frac{1+Cs3g\,Rs3g\,s}{Rs3g}\right)\left(\frac{Rs1s3}{1+Cs1s3\,Rs1s3\,s}+\frac{1}{Cas1\,s+Cbs1\,s+Ccs1\,s+\frac{1+Cs1g\,Rs1g\,s}{Rs1g}}+\frac{1}{Cas3\,s+Cbs3\,s+Ccs3\,s+\frac{1+Cs3g\,Rs3g\,s}{Rs3g}}\right)\right)\right)\Big/$$
$$\left(\frac{Rs2s3}{1+Cs2s3\,Rs2s3\,s}+\frac{1}{Cas2\,s+Cbs2\,s+Ccs2\,s+\frac{1+Cs2g\,Rs2g\,s}{Rs2g}}+Rs1s3\Big/\left((1+Cs1s3\,Rs1s3\,s)\left(Cas3\,s+Cbs3\,s+Ccs3\,s+\frac{1+Cs3g\,Rs3g\,s}{Rs3g}\right)\right.\right.$$
$$\left.\left.\left(\frac{Rs1s3}{1+Cs1s3\,Rs1s3\,s}+\frac{1}{Cas1\,s+Cbs1\,s+Ccs1\,s+\frac{1+Cs1g\,Rs1g\,s}{Rs1g}}+\frac{1}{Cas3\,s+Cbs3\,s+Ccs3\,s+\frac{1+Cs3g\,Rs3g\,s}{Rs3g}}\right)\right)+$$
$$1\Big/\left(\left(Cas1\,s+Cbs1\,s+Ccs1\,s+\frac{1+Cs1g\,Rs1g\,s}{Rs1g}\right)\left(Cas3\,s+Cbs3\,s+Ccs3\,s+\frac{1+Cs3g\,Rs3g\,s}{Rs3g}\right)\right.$$
$$\left.\left.\left(\frac{Rs1s3}{1+Cs1s3\,Rs1s3\,s}+\frac{1}{Cas1\,s+Cbs1\,s+Ccs1\,s+\frac{1+Cs1g\,Rs1g\,s}{Rs1g}}+\frac{1}{Cas3\,s+Cbs3\,s+Ccs3\,s+\frac{1+Cs3g\,Rs3g\,s}{Rs3g}}\right)\right)\right)\Big/$$
$$\left((1+Cs1s2\,Rs1s2\,s)\left(\frac{Rs1s2}{1+Cs1s2\,Rs1s2\,s}+Rs1s3\Big/\left((1+Cs1s3\,Rs1s3\,s)\left(Cas1\,s+Cbs1\,s+Ccs1\,s+\frac{1+Cs1g\,Rs1g\,s}{Rs1g}\right)\right.\right.\right.$$
$$\left.\left.\left.\left(\frac{Rs1s3}{1+Cs1s3\,Rs1s3\,s}+\frac{1}{Cas1\,s+Cbs1\,s+Ccs1\,s+\frac{1+Cs1g\,Rs1g\,s}{Rs1g}}+\frac{1}{Cas3\,s+Cbs3\,s+Ccs3\,s+\frac{1+Cs3g\,Rs3g\,s}{Rs3g}}\right)\right)\right)+$$
$$\left(\left(\left(\frac{Rs2s3}{1+Cs2s3\,Rs2s3\,s}+Rs1s3\Big/\left((1+Cs1s3\,Rs1s3\,s)\left(Cas3\,s+Cbs3\,s+Ccs3\,s+\frac{1+Cs3g\,Rs3g\,s}{Rs3g}\right)\right.\right.\right.\right.$$
$$\left.\left.\left.\left.\left(\frac{Rs1s3}{1+Cs1s3\,Rs1s3\,s}+\frac{1}{Cas1\,s+Cbs1\,s+Ccs1\,s+\frac{1+Cs1g\,Rs1g\,s}{Rs1g}}+\frac{1}{Cas3\,s+Cbs3\,s+Ccs3\,s+\frac{1+Cs3g\,Rs3g\,s}{Rs3g}}\right)\right)\right)\right)$$
$$\left(\frac{1}{Cas2\,s+Cbs2\,s+Ccs2\,s+\frac{1+Cs2g\,Rs2g\,s}{Rs2g}}+1\Big/\left(\left(Cas1\,s+Cbs1\,s+Ccs1\,s+\frac{1+Cs1g\,Rs1g\,s}{Rs1g}\right)\left(Cas3\,s+Cbs3\,s+Ccs3\,s+\right.\right.\right.$$
$$\left.\left.\left.\frac{1+Cs3g\,Rs3g\,s}{Rs3g}\right)\left(\frac{Rs1s3}{1+Cs1s3\,Rs1s3\,s}+\frac{1}{Cas1\,s+Cbs1\,s+Ccs1\,s+\frac{1+Cs1g\,Rs1g\,s}{Rs1g}}+\frac{1}{Cas3\,s+Cbs3\,s+Ccs3\,s+\frac{1+Cs3g\,Rs3g\,s}{Rs3g}}\right)\right)\right)\Big/$$
$$\left(\frac{Rs2s3}{1+Cs2s3\,Rs2s3\,s}+\frac{1}{Cas2\,s+Cbs2\,s+Ccs2\,s+\frac{1+Cs2g\,Rs2g\,s}{Rs2g}}+Rs1s3\Big/\left((1+Cs1s3\,Rs1s3\,s)\left(Cas3\,s+Cbs3\,s+Ccs3\,s+\frac{1+Cs3g\,Rs3g\,s}{Rs3g}\right)\right.\right.$$
$$\left.\left.\left(\frac{Rs1s3}{1+Cs1s3\,Rs1s3\,s}+\frac{1}{Cas1\,s+Cbs1\,s+Ccs1\,s+\frac{1+Cs1g\,Rs1g\,s}{Rs1g}}+\frac{1}{Cas3\,s+Cbs3\,s+Ccs3\,s+\frac{1+Cs3g\,Rs3g\,s}{Rs3g}}\right)\right)+$$
$$1\Big/\left(\left(Cas1\,s+Cbs1\,s+Ccs1\,s+\frac{1+Cs1g\,Rs1g\,s}{Rs1g}\right)\left(Cas3\,s+Cbs3\,s+Ccs3\,s+\frac{1+Cs3g\,Rs3g\,s}{Rs3g}\right)\right.$$
$$\left.\left.\left(\frac{Rs1s3}{1+Cs1s3\,Rs1s3\,s}+\frac{1}{Cas1\,s+Cbs1\,s+Ccs1\,s+\frac{1+Cs1g\,Rs1g\,s}{Rs1g}}+\frac{1}{Cas3\,s+Cbs3\,s+Ccs3\,s+\frac{1+Cs3g\,Rs3g\,s}{Rs3g}}\right)\right)\right)$$

As with the evaluation of the Thévenin impedance, the Thévenin equivalent voltage of the full circuit model can be derived by implementing the impedances of equation 6.37 into equations (B.25) to (B.29). The Mathimatica code used to solve the Thévenin voltage are:

```
Zas1 = 1 / (s * Cas1)
Zbs1 = 1 / (s * Cbs1)
Zcs1 = 1 / (s * Ccs1)
Zs1g = Rs1g / (s * Rs1g * Cs1g + 1)

Zas2 = 1 / (s * Cas2)
Zbs2 = 1 / (s * Cbs2)
Zcs2 = 1 / (s * Ccs2)
Zs2g = Rs2g / (s * Rs2g * Cs2g + 1)

Zas3 = 1 / (s * Cas3)
Zbs3 = 1 / (s * Cbs3)
Zcs3 = 1 / (s * Ccs3)
Zs3g = Rs3g / (s * Rs3g * Cs3g + 1)

Zs1s2 = Rs1s2 / (s * Rs1s2 * Cs1s2 + 1)
Zs1s3 = Rs1s3 / (s * Rs1s3 * Cs1s3 + 1)
Zs2s3 = Rs2s3 / (s * Rs2s3 * Cs2s3 + 1)

Z1 = 1 / Zas1 + 1 / Zbs1 + 1 / Zcs1 + 1 / Zs1s2 + 1 / Zs1s3 + 1 / Zs1g
Z2 = 1 / Zas2 + 1 / Zbs2 + 1 / Zcs2 + 1 / Zs1s2 + 1 / Zs2s3 + 1 / Zs2g
Z3 = 1 / Zas3 + 1 / Zbs3 + 1 / Zcs3 + 1 / Zs1s3 + 1 / Zs2s3 + 1 / Zs3g

Za = (Z1 / Zs2s3) + 1 / (Zs1s2 * Zs1s3)
Zb = (Z2 / Zs1s3) + 1 / (Zs1s2 * Zs1s3)
Zc = (Z3 / Zs1s2) + 1 / (Zs1s3 * Zs2s3)

Vx = -va / Zas1 - vb / Zbs1 - vc / Zcs1
Vy = -va / Zas2 - vb / Zbs2 - vc / Zcs2
Vz = -va / Zas3 - vb / Zbs3 - vc / Zcs3

G1 = Za / Zs2s3 + Zb / Zs1s3 + Z3 / (Zs1s2 * Zs1s2) - Z1 * Z2 * Z3
G2 = Vx * Zb + Vz * (Z1 * Z2 - 1 / (Zs1s2 * Zs1s2))

Vth = Vz * Zs1s3 - (Zs1s3 / Zs2s3 + 1) * (1 / Zb) * (Vz / Zs1s2 - Vy / Zs1s3 + Zc * (G2 - Vy * Za) / G1) +
   Z3 * Zs1s3 * (G2 + Vy * Za) / G1
```

The results obtained by this evaluation are not illustrated as the equation is too excessive.

### B.4.3. High frequency equivalent circuit

Figure B.1 shows the high frequency equivalent circuit for a three-element sensor in a ). The equivalent Thévenin voltage and impedance of the ideal circuit are evaluated by implementing the capacitances into equations (B.11) to (B.29). Equation 6.38 presents the impedances that are used in these equations.

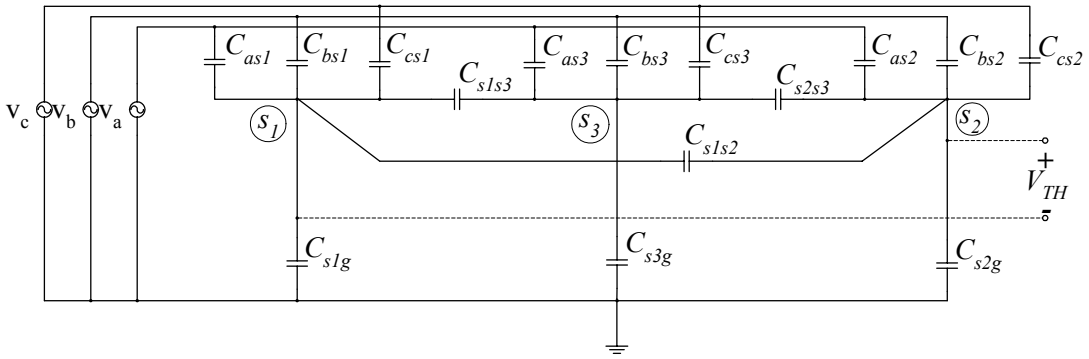


**Figure B.10: Equivalent circuit model for the three-element plate sensor, if the node-voltage method is used.**

The Mathematica codec used to solve the Thévenin impedance and voltages are the same as that for the ideal circuit, except that the impedances are the same as the impedances illustrated in equation 5.38. The Thévenin impedance is now given by the relationship

$$
\left(1 \Big/ \left(Cs1s3\,s\,(Cas1\,s + Cbs1\,s + Ccs1\,s + Cs1g\,s)\right.\right.
$$
$$
\left.\left.\left(\frac{1}{Cs1s3\,s} + \frac{1}{Cas1\,s + Cbs1\,s + Ccs1\,s + Cs1g\,s} + \frac{1}{Cas3\,s + Cbs3\,s + Ccs3\,s + Cs3g\,s}\right)\right) +\right.
$$
$$
\left(\left(\frac{1}{Cs2s3\,s} + 1 \Big/ \left(Cs1s3\,s\,(Cas3\,s + Cbs3\,s + Ccs3\,s + Cs3g\,s)\right.\right.\right.
$$
$$
\left.\left.\left.\left(\frac{1}{Cs1s3\,s} + \frac{1}{Cas1\,s + Cbs1\,s + Ccs1\,s + Cs1g\,s} + \frac{1}{Cas3\,s + Cbs3\,s + Ccs3\,s + Cs3g\,s}\right)\right)\right)\right.
$$
$$
\left.\left(\frac{1}{Cas2\,s + Cbs2\,s + Ccs2\,s + Cs2g\,s} + 1 \Big/ \left((Cas1\,s + Cbs1\,s + Ccs1\,s + Cs1g\,s)\right.\right.\right.
$$
$$
(Cas3\,s + Cbs3\,s + Ccs3\,s + Cs3g\,s)
$$
$$
\left.\left.\left.\left.\left(\frac{1}{Cs1s3\,s} + \frac{1}{Cas1\,s + Cbs1\,s + Ccs1\,s + Cs1g\,s} + \frac{1}{Cas3\,s + Cbs3\,s + Ccs3\,s + Cs3g\,s}\right)\right)\right)\right) \Big/
$$
$$
\left(\frac{1}{Cs2s3\,s} + \frac{1}{Cas2\,s + Cbs2\,s + Ccs2\,s + Cs2g\,s} + 1 \Big/ \left(Cs1s3\,s\,(Cas3\,s + Cbs3\,s + Ccs3\,s + Cs3g\,s)\right.\right.
$$
$$
\left.\left.\left(\frac{1}{Cs1s3\,s} + \frac{1}{Cas1\,s + Cbs1\,s + Ccs1\,s + Cs1g\,s} + \frac{1}{Cas3\,s + Cbs3\,s + Ccs3\,s + Cs3g\,s}\right)\right) +\right.
$$
$$
1 \Big/ \left((Cas1\,s + Cbs1\,s + Ccs1\,s + Cs1g\,s)\,(Cas3\,s + Cbs3\,s + Ccs3\,s + Cs3g\,s)\right.
$$
$$
\left.\left.\left.\left(\frac{1}{Cs1s3\,s} + \frac{1}{Cas1\,s + Cbs1\,s + Ccs1\,s + Cs1g\,s} + \frac{1}{Cas3\,s + Cbs3\,s + Ccs3\,s + Cs3g\,s}\right)\right)\right)\right) \Big/
$$
$$
\left(Cs1s2\,s\left(\frac{1}{Cs1s2\,s} + 1 \Big/ \left(Cs1s3\,s\,(Cas1\,s + Cbs1\,s + Ccs1\,s + Cs1g\,s)\right.\right.\right.
$$
$$
\left.\left.\left.\left(\frac{1}{Cs1s3\,s} + \frac{1}{Cas1\,s + Cbs1\,s + Ccs1\,s + Cs1g\,s} + \frac{1}{Cas3\,s + Cbs3\,s + Ccs3\,s + Cs3g\,s}\right)\right) +\right.\right.
$$
$$
\left.\left.\left(\left(\frac{1}{Cs2s3\,s} + 1 \Big/ \left(Cs1s3\,s\,(Cas3\,s + Cbs3\,s + Ccs3\,s + Cs3g\,s)\right.\right.\right.\right.
$$
$$
\left.\left.\left.\left.\left(\frac{1}{Cs1s3\,s} + \frac{1}{Cas1\,s + Cbs1\,s + Ccs1\,s + Cs1g\,s} + \frac{1}{Cas3\,s + Cbs3\,s + Ccs3\,s + Cs3g\,s}\right)\right)\right)\right.\right.
$$
$$
\left.\left.\left(\frac{1}{Cas2\,s + Cbs2\,s + Ccs2\,s + Cs2g\,s} + 1 \Big/ \left((Cas1\,s + Cbs1\,s + Ccs1\,s + Cs1g\,s)\right.\right.\right.\right.
$$
$$
(Cas3\,s + Cbs3\,s + Ccs3\,s + Cs3g\,s)
$$
$$
\left.\left.\left.\left.\left.\left(\frac{1}{Cs1s3\,s} + \frac{1}{Cas1\,s + Cbs1\,s + Ccs1\,s + Cs1g\,s} + \frac{1}{Cas3\,s + Cbs3\,s + Ccs3\,s + Cs3g\,s}\right)\right)\right)\right)\right) \Big/
$$
$$
\left(\frac{1}{Cs2s3\,s} + \frac{1}{Cas2\,s + Cbs2\,s + Ccs2\,s + Cs2g\,s} + 1 \Big/ \left(Cs1s3\,s\,(Cas3\,s + Cbs3\,s + Ccs3\,s + Cs3g\,s)\right.\right.
$$
$$
\left.\left.\left(\frac{1}{Cs1s3\,s} + \frac{1}{Cas1\,s + Cbs1\,s + Ccs1\,s + Cs1g\,s} + \frac{1}{Cas3\,s + Cbs3\,s + Ccs3\,s + Cs3g\,s}\right)\right) +\right.
$$
$$
\left.1 \Big/ \left((Cas1\,s + Cbs1\,s + Ccs1\,s + Cs1g\,s)\,(Cas3\,s + Cbs3\,s + Ccs3\,s + Cs3g\,s)\right.\right.
$$
$$
\left.\left.\left(\frac{1}{Cs1s3\,s} + \frac{1}{Cas1\,s + Cbs1\,s + Ccs1\,s + Cs1g\,s} + \frac{1}{Cas3\,s + Cbs3\,s + Ccs3\,s + Cs3g\,s}\right)\right)\right)\right)
$$

(B.30)

The Thévenin voltage is given by the relationship

$$
\begin{aligned}
&\frac{-Cas3\ s\ va - Cbs3\ s\ vb - Ccs3\ s\ vc}{Cs1s3\ s} + \\
&((Cas3\ s + Cbs3\ s + Ccs3\ s + Cs1s3\ s + Cs2s3\ s + Cs3g\ s)\ ((Cs1s2\ Cs2s3\ s^2 + Cs1s3\ s \\
&\quad (Cas2\ s + Cbs2\ s + Ccs2\ s + Cs1s2\ s + Cs2g\ s + Cs2s3\ s))\ (-Cas1\ s\ va - Cbs1\ s\ vb - Ccs1\ s\ vc) + \\
&\quad (Cs1s2\ Cs1s3\ s^2 + Cs2s3\ s\ (Cas1\ s + Cbs1\ s + Ccs1\ s + Cs1g\ s + Cs1s2\ s + Cs1s3\ s))\ (-Cas2\ s\ va - Cbs2\ s\ vb - Ccs2\ s\ vc) + \\
&\quad (-Cs1s2^2\ s^2 + (Cas1\ s + Cbs1\ s + Ccs1\ s + Cs1g\ s + Cs1s2\ s + Cs1s3\ s) \\
&\quad\quad (Cas2\ s + Cbs2\ s + Ccs2\ s + Cs1s2\ s + Cs2g\ s + Cs2s3\ s))\ (-Cas3\ s\ va - Cbs3\ s\ vb - Ccs3\ s\ vc)))\ / \\
&(Cs1s3\ s\ (Cs1s2^2\ s^2\ (Cas3\ s + Cbs3\ s + Ccs3\ s + Cs1s3\ s + Cs2s3\ s + Cs3g\ s) - \\
&\quad (Cas1\ s + Cbs1\ s + Ccs1\ s + Cs1g\ s + Cs1s2\ s + Cs1s3\ s)\ (Cas2\ s + Cbs2\ s + Ccs2\ s + \\
&\quad\quad Cs1s2\ s + Cs2g\ s + Cs2s3\ s)\ (Cas3\ s + Cbs3\ s + Ccs3\ s + Cs1s3\ s + Cs2s3\ s + Cs3g\ s) + \\
&\quad Cs2s3\ s\ (Cs1s2\ Cs1s3\ s^2 + Cs2s3\ s\ (Cas1\ s + Cbs1\ s + Ccs1\ s + Cs1g\ s + Cs1s2\ s + Cs1s3\ s)) + \\
&\quad Cs1s3\ s\ (Cs1s2\ Cs2s3\ s^2 + Cs1s3\ s\ (Cas2\ s + Cbs2\ s + Ccs2\ s + Cs1s2\ s + Cs2g\ s + Cs2s3\ s)))) - \\
&\left(\left(1 + \frac{Cs2s3}{Cs1s3}\right)\ (-Cs1s3\ s\ (-Cas2\ s\ va - Cbs2\ s\ vb - Ccs2\ s\ vc) + \right. \\
&\quad Cs1s2\ s\ (-Cas3\ s\ va - Cbs3\ s\ vb - Ccs3\ s\ vc) + \\
&\quad ((Cs1s3\ Cs2s3\ s^2 + Cs1s2\ s\ (Cas3\ s + Cbs3\ s + Ccs3\ s + Cs1s3\ s + Cs2s3\ s + Cs3g\ s)) \\
&\quad\quad ((Cs1s2\ Cs2s3\ s^2 + Cs1s3\ s\ (Cas2\ s + Cbs2\ s + Ccs2\ s + Cs1s2\ s + Cs2g\ s + Cs2s3\ s)) \\
&\quad\quad\quad (-Cas1\ s\ va - Cbs1\ s\ vb - Ccs1\ s\ vc) - (Cs1s2\ Cs1s3\ s^2 + Cs2s3\ s\ (Cas1\ s + Cbs1\ s + \\
&\quad\quad\quad\quad Ccs1\ s + Cs1g\ s + Cs1s2\ s + Cs1s3\ s))\ (-Cas2\ s\ va - Cbs2\ s\ vb - Ccs2\ s\ vc) + \\
&\quad\quad (-Cs1s2^2\ s^2 + (Cas1\ s + Cbs1\ s + Ccs1\ s + Cs1g\ s + Cs1s2\ s + Cs1s3\ s)\ (Cas2\ s + \\
&\quad\quad\quad Cbs2\ s + Ccs2\ s + Cs1s2\ s + Cs2g\ s + Cs2s3\ s))\ (-Cas3\ s\ va - Cbs3\ s\ vb - Ccs3\ s\ vc)))\ / \\
&\quad (Cs1s2^2\ s^2\ (Cas3\ s + Cbs3\ s + Ccs3\ s + Cs1s3\ s + Cs2s3\ s + Cs3g\ s) - \\
&\quad\quad (Cas1\ s + Cbs1\ s + Ccs1\ s + Cs1g\ s + Cs1s2\ s + Cs1s3\ s)\ (Cas2\ s + Cbs2\ s + Ccs2\ s + \\
&\quad\quad\quad Cs1s2\ s + Cs2g\ s + Cs2s3\ s)\ (Cas3\ s + Cbs3\ s + Ccs3\ s + Cs1s3\ s + Cs2s3\ s + Cs3g\ s) + \\
&\quad\quad Cs2s3\ s\ (Cs1s2\ Cs1s3\ s^2 + Cs2s3\ s\ (Cas1\ s + Cbs1\ s + Ccs1\ s + Cs1g\ s + Cs1s2\ s + Cs1s3\ s)) + \\
&\quad\quad Cs1s3\ s\ (Cs1s2\ Cs2s3\ s^2 + Cs1s3\ s\ (Cas2\ s + Cbs2\ s + Ccs2\ s + Cs1s2\ s + Cs2g\ s + Cs2s3\ s))))\Big)\ / \\
&(Cs1s2\ Cs2s3\ s^2 + Cs1s3\ s\ (Cas2\ s + Cbs2\ s + Ccs2\ s + Cs1s2\ s + Cs2g\ s + Cs2s3\ s))
\end{aligned}
$$

(B.31)

Using a mathematical software program the Thévenin impedance and voltage can easily be calculated.

## B.5. Preliminary work done for simplifying equivalent equations

### B.5.1. Introduction to simplification methods

Before the final statements were achieved concerning the simplification of equations the following work were done.

To simplify the equations the capacitive values that are much smaller than the other are going to be left out of the equations. For instance, if two capacitances, with an order difference of more than two or three, are added with each other, the capacitance that is smaller can be left out. This is the method that is used to simplify the equations. The capacitance between the

transmission line and the sensor are more than three orders smaller than the capacitance between the sensor and ground, or the capacitance between the different plates of the sensor.

Two different simplification methods, *Method 1* and *Method 2* are used on each equation that must be simplified. The two methods are declared as:

*Method 1:* When two line-to-sensor capacitances are multiplied with each other and added with a capacitance that consists out of two sensor-to-ground capacitances, or two sensor-to-sensor capacitances, the term of the two line-to-sensor capacitances can be left out. This is done because if the order difference between the line-to-sensor capacitance and the sensor-to-ground capacitance are doubled, the order difference is so large that the smaller term can be left out.

*Method 2:* All the terms that are left out in *Method 1* are also left out in this method. Terms which have an order difference of three or more are also left out, as explained underneath:

(line-to-sensor)*(line-to-sensor) + (line-to-sensor)*(sensor-to-ground)
= (line-to-sensor)*(sensor-to-ground)

(line-to-sensor)*(sensor-to-ground) + (sensor-to-ground)*(sensor-to-ground)
= (sensor-to-ground)*(sensor-to-ground)

In the above explanation al the "sensor-to-ground" factors can be replaced by "sensor-to-sensor" capacitances.



### B.5.2. Two-element parallel plate sensor

#### B.5.2.1. Simplifying the Thévenin voltage

The Thévenin voltage of the two-element parallel plate sensor, given by the equation (B.32), must be simplified. To simplify it, the numerator and denominator are evaluated separately. The Thévenin voltage is given by the relationship

$$V_{th} = (-C_{bs2}C_{cs1}v_b + C_{bs1}C_{cs2}v_b - C_{bs2}C_{s1g}v_b + C_{bs1}C_{s2g}v_b + C_{bs2}C_{cs1}v_c - C_{bs1}C_{cs2}v_c - C_{cs2}C_{s1g}v_c + C_{cs1}C_{s2g}v_c - C_{as2}(C_{cs1}v_a + C_{s1g}v_a + C_{bs1}(v_a - v_b) - C_{cs1}v_c) + C_{as1}(C_{bs2}v_a + C_{cs2}v_a + C_{s2g}v_a - C_{bs2}v_b - C_{cs2}v_c)) / (C_{bs1}C_{bs2} + C_{bs2}C_{cs1} + C_{bs1}C_{cs2} + C_{cs1}C_{cs2} + C_{bs2}C_{s1g} + C_{cs2}C_{s1g} + C_{bs1}C_{s1s2} + C_{bs2}C_{s1s2} + C_{cs1}C_{s1s2} + C_{cs2}C_{s1s2} + C_{s1g}C_{s1s2} + C_{as2}(C_{bs1} + C_{cs1} + C_{s1g} + C_{s1s2}) + C_{bs1}C_{s2g} + C_{cs1}C_{s2g} + C_{s1g}C_{s2g} + C_{s1s2}C_{s2g} + C_{as1}(C_{as2} + C_{bs2} + C_{cs2} + C_{s1s2} + C_{s2g}))$$

(B.32)

The numerator and denominator are defined below.

**Numerator:**

From equation (B.32) the numerator, $N_1$, is defined as

$$N_1 = (-C_{bs2}C_{cs1}v_b + C_{bs1}C_{cs2}v_b - C_{bs2}C_{s1g}\,v_b + C_{bs1}C_{s2g}v_b + C_{bs2}C_{cs1}v_c - C_{bs1}C_{cs2}v_c - C_{cs2}C_{s1g}v_c + C_{cs1}C_{s2g}v_c - C_{as2}(C_{cs1}v_a + C_{s1g}v_a + C_{bs1}(v_a - v_b) - C_{cs1}v_c) + C_{as1}(C_{bs2}v_a + C_{cs2}v_a + C_{s2g}v_a - C_{bs2}v_b - C_{cs2}v_c))$$

$$= v_a(C_{as1}C_{bs2} + C_{as1}C_{cs2} + C_{as1}C_{s2g} - C_{as2}C_{bs1} - C_{as2}C_{cs1} - C_{as2}C_{s1g}) + v_b(C_{bs1}C_{as2} + C_{bs1}C_{cs2} + C_{bs1}C_{s2g} - C_{bs2}C_{as1} - C_{bs2}C_{cs1} - C_{bs2}C_{s1g}) + v_c(C_{cs1}C_{as2} + C_{cs1}C_{bs2} + C_{cs1}C_{s2g} - C_{cs2}C_{as1} - C_{cs2}C_{bs1} - C_{cs2}C_{s1g}) \quad \text{(B.33)}$$

If $C_{A1} = (C_{bs2} + C_{cs2} + C_{s2g})$ , $C_{A2} = (C_{bs1} + C_{cs1} + C_{s1g})$,

$C_{B1} = (C_{as2} + C_{cs2} + C_{s2g})$ , $C_{B2} = (C_{as1} + C_{cs1} + C_{s1g})$,

$C_{C1} = (C_{as2} + C_{bs2} + C_{s2g})$ and $C_{C2} = (C_{as1} + C_{bs1} + C_{s1g})$

equation (B.33) can be redefined and given by

$$N_1 = v_a(C_{as1}C_{A1} - C_{as2}C_{A2}) + v_b(C_{bs1}C_{B1} - C_{bs2}C_{B2}) + v_c(C_{cs1}C_{C1} - C_{cs2}C_{C2})\,. \quad \text{(B.34)}$$

**Denominator:**

From equation (B.32) the denominator, T1, is given by the relationship

$$T_1 = (C_{bs1}C_{bs2} + C_{bs2}C_{cs1} + C_{bs1}C_{cs2} + C_{cs1}C_{cs2} + C_{bs2}C_{s1g} + C_{cs2}C_{s1g} + C_{bs1}C_{s1s2} + C_{bs2}C_{s1s2} + C_{cs1}C_{s1s2} + C_{cs2}C_{s1s2} + C_{s1g}C_{s1s2} + C_{as2}(C_{bs1} + C_{cs1} + C_{s1g} + C_{s1s2}) + C_{bs1}C_{s2g} + C_{cs1}C_{s2g} + C_{s1g}C_{s2g} + C_{s1s2}C_{s2g} + C_{as1}(C_{as2} + C_{bs2} + C_{cs2} + C_{s1s2} + C_{s2g}))$$

$$= C_{as1}(C_{as2} + C_{bs2} + C_{cs2} + C_{s1s2} + C_{s2g}) + C_{bs1}(C_{as2} + C_{bs2} + C_{cs2} + C_{s1s2} + C_{s2g}) + C_{cs1}(C_{as2} + C_{bs2} + C_{cs2} + C_{s1s2} + C_{s2g}) + C_{s1g}(C_{as2} + C_{bs2} + C_{cs2} + C_{s1s2} + C_{s2g}) + C_{s1s2}(C_{as2} + C_{bs2} + C_{cs2} + C_{s2g})\,. \quad \text{(B.35)}$$

Now let, $t_1 = (C_{as2} + C_{bs2} + C_{cs2} + C_{s2g})$ and $t_2 = (C_{as1} + C_{bs1} + C_{cs1} + C_{s1g})$

then,

$$T_1 = C_{as1}(t_1 + C_{s2g}) + C_{bs1}(t_1 + C_{s2g}) + C_{cs1}(t_1 + C_{s2g}) + C_{s1g}(t_1 + C_{s2g}) + C_{s1s2}t_1$$

$$= (t_1 + C_{s2g})t_2 + C_{s1s2}t_1\,. \quad \text{(B.36)}$$

Thus, from equations (B.34) and (B.36), equation (B.32)can be redefined as

$$V_{th} = \frac{v_a\left(C_{as1}C_{A1} - C_{as2}C_{A2}\right) + v_b\left(C_{bs1}C_{B1} - C_{bs2}C_{B2}\right) + v_c\left(C_{cs1}C_{C1} - C_{cs2}C_{C2}\right)}{t_2\left(t_1 + C_{s2g}\right) + t_1C_{s1s2}}\,. \quad \text{(B.37)}$$

If the methods described in section B.5.1 are used, equation (B.37) can be simplified as (again the numerator and denominator are evaluated separately) discussed below.

### *Method 1*

**Numerator:**

For *method 1* the numerator, presented in equation (B.33), stays the same.

**Denominator:**

Equation (B.35) illustrates that $C_{s1g}$ and $C_{s1s2}$ are multiplied separately with the last two terms. Thus, any terms that consists out of two line-to-sensor capacitances that are multiplied with each other, are ignored. Equation (B.35) is then reduced to

$$\begin{aligned} T_1 = \; & C_{as1}(C_{s1s2} + C_{s2g}) + C_{bs1}(C_{s1s2} + C_{s2g}) + C_{cs1}(C_{s1s2} + C_{s2g}) + \\ & C_{s1g}(C_{as2} + C_{bs2} + C_{cs2} + C_{s1s2} + C_{s2g}) + C_{s1s2}(C_{as2} + C_{bs2} + C_{cs2} + C_{s2g}) \\ = \; & (C_{as1} + C_{bs1} + C_{cs1})(C_{s1s2} + C_{s2g}) + C_{s1g}(t_1 + C_{s2g}) + C_{s1s2}t_1 \; . \end{aligned} \tag{B.38}$$

The simplified equation, using *method 1*, for the Thévenin voltage is defined as

$$V_{th} = \frac{v_a\left(C_{as1}C_{A1} - C_{as2}C_{A2}\right) + v_b\left(C_{bs1}C_{B1} - C_{bs2}C_{B2}\right) + v_c\left(C_{cs1}C_{C1} - C_{cs2}C_{C2}\right)}{\left(C_{as1} + C_{bs1} + C_{cs1}\right)\left(C_{s1s2} + C_{s2g}\right)\left(t_1 + C_{s2g}\right) + t_1 C_{s1s2}} \; . \tag{B.39}$$

### *Method 2*

**Numerator:**

For *method 2* equation (B.33) changes to

$$N_2 = v_a(C_{as1}C_{s2g} - C_{as2}C_{s1g}) + v_b(C_{bs1}C_{s2g} - C_{bs2}C_{s1g}) + v_c(C_{cs1}C_{s2g} - C_{cs2}C_{s1g}) \; . \tag{B.40}$$

**Denominator:**

From equation (B.35) the denominator is simplified to the relationship

$$T_2 = C_{s1g}(C_{s1s2} + C_{s2g}) + C_{s1s2}C_{s2g} \; . \tag{B.41}$$

The simplified equation for the Thévenin voltage, using *method 2* is given by the relationship

$$V_{th} = \frac{v_a\left(C_{as1}C_{s2g} - C_{as2}C_{s1g}\right) + v_b\left(C_{bs1}C_{s2g} - C_{bs2}C_{s1g}\right) + v_c\left(C_{cs1}C_{s2g} - C_{cs2}C_{s1g}\right)}{C_{s1g}\left(C_{s1s2} + C_{s2g}\right) + C_{s1s2}C_{s2g}} \; . \tag{B.42}$$

#### B.5.2.2. Simplifying the Thévenin impedance

The Thévenin impedance of the two-element parallel plate sensor is defined as

$$\begin{aligned} Z_{th} = \; & (C_{as1} + C_{as2} + C_{bs1} + C_{bs2} + C_{cs1} + C_{cs2} + C_{s1g} + C_{s2g}) \,/\, (C_{s1s2}(C_{as1} + C_{as2} + C_{bs1} + C_{bs2} + \\ & C_{cs1} + C_{cs2} + C_{s1g} + C_{s2g}) + (C_{as1} + C_{bs1} + C_{cs1} + C_{s1g})(C_{as2} + C_{bs2} + C_{cs2} + C_{s2g}))s \end{aligned} \tag{B.43}$$

To simplify this equation let,

$$t_3 = C_{as1} + C_{bs1} + C_{cs1} + C_{s1g}$$

and

$$t_4 = C_{as2} + C_{bs2} + C_{cs2} + C_{s2g}$$

then

$$Z_{th} = \frac{t_3 + t_4}{\left[C_{s1s2}(t_3 + t_4) + t_3 t_4\right]s} \quad . \tag{B.44}$$

From equation (B.44) it is noticed that the equivalent Thévenin impedance $Z_{th}$ for this approximation is a pure capacitor and is given by

$$Z_{TH} = \frac{1}{sC_{TH}} \tag{B.45}$$

where $C_{th}$ is defined as

$$C_{th} = \frac{\left[C_{s1s2}(t_3 + t_4) + t_3 t_4\right]}{t_3 + t_4} \quad . \tag{B.46}$$

If the methods that are described in section B.5.1 are used, equation (B.45) can be simplified as explained in the following sections. The numerator and denominator are again simplified separately.



### *Method 1*

**Numerator:**

From equation (B.44) and from the relationships of $t_3$ and $t_4$ it is concluded that the numerator stays the same.

**Denominator:**

Let $T_2$ be the denominator of equation (B.44) then it can be given by the relationship

$$\begin{aligned} T_2 &= [C_{s1s2}(t_3 + t_4) + (C_{as1} + C_{bs1} + C_{cs1} + C_{s1g})(C_{as2} + C_{bs2} + C_{cs2} + C_{s2g})]s \\ &= [C_{s1s2}(t_3 + t_4) + C_{s2g}(C_{as1} + C_{bs1} + C_{cs1}) + C_{s1g}(C_{as2} + C_{bs2} + C_{cs2} + C_{s2g})]s \end{aligned} \tag{B.47}$$

Thus the simplified equation, using *method 1*, for the Thévenin impedance is denoted by

$$Z_{th} = \frac{t_3 + t_4}{\left[C_{s1s2}(t_3 + t_4) + C_{s2g}(C_{as1} + C_{bs1} + C_{cs1}) + C_{s1g} t_4\right]s} \tag{B.48}$$

### *Method 2*

**Numerator:**

From equation (B.44) and from the relationships of $t_3$ and $t_4$ it is noticed that the numerator stays the same.

**Denominator:**

From equation (B.44) the denominator $T_4$ is reduced to

$$T_4 = [C_{s1s2}(C_{s1g} + C_{s2g}) + C_{s1g}C_{s2g}]s \quad . \tag{B.49}$$

The simplified equation, using *method 2*, for the Thévenin impedance is thus denoted by

$$Z_{th} = \frac{t_3 + t_4}{\left[C_{s1s2}\left(C_{s1g} + C_{s2g}\right) + C_{s1g}C_{s2g}\right]s} \quad . \tag{B.50}$$

### B.5.3. Three-element parallel plate sensor

The equation of the three element sensor has to be simplified. The two methods described in section B.5 are going to be used to simplify this equation and the numerator and denominator are going to be looked at separately. The following substitutions are going to be made:

$$t_3 = C_{as1} + C_{bs1} + C_{cs1} + C_{s1g} \tag{B.51}$$

$$t_4 = C_{as2} + C_{bs2} + C_{cs2} + C_{s2g} \tag{B.52}$$

$$t_5 = C_{as3} + C_{bs3} + C_{cs3} + C_{s3g}. \tag{B.53}$$

The numerator and denominator can then be defined as discussed in the following section.

#### B.5.3.1. Numerator:

From equation (B.30) the numerator is denoted by

$$N_3 = \frac{1}{C_{s1s2}}\left[\frac{1}{C_{s2s3}}\left(\frac{1}{t_4} + \frac{1}{t_3 t_5\left(\frac{1}{t_3} + \frac{1}{C_{s1s3}} + \frac{1}{t_5}\right)}\right) + \frac{\left(\frac{1}{t_3} + \frac{t_3\left(\frac{1}{t_3} + \frac{1}{C_{s1s3}} + \frac{1}{t_5}\right)}{t_4}\right)}{C_{s1s3}t_5^2\left(\frac{1}{t_3} + \frac{1}{C_{s1s3}} + \frac{1}{t_5}\right)^2}\right] + \frac{\left[\left(\frac{t_3}{t_5} + \frac{C_{s1s3}}{t_5} + \frac{t_3 C_{s1s3}\left(\frac{1}{t_3} + \frac{1}{C_{s1s3}} + \frac{1}{t_5}\right)}{t_4} + \frac{t_3 + C_{s1s3} + \frac{t_3 C_{s1s3}}{t_5}}{C_{s2s3}}\right)s\right]}{\left[t_3 + C_{s1s3} + \frac{t_3 C_{s1s3}}{t_5}\right]^2} \quad . \tag{B.54}$$

Let

$$g_1 = \frac{1}{t_3} + \frac{1}{C_{s1s3}} + \frac{1}{t_5} \tag{B.55}$$

and

$$g_2 = t_3 + C_{s1s3} + \frac{t_3 C_{s1s3}}{t_5} \tag{B.56}$$

then, from equations (B.51), (B.52) and (B.53), the simplified numerator is defined as

$$N_3 = \frac{1}{C_{s2s3}C_{s1s2}}\left(\frac{1}{t_4} + \frac{1}{t_3 t_5 g_1}\right) + \frac{\left(\frac{1}{t_3 g_1} + \frac{t_3}{t_4}\right)}{C_{s1s2}C_{s1s3}t_5^2 g_1} + \left(\frac{t_3 + C_{s1s3}}{t_5 g_2^2} + \frac{t_3 C_{s1s3} g_1}{t_4 g_2^2} + \frac{1}{C_{s2s3} g_2}\right)s \tag{B.57}$$

### B.5.3.2. Denominator

From equation (B.30) the denominator can be defined as

$$\begin{aligned}
&\Big(\Big((Cas3\,Cbs1 + Cas3\,Cbs2 + Cbs1\,Cbs3 + Cbs2\,Cbs3 + Cas3\,Ccs1 + Cbs3\,Ccs1 + \\
&\quad Cas3\,Ccs2 + Cbs3\,Ccs2 + Cbs1\,Ccs3 + Cbs2\,Ccs3 + Ccs1\,Ccs3 + Ccs2\,Ccs3 + \\
&\quad Cas3\,Cslg + Cbs3\,Cslg + Ccs3\,Cslg + Cas3\,Csls3 + Cbs1\,Csls3 + Cbs2\,Csls3 + \\
&\quad Cbs3\,Csls3 + Ccs1\,Csls3 + Ccs2\,Csls3 + Ccs3\,Csls3 + Cslg\,Csls3 + Cas3\,Cs2g + \\
&\quad Cbs3\,Cs2g + Ccs3\,Cs2g + Csls3\,Cs2g + Cas3\,Cs2s3 + Cbs1\,Cs2s3 + Cbs2\,Cs2s3 + \\
&\quad Cbs3\,Cs2s3 + Ccs1\,Cs2s3 + Ccs2\,Cs2s3 + Ccs3\,Cs2s3 + Cslg\,Cs2s3 + \\
&\quad Cs2g\,Cs2s3 + (Cbs1 + Cbs2 + Ccs1 + Ccs2 + Cslg + Csls3 + Cs2g + Cs2s3)\,Cs3g + \\
&\quad Cas1\,(Cas3 + Cbs3 + Ccs3 + Csls3 + Cs2s3 + Cs3g) + \\
&\quad Cas2\,(Cas3 + Cbs3 + Ccs3 + Csls3 + Cs2s3 + Cs3g))\,/ \\
&\quad ((Cas2 + Cbs2 + Ccs2 + Cs2g)\,Cs2s3 \\
&\quad (Cbs1\,Cbs3 + Cbs3\,Ccs1 + Cbs1\,Ccs3 + Ccs1\,Ccs3 + Cbs3\,Cslg + Ccs3\,Cslg + \\
&\quad Cbs1\,Csls3 + Cbs3\,Csls3 + Ccs1\,Csls3 + Ccs3\,Csls3 + Cslg\,Csls3 + \\
&\quad Cas3\,(Cbs1 + Ccs1 + Cslg + Csls3) + (Cbs1 + Ccs1 + Cslg + Csls3)\,Cs3g + \\
&\quad Cas1\,(Cas3 + Cbs3 + Ccs3 + Csls3 + Cs3g))) + \\
&\frac{1}{Csls2}\left(\frac{1}{Cas2 + Cbs2 + Ccs2 + Cs2g} + \frac{1}{Cs2s3} + \right. \\
&\quad 1\Big/\Big((Cas1 + Cbs1 + Ccs1 + Cslg)\,(Cas3 + Cbs3 + Ccs3 + Cs3g) \\
&\quad \left.\left(\frac{1}{Cas1 + Cbs1 + Ccs1 + Cslg} + \frac{1}{Csls3} + \frac{1}{Cas3 + Cbs3 + Ccs3 + Cs3g}\right)\right) + \\
&\quad 1\Big/\Big(Csls3\,(Cas3 + Cbs3 + Ccs3 + Cs3g) \\
&\quad \left.\left.\left(\frac{1}{Cas1 + Cbs1 + Ccs1 + Cslg} + \frac{1}{Csls3} + \frac{1}{Cas3 + Cbs3 + Ccs3 + Cs3g}\right)\right)\right)\Big)\,s\Big)
\end{aligned} \tag{B.58}$$

The denominator is also going to be broken down into different parts so that it can be evaluated and simplified. The denominator of the equation are broken down into three parts, otherwise the equation is too complicated.

**Part one:**

```
(Cas3 Cbs1 + Cas3 Cbs2 + Cbs1 Cbs3 + Cbs2 Cbs3 + Cas3 Ccs1 + Cbs3 Ccs1 +
  Cas3 Ccs2 + Cbs3 Ccs2 + Cbs1 Ccs3 + Cbs2 Ccs3 + Ccs1 Ccs3 + Ccs2 Ccs3 +
  Cas3 Cs1g + Cbs3 Cs1g + Ccs3 Cs1g + Cas3 Cs1s3 + Cbs1 Cs1s3 + Cbs2 Cs1s3 +
  Cbs3 Cs1s3 + Ccs1 Cs1s3 + Ccs2 Cs1s3 + Ccs3 Cs1s3 + Cs1g Cs1s3 + Cas3 Cs2g +
  Cbs3 Cs2g + Ccs3 Cs2g + Cs1s3 Cs2g + Cas3 Cs2s3 + Cbs1 Cs2s3 + Cbs2 Cs2s3 +
  Cbs3 Cs2s3 + Ccs1 Cs2s3 + Ccs2 Cs2s3 + Ccs3 Cs2s3 + Cs1g Cs2s3 +
  Cs2g Cs2s3 + (Cbs1 + Cbs2 + Ccs1 + Ccs2 + Cs1g + Cs1s3 + Cs2g + Cs2s3) Cs3g +
  Cas1 (Cas3 + Cbs3 + Ccs3 + Cs1s3 + Cs2s3 + Cs3g) +
  Cas2 (Cas3 + Cbs3 + Ccs3 + Cs1s3 + Cs2s3 + Cs3g))
```

(B.59)

The first part $P_1$ can be defined as

$$\begin{aligned} P_1 = {} & C_{as3}(C_{as1}+ C_{as2} + C_{bs1} + C_{bs2} + C_{cs1} + C_{cs2} + C_{s1g} + C_{s2g} + C_{s1s3} + C_{s2s3}) + \\ & C_{bs3}(C_{as1}+ C_{as2} + C_{bs1} + C_{bs2} + C_{cs1} + C_{cs2} + C_{s1g} + C_{s2g} + C_{s1s3} + C_{s2s3}) + \\ & C_{cs3}(C_{as1} + C_{as2} + C_{bs1} + C_{bs2} + C_{cs1} + C_{cs2} + C_{s1g} + C_{s2g} + C_{s1s3} + C_{s2s3}) + \\ & C_{s3g}(C_{as1}+ C_{as2} + C_{bs1} + C_{bs2} + C_{cs1} + C_{cs2} + C_{s1g} + C_{s2g} + C_{s1s3} + C_{s2s3}) + \\ & C_{s1s3}(C_{as1} + C_{as2} + C_{bs1} + C_{bs2} + C_{cs1} + C_{cs2} + C_{s1g} + C_{s2g}) + \\ & C_{s2s3}(C_{as1} + C_{as2} + C_{bs1} + C_{bs2} + C_{cs1} + C_{cs2} + C_{s1g} + C_{s2g}) \quad . \end{aligned} \tag{B.60}$$

Now let

$$t_6 = C_{as1} + C_{as2} + C_{bs1} + C_{bs2} + C_{cs1} + C_{cs2} + C_{s1g} + C_{s2g} \tag{B.61}$$

and

$$t_7 = C_{s1s3} + C_{s2s3} \tag{B.62}$$

then from equations (B.60), (B.61) and (B.62) the first part $P_1$ is denoted by

$$P_1 = (C_{as3} + C_{bs3} + C_{cs3} + C_{s3g})(t_6 + t_7) + t_6 t_7 \quad . \tag{B.63}$$

**Part two:**

```
((Cas2 + Cbs2 + Ccs2 + Cs2g) Cs2s3
  (Cbs1 Cbs3 + Cbs3 Ccs1 + Cbs1 Ccs3 + Ccs1 Ccs3 + Cbs3 Cs1g +
    Ccs3 Cs1g + Cbs1 Cs1s3 + Cbs3 Cs1s3 + Ccs1 Cs1s3 +
    Ccs3 Cs1s3 + Cs1g Cs1s3 + Cas3 (Cbs1 + Ccs1 + Cs1g + Cs1s3) +
    (Cbs1 + Ccs1 + Cs1g + Cs1s3) Cs3g + Cas1 (Cas3 + Cbs3 + Ccs3 + Cs1s3 + Cs3g))
```

(B.64)

From equations (B.51), (B.52) and (B.53) the second part $P_2$ can be denoted by

$$P_2 = t_4 C_{s2s3}(t_5 + C_{s1s3})( t_3 + C_{s1s3}) \quad . \tag{B.65}$$

**Part three:**

$$\frac{1}{Cs1s2}\left(\frac{1}{Cas2+Cbs2+Ccs2+Cs2g}+\frac{1}{Cs2s3}+\right.$$
$$1\Big/\left((Cas1+Cbs1+Ccs1+Cs1g)\ (Cas3+Cbs3+Ccs3+Cs3g)\right.$$
$$\left.\left(\frac{1}{Cas1+Cbs1+Ccs1+Cs1g}+\frac{1}{Cs1s3}+\frac{1}{Cas3+Cbs3+Ccs3+Cs3g}\right)\right)+ \qquad \text{(B.66)}$$
$$1\Big/\left(Cs1s3\ (Cas3+Cbs3+Ccs3+Cs3g)\right.$$
$$\left.\left.\left(\frac{1}{Cas1+Cbs1+Ccs1+Cs1g}+\frac{1}{Cs1s3}+\frac{1}{Cas3+Cbs3+Ccs3+Cs3g}\right)\right)\right)$$

From equations (B.51), (B.52), (B.53) and (B.54) the third part $P_3$ can be denoted by

$$P_3=\frac{1}{C_{s1s2}}\left(\frac{1}{t_4}+\frac{1}{C_{s2s3}}+\frac{1}{t_3t_5g_1}+\frac{1}{C_{s1s3}t_5g_1}\right)\ . \qquad \text{(B.67)}$$

The three parts are combined to form the denominator. From equations (B.63), (B.66) and (B.67) the denominator is defined by

$$T_5=\frac{t_5(t_6+t_7)+t_6t_7}{t_4C_{s2s3}(t_5+C_{s1s3})(t_3+C_{s1s3})}+\frac{1}{C_{s1s2}}\left(\frac{1}{t_4}+\frac{1}{C_{s2s3}}+\frac{1}{t_3t_5g_1}+\frac{1}{C_{s1s3}t_5g_1}\right)\ . \qquad \text{(B.68)}$$

### B.5.3.3. Complete equivalent Thévenin impedance equation of the three-element parallel plate sensor

From equations (B.57) and (B.68), the equivalent equation for the Thévenin impedance of the three-element parallel plate sensor is denoted by

$$Z_{th}=\frac{\left[\frac{1}{C_{s2s3}C_{s1s2}}\left(\frac{1}{t_4}+\frac{1}{t_3t_5g_1}\right)+\frac{\left(\frac{1}{t_3g_1}+\frac{t_3}{t_4}\right)}{C_{s1s2}C_{s1s3}t_5^2g_1}+\frac{1}{g_2^2}\left(\frac{t_3+C_{s1s3}}{t_5}+\frac{t_3C_{s1s3}g_1}{t_4}+\frac{g_2}{C_{s2s3}}\right)s\right]}{\frac{t_5(t_6+t_7)+t_6t_7}{t_4C_{s2s3}(t_5+C_{s1s3})(t_3+C_{s1s3})}+\frac{1}{C_{s1s2}}\left(\frac{1}{t_4}+\frac{1}{C_{s2s3}}+\frac{1}{t_3t_5g_1}+\frac{1}{C_{s1s3}t_5g_1}\right)} \qquad \text{(B.69)}$$

### B.5.4. Simplified representation of the three-element parallel plate sensor

By using the methods explained in section B.5.1, the Thévenin impedance of the three-element parallel plate sensor, given by equation (B.69), is going to be simplified. Firstly $t_3$, $t_4$, $t_5$, $t_6$, $g_1$ and $g_2$, are simplified by using the two methods.

For *method 1*:

$$t_3 = C_{as1} + C_{bs1} + C_{cs1} + C_{s1g} \qquad \text{(B.70)}$$

$$t_4 = C_{as2} + C_{bs2} + C_{cs2} + C_{s2g} \tag{B.71}$$

$$t_5 = C_{as3} + C_{bs3} + C_{cs3} + C_{s3g} \tag{B.72}$$

$$t_6 = C_{as1} + C_{as2} + C_{bs1} + C_{bs2} + C_{cs1} + C_{cs2} + C_{s1g} + C_{s2g} \tag{B.73}$$

$$t_7 = C_{s1s3} + C_{s2s3} \tag{B.74}$$

$$g_1 = \frac{1}{t_3} + \frac{1}{C_{s1s3}} + \frac{1}{t_5} \tag{B.75}$$

$$g_2 = t_3 + C_{s1s3} + \frac{t_3 C_{s1s3}}{t_5} \tag{B.76}$$

Everything stays the same in *method 1*.

For *method 2*:

$$t_3 = C_{s1g} \tag{B.77}$$

$$t_4 = C_{s2g} \tag{B.78}$$

$$t_5 = C_{s3g} \tag{B.79}$$

$$t_6 = C_{s1g} + C_{s2g} \tag{B.80}$$

$$t_7 = C_{s1s3} + C_{s2s3} \tag{B.81}$$

$$g_1 = \frac{1}{C_{s1g}} + \frac{1}{C_{s1s3}} + \frac{1}{C_{s3g}} \tag{B.82}$$

$$g_2 = C_{s1g} + C_{s1s3} + \frac{C_{s1g} C_{s1s3}}{C_{s3g}} \tag{B.83}$$



#### B.5.4.1. *Method 1*

**Numerator:**

By using *method 1* the numerator is simplified to

$$N_3 = \frac{1}{C_{s2s3} C_{s1s2}} \left( \frac{1}{t_4} + \frac{1}{t_3 t_5 g_1} \right) + \frac{\left( \frac{1}{t_3 g_1} + \frac{t_3}{t_4} \right)}{C_{s1s2} C_{s1s3} t_5^2 g_1} \tag{B.84}$$

**Denominator:**

The denominator stays the same. The simplified equation for the Thévenin impedance for *method 1* is thus defined as

$$Z_{th}=\frac{\left[\frac{1}{C_{s2s3}C_{s1s2}}\left(\frac{1}{t_4}+\frac{1}{t_3t_5g_1}\right)+\frac{\left(\frac{1}{t_3g_1}+\frac{t_3}{t_4}\right)}{C_{s1s2}C_{s1s3}t_5^2g_1}\right]}{\frac{t_5(t_6+t_7)+t_6t_7}{t_4C_{s2s3}(t_5+C_{s1s3})(t_3+C_{s1s3})}+\frac{1}{C_{s1s2}}\left(\frac{1}{t_4}+\frac{1}{C_{s2s3}}+\frac{1}{t_3t_5g_1}+\frac{1}{C_{s1s3}t_5g_1}\right)} \tag{B.85}$$

### B.5.4.2. *Method 2*

**Numerator:**

By using *method 2* the numerator is simplified to the same equation as in *method 1*, as discussed below:

$$N_3=\frac{1}{C_{s2s3}C_{s1s2}}\left(\frac{1}{t_4}+\frac{1}{t_3t_5g_1}\right)+\frac{\left(\frac{1}{t_3g_1}+\frac{t_3}{t_4}\right)}{C_{s1s2}C_{s1s3}t_5^2g_1}. \tag{B.86}$$

**Denominator:**

The denominator stays the same.

**Conclusion**

The simplified Thévenin impedance for *method 2* is the same as the impedance denoted by equation (B.86). The original Thévenin impedance can not be simplified that much by using these two methods. The equations obtained in sections B.4.2 and B.4.3 are too expansive and must be simplified. The command "*FullSimplify*" in Mathematica is used in simplifying the equations. In this section the Thévenin impedance of the ideal circuit are simplified, just to illustrate the concept of simplifying equivalent Thévenin equations. The denominator of the equation is broken up into three parts so that it is usable.

# Appendix C. Original capacitive coupling methods

This chapter discusses the original methods developed for determining the voltage coupling relationships for a three-phase transmission line configuration with multiple capacitive sensors located near the earth plane. A typical 400 kV transmission line configuration is used, namely a three-phase, flat, single circuit line configuration.

## C.1. Voltage relationships if three sensor are centralised underneath phases

Figure C.1 shows the geometric arrangement of three floating single-element plate sensors located symmetrically between a three-phase, flat, single-circuit, transmission line configuration and an infinite ground plane. The same notations presented in Chapter 5 are used for the various elements and dimensions in this chapter.

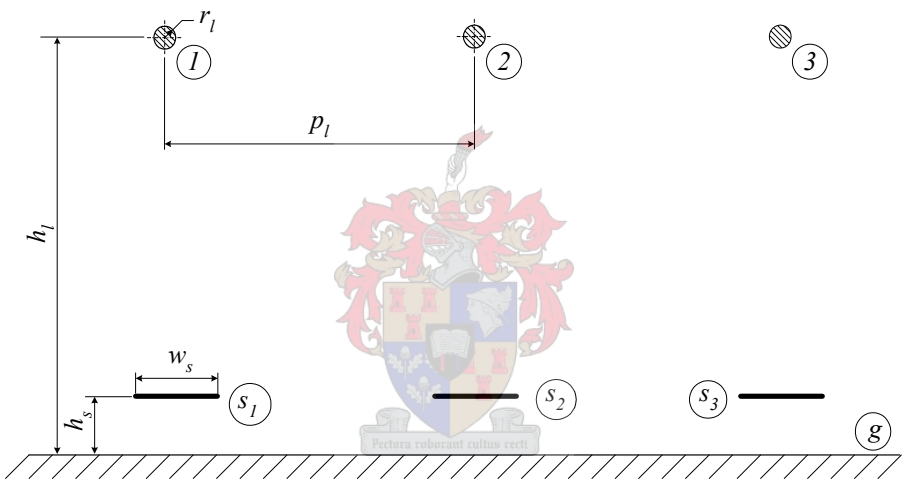


**Figure C.1: Topology of three single-element plate sensors underneath a flat three-phase single circuit line configuration.**

Figure C.2 shows the relevant phase voltages $v_{p1}$, $v_{p2}$ and $v_{p3}$ and induced voltages $v_{s1}$, $v_{s2}$ and $v_{s3}$. A set of voltage transfer functions, namely $G_{s1p1}$, $G_{s1p2}$, $G_{s1p3}$, $G_{s2p1}$, $G_{s2p2}$, $G_{s2p3}$, $G_{s3p1}$, $G_{s3p2}$ and $G_{s3p3}$ are defined to assist in presenting the capacitive coupling elements between phase conductors and sensors.

The same linear system of equations and transfer function matrix presented in equations (5.1) and (5.4) are used to determine the unknown voltages. However in the original methods certain assumptions were made that reduced the number unknown transfer functions.

In the original methods it is assumed that if the distance between a sensor and a conductor is the same as the distance between another sensor and conductor the two corresponding transfer

functions are the same. Thus from this assumption transfer functions $G_5 = G_1$ and $G_4 = G_2$. The constant factors $k$ and $p$ then equals 1 in equation 5.59.

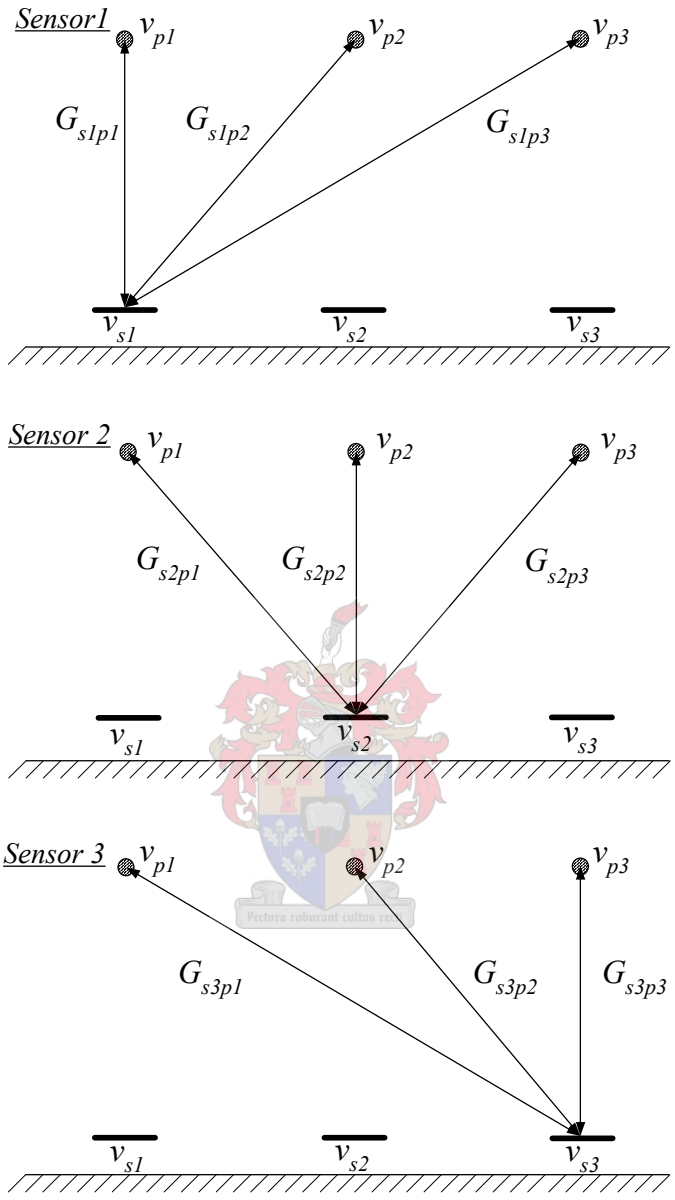


**Figure C.2: Voltage transfer function definitions for a three single-element plate sensor topology.**

The symmetry of the topology shown in Figure C.1 as well as the assumptions made give rise to the following simplifying relationships:

$$G_1 = G_{s1p1} = G_{s2p2} = G_{s3p3}$$

$$G_2 = G_{s1p2} = G_{s2p1} = G_{s2p3} = G_{s3p2}$$

and

$$G_3 = G_{s1p3} = G_{s3p1}$$

The transfer function matrix **G** is then given by the relationship

$$\boldsymbol{G} = \begin{bmatrix} G_1 & G_2 & G_3 \\ G_2 & G_3 & G_2 \\ G_3 & G_2 & G_1 \end{bmatrix}. \tag{C.1}$$

Figure C.3 illustrates the representations of the transfer functions for the above transfer function matrix.

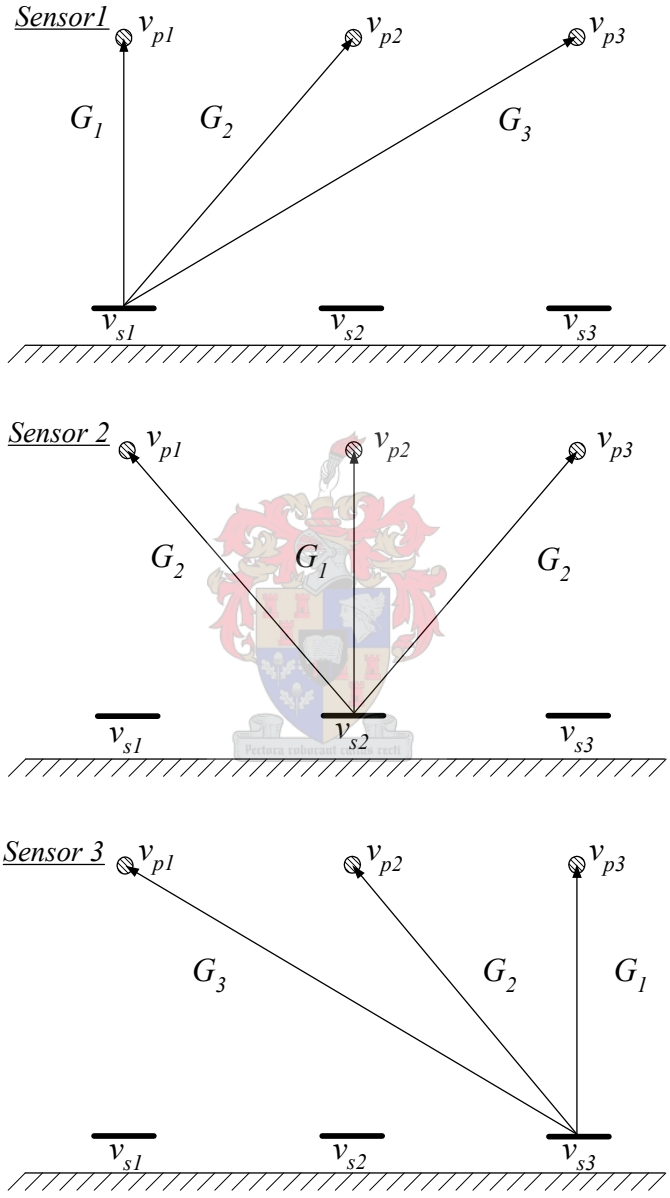


**Figure C.3: Voltage transfer function definitions for a three single-element plate sensor topology.**

The sensor voltages for the topologies shown in Figure C.1 can be expressed in the form

$$v_{s1}(t) = G_1 v_{p1}(t) + G_2 v_{p2}(t) + G_3 v_{p3}(t) \ , \tag{C.2}$$

$$v_{s2}(t) = G_2 v_{p1}(t) + G_1 v_{p2}(t) + G_2 v_{p3}(t) \tag{C.3}$$

and

$$v_{s3}(t) = G_3 v_{p1}(t) + G_2 v_{p2}(t) + G_1 v_{p3}(t) \tag{C.4}$$

By solving equations (C.2), (C.3) and (C.4) simultaneously transfer function $G_1$ is given by the relationship

$$G_1 = \frac{v_1 v_3 m_3 - v_1^2 m_1 + v_3^2 m_3 - v_1 v_3 m_1 + v_1 v_2 m_2 - v_2 v_3 m_2}{-v_1^3 - v_1^2 v_3 + v_1 v_2^2 - v_2^2 v_3 + v_1 v_3^2 + v_3^3} .$$

Now, let

$$k_1 = v_1^3 + v_1^2 v_3 - v_1 v_2^2 - v_1 v_3^2 + v_2^2 v_3 - v_3^3$$

then the unknown coupling factors $G_1$, $G_2$ and $G_3$ are given by the relationships

$$G_1 = \frac{m_1 v_1 (v_1 + v_3) + m_2 v_2 (v_3 - v_1) - m_3 v_3 (v_1 + v_3)}{k_1} , \tag{C.5}$$

$$G_2 = \frac{m_1 (-v_1 v_2) + m_2 (v_1^2 - v_3^2) + m_3 v_2 v_3}{k_1} \tag{C.6}$$

and

$$G_3 = \frac{m_1 (v_2^2 - v_1 v_3 - v_3^2) + m_2 v_2 (v_3 - v_1) + m_3 (v_1^2 + v_1 v_3 - v_2^2)}{k_1} . \tag{C.7}$$

## C.2. Sensor located near centre phase

Figure C.4 illustrates a three-phase line configuration if all the three sensors are placed in the vicinity of the centre conductor's vertical axis. In all the methods discussed the centre sensor $s_2$ is located directly under the centre conductor $p_2$, and sensor $s_1$ and $s_2$ are positioned symmetrically relative to sensor $s_2$ as illustrated in Figure C.4, Figure C.6 and Figure C.8. This causes that the symmetry relationships in the voltage transfer function matrix and the capacitive coupling matrix are maintained.

The distance $b_l$ between each sensor is smaller than half of the distance $p_l$ between the two transmission lines. The transfer function matrix for this method is evaluated as in the previous method except. The only difference is that instead of three unknown transfer functions there are now five as illustrated in Figure C.5. The same results are obtained if the sensors are positioned more than half of the distance $p_l$ from each other.

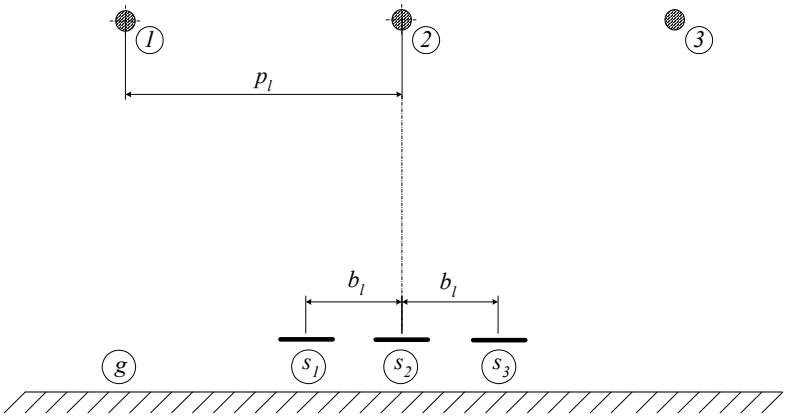


**Figure C.4:Two-dimensional view of the three-phase transmission line and three plate sensors if the three sensors are placed near the centre conductor's axis.**

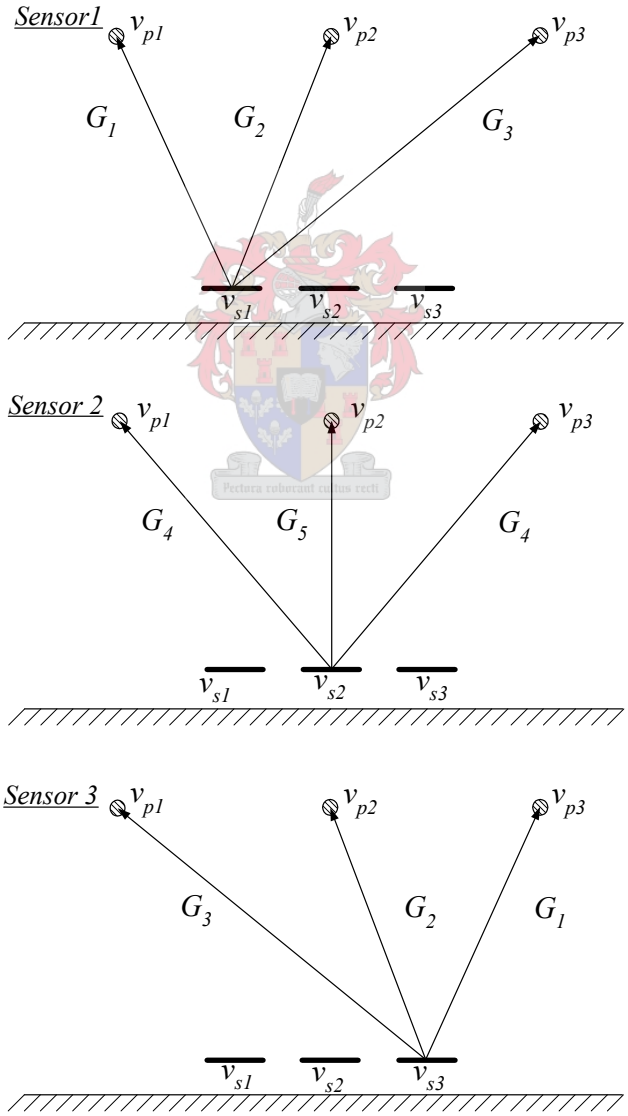


**Figure C.5: Voltage transfer function definitions for a three single-element plate sensor topology if the three sensors are placed near the centre conductor's axis.**

The transfer function matrix **G** is then given by the relationship

$$\boldsymbol{G} = \begin{bmatrix} G_1 & G_2 & G_3 \\ G_4 & G_5 & G_4 \\ G_3 & G_2 & G_1 \end{bmatrix}. \tag{C.8}$$

Due to the fact there are 5 unknown transfer functions the linear system presenting the voltages induced on the sensors from the overhead phase voltages can not be solved. The second method of placing the sensors near the centre conductor's axis does not seem feasible.

### C.3. Centralising two sensor between the different phases

For this method *sensor 2* is centralized beneath the centre conductor *2* and *sensors 1* and *3* are each located half the distance of $p_l$ from *sensor 2*. Figure C.6 shows the three-phase line configuration with the three sensors as explained above. The distance $b_l$ between each sensor is half of distance $p_l$.

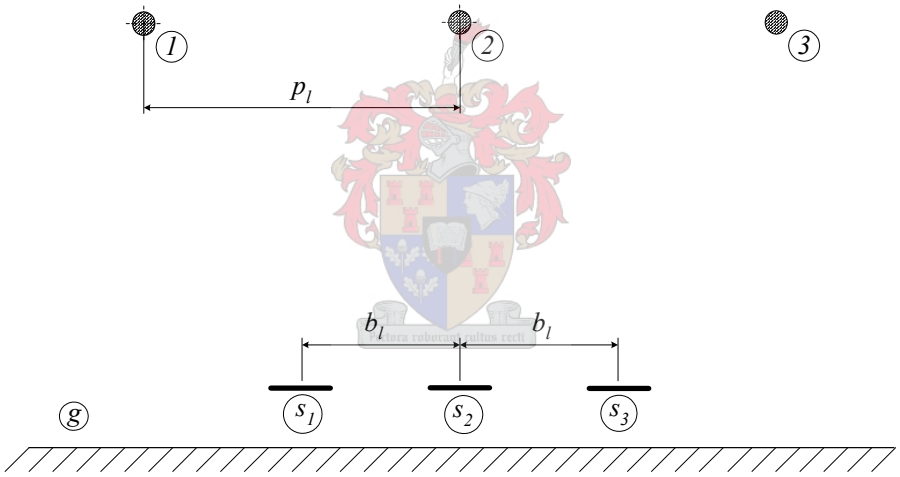


**Figure C.6: Two-dimensional view of the three-phase transmission line and three plate sensors, if the sensors are placed in the centre of two overhead conductors.**

The transfer functions are evaluated as in the first method. Figure C.7 illustrates the different coupling factors for this line configuration. There is one less unknown coupling factor than in the previous method. The transfer function matrix **G** is then given by the relationship

$$\boldsymbol{G} = \begin{bmatrix} G_1 & G_1 & G_2 \\ G_3 & G_4 & G_3 \\ G_2 & G_1 & G_1 \end{bmatrix}. \tag{C.9}$$

The linear equations for the voltages induced on each sensor are given by the relationships

$$v_{s1} = G_1 v_{p1} + G_1 v_{p2} + G_2 v_{p3} \ , \tag{C.10}$$

$$v_{s2} = G_3 v_{p1} + G_4 v_{p2} + G_3 v_{p3} \tag{C.11}$$

and

$$v_{s3} = G_2 v_{p1} + G_1 v_{p2} + G_1 v_{p3} \ . \tag{C.12}$$

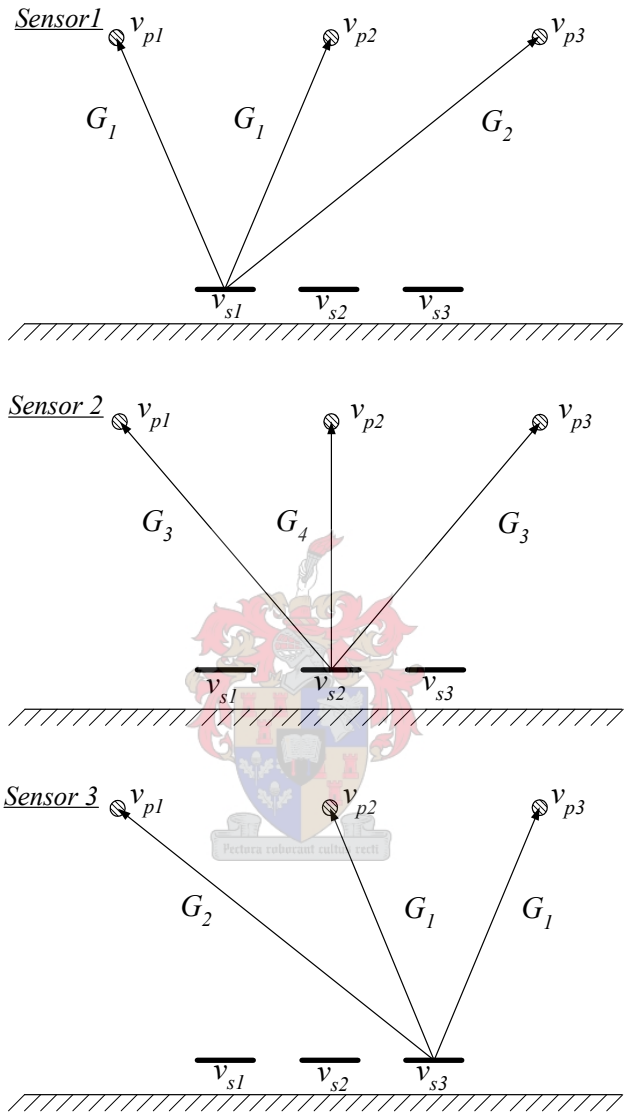


**Figure C.7: Voltage transfer function definitions for a three single-element plate sensor topology if two of the sensors are located centralised between the different phases.**

Solving equations (C.10) and (C.12) simultaneously the two unknown transfer functions $G_1$ and $G_2$ are given by the relationships

$$G_1 = \frac{m_1\left(v_1 + v_3\right) - m_2 v_3}{\left(v_1^2 + v_1 v_2 + v_1 v_3\right)} \tag{C.13}$$

and

$$G_2 = \frac{m_2\left(v_1 + v_2\right) - m_1 v_2}{\left(v_1^2 + v_1 v_2 + v_1 v_3\right)} \quad . \tag{C.14}$$

Equation (C.11) can however not be solved due to the fact that it has two unknown transfer functions $G_3$ and $G_4$.

## C.4. Single-element plate sensor arrangement with five sensors

Unlike the previous methods, this method employs five sensors. More accurate measurements are suspected to be made by using five sensors. This introduces redundancy into the set of equations, and can be used for checking and possible calibration purposes. Three sensors are centralised underneath each phase conductor while the other two sensors are place centralised between the different phases. Figure C.8 shows a topology with five floating sensors arranged symmetrically with respect to the centre phase conductor. The distance $b_l$ between each sensor is half of the distance $p_l$ between the two conductors.

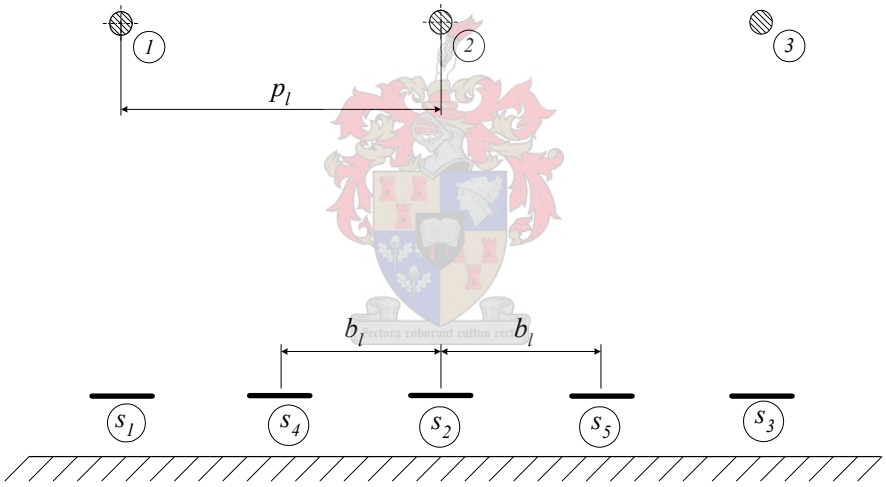


**Figure C.8: Two-dimensional view of the three-phase transmission line if five sensors are spaced evenly underneath the transmission lines.**

Figure C.9 shows the relevant phase and sensor voltages and defines the set of voltage transfer functions. Due to the fact that $b_l$ is half of $p_l$ it is concluded that the transfer function between *sensor 4* and *conductor 1* is the same as the transfer function between *sensor 4* and *conductor 2*. The five linear equations for the voltages induced on the five sensors are given by the relationships

$$v_{s1} = G_1 v_{p1} + G_2 v_{p2} + G_3 v_{p3} \ , \tag{C.15}$$

$$v_{s2} = G_2 v_{p1} + G_1 v_{p2} + G_1 v_{p3} \ , \tag{C.16}$$

$$v_{s3} = G_3 v_{p1} + G_2 v_{p2} + G_1 v_{p3} \ , \tag{C.17}$$

$$v_{s4} = G_4 v_{p1} + G_4 v_{p2} + G_5 v_{p3} \tag{C.18}$$

and

$$v_{s5} = G_5 v_{p1} + G_4 v_{p2} + G_4 v_{p3} \ . \tag{C.19}$$

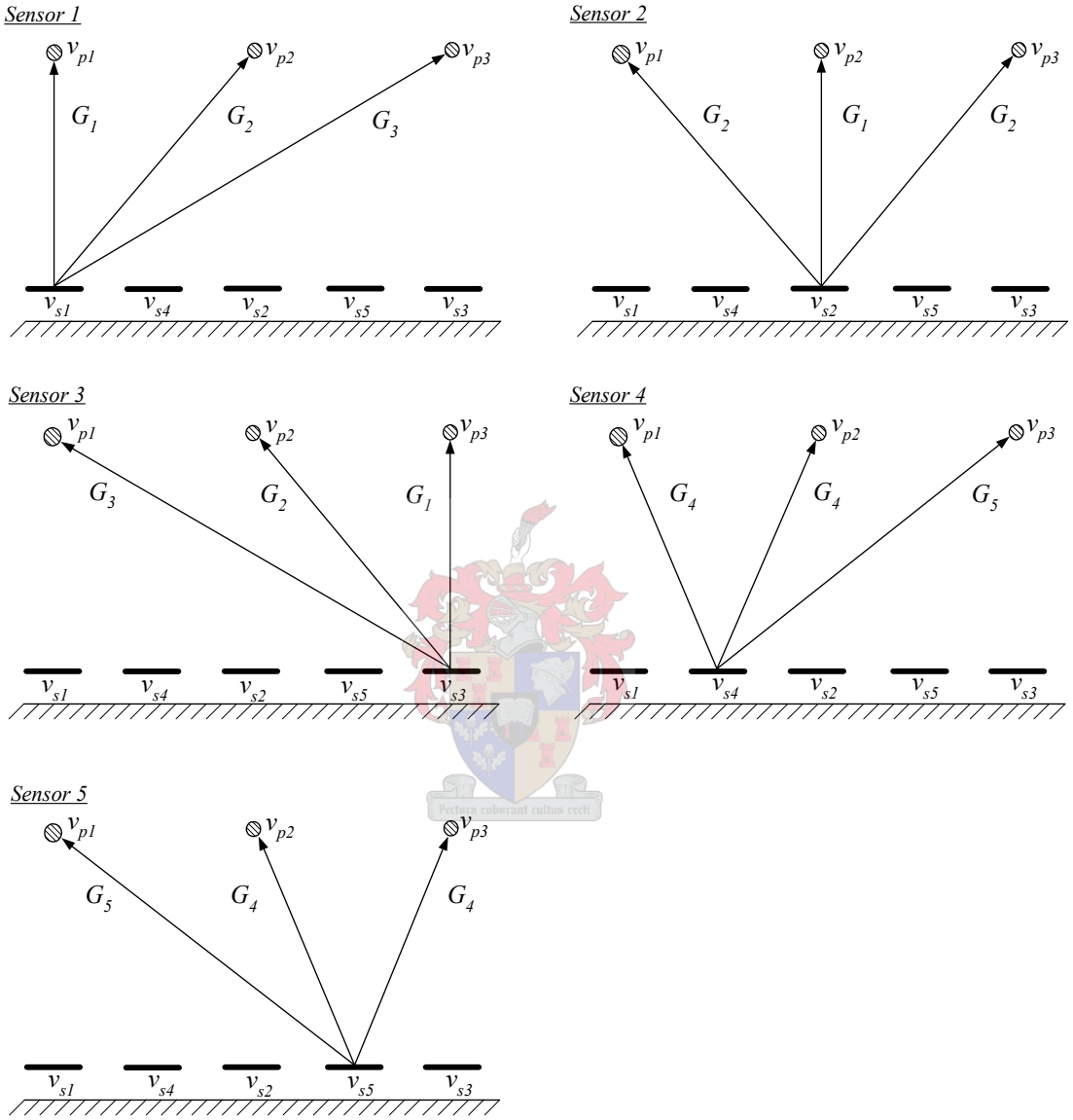


**Figure C.9: Voltage transfer function definitions for a five single-element plate sensor topology if the five sensors are placed as illustrated in Figure C.8.**

The five unknown transfer functions $G_1$, $G_2$, $G_3$, $G_4$ and $G_5$ are solved simultaneously in Mathematica (mathematical software program). The transfer function are given by the relationships

$$G_1 = \frac{m_1 v_1 (v_1 + v_3) + m_2 v_2 (v_3 - v_1) - m_3 v_3 (v_1 + v_3)}{k_1} \ , \tag{C.20}$$

$$G_2 = \frac{m_1\left(-v_1 v_2\right) + m_2\left(v_1^2 - v_3^2\right) + m_3 v_2 v_3}{k_1} \quad , \tag{C.21}$$

$$G_3 = \frac{m_1\left(v_2^2 - v_1 v_3 - v_3^2\right) + m_2 v_2\left(v_3 - v_1\right) + m_3\left(v_1^2 + v_1 v_3 - v_2^2\right)}{k_1} \quad , \tag{C.22}$$

$$G_4 = \frac{m_4 v_1 - m_5 v_3}{\left(v_1 - v_3\right)\left(v_1 + v_2 + v_3\right)} \tag{C.23}$$

and

$$G_5 = \frac{m_5\left(v_1 + v_2\right) - m_4\left(v_2 + v_3\right)}{\left(v_1 - v_3\right)\left(v_1 + v_2 + v_3\right)} \tag{C.24}$$

where

$$k_1 = v_1^3 + v_1^2 v_3 - v_1 v_2^2 - v_1 v_3^2 + v_2^2 v_3 - v_3^3 .$$

Figure C.10 shows an additional method of the placing the five sensors underneath the line configurations. Figure C.12 shows the relevant phase and sensor voltages and defines the set of transfer functions where the following simplify relationships are used:

$G_1 = G_{s1p1} = G_{s3p3} = G_{s2p2}$

$G_2 = G_{s1p2} = G_{s3p2} = G_{s2p1} = G_{s2p3}$

$G_3 = G_{s1p3} = G_{s3p1}$

$G_4 = G_{s4p1} = G_{s5p3}$

$G_5 = G_{s4p2} = G_{s5p2}$

$G_6 = G_{s4p3} = G_{s5p1}$

The voltage transfer function matrix **G** is then given by

$$\boldsymbol{G} = \begin{bmatrix} G_1 & G_2 & G_3 \\ G_2 & G_1 & G_2 \\ G_3 & G_2 & G_1 \\ G_4 & G_5 & G_6 \\ G_6 & G_5 & G_4 \end{bmatrix} . \tag{3.25}$$

The extra two sensors are placed outside sensors $s_1$ and $s_3$ so that a greater differentiation between the different transfer functions is created. For example, the further sensor $s_5$ is placed away from sensor $s_3$, the more transfer function $G_1$, $G_2$ and $G_3$ (differ from transfer function $G_4$, $G_5$ and $G_6$. Figure C.11 shows that the biggest difference between the vectors $m_3$ (the vectors from sensor $s_3$ to the three phases) and the vectors $m_{5a}$, $m_{5b}$ and $m_{5c}$ (the vectors from sensors $s_{5a}$, $s_{5b}$ and $s_{5c}$ to the three phases) is between $m_3$ and $m_{5c}$.

Thus, the greater the distance that the extra sensors (sensors $s_4$ and $s_5$) are placed from the sensors underneath the outside transmission lines (sensors $s_1$ and $s_3$), the greater the difference is between the transfer functions. This distance must however be inside a certain range where the electric fields are strong enough to induce a voltage onto the sensors. The greater the difference between the transfer functions is, the more accurate the unknown transmission line voltages can be calculated.

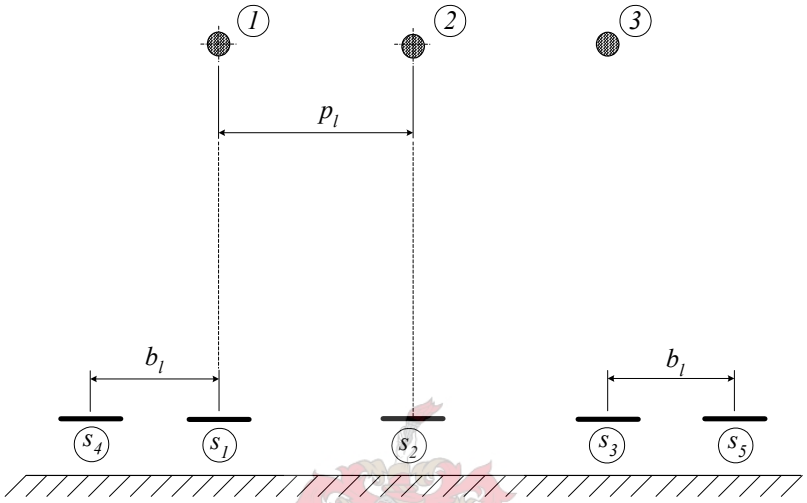


**Figure C.10: Two-dimensional view of a three-phase transmission line and five sensors, where two sensors are placed on the outside of the two outer conductors.**

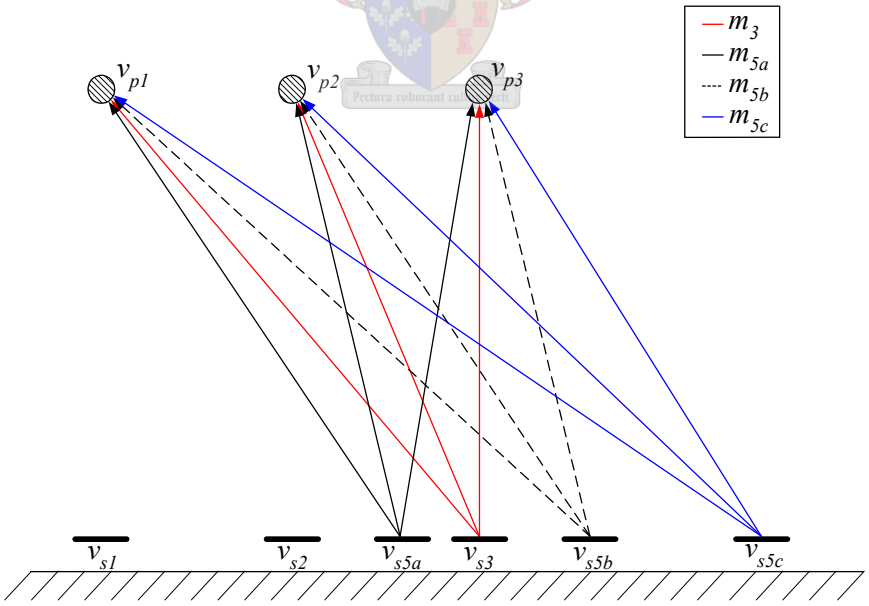


**Figure C.11: Two-dimensional view showing the difference between the various transfer functions when the sensors are placed at different positions.**

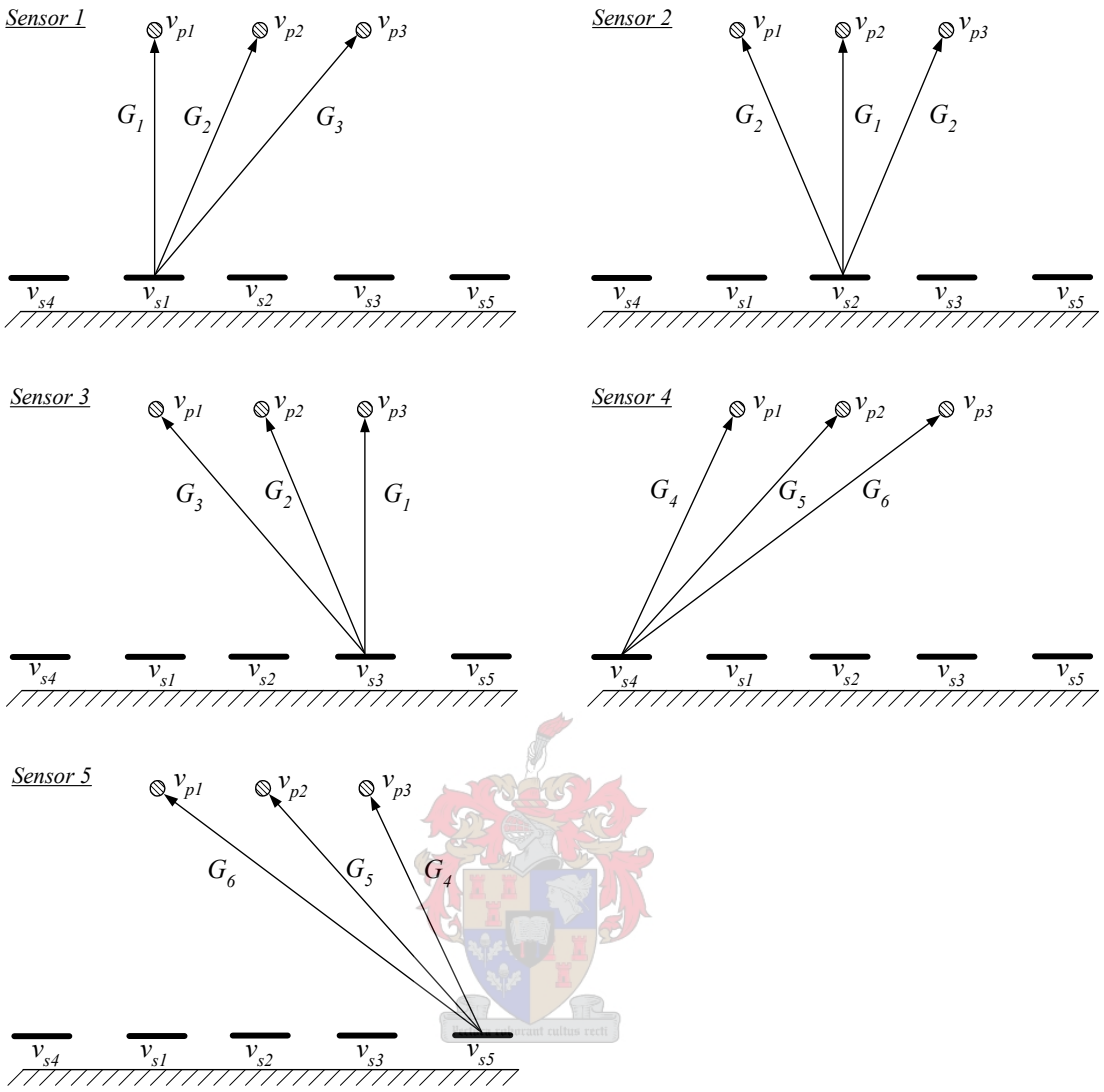


**Figure C.12: Voltage transfer function definitions for a five single-element plate sensor topology if the five sensors are placed as illustrated in Figure C.10.**

The five linear equations for the voltages induced on the five sensors are given by the relationships

$$v_{s1} = G_1 v_{p1} + G_2 v_{p2} + G_3 v_{p3} \ , \tag{C.26}$$

$$v_{s2} = G_2 v_{p1} + G_1 v_{p2} + G_2 v_{p3} \ , \tag{C.27}$$

$$v_{s3} = G_3 v_{p1} + G_2 v_{p2} + G_1 v_{p3} \ , \tag{C.28}$$

$$v_{s4} = G_4 v_{p1} + G_5 v_{p2} + G_6 v_{p3} \tag{C.29}$$

and

$$v_{s5} = G_6 v_{p1} + G_5 v_{p2} + G_4 v_{p3} \, . \tag{C.30}$$

The six transfer functions ($G_1$ to $G_6$) can not be evaluated as there are only five equations. A method must thus be found where only five unknown transfer functions, instead of six, are created by the sensor topology. To accomplish this, sensors $s_4$ and $s_5$ are placed in such a way that some of the transfer functions associated with these two sensors is similar to transfer functions associated with some of the other sensors. For this reason sensor $s_4$ and $s_5$ are placed the same distance from sensors $s_1$ and $s_3$. The distances between all five sensors are thus the same. Figure C.13 illustrates the transfer functions between the transmission line and the five sensors. Equations (C.26) to (C.30) can now be deduced to

$$v_{s1} = G_1 v_{p1} + G_2 v_{p2} + G_3 v_{p3} \ , \tag{C.31}$$

$$v_{s2} = G_2 v_{p1} + G_1 v_{p2} + G_2 v_{p3} \ , \tag{C.32}$$

$$v_{s3} = G_3 v_{p1} + G_2 v_{p2} + G_1 v_{p3} \ , \tag{C.33}$$

$$v_{s4} = G_2 v_{p1} + G_3 v_{p2} + G_4 v_{p3} \tag{C.34}$$

and

$$v_{s5} = G_4 v_{p1} + G_3 v_{p2} + G_2 v_{p3} \ . \tag{C.35}$$

Mathematica are used to solve the five equations simultaneously. The four transfer functions are given by the relationships

$$G_1 = \frac{m_1 v_1 \left(v_1 + v_3\right) + m_2 v_2 \left(v_3 - v_1\right) - m_3 v_3 \left(v_1 + v_3\right)}{k_1}, \tag{C.36}$$

$$G_2 = \frac{m_1 \left(-v_1 v_2\right) + m_2 \left(v_1^2 - v_3^2\right) + m_3 v_2 v_3}{k_1}, \tag{C.37}$$

$$G_3 = \frac{m_1 \left(v_2^2 - v_1 v_3 - v_3^2\right) + m_2 v_2 \left(v_3 - v_1\right) + m_3 \left(v_1^2 + v_1 v_3 - v_2^2\right)}{k_1} \tag{C.38}$$

and

$$G_4 = \frac{m_4}{v_3} + \frac{\left(v_1 + v_2\right)\left[m_1 v_1 v_2 - m_2 \left(v_1^2 - v_3^2\right) - m_3 v_2 v_3\right]}{v_3 k_1} \tag{C.39}$$

where

$$k_1 = v_1^3 + v_1^2 v_3 - v_1 v_2^2 - v_1 v_3^2 + v_2^2 v_3 - v_3^3 .$$

The equations for transfer functions $G_1$, $G_2$ and $G_3$ are the same as equations (C.20), (C.21) and (C.22).

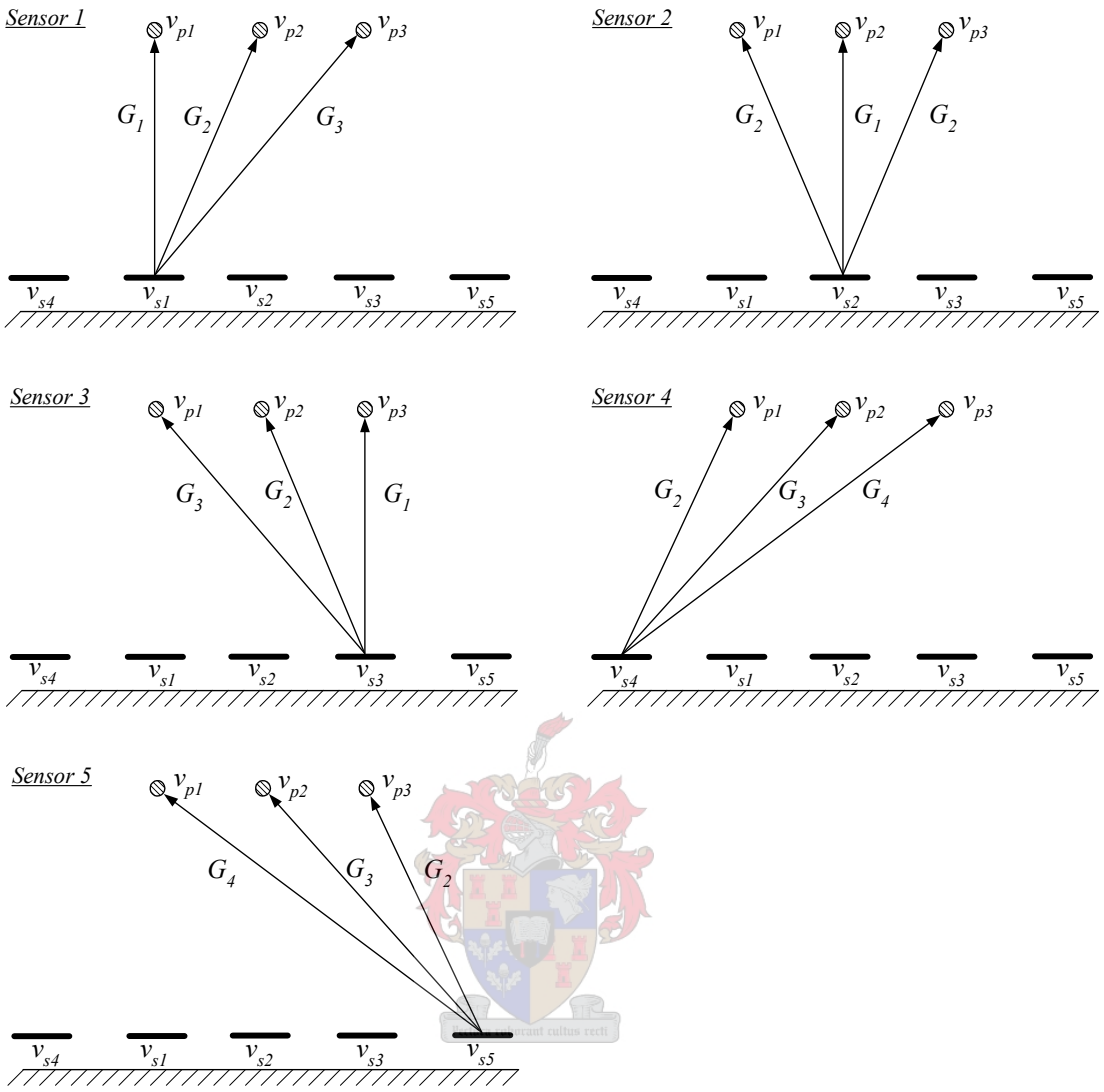


**Figure C.13 Voltage transfer function definitions for a five single-element plate sensor topology if the five sensors are placed the same distance from each other with the three middle sensors centralised beneath the overhead conductors.**

# Appendix D. Datasheets

## D.1. KEMET capacitors [75]

KEMET

### CERAMIC MOLDED AXIAL & RADIAL
PERFORMANCE CHARACTERISTICS

**GENERAL**

**Working Voltage:**
C0G – 50, 100 & 200 Volts
X7R – 50, 100 & 200 Volts

**Temperature Characteristics:**
C0G – 0 ±30 PPM/°C from -55°C to +125°C
X7R – ±15% from -55°C to +125°C

**Capacitance Tolerance:**
C0G – ±0.5 pF, ±1%, ±2%, ±5%, ±10%, ±20%
(±0.5 pF is tightest available tolerance)
X7R – ±10%, ±20%, -0 +100%, -20% +80%

**Construction:**
Monolithic block of ceramic dielectric with interdigitated internal electrodes, encapsulated in a molded case, and having axial or radial leads. Meets flame test requirements of UL Standard 94V-0.

**Terminal Strength:**
EIA-198 Method 303 Condition A (2.2 kg)

**ELECTRICAL**

**Capacitance:**
Within specified tolerance when measured with 1 volt rms at 1 kHz (1000 pF or less at 1 MHz for C0G).

**Dissipation Factor:**
25°C at 1 kHz (1000 pF or less at 1 MHz for C0G).
C0G – .15% maximum
X7R – 2.5% maximum

**Insulation Resistance:**
After 2 minutes electrification at 25°C and rated voltage
C0G – 100K megohms or 1000 megohm - µF, whichever is less.
X7R – 100K megohms or 1000 megohm - µF, whichever is less.

**Dielectric Withstanding Voltage:**
250% of rated voltage for 5 seconds with current limited to 50 mA at 25°C.

**Life Test:**
2000 hours at 200% of rated voltage at 125°C. Post-Test limits at 25°C are:

Capacitance Change:
C0G – less than 3% or 0.25 pF, whichever is higher
X7R – ±20% of initial value

Dissipation Factor:
C0G – .25% maximum
X7R – 3.0% maximum

Insulation Resistance:
C0G – 10K megohms or 100 megohm - µF, whichever is less
X7R – 10K megohms or 100 megohm - µF, whichever is less

Dielectric Withstanding Voltage:
250% of rated voltage for 5 seconds with current limited to 50 mA.

**ENVIRONMENTAL**

**Moisture Resistance:**
MIL-STD-202, Method 106, or EIA-198, Method 204, Condition A, except 20 cycles.

Insulation Resistance:
C0G – 10K megohms or 100 megohm - µF, whichever is less
X7R – 10K megohms or 100 megohm - µF, whichever is less

Dielectric Withstanding Voltage:
250% of rated voltage for 5 seconds with current limited to 50 mA.

**Immersion Cycling:**
MIL-STD-202, Method 104, Condition B. Post-Test limits at 25°C are:

Insulation Resistance:
C0G – 10K megohms or 100 megohm - µF, whichever is less
X7R – 10K megohms or 100 megohm - µF, whichever is less

**Solderability:**
MIL-STD-202, Method 208, Sn62 solder, 245°C for 5 ±1/2 seconds.

**Resistance to Soldering Heat:**
MIL-STD-202, Method 210, Condition B (260°C, 10 secs). Depth of immersion — to a minimum of .050" from the capacitor body.

**Lead Material:**
Axial: Solder-coated copper clad steel
Radial: Solder-coated copper

## D.2. Cable manufacturers

**Table D.1: Uniform code of conductors and comparisons for British Standards [63].**

**British Sizes BS 215, Part 2: 1970**

**ACSR**

**TABLE-7A**

| Code name | Nominal Area | Stranding & Wire Diameter | | Approximate Overall Diameter | Sectional Area | | | Approximate weight | Breaking Load | DC Resistance | Current Rating |
|---|---|---|---|---|---|---|---|---|---|---|---|
| | | Aluminium | Steel | | Aluminium | Steel | Total | | | | |
| | mm² | mm | mm | mm | mm² | mm² | mm² | kg/km | kN | ohm/km | A |
| Gopher | 25 | 6/2.36 | 1/2.36 | 7.08 | 26.24 | 4.38 | 30.62 | 106 | 9.61 | 1.0930 | 126 |
| Weasel | 30 | 6/2.59 | 1/2.59 | 7.77 | 31.61 | 5.27 | 36.88 | 128 | 11.45 | 0.9077 | 134 |
| Ferret | 40 | 6/3.00 | 1/3.00 | 9.00 | 42.41 | 7.07 | 49.48 | 172 | 15.20 | 0.6766 | 161 |
| Rabbit | 50 | 6/3.35 | 1/3.35 | 10.05 | 52.88 | 8.82 | 61.70 | 214 | 18.35 | 0.5426 | 185 |
| Horse | 70 | 12/2.79 | 7/2.79 | 13.95 | 73.37 | 42.83 | 116.20 | 538 | 61.20 | 0.3936 | 268 |
| Dog | 100 | 6/4.72 | 7/1.57 | 14.15 | 105.00 | 13.50 | 118.50 | 394 | 32.70 | 0.2733 | 278 |
| Wolf | 150 | 30/2.59 | 7/2.59 | 18.13 | 158.10 | 36.80 | 194.90 | 726 | 69.20 | 0.1828 | 355 |
| Dingo | 150 | 18/3.35 | 1/3.35 | 16.75 | 158.70 | 8.80 | 167.50 | 506 | 35.70 | 0.1815 | 349 |
| Lynx | 175 | 30/2.79 | 7/2.79 | 19.53 | 183.40 | 42.80 | 226.20 | 842 | 79.80 | 0.1576 | 386 |
| Caracal | 175 | 18/3.61 | 1/3.61 | 18.05 | 184.30 | 10.20 | 194.50 | 587 | 41.10 | 0.1563 | 383 |
| Panther | 200 | 30/3.00 | 7/3.00 | 21.00 | 212.10 | 49.20 | 261.50 | 974 | 92.25 | 0.1363 | 421 |
| Jaguar | 200 | 18/3.86 | 1/3.86 | 19.30 | 210.60 | 11.70 | 222.30 | 671 | 46.55 | 0.1367 | 415 |
| Zebra | 400 | 54/3.18 | 7/3.18 | 28.62 | 428.90 | 55.60 | 484.50 | 1621 | 131.90 | 0.0674 | 635 |

**British Sizes BS EN 50182:2001**

**TABLE-7B**

| Code name | Stranding & Wire Diameter | | Approximate Overall Diameter | Sectional Area | | | Approximate weight | Breaking Load | DC Resistance | Current Rating |
|---|---|---|---|---|---|---|---|---|---|---|
| | Aluminium | Steel | | Aluminium | Steel | Total | | | | |
| | mm | mm | mm | mm² | mm² | mm² | kg/km | kN | ohm/km | A |
| Mole | 6/1.50 | 1/1.50 | 4.50 | 10.6 | 1.77 | 12.4 | 42.8 | 4.14 | 2.7027 | 67 |
| Squirrel | 6/2.11 | 1/2.11 | 6.33 | 21.0 | 3.50 | 24.5 | 84.7 | 7.87 | 1.3659 | 109 |
| Fox | 6/2.79 | 1/2.79 | 8.37 | 36.7 | 6.11 | 42.8 | 148.1 | 13.21 | 0.7812 | 147 |
| Mink | 6/3.66 | 1/3.66 | 11.00 | 63.1 | 10.50 | 73.6 | 254.9 | 21.67 | 0.4540 | 174 |
| Skunk | 12/2.59 | 7/2.59 | 13.00 | 63.2 | 36.90 | 100.1 | 463.0 | 52.79 | 0.4568 | 246 |
| Beaver | 6/3.99 | 1/3.99 | 12.00 | 75.0 | 12.50 | 87.5 | 302.9 | 25.76 | 0.3820 | 193 |
| Racoon | 6/4.10 | 1/4.10 | 12.30 | 78.8 | 13.10 | 92.4 | 318.3 | 27.06 | 0.3635 | 231 |
| Otter | 6/4.22 | 1/4.22 | 12.70 | 83.9 | 14.00 | 97.9 | 338.8 | 28.81 | 0.3415 | 240 |
| Cat | 6/4.50 | 1/4.50 | 13.50 | 95.4 | 15.90 | 111.3 | 385.3 | 32.76 | 0.3003 | 248 |
| Hare | 6/4.72 | 1/4.72 | 14.20 | 105.0 | 17.50 | 122.5 | 423.8 | 36.04 | 0.2730 | 273 |
| Coyote | 26/2.54 | 7/1.91 | 15.90 | 131.7 | 20.10 | 151.8 | 520.7 | 45.86 | 0.2192 | 311 |
| Cougar | 18/3.05 | 1/3.05 | 15.30 | 131.5 | 7.31 | 138.8 | 418.8 | 29.74 | 0.2188 | 314 |
| Tiger | 30/2.36 | 7/2.36 | 16.50 | 131.2 | 30.60 | 161.8 | 602.2 | 57.87 | 0.2202 | 323 |
| Lion | 30/3.18 | 7/3.18 | 22.30 | 238.3 | 55.60 | 293.9 | 1093.4 | 100.47 | 0.1213 | 448 |
| Bear | 30/3.35 | 7/3.35 | 23.50 | 264.4 | 61.70 | 326.1 | 1213.4 | 111.50 | 0.1093 | 481 |
| Goat | 30/3.71 | 7/3.71 | 26.00 | 324.3 | 75.70 | 400.0 | 1488.2 | 135.13 | 0.0891 | 542 |
| Sheep | 30/3.99 | 7/3.99 | 27.90 | 375.1 | 87.50 | 462.6 | 1721.3 | 156.30 | 0.0771 | 592 |
| Antelope | 54/2.97 | 7/2.97 | 26.70 | 374.1 | 48.50 | 422.6 | 1413.8 | 118.88 | 0.0773 | 588 |
| Bison | 54/3.00 | 7/3.00 | 27.00 | 381.7 | 49.50 | 431.2 | 1442.5 | 121.30 | 0.0758 | 595 |
| Deer | 30/4.27 | 7/4.27 | 29.90 | 429.6 | 100.20 | 529.8 | 1971.4 | 179.00 | 0.0673 | 639 |
| Elk | 30/4.50 | 7/4.50 | 31.50 | 477.1 | 111.30 | 588.4 | 2189.5 | 198.80 | 0.0606 | 679 |
| Camel | 54/3.35 | 7/3.35 | 30.20 | 476.0 | 61.70 | 537.7 | 1798.8 | 146.40 | 0.0608 | 677 |
| Moose | 54/3.53 | 7/3.53 | 31.80 | 528.5 | 68.50 | 597.0 | 1997.3 | 159.92 | 0.0547 | 763 |

**Table D.2: Uniform code of conductors and comparisons for American Standards [63].**

American Sizes ASTM B 232/B 232M-99

ACSR

TABLE-9

| Code Name | Area | | | Stranding and Wire Diameter | | Overall Diameter | Weight | Breaking Load | DC Resistance at 20°C | Current Rating |
|---|---|---|---|---|---|---|---|---|---|---|
| | Aluminium | Steel | Total | Aluminium | Steel | | | | | |
| | $mm^2$ | $mm^2$ | $mm^2$ | mm | mm | mm | kg/ km | kN | ohm/ km | A |
| Turkey | 13.29 | 2.21 | 15.5 | 6/1.68 | 1/1.68 | 5.04 | 53.6 | 5.2 | 2.15700 | 78 |
| Swan | 21.16 | 3.55 | 24.71 | 6/2.12 | 1/2.12 | 6.36 | 85.3 | 8.3 | 1.35600 | 105 |
| Swanate | 21.16 | 5.35 | 26.51 | 7/1.96 | 1/2.61 | 6.53 | 99.6 | 10.5 | 1.35600 | 104 |
| Sparrow | 33.61 | 5.61 | 39.22 | 6/2.67 | 1/2.67 | 8.01 | 135.7 | 12.7 | 0.85300 | 139 |
| Sparate | 33.61 | 8.52 | 42.13 | 7/2.47 | 1/3.30 | 8.24 | 158.7 | 16.1 | 0.85300 | 138 |
| Robin | 42.39 | 7.1 | 49.49 | 6/3.00 | 1/3.00 | 9 | 171.1 | 15.8 | 0.67650 | 160 |
| Raven | 53.48 | 8.9 | 62.38 | 6/3.37 | 1/3.37 | 10.11 | 216.1 | 19.4 | 0.53640 | 183 |
| Quail | 67.42 | 11.23 | 78.65 | 6/3.78 | 1/3.78 | 11.34 | 272.0 | 23.6 | 0.42550 | 210 |
| Pigeon | 85.03 | 14.19 | 99.22 | 6/4.25 | 1/4.25 | 12.75 | 343.0 | 29.5 | 0.33730 | 241 |
| Penguin | 107.23 | 17.87 | 125.1 | 6/4.77 | 1/4.77 | 14.31 | 432.7 | 37.1 | 0.26760 | 276 |
| Waxwing | 135.16 | 7.48 | 142.64 | 18/3.09 | 1/3.09 | 15.45 | 430.2 | 30.6 | 0.21330 | 319 |
| Partridge | 135.16 | 22 | 157.16 | 26/2.57 | 7/2.00 | 16.28 | 545.9 | 50.3 | 0.21420 | 323 |
| Ostrich | 152 | 24.77 | 176.77 | 26/2.73 | 7/2.12 | 17.28 | 613.4 | 56.5 | 0.19060 | 346 |
| Linnet | 170.45 | 27.74 | 198.19 | 26/2.89 | 7/2.25 | 18.31 | 687.5 | 62.7 | 0.16990 | 371 |
| Oriole | 170.45 | 39.81 | 210.26 | 30/2.69 | 7/2.69 | 18.83 | 783.3 | 77.0 | 0.17040 | 372 |
| Chickdee | 201.42 | 11.16 | 212.58 | 18/3.77 | 1/3.77 | 18.85 | 641.3 | 44.2 | 0.14320 | 403 |
| Brant | 201.42 | 26.13 | 227.55 | 24/3.27 | 7/2.18 | 19.61 | 761.0 | 64.9 | 0.14380 | 405 |
| Ibis | 201.42 | 32.77 | 234.19 | 26/3.14 | 7/2.44 | 19.88 | 812.4 | 72.5 | 0.14380 | 403 |
| Lark | 201.42 | 46.97 | 248.39 | 30/2.92 | 7/2.92 | 20.44 | 925.2 | 90.3 | 0.14420 | 410 |
| Pelican | 241.68 | 13.42 | 255.1 | 18/4.14 | 1/4.14 | 20.7 | 769.7 | 52.5 | 0.11930 | 449 |
| Flicker | 241.68 | 31.29 | 272.97 | 24/3.58 | 7/2.39 | 21.49 | 913.5 | 76.1 | 0.11990 | 454 |
| Hawk | 241.68 | 39.35 | 281.03 | 26/3.44 | 7/2.68 | 21.8 | 975.1 | 86.7 | 0.11990 | 455 |
| Hen | 241.68 | 56.39 | 298.07 | 30/3.20 | 7/3.20 | 22.4 | 1110.3 | 105.9 | 0.12020 | 457 |
| Osprey | 282 | 15.68 | 297.68 | 18/4.47 | 1/4.47 | 22.35 | 897.7 | 60.9 | 0.10220 | 492 |
| Parakeet | 282 | 36.58 | 318.58 | 24/3.87 | 7/2.58 | 23.22 | 1065.6 | 88.1 | 0.10280 | 492 |
| Dove | 282 | 45.94 | 327.94 | 26/3.72 | 7/2.89 | 23.55 | 1138.6 | 100.5 | 0.10280 | 499 |
| Eagle | 282 | 65.81 | 347.81 | 30/3.46 | 7/3.46 | 24.21 | 1295.6 | 123.7 | 0.10300 | 500 |
| Peacock | 306.58 | 39.74 | 346.32 | 24/4.03 | 7/2.69 | 24.2 | 1158.9 | 95.6 | 0.09449 | 522 |
| Squab | 306.58 | 49.94 | 356.52 | 26/3.87 | 26/.1525 | 24.51 | 1237.0 | 106.8 | 0.09449 | 523 |
| Wood Duc | 306.58 | 71.55 | 378.13 | 30/3.61 | 7/3.61 | 25.25 | 1408.4 | 128.5 | 0.09473 | 523 |
| Teal | 306.58 | 69.87 | 376.45 | 30/3.61 | 19/2.16 | 25.24 | 1396.6 | 133.4 | 0.09475 | 527 |
| Kingbird | 322.39 | 17.74 | 340.13 | 18/4.78 | 1/4.78 | 23.88 | 1026.6 | 69.4 | 0.89420 | 530 |
| Rook | 322.26 | 41.81 | 364.07 | 24/4.14 | 7/2.76 | 24.84 | 1217.6 | 101.0 | 0.08989 | 537 |
| Grosbeak | 300.26 | 52.52 | 374.78 | 26/3.97 | 7/3.09 | 25.15 | 1300.8 | 112.1 | 0.08989 | 538 |
| Scoter | 322.26 | 75.22 | 397.48 | 30/3.70 | 7/3.70 | 25.88 | 1480.7 | 134.8 | 0.09011 | 541 |
| Egret | 322.26 | 7.48 | 395.74 | 30/3.70 | 19/2.22 | 25.9 | 1469.0 | 140.1 | 0.09012 | 542 |
| Flamingo | 337.74 | 43.81 | 381.55 | 24/4.23 | 7/2.82 | 25.4 | 1276.6 | 105.4 | 0.08576 | 552 |
| Gannet | 337.81 | 55.03 | 392.84 | 26/4.07 | 7/3.16 | 28.3 | 1363.3 | 117.4 | 0.08576 | 618 |
| Stilt | 362.64 | 46.97 | 409.61 | 24/4.39 | 7/2.92 | 26.31 | 1370.4 | 113.4 | 0.07989 | 577 |
| Starling | 362.58 | 59.03 | 421.61 | 26/4.21 | 7/3.28 | 26.68 | 1463.7 | 126.3 | 0.07992 | 578 |
| Redwing | 362.58 | 82.64 | 445.22 | 30/3.92 | 19/2.35 | 27.43 | 1650.6 | 153.9 | 0.08009 | 581 |
| Tern | 402.84 | 27.87 | 430.71 | 45/3.38 | 7/2.25 | 27.03 | 1331.8 | 98.3 | 0.07192 | 610 |
| Condor | 402.84 | 52.19 | 455.03 | 54/3.08 | 7/3.08 | 27.72 | 1520.7 | 125.4 | 0.07192 | 614 |
| Cuckoo | 402.9 | 52.2 | 455.1 | 24/4.62 | 7/3.08 | 27.74 | 1522.2 | 124.1 | 0.07190 | 614 |
| Darke | 402.84 | 65.61 | 468.45 | 26/4.44 | 7/3.45 | 28.11 | 1626.4 | 140.1 | 0.07192 | 614 |

**Table D.3: Uniform code of conductors and comparisons for American Standards (continue) [63].**

American Sizes ASTM B 232/B 232M-99

ACSR

TABLE-9 (Contd)

| Code Name | Area | | | Stranding and Wire Diameter | | Overall Diameter | Weight | Breaking Load | DC Resistance at 20°C | Current Rating |
|---|---|---|---|---|---|---|---|---|---|---|
| | Aluminium | Steel | Total | Aluminium | Steel | | | | | |
| | $mm^2$ | $mm^2$ | $mm^2$ | mm | mm | mm | kg/ km | | $mm^2$ | $mm^2$ |
| Mallard | 402.84 | 91.87 | 494.71 | 30/4.14 | 19/2.48 | 28.96 | 1836.0 | 170.8 | 0.07208 | 618 |
| Ruddy | 455.81 | 31.54 | 487.35 | 45/3.59 | 7/2.40 | 28.73 | 1507.3 | 108.3 | 0.06356 | 656 |
| Canary | 456.06 | 59.1 | 515.16 | 54/3.28 | 7/3.28 | 29.52 | 1723.1 | 141.9 | 0.06352 | 660 |
| Rail | 483.42 | 33.42 | 516.84 | 45/3.70 | 7/2.47 | 29.61 | 1598.1 | 115.2 | 0.05994 | 679 |
| Cardinal | 483.42 | 62.65 | 546.07 | 54/3.38 | 7/3.38 | 30.42 | 1825.9 | 150.3 | 0.05994 | 681 |
| Ortlan | 523.68 | 36.19 | 559.87 | 45/3.85 | 7/2.57 | 30.81 | 1730.5 | 123.2 | 0.05531 | 712 |
| Curlew | 523.68 | 67.87 | 591.55 | 54/3.52 | 7/3.52 | 31.68 | 1977.6 | 162.8 | 0.05531 | 15 |
| Bluejay | 563.93 | 39.03 | 602.96 | 45/4.00 | 7/2.66 | 31.98 | 1866.0 | 132.6 | 0.05161 | 743 |
| Finch | 563.93 | 71.48 | 635.41 | 54/3.65 | 19/2.19 | 32.85 | 2127.8 | 173.9 | 0.05161 | 746 |
| Bunting | 604.26 | 41.55 | 645.81 | 45/4.14 | 7/2.76 | 33.12 | 1996.9 | 141.9 | 0.04820 | 772 |
| Grackle | 604.26 | 76.52 | 680.78 | 54/3.77 | 19/2.27 | 33.97 | 2278.1 | 185.9 | 0.04820 | 773 |
| Bittern | 644.51 | 44.52 | 689.03 | 45/4.27 | 7/2.85 | 34.17 | 2130.8 | 151.7 | 0.04518 | 802 |
| Pheasant | 644.51 | 81.68 | 726.19 | 54/3.90 | 19/2.34 | 35.1 | 2431.4 | 193.9 | 0.04518 | 807 |
| Dipper | 685.16 | 47.1 | 732.26 | 45/4.40 | 7/2.92 | 35.16 | 2263.0 | 161.0 | 0.04259 | 831 |
| Martin | 684.84 | 86.71 | 771.55 | 54/4.02 | 19/2.41 | 36.17 | 2581.7 | 205.9 | 0.04259 | 835 |
| Bobolink | 725.16 | 50.32 | 775.48 | 45/4.53 | 7/3.02 | 36.24 | 2397.2 | 170.8 | 0.04016 | 859 |
| Plover | 725.16 | 91.81 | 816.97 | 54/4.14 | 19/2.48 | 37.24 | 2734.9 | 218.0 | 0.04016 | 862 |
| Nuthatch | 765.16 | 52.9 | 818.06 | 45/4.65 | 7/3.10 | 37.2 | 2529.6 | 178.4 | 0.03802 | 886 |
| Parrot | 765.16 | 97.16 | 62.32 | 54/4.25 | 19/2.55 | 38.25 | 2883.7 | 230.4 | 0.03802 | 890 |
| Lapwing | 805.8 | 55.48 | 861.28 | 45/4.77 | 7/3.18 | 38.16 | 2663.5 | 187.3 | 0.03612 | 911 |
| Falcon | 805.8 | 102.32 | 908.12 | 54/4.36 | 19/2.62 | 39.26 | 3038.5 | 242.9 | 0.03612 | 917 |
| Chuckar | 901.93 | 73.55 | 975.48 | 84/3.70 | 19/2.22 | 40.7 | 3083.1 | 228.2 | 0.03228 | 975 |
| **HIGH STRENGTH STRANDINGS** | | | | | | | | | | |
| Grouse | 40.52 | 14.13 | 54.65 | 8/2.54 | ¼.24 | 9.32 | 221.4 | 23.1 | 0.7113 | 155 |
| Petrel | 51.61 | 30.06 | 81.67 | 12/2.34 | 7/2.34 | 11.71 | 337.7 | 46.3 | 0.5617 | 187 |
| Minorca | 56.13 | 32.77 | 88.9 | 12/2.44 | 7/2.44 | 12.22 | 411.1 | 50.3 | 0.5161 | 197 |
| Leghorn | 68.58 | 39.81 | 108 | 12/2.69 | 7/2.69 | 13.46 | 499.2 | 60.5 | 0.4249 | 221 |
| Guinea | 80.58 | 46.97 | 127.55 | 12/2.92 | 7/2.92 | 14.63 | 589.7 | 71.2 | 0.3596 | 244 |
| Dotterel | 89.61 | 52.32 | 141.93 | 12/3.08 | 7/3.08 | 15.42 | 656.1 | 77.0 | 0.3232 | 260 |
| Dorking | 96.71 | 56.39 | 153.1 | 12/3.20 | 7/3.20 | 16.03 | 707.8 | 83.2 | 0.2996 | 272 |
| Cochin | 107.1 | 62.45 | 169.55 | 12/3.37 | 7/3.37 | 16.84 | 783.9 | 92.1 | 0.2706 | 288 |
| Brahma | 102.97 | 91.87 | 194.84 | 16/2.86 | 19/2.48 | 18.14 | 1003.8 | 126.3 | 0.2814 | 287 |

**Table D.4: Conductor configurations**

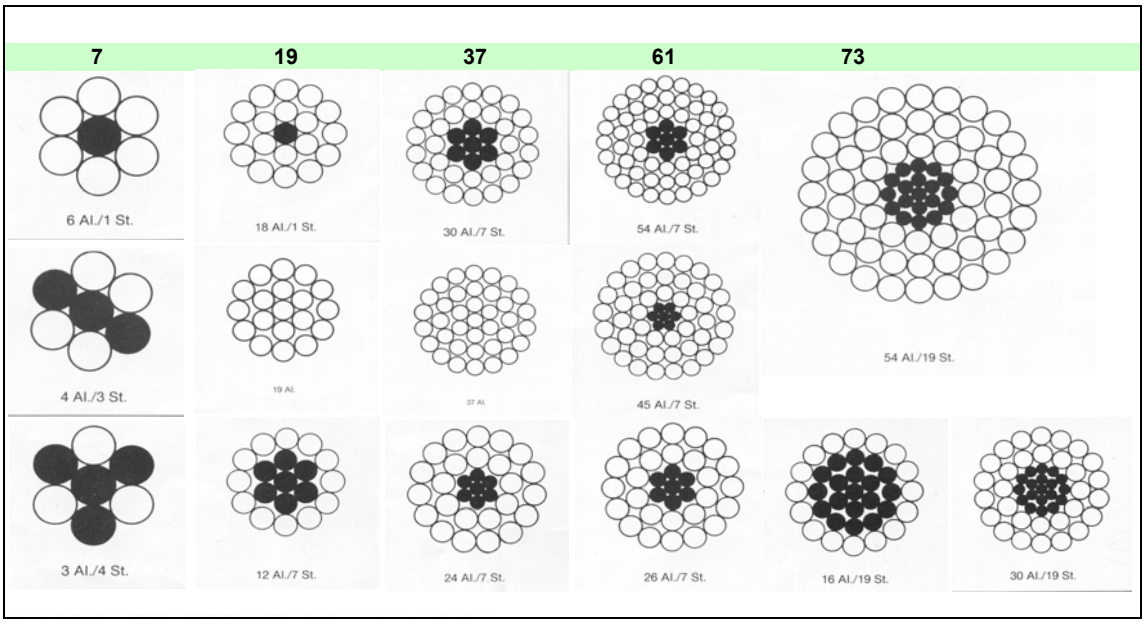


**Table D.5: Conductor Configurations**

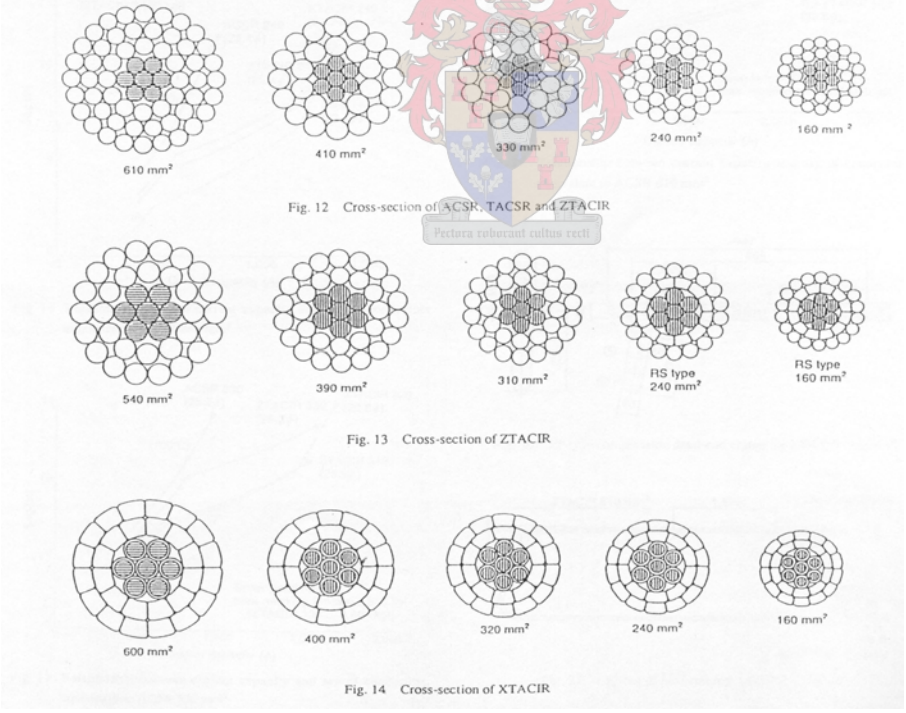


**Figure D.1: Photograph of different conductors used by ESKOM.**

# Appendix E. Tower configurations

The tower data for different 132kV power lines are given in the following tables.

**Table E.1:** ***132kV Type M14 DWG*** **tower data.**

| 132kV SC Type M14 DWG INPUT | Horizontal [m] | Vertical [m] | Conductor | | | |
|---|---|---|---|---|---|---|
| | | | Min | Typ | Max | SW |
| Neutral 1 | 0 | 20 | | Kingbird | | OPGW138 |
| Neutral 2 | 0 | 20 | | | | |
| Phase A | -1.5 | 14 | | | | |
| Phase B | 1.5 | 15.1 | | | | |
| Phase C | -1.5 | 16.2 | | | | |

**Table E.2:** ***132kV Type 218A*** **tower data.**

| 132kV DC Type 218A DWG INPUT | Horizontal [m] | Vertical [m] | Conductor | | | |
|---|---|---|---|---|---|---|
| | | | Min | Typ | Max | SW |
| Neutral 1 | -1.65 | 29.4 | Wolf | Goat | 2xBear | 19/0.104 |
| Neutral 2 | 1.65 | 29.4 | | | | |
| Phase A | -4.1 | 17.7 | | | | |
| Phase B | -4.1 | 21.5 | | | | |
| Phase C | -4.1 | 25.3 | | | | |
| Phase `A | 4.1 | 17.7 | | | | |
| Phase `B | 4.1 | 21.5 | | | | |
| Phase `C | 4.1 | 25.3 | | | | |

**Table E.3:** ***132kV, Type 247A,*** **tower data**

| 132kV DC Type 247A DWG INPUT | Horizontal [m] | Vertical [m] |
|---|---|---|
| Neutral 1 | -2.8 | 31.15 |
| Neutral 2 | 2.8 | 31.15 |
| Phase A | -3.6 | 17.1 |
| Phase B | -3.6 | 22.3 |
| Phase C | -3.6 | 27.4 |
| Phase `A | 3.6 | 17.1 |
| Phase `B | 3.6 | 22.3 |
| Phase `C | 3.6 | 27.4 |

**Table E.4:** ***132kV, Type 224A*** **tower data.**

| 132kV SC Type 224A DWG INPUT | Horizontal [m] | Vertical [m] | Conductor | | | |
|---|---|---|---|---|---|---|
| | | | Min | Typ | Max | SW |
| Neutral 1 | -4.51 | 19.85 | Wolf | 2xWolf | 2xBear | 7/3.35 |
| Neutral 2 | 4.51 | 19.85 | | | | |
| Phase A | -6 | 14.738 | | | | |
| Phase B | 0 | 14.738 | | | | |
| Phase C | 6 | 14.738 | | | | |

**Table E.5:** ***132kV, Type 240A*** **Tower data.**

| 132kV SC Type 240A DWG INPUT | Horizontal [m] | Vertical [m] | Conductor | | | |
|---|---|---|---|---|---|---|
| | | | Min | Typ | Max | SW |
| Neutral 1 | -4.85 | 20.722 | Wolf | Bear | Zebra | 19/6.25 |
| Neutral 2 | 4.85 | 20.722 | | | | |
| Phase A | -5.5 | 17.575 | | | | |
| Phase B | 0 | 17.575 | | | | |
| Phase C | 5.5 | 17.575 | | | | |

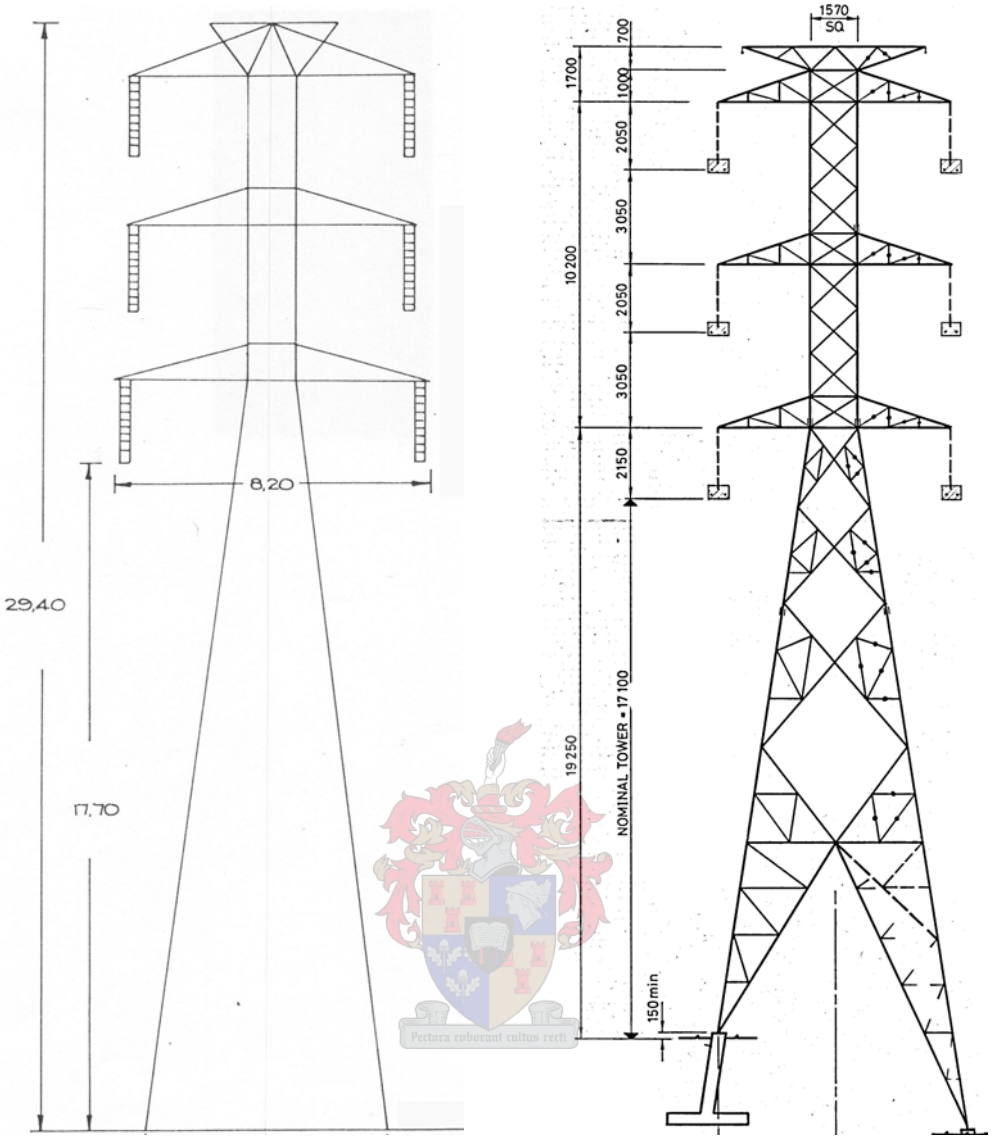


**Figure E.1: (a) 132kV Type 218A tower** **(b) 132kV Type 247A tower.**

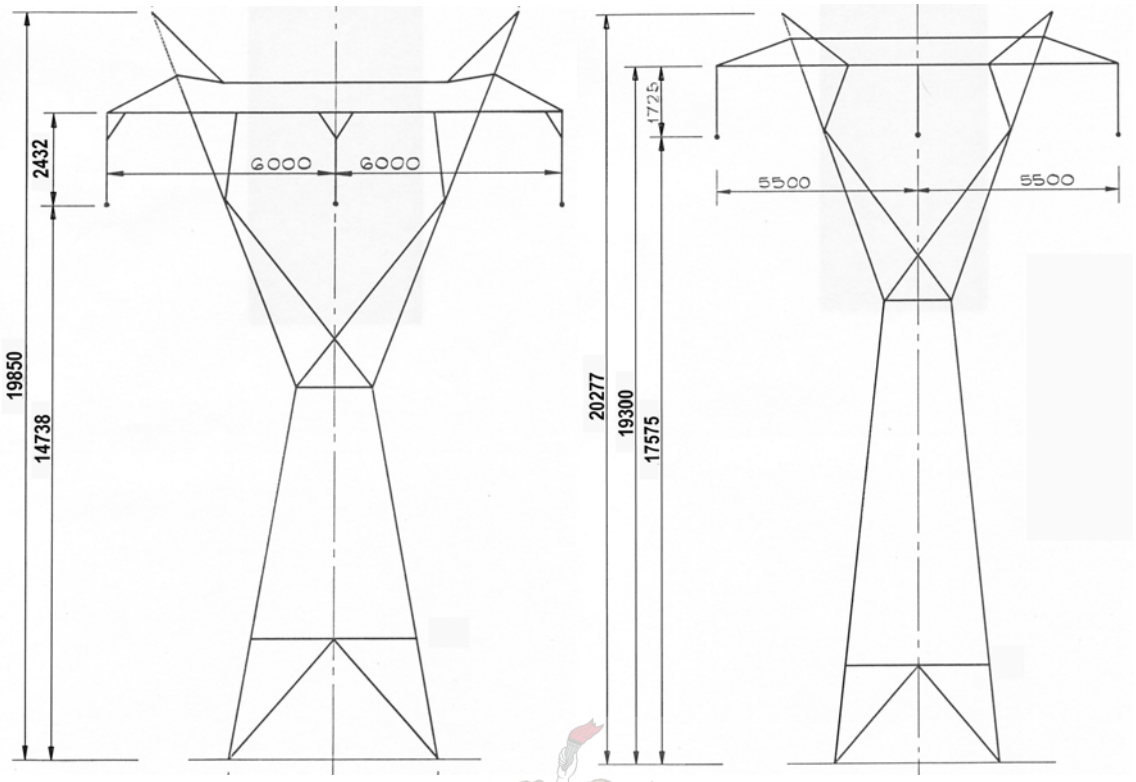


**Figure E.2: (a)** ***132kV, Type 224A*** **tower** **(b)** ***132kV, Type 240A*** **tower**

# Appendix F. Triggering system

## F.1. Biquad, bandpass filter

The circuit in Figure F.1 is a normalized bandpass filter with a given Q and G. The gain of a bandpass filter is defined as the value of its transfer function *H(s)* at the centre frequency $\omega_0$, since s = $j\omega_0$. The gain of the bandpass filter is *G*. The quality factor *Q* is defined by [51]

$$Q = \frac{\omega}{B} \tag{F.1}$$

and $B = \omega_U - \omega_L$, where *B* is defined as the bandwidth, $\omega_U$ as the upper frequency and $\omega_L$ as the lower frequency. For the de-normalized case the transfer function is given as [51]

$$\frac{V_2}{V_1} = \frac{\frac{G\omega_0 s}{Q}}{s^2 + \frac{\omega_0 s}{Q} + \omega_0^2} \ . \tag{F.2}$$

This results in [51]

$$\begin{aligned} R_1 &= \frac{Q}{G\omega_0 C} \\ R_2 &= \frac{Q}{\omega_0 C} \\ R_3 &= \frac{1}{\omega_0^2 R_4 C^2} \end{aligned} \tag{F.3}$$



where $R_4$ and *C* are arbitrary. $R_1$, $R_2$, $R_3$, $R_4$, and *C* are shown in Figure F.1. If $R_4$ is selected equal to $R_3$, then by the last relationship in equation (F.3), $R_3$ can be defined as [51]

$$R_3 = R_4 = \frac{1}{\omega_0 C} \ . \tag{F.4}$$

The biquad circuit is easily tuned and the centre frequency may be adjusted by varying $R_3$, *Q* may be adjusted by varying $R_2$, and the gain may be adjusted by varying $R_1$. The circuit in Figure F.1 is designed by using equations (F.2), (F.3) and(F.4). This circuit is implemented into the triggering system. The gain is set as 1 and the quality factor is set equal to 5.

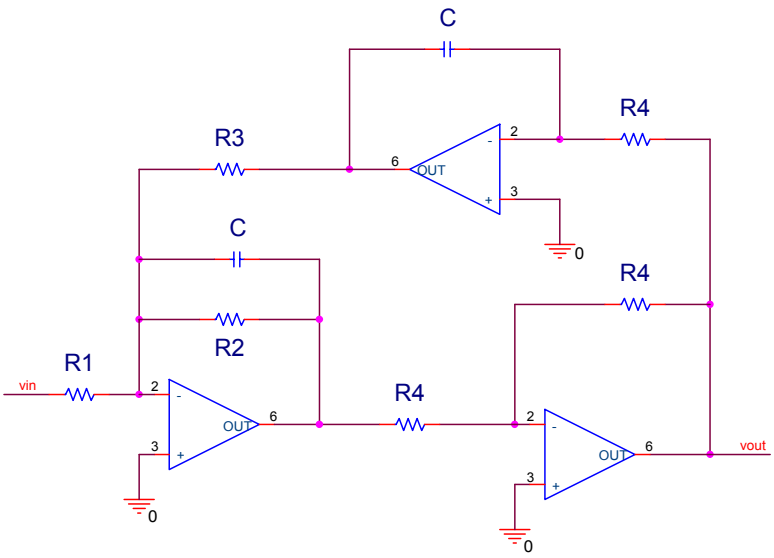


**Figure F.1 : A normalized biquad bandpass filter.**

## F.2. Low pass filters

### F.2.1. Preliminary definitions

A low-pass filter has a single passband ($0 < \omega < \omega_c$) and *cutoff* frequency $\omega_c$, with all frequencies higher than $\omega_c$ constituting to the stopband. The *bandwidth* is defined as $B = \omega_c$. The passband and stopband are clearly indicated in the ideal case but in the realizable case the cut-off point must be defined. Normally $\omega_c$ is the point at which $|H(j\omega)|$ is $1/\sqrt{2} = 0.707$ times its maximum value $A$. Since $|H(j\omega)|^2$ is often related to power, and at $\omega_c$, $|H(j\omega)|^2$ is half its maximum value, the point $\omega_c$ is called also the *half-power* point.

The *loss* is converted to decibels (dB) by multiplying it by the factor $20\log_{10}e$. That is the loss in dB is given by [51]

$$\begin{aligned}\alpha_{dB} &= (20\log_{10} e)\alpha \\ &= -20\log_{10} e^{-\alpha} \\ &= -20\log_{10}|H(j\omega)|\end{aligned} \quad . \tag{F.5}$$

Finally, at $\omega_c$, the loss $\alpha_{dB}$, is given by [51]

$$\begin{aligned}\alpha_{dB}(\omega_c) &= -20\log_{10}\frac{A}{\sqrt{2}} \\ &= 3 - 20\log_{10} A \\ &= 3 + \alpha_{dB_{\min}}\end{aligned} \quad . \tag{F.6}$$

Thus at $\omega_c$ the loss is 3dB greater than the minimum loss $\alpha_{dBmin}$, and for this reason $\omega_c$ is occasionally called the 3 dB point. There is some passage in the stopband in the non-ideal

case (as well as some attenuation in the passband). Thus it is convenient to define the stopband as $\omega_c > \omega_1$, where $\omega_1$ is the point at which the response reaches and remains with increasing $\omega$ below some specified value. The interval ($\omega_c < \omega < \omega_1$) in which the response is monotonically decreasing is then referred as the *transition* band [51].

### F.2.2. VCVS, low pass filter

The low-pass filter that is used for the triggering system is the second-order *VCVS* low-pass filter [51]. This low-pass filter achieves the transfer function denoted by [51]

$$\frac{V_2}{V_1} = \frac{Gb_0}{s^2 + b_1 s + b_0} \tag{F.7}$$

provided that [51]

$$\begin{aligned} b_0 &= \frac{1}{R_1 R_2 C_1 C_2} \\ b_1 &= \frac{1}{C_2}\left(\frac{1}{R_1} + \frac{1}{R_2}\right) + \frac{1}{R_2 C_1}(1-\mu) \\ G &= \mu = 1 + \frac{R_4}{R_3} \end{aligned} \tag{F.8}$$

holds. The elements of the second-order *VCVS* low-pass filter are numbered as shown in Figure F.2. Resistors $R_3$ and $R_4$ are arbitrary except that their ration must be fixed. However, for best operation they should be chosen to minimize the DC offset of the op amp. Theoretical there is no voltage difference between the positive and negative terminals of the op-amp, but in order for a real op-amp to work there must be a slight current in its leads. Thus the offset voltage will be minimized if the resistance $R_1 - R_2$ and $R_3R_4/(R_3-R_4)$ of the two parallel input paths are equal. From this condition and the last equation in (F.8) μ can be defined as [51]

$$\mu = 1 + \frac{R_4}{R_3} = \frac{(R_3 + R_4)R_4}{R_3 R_4} = \frac{R_4}{R_1 + R_2} \ .$$

Thus for minimum DC offset $R_3$ and $R_4$ can be defined by the relationships [51]

$$\begin{aligned} R_4 &= \mu R_{eq} \\ R_3 &= \frac{R_4}{\mu - 1} = \frac{\mu R_{eq}}{\mu - 1}, \qquad \mu \neq 1 \end{aligned} \tag{F.9}$$

where

$$R_{eq} = R_1 + R_2 \ . \tag{F.10}$$

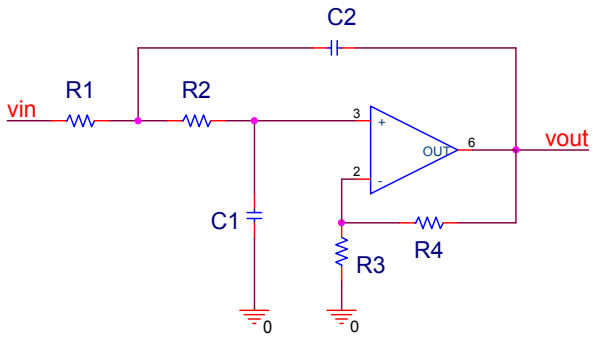


**Figure F.2 : A second-order VCVS low-pass filter [51].**

Taking $C_2 = 1F$ in Figure F.2, equation (F.8) changes to [51]

$$\begin{aligned} G &= \mu = 1 + \frac{R_4}{R_3} \geq 1 \\ b_0 &= \frac{G_1 G_2}{C_1} \\ b_1 &= G_1 + G_2 + (1-\mu)\frac{G_2}{C_1} \end{aligned} \quad . \tag{F.11}$$

Substituting the first two relationships of equation (F.11) into the third yields [51]

$$G_1^2 - b_1 G_1 + b_0 (C_1 + 1 - G) = 0$$

from which, with equation (F.8), $G_1$ and $G_2$ are defined as [51]

$$\begin{aligned} G_1 &= \frac{b_1 + \sqrt{b_1^2 - 4b_0(C_1 + 1 - G)}}{2} \\ G_2 &= \frac{C_1 b_0}{G_1} \end{aligned} \quad . \tag{F.12}$$

Also for minimum DC offset, from equation (F.9), $R_3$ and $R_4$ can be denoted as [51]

$$\begin{aligned} R_4 &= G(R_1 + R_2) \\ R_3 &= \frac{G(R_1 + R_2)}{G-1}, \qquad G \neq 1 \end{aligned} \quad . \tag{F.13}$$

If $G = 1$, then $R_4 = 0$ and $R_3 = \infty$. Therefore, given the type of filter ($b_0$ and $b_1$) and the gain $G$, $C_1$ is selected so that $G_1$ is real, requiring from equation (F.12) that [51]

$$0 < C_1 \leq G - 1 + \frac{b_1^2}{4b_0} \quad . \tag{F.14}$$

The resistance is found from equations (F.12) and (F.13) while de-normalizing to the required $C_2$ and $\omega_c$.

A *VCVS* low-pass filter is one of the more popular configurations with non-inverting gain. It requires a minimal number of elements, has a relative ease of adjustment of characteristics and a low output impedance (Hu-1) [51].

**F.2.3. Calculations done for the design of the VCVS, low-pass filter**

Although the triggering system is used for measuring a 50Hz, three-phase sinusoidal waveform, it is decided to take $f_c$ = 100Hz. Thus all frequencies between 0 and 100Hz will pass through the filter which will work perfectly for the 50Hz waveforms.

Thus, $\omega_c = 2\pi f_c = 2\pi 100$ rad/s. A second order Butterworth filter with the following characteristics is designed:

$\left(b_0 = 1, b_1 = \sqrt{2}\right)$ and $G = 1$ .

Choosing $C_2 = 0.1\mu F = 1x10^{-7}$ F $k_i$ is defined as

$$k_i = \frac{1}{\omega_c C} = \frac{1}{(2\pi 100)10^{-7}} .$$

Then, from equation (F.14), the relationship for $C_1$ can be given as $C_1 \le \frac{1}{2}$. Choosing $C_1 = 0.47F$ and implementing equation (F.12) the relationship for $G_1$ and $R_1$ can be given as

$$G_1 = 0.8803$$
$$R_1 = \frac{1}{G_1} = 1.13596\Omega .$$

The de-normalized resistances are then defined as

$$\begin{aligned} R_1 = R_2 &= 1.13596 k_i = 1.13596\left(15.9155x10^3\right) \\ &= 18.08k\Omega \\ C_1 &= 0.47(0.1\mu F) = 0.047\mu F \\ &= 47nF \end{aligned} \quad . \qquad \text{(F.15)}$$

Figure 4.27 shows the complete low-pass filter, including the non-inverting op-amp that is used in the triggering system.

Figure F.3 presents the frequency response of the VCVS, second-order low-pass filter. From this figure it can be seen that the -3dB point is at 126Hz. All frequencies over 126Hz will be blocked by the low-pass filter. Figure F.4 shows the output voltage of the low-pass filter for frequencies from 10Hz tot 1000Hz, illustrating the passband, transition band and stopband. From this figure $\omega_1$ can be taken as 280Hz, thus the transition band is between 126Hz and 280Hz.

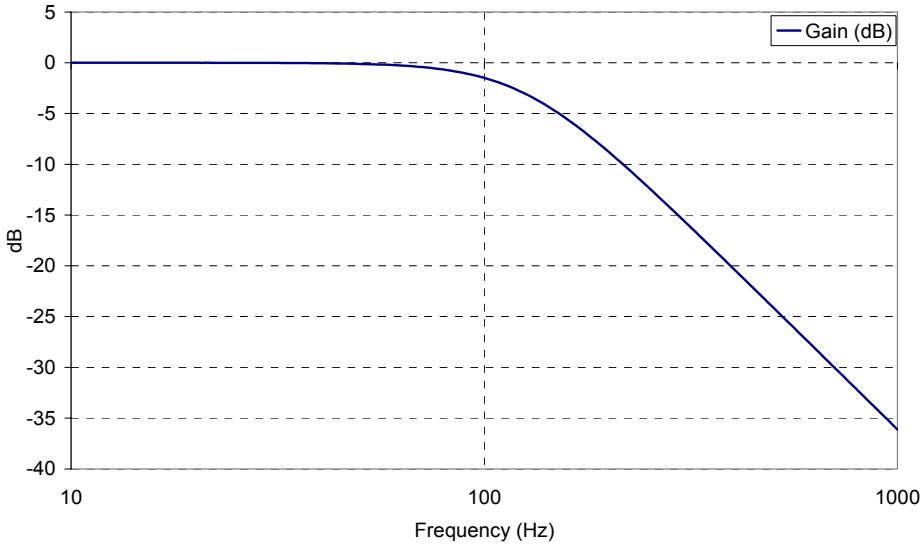


**Figure F.3 : The frequency response of the VCVS, second-order low-pass filter for frequencies from 10Hz to 1000Hz.**

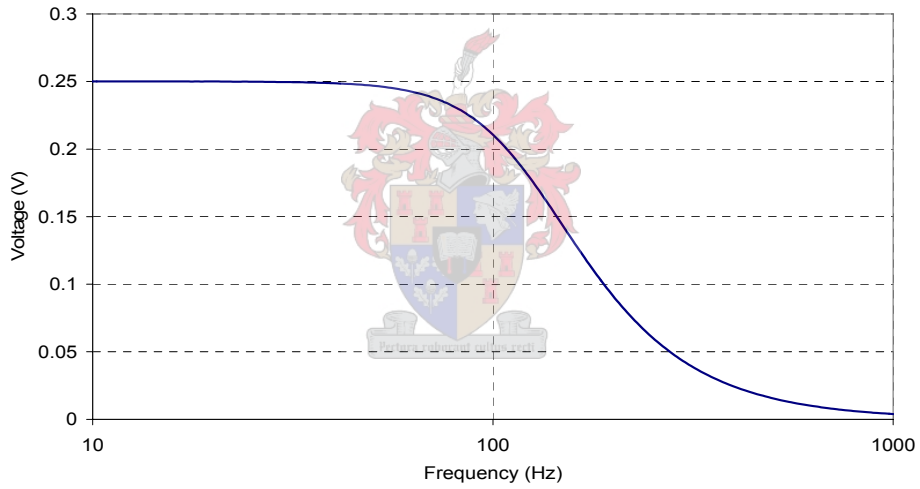


**Figure F.4 : Output voltage of the VCVS, second-order low-pass filter for frequencies from 10Hz to 1000Hz, illustrating the passband, transition band and stopband.**

## F.3. Window comparator with Schmitt trigger

The comparator used in this project is the LM319. The LM319 is a precision high speed dual comparator fabricated on a single monolithic chip. It is designed to operate over a wide range of supply voltages down to a single 5V logic supply and ground. It also has a higher gain and lower input currents than some of the other devices [54]. The LM319 accommodates separate input and output power supplies. The circuit's input limit is ±2.5V because of the maximum differential-input limit of the LM319. The input voltage of the comparator used in the

triggering system did not exceed a ±5V differential voltage between $V_{REF}$ and $V_{IN}$ or $-V_{REF}$, thus no clamping network has to be incorporated [53].

A Schmitt trigger is usually incorporated with a window comparator. The Schmitt trigger uses positive feedback with a loop-gain greater than unity to produce a bistable characteristic. Figure F.5 shows the configuration of an inverting Schmitt trigger. Positive feedback occurs because the feedback resistor is connected between the output and non-inverting input terminals. Voltage $v_+$, in terms of the output voltage can be found by using a voltage divider equation to yield [53]

$$v_+ = \left(\frac{R_1}{R_1 + R_2}\right) v_O \ . \tag{F.16}$$

Voltage $v_+$ does not remain constant; rather, it is a function of the output voltage. Input signal $v_I$ is applied to the inverting terminal. For the Schmitt trigger used in the comparator, the crossover voltages are shifted in a positive direction by applying a reference voltage. Figure F.5(a) shows an inverting Schmitt trigger with a reference voltage $V_{REF}$. Figure F.5(b) shows the complete voltage transfer characteristics.

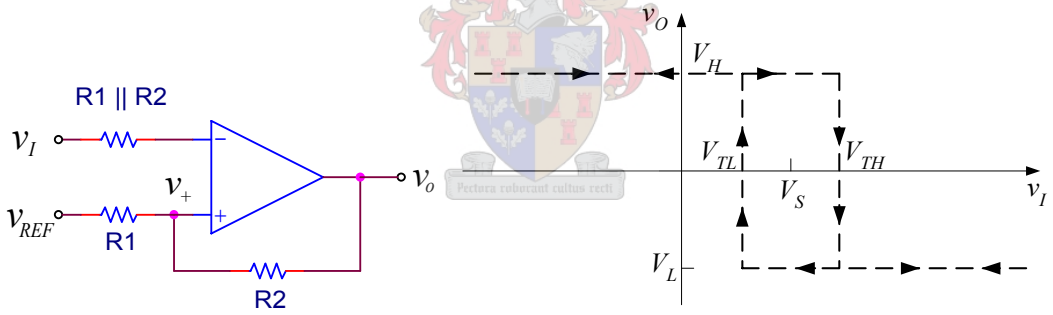


**Figure F.5 : (a) Inverting Schmitt trigger circuit with applied reference voltage and (b) voltage characteristics, showing hysteresis effect [52].**

The switching voltage $V_S$, assuming $V_H$ and $V_L$ are symmetrical about zero, is given by the relationship

$$V_S = \left(\frac{R_2}{R_1 + R_2}\right) V_{REF} \ . \tag{F.17}$$

The switching voltage is not the same as the reference voltage. The upper and lower crossover voltage are denoted by [53]

$$V_{TH} = V_S + \left(\frac{R_1}{R_1 + R_2}\right) V_H \tag{F.18}$$

and

$$V_{TL} = V_S + \left(\frac{R_1}{R_1 + R_2}\right) v_L \ . \tag{F.19}$$

As shown, the crossover voltages depend on whether the input voltage is increasing or decreasing. The complete transfer characteristics therefore show a *hysteresis effect* [52].

A non inverting Schmitt trigger can be designed by applying the input signal to the network connected to the comparator's non-inverting terminal. The inverting terminal is held essentially at ground potential, and the input signal is applied to resistor $R_1$, which is connected to the comparator's non-inverting terminal. Figure F.6(a) shows a non-inverting Schmitt trigger with a reference voltage and Figure F.6(b) shows the complete voltage transfer characteristics. The switching voltage $V_S$, again assuming $V_H$ and $V_L$ are symmetrical about zero, is given by the relationship [52]

$$V_S = \left(1 + \frac{R_1}{R_2}\right) V_{REF} \tag{F.20}$$

and the upper and lower crossover voltages are denoted by [52]

$$V_{TH} = V_s - \left(\frac{R_1}{R_2}\right) V_L \tag{F.21}$$

and

$$V_{TL} = V_s - \left(\frac{R_1}{R_2}\right) V_H \ . \tag{F.22}$$

If the output saturation voltages are symmetrical such that $V_L = -V_H$, then the crossover voltages are symmetrical about the switching voltage $V_S$.

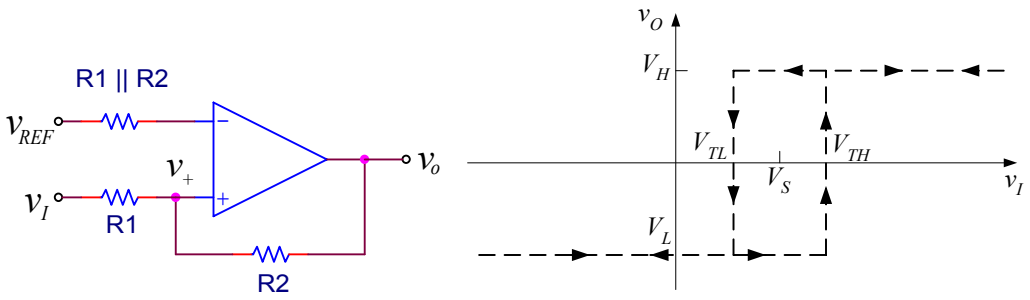


**Figure F.6 : (a) Non-inverting Schmitt trigger circuit and (b) voltage transfer characteristics [52].**

Figure 4.32 shows that resistors $R_8$ and $R_{11}$ are used to produce positive feedback for the non-inverting and inverting Schmitt triggers respectively.

## F.4. Re-triggerable monostable multi-vibrator

A monostable multi-vibrator is created by modifying the Schmitt trigger oscillator [52, 55]. The SN74LS122, re-triggerable monostable multi-vibrator was used in the triggering system. This d-c triggered multi-vibrators output pulse-duration was controlled by a selection of external resistance and capacitance values. For improved pulse duration accuracy and repeatability, an external resistor was connected between $R_{ext}/C_{ext}$ and $V_{CC}$ with $R_{int}$ open-circuited. An external variable resistance was also connected between $R_{ext}/C_{ext}$ and $V_{CC}$. Figure F.7 shows the output pulse control of the re-triggerable monostable multi-vibrator, when using a retrigger pulse. The retrigger pulse must start 0.22 x $C_{ext}$ (in pF) nanoseconds after the initial trigger pulse otherwise the retrigger pulse will be ignored [56].

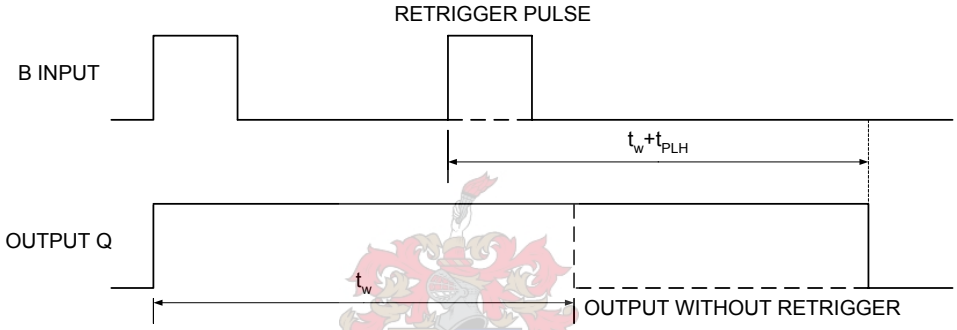


**Figure F.7 : Output pulse control of the SN74LS122 using a retrigger pulse [56].**

As stated before the output pulse duration was determined by the values of external capacitance and timing capacitance. Figure F.8 shows the connections of the timing components. The output pulse width was given by the relationship [56]

$$t_w = KR_T C_{ext} \quad . \tag{F.23}$$

where $K$ is a multiplier factor, $R_T$ is in kΩ, $C_{ext}$ is in pF and $t_w$ is in ns. For maximum immunity, system ground should be applied to the $C_{ext}$ node, even though $C_{ext}$ is already tied to the ground lead internally [56].

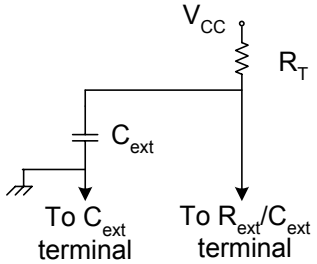


**Figure F.8 : Timing component connections of the SN74LS122 [56].**

$R_T$ consisted out of a 1Meg variable resister in parallel with a 240kΩ resister. This was done so that the output pulse duration could be varied. The maximum value of the parallel combination was 192kΩ. The value of the external capacitance was chosen as $C_{ext}$ = 330nF and from the datasheets of the SN74LS122 [56], $K$ = 0.33. Thus, from equation (F.23), $t_w$ is denoted by

$$t_w = 0.33 R_T 330x10^3 \tag{F.24}$$

where $R_{Tmaks} = 192\text{k}\Omega$,

$t_{wmaks} = 21\text{ms}$,

$R_{Tmin} = 0\text{k}\Omega$

and

$t_{wmin} = 0\text{ms}$ .

The basic output pulse could thus be varied in such a way that it could be made certain to test if the comparator was still sending retrigger pulses.

## F.5. Optocoupler

The 6N137 is an optically gate that combines a GaAsP light emitting diode and an integrated high gain photo detector. An enable input allows the detector to be strobed. The output of the detector IC is an open collector Schottky-clamped transistor. The internal shield provides a guaranteed common mode transient immunity specification 5,000 V/μs. Maximum ac and dc circuit isolation are provided and the 6N137 is suitable for high-speed logic interfacing, input/output buffering, as line receivers in environments that have extremely high ground or induced noise. Figure F.9 shows the functional diagram of the 6N137 optocoupler and Table F.1 tabulates the truth table of this optocoupler. The typical Input Forward Voltage (the voltage between pins 2 and 3), $V_F$, is 1,5V when the input current is 10mA. From the truth table it is determined that pin 7 (ENABLE) does not have to be connected and that the Output s the invert of the input (LED).

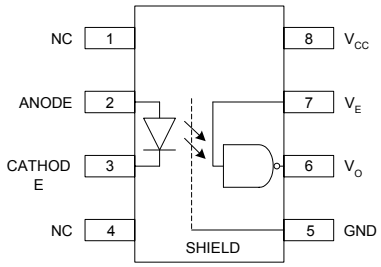


**Figure F.9 : Functional diagram of 6N137 optocoupler.**

**Table F.1 : Truth table of 6N137 optocoupler (positive logic).**

| LED | ENABLE | OUPUT |
|---|---|---|
| ON | H | L |
| OFF | H | H |
| ON | L | H |
| OFF | L | H |
| ON | NC | L |
| OFF | NC | H |

### F.5.1. Measurements to test the triggering through the optocoupler

The tests discussed in this section are performed for proper evaluation of the first field measurements that were done with the new three-element parallel plate sensors. These field measurements were taken underneath a 400kV, three-phase transmission line (just outside Muldersvlei substation). (Section 7.4)

#### F.5.1.1. Measurements to test the triggering of the HandyScope 3

For this test a 50Hz, 2.135V, square wave is applied and the trigger output of the HandyScope 3 is measured. Figure F.10 shows the applied signal and the triggered waveform.

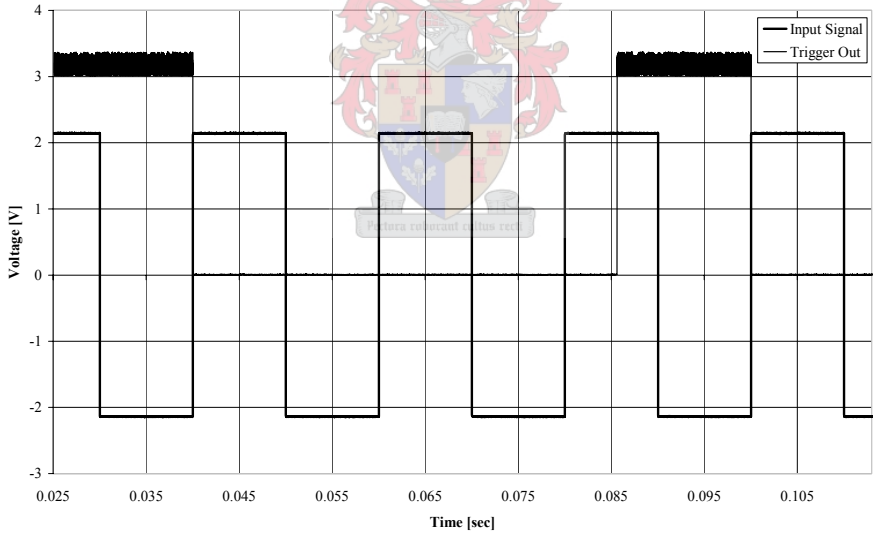


**Figure F.10: Waveform of the *Trigger Output* if a 50Hz, square wave is measured.**

The sample frequency is set to 500kS/sec and the record length to 100 000 samples. The trigger mode of the first oscilloscope is set to trigger on a rising edge. The second oscilloscope measures the *Trigger Out* pin of the first oscilloscope. The *Trigger Out* has a voltage level of 3.3V (logic high) while it is not triggered. Upon triggering (rising edge of square wave) the voltage level of the *Trigger Out* goes to zero (logic low). The Voltage will stay 0V until all measurements have been completed by the oscilloscope (this elapsed time is

proportional to the sample frequency and record length of the first oscilloscope), where after the *Trigger Out* will again consume a logic high.

### F.5.1.2. Measurements to test the total elapsed time for triggering

The elapsed time that it takes for the signal to travel through the optocoupler has to be tested to make certain that the two oscilloscopes trigger at the same instant. Figure F.11 shows the waveforms of the input signal vs. the output signal of the optocoupler. The output signal is the inverse of the input signal. The second oscilloscope triggers when the external trigger receives a voltage of 1.623V or more. The voltage level at which the second oscilloscope triggers is tested by measuring a saw tooth wave and checking at which voltage it passes through 0 seconds (the trigger is set at 0 seconds). Different test with different sample frequency settings of the oscilloscope are done. With all these tests the elapsed time are 200ns.

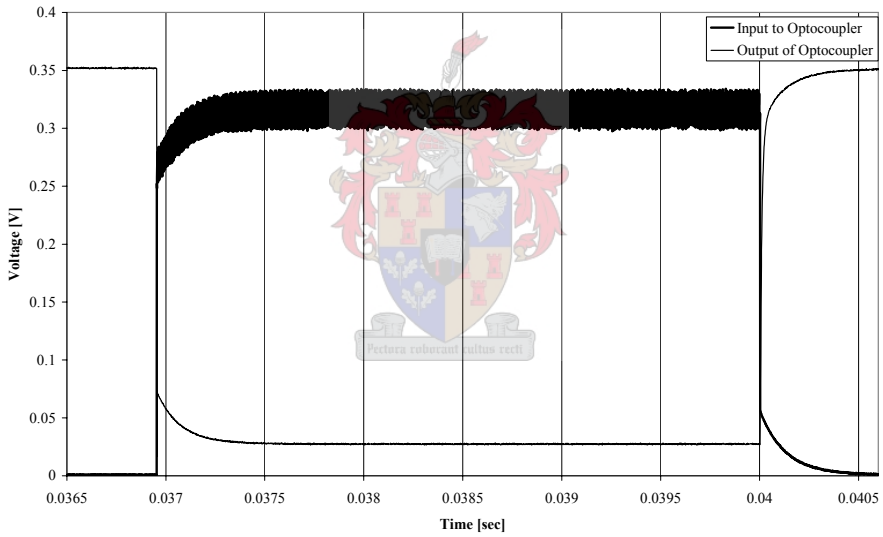


**Figure F.11: Waveform of the input signal vs. the output signal of the Optocoupler.**

# Appendix G. Span calculations for transmission lines

## G.1. Calculating changes of tension

The parabolic expression is sufficiently accurate as long as the sag is less than 5% of the span length. The final un-tensioned conductor length equals the initial un-tensioned length plus any extension due to a change in temperature. The arc length of a conductor in a level span is given by

$$l = \frac{2T}{w}\sinh\left(\frac{wL}{2T}\right) \quad , \qquad \text{(catenary)}$$

or

$$l = L + \frac{w^2 L^3}{24T^2} \qquad \text{(parabola)}$$

where the tension calculation symbols are as follows:

- L = span (horizontal tension between supports) [m]
- l = length of span measured along the conductor (the arc length) [m]
- T = horizontal component of tension [N]
- w = either vertical force in still air, or resultant force with wind, per unit length of conductor in the span [N/m]
- A = conductor cross-sectional area [$m^2$]
- E = effective modulus of elasticity
- α = effective coefficient of expansion
- θ = temperature [˚C]
- S = sag of the conductor at mid-span, measured vertically [m]
- h = difference in height of conductor attachment points at each end of the span [m]
- x = horizontal distance from the origin or lowest point in the span [m]
- y = vertical distance from the lowest point in the span [m]
- c = T/w (the catenary constant) .

From this must be deducted the elastic stretch, given by TL/EA. The extension due to any change of temperature, given by $L\alpha(\theta_2 - \theta_1)$ must be added. From the above, the 'change of state' formula becomes:

for the catenary

$$\left[\left(\frac{2T_1}{w_1}\right)\sinh\left(\frac{w_1 L}{2T_1}\right)\right] - \left[\left(\frac{2T_2}{w_2}\right)\sinh\left(\frac{w_2 L}{2T_2}\right)\right] + \left[\left(\frac{L}{AE}\right)\left(T_2 - T_1\right)\right] + \alpha L\left(\theta_2 - \theta_1\right) = 0 \quad ,$$

or for the parabola

$$\frac{L^3}{24}\left[\left(\frac{w_1}{T_1}\right)^2-\left(\frac{w_2}{T_2}\right)^2\right]+\frac{L}{AE}(T_2-T_1)+\alpha L(\theta_2-\theta_1)=0 \quad .$$

For calculating changes of tension, there is an exceedingly small difference between the two methods for spans less than 1km in length. Since the final tension appears in two terms in each case, the solution is usually found by iteration. If using a programmable calculator or computer, one method of solution is by the Raphson-Newton approximation. If a trail value is used for $T_2$, the value of the left hand side (LHS) of the equation will represent the error in terms of length of conductor. This, divided by the differential of the LHS with respect to $T_2$, will yield a correction to be subtracted from the original trail of $T_2$, for the next iteration.

($T_2$ new value) = ($T_2$ old value) – correction

$$Correction=\frac{(LHS)}{\left(\frac{w^2L^3}{12T_2^3}+\frac{L}{EA}\right)}$$

Usually two to five iterations are necessary to find a solution correct to 1 Newton [61].

Calculating the sag for inclined spans, the same equations are essentially used that were used for level spans. However, the span is considered to consist of two separate sections, one to the right of the low point and the other to the left. The sag for each direction from the low point is then calculated.



## G.2. Initial versus Final Sags and Tensions

Rather than calculated as a function of time, most sag-tension calculations are based on initial and final loading conditions. Initial sags and tensions are simply the sags and tensions at the time the line is built. Final sags and tensions are calculated assuming (60) the specified ice and wind loading has occurred, and (61) the conductor has experienced 10 years of creep elongation at a conductor temperature of 60˚F at the user-specified initial tension.

To illustrate the result of typical sag-tension calculations, the following tables present initial and final sag-tension data for different conductors. Typical tension constraints of 15% final unloaded at 60˚F, 25% initial unloaded at 60˚F, and 60% initial at maximum loading are used. With most sag-tension calculation methods, final sags are calculated for both heavy ice/wind loads and for creep elongation. The final sag-tension values reported to the user are those

with the greatest increase in sag [60]. In the following tables typical sag and tension data are given.

**Table G.1: Typical Sag and Tension data, 795 KCMIL – 26/7 ACSR "Drake", 300 - and 1000 ft spans.**

Conductor: Drake
795 kcmil - 26/7 ACSR
Area = 0.7264 $in^2$
Creep is a factor

**Span = 300 ft**
*NESC Light Loading District*

| Temp, °F | Ice, in | Wind, lbs/ft2 | K, lbs/ft | Weight, lbs/ft | Final | | Initial | |
|---|---|---|---|---|---|---|---|---|
| | | | | | Sag, ft | Tension, lbs | Sag, ft | Tension, lbs |
| 30 | 0.00 | 9.00 | 0.05 | 1.424 | 2.37 | 6769 | 2.09 | 7664 |
| 30 | 0.00 | 0.00 | 0.00 | 1.094 | 1.93 | 6364 | 1.66 | 7404 |
| 60 | 0.00 | 0.00 | 0.00 | 1.094 | 2.61 | 4725* | 2.04 | 6033 |
| 90 | 0.00 | 0.00 | 0.00 | 1.094 | 3.46 | 3556 | 2.57 | 4792 |
| 120 | 0.00 | 0.00 | 0.00 | 1.094 | 1.00 | 3077 | 3.25 | 3785 |
| 167 | 0.00 | 0.00 | 0.00 | 1.094 | 4.60 | 2678 | 4.49 | 2746 |
| 212 | 0.00 | 0.00 | 0.00 | 1.094 | 5.20 | 2371 | 5.2 | 2371 |

* Design Condition

Conductor: Drake
795 kcmil - 26/7 ACSR
Area = 0.7264 $in^2$
Creep is a factor

**Span = 1000 ft**
*NESC Light Loading District*

| Temp, °F | Ice, in | Wind, lbs/ft2 | K, lbs/ft | Weight, lbs/ft | Final | | Initial | |
|---|---|---|---|---|---|---|---|---|
| | | | | | Sag, ft | Tension, lbs | Sag, ft | Tension, lbs |
| 30 | 0.00 | 9.00 | 0.05 | 1.424 | 28.42 | 6290 | 27.25 | 6558 |
| 30 | 0.00 | 0.00 | 0.00 | 1.094 | 27.26 | 5036 | 25.70 | 5339 |
| 60 | 0.00 | 0.00 | 0.00 | 1.094 | 29.07 | 4725* | 27.36 | 5018 |
| 90 | 0.00 | 0.00 | 0.00 | 1.094 | 30.82 | 4460 | 28.98 | 4740 |
| 120 | 0.00 | 0.00 | 0.00 | 1.094 | 32.50 | 4232 | 30.56 | 4498 |
| 167 | 0.00 | 0.00 | 0.00 | 1.094 | 34.49 | 3990 | 32.56 | 4175 |
| 212 | 0.00 | 0.00 | 0.00 | 1.094 | 35.75 | 3851 | 35.14 | 3917 |

* Design Condition

**Table G.2: Typical Sag and Tension data, 795 KCMIL – 26/7 ACSR "Drake", 300 - and 1000 ft spans.**

Conductor: Drake
795 kcmil - 26/7 ACSR
Area = 0.7264 $in^2$
Creep is a factor

**Span = 300 ft**
*NESC Light Loading District*

| Temp, °F | Ice, in | Wind, lbs/ft2 | K, lbs/ft | Weight, lbs/ft | Final | | Initial | |
|---|---|---|---|---|---|---|---|---|
| | | | | | Sag, ft | Tension, lbs | Sag, ft | Tension, lbs |
| 0 | 0.50 | 4.00 | 0.30 | 2.509 | 2.91 | 9695 | 2.88 | 9802 |
| 32 | 0.50 | 0.00 | 0.00 | 2.094 | 3.13 | 7528 | 2.88 | 8188 |
| -20 | 0.00 | 0.00 | 0.00 | 1.094 | 1.26 | 9733 | 1.26 | 9756 |
| 0 | 0.00 | 0.00 | 0.00 | 1.094 | 1.48 | 8327 | 1.4 | 8818 |
| 30 | 0.00 | 0.00 | 0.00 | 1.094 | 1.93 | 6364 | 1.66 | 7404 |
| 60 | 0.00 | 0.00 | 0.00 | 1.094 | 2.61 | 4725* | 2.04 | 6033 |
| 90 | 0.00 | 0.00 | 0.00 | 1.094 | 3.46 | 3556 | 2.57 | 4792 |
| 120 | 0.00 | 0.00 | 0.00 | 1.094 | 4.00 | 3077 | 3.25 | 3785 |
| 167 | 0.00 | 0.00 | 0.00 | 1.094 | 4.60 | 2678 | 4.49 | 2746 |
| 212 | 0.00 | 0.00 | 0.00 | 1.094 | 5.20 | 2371 | 5.2 | 2371 |

* Design Condition

Conductor: Drake
795 kcmil - 26/7 ACSR
Area = 0.7264 $in^2$
Creep is a factor

**Span = 1000 ft**
*NESC Light Loading District*

| Temp, °F | Ice, in | Wind, lbs/ft2 | K, lbs/ft | Weight, lbs/ft | Final | | Initial | |
|---|---|---|---|---|---|---|---|---|
| | | | | | Sag, ft | Tension, lbs | Sag, ft | Tension, lbs |
| 0 | 0.50 | 4.00 | 0.30 | 2.509 | 30.07 | 10479 | 30.07 | 10479 |
| 32 | 0.50 | 0.00 | 0.00 | 2.094 | 30.56 | 8607 | 29.94 | 8785 |
| -20 | 0.00 | 0.00 | 0.00 | 1.094 | 24.09 | 5694 | 22.77 | 6023 |
| 0 | 0.00 | 0.00 | 0.00 | 1.094 | 25.38 | 5406 | 23.9 | 5738 |
| 30 | 0.00 | 0.00 | 0.00 | 1.094 | 27.26 | 5036 | 25.59 | 5362 |
| 60 | 0.00 | 0.00 | 0.00 | 1.094 | 29.07 | 4725* | 27.25 | 5038 |
| 90 | 0.00 | 0.00 | 0.00 | 1.094 | 30.82 | 4460 | 28.87 | 4758 |
| 120 | 0.00 | 0.00 | 0.00 | 1.094 | 32.50 | 4232 | 30.45 | 4513 |
| 167 | 0.00 | 0.00 | 0.00 | 1.094 | 34.36 | 4005 | 32.85 | 4187 |
| 212 | 0.00 | 0.00 | 0.00 | 1.094 | 35.62 | 3865 | 35.05 | 3928 |

* Design Condition

**Table G.3: Typical Sag and Tension data, 795 KCMIL – 26/7 ACSR "Drake", 300 - and 1000 ft spans.**

Conductor: Drake
795 kcmil - 37 Strands AAC
Area = 0.7261 $in^2$
Creep is a factor

**Span = 300 ft**
*NESC Light Loading District*

| Temp, °F | Ice, in | Wind, lbs/ft2 | K, lbs/ft | Weight, lbs/ft | Final | | Initial | |
|---|---|---|---|---|---|---|---|---|
| | | | | | Sag, ft | Tension, lbs | Sag, ft | Tension, lbs |
| 30 | 0.00 | 9.00 | 0.05 | 1.409 | 1.59 | 9980 | 1.31 | 12373 |
| 30 | 0.00 | 0.00 | 0.00 | 1.093 | 1.26 | 9776 | 1.03 | 11976 |
| 60 | 0.00 | 0.00 | 0.00 | 1.093 | 1.60 | 7688 | 1.16 | 10589* |
| 90 | 0.00 | 0.00 | 0.00 | 1.093 | 2.12 | 5806 | 1.34 | 9159 |
| 120 | 0.00 | 0.00 | 0.00 | 1.093 | 2.69 | 4572 | 1.59 | 7713 |
| 167 | 0.00 | 0.00 | 0.00 | 1.093 | 3.11 | 3957 | 2.22 | 5545 |
| 212 | 0.00 | 0.00 | 0.00 | 1.093 | 3.58 | 3435 | 3.17 | 3877 |

* Design Condition

Conductor: Drake
795 kcmil - 16 ACSR/SD
Area = 0.7261 $in^2$
Creep is a factor

**Span = 1000 ft**
*NESC Light Loading District*

| Temp, °F | Ice, in | Wind, lbs/ft2 | K, lbs/ft | Weight, lbs/ft | Final | | Initial | |
|---|---|---|---|---|---|---|---|---|
| | | | | | Sag, ft | Tension, lbs | Sag, ft | Tension, lbs |
| 30 | 0.00 | 9.00 | 0.05 | 1.409 | 17.21 | 10250 | 15.10 | 11676 |
| 30 | 0.00 | 0.00 | 0.00 | 1.093 | 15.22 | 8988 | 12.69 | 10779 |
| 60 | 0.00 | 0.00 | 0.00 | 1.093 | 17.21 | 7950* | 13.98 | 9780 |
| 90 | 0.00 | 0.00 | 0.00 | 1.093 | 19.26 | 7108 | 15.44 | 8861 |
| 120 | 0.00 | 0.00 | 0.00 | 1.093 | 21.31 | 6428 | 17.03 | 8037 |
| 167 | 0.00 | 0.00 | 0.00 | 1.093 | 24.27 | 5647 | 19.69 | 6954 |
| 212 | 0.00 | 0.00 | 0.00 | 1.093 | 25.62 | 5352 | 22.32 | 6136 |

* Design Condition

**Table G.4: Typical Sag and Tension data, 795 KCMIL – 26/7 ACSR "Drake", 300 - and 1000 ft spans.**

Conductor: Drake
795 kcmil - 16 ACSR/SD
Area = 0.7261 $in^2$
Creep is a factor

**Span = 300 ft**
*NESC Light Loading District*

| Temp, °F | Ice, in | Wind, lbs/ft2 | K, lbs/ft | Weight, lbs/ft | Final | | Initial | |
|---|---|---|---|---|---|---|---|---|
| | | | | | Sag, ft | Tension, lbs | Sag, ft | Tension, lbs |
| 0 | 0.50 | 4.00 | 0.30 | 2.486 | 2.19 | 12774 | 2.03 | 13757 |
| 32 | 0.50 | 0.00 | 0.00 | 2.074 | 2.25 | 10377 | 1.90 | 12256 |
| -20 | 0.00 | 0.00 | 0.00 | 1.093 | 0.19 | 13447 | 0.87 | 14156 |
| 0 | 0.00 | 0.00 | 0.00 | 1.093 | 1.03 | 11962 | 0.92 | 13305 |
| 30 | 0.00 | 0.00 | 0.00 | 1.093 | 1.26 | 9776 | 1.03 | 11976 |
| 60 | 0.00 | 0.00 | 0.00 | 1.093 | 1.60 | 7688 | 1.12 | 10589* |
| 90 | 0.00 | 0.00 | 0.00 | 1.093 | 2.12 | 5806 | 1.34 | 9159 |
| 120 | 0.00 | 0.00 | 0.00 | 1.093 | 2.69 | 4572 | 1.59 | 7713 |
| 167 | 0.00 | 0.00 | 0.00 | 1.093 | 3.11 | 3957 | 2.22 | 5545 |
| 212 | 0.00 | 0.00 | 0.00 | 1.093 | 3.58 | 3435 | 3.17 | 3877 |

* Design Condition

Conductor: Drake
795 kcmil - 16 ACSR/SD
Area = 0.7261 $in^2$
Creep is a factor

**Span = 1000 ft**
*NESC Light Loading District*

| Temp, °F | Ice, in | Wind, lbs/ft2 | K, lbs/ft | Weight, lbs/ft | Final | | Initial | |
|---|---|---|---|---|---|---|---|---|
| | | | | | Sag, ft | Tension, lbs | Sag, ft | Tension, lbs |
| 0 | 0.50 | 4.00 | 0.30 | 2.486 | 20.65 | 15089 | 20.36 | 15299 |
| 32 | 0.50 | 0.00 | 0.00 | 2.074 | 20.16 | 12607 | 19.32 | 13445 |
| -20 | 0.00 | 0.00 | 0.00 | 1.093 | 12.20 | 11205 | 10.89 | 12552 |
| 0 | 0.00 | 0.00 | 0.00 | 1.093 | 13.35 | 10244 | 11.56 | 11832 |
| 30 | 0.00 | 0.00 | 0.00 | 1.093 | 15.22 | 8988 | 12.69 | 10779 |
| 60 | 0.00 | 0.00 | 0.00 | 1.093 | 17.21 | 7950* | 13.98 | 9780 |
| 90 | 0.00 | 0.00 | 0.00 | 1.093 | 19.26 | 7108 | 15.44 | 8861 |
| 120 | 0.00 | 0.00 | 0.00 | 1.093 | 21.31 | 6428 | 17.03 | 8037 |
| 167 | 0.00 | 0.00 | 0.00 | 1.093 | 24.27 | 5647 | 19.69 | 6954 |
| 212 | 0.00 | 0.00 | 0.00 | 1.093 | 25.62 | 5352 | 22.32 | 6136 |

* Design Condition

# Appendix H. MATLAB programs

## H.1. Frequency response of Butterworth Filter

```
%Plot Frequency response of 2nd order Butterworth Filter

Sf = 100000;                    %Sampling Frequency
fn = 500;                      %Cut-off frequency
Wn = (2*pi()*fn);               %Angular cut-off frequensy
[b,a] = butter(2,Wn,'s')         %Design lowpass filter

w = logspace(0,4);               %Vector of angular frequencies
h = freqs(b,a,w);
mag = abs(h);
magdB = 20*log10(mag);
phase = angle(h);
phasedeg = phase*180/pi();
f=w/(2*pi());

figure;
subplot(2,1,1),semilogx(f,magdB);grid;
axis([10 1000 -4 0]);
xlabel('Frequnecy (Hz)','FontSize',12);
ylabel('Magnitude (dB)','FontSize',12);
subplot(2,1,2),semilogx(f,phasedeg);grid;
axis([10 1000 -100 0]);
xlabel('Frequnecy (Hz)','FontSize',12);
ylabel('Phase','FontSize',12);
```

## H.2. Comparison between original waveform and filtered waveform

```
%Compare waveform with noise with filtered waveform

%Finding the file that contains the data
clear;
tel = 1;
tel = 1
text = ['select sensor nr. '  int2str(tel)];
[filename,pathname] = uigetfile('*.dat',text);
if isequal(filename,0)
   disp('User selected cancel');
   break;
else
   disp(['User selected', fullfile(pathname, filename)]);
   Cell_filename(tel) = {filename}
   Cell_pathname(tel) = {pathname};
   length(Cell_filename)
end

%Decalring properties of plot
data_scale = {2,1.5,2};
figure;
hold on;
```

```
Color_set = {'k', 'r--', 'b-.'};
Legend_data = {'Original','Filtered', 'Sensor C'};
Legend_used = cell(2,1);

%Design filter
Sf = 100000;                    %Sampling frequency
fn = 500;                      %Cut-off frequency
Wn = 2*pi()*fn/(pi()*Sf);       %Normalized cut-off frequency
[b,a] = butter(2,Wn,'low')      %Design lowpass filter

%Read in Data from file and plot the data
int = 1;
work_file = fopen(Cell_filename{int});
C = textscan(work_file, '%*f %f32 %f32 %f32 %f32 %*f %*f %*f %*f %*f', 'delimiter', ',',
'headerLines', 5)
fclose(work_file);
Legend_used{int} = Legend_data{int};
Legend_used{int+1} = Legend_data{int+1};
hold on;
plot(C{1,1},C{1,2}*data_scale{int},Color_set{int});
y1=filter(b,a,C{1,2});
plot(C{1,1},y1*data_scale{int},Color_set{int+1},'LineWidth',2);

grid on;
axis([0 0.04 -0.1 0.1]);
xlabel('Time (sec)','FontSize',16);
ylabel('Voltage (V)','FontSize',16);
legend(Legend_used,'FontSize',16);
```


### H.3. Plotting the three filtered waveforms

```
clear;
tel = 1;
for tel = 1:1
   text = ['select sensor nr. '  int2str(tel)];
   [filename,pathname] = uigetfile('*.dat',text);
   if isequal(filename,0)
      disp('User selected cancel');
      break;
   else
      disp(['User selected', fullfile(pathname, filename)]);
      Cell_filename(tel) = {filename};
      Cell_pathname(tel) = {pathname};
   end
end

%Declaring properties of plot
data_scale = {2,1.5,2};
figure;
hold on;
Color_set = {'k', 'r--', 'b-.'};
Legend_data = {'Sensor A', 'Sensor B', 'Sensor C'};
Legend_used = cell(3,1);
```

```
%Design filter
Sf = 100000;                    %Sampling frequency
fn = 500;                      %Cut-off frequency
Wn = 2*pi()*fn/(pi()*Sf);       %Normalized cut-off frequency
[b,a] = butter(2,Wn,'low')      %Design lowpass filter

%Read in Data from file and plot the data
for int = 1:length(Cell_filename)
   work_file = fopen(Cell_filename{int});
   C = textscan(work_file, '%*f %f32 %f32 %f32 %f32 %*f %*f %*f %*f %*f', 'delimiter', ',',
'headerLines', 5)
   fclose(work_file);
   hold on;

   %Plot phase A
   y1=filter(b,a,C{1,2});
   plot(C{1,1},y1*data_scale{int},Color_set{int},'LineWidth',2);
   Legend_used{int} = Legend_data{int};

   %Plot phase B
   y2=filter(b,a,C{1,3});
   plot(C{1,1},y2*data_scale{int+1},Color_set{int+1},'LineWidth',2);
   Legend_used{int+1} = Legend_data{int+1};

   %Plot phase C
   y3=filter(b,a,C{1,4});
   plot(C{1,1},y3*data_scale{int+2},Color_set{int+2},'LineWidth',2);
   Legend_used{int+2} = Legend_data{int+2};
end;

grid on;
axis([0.001 0.021 -0.3 0.3]);
xlabel('Time (sec)','FontSize',16);
ylabel('Voltage (V)','FontSize',16);
legend(Legend_data,'FontSize',16);
```

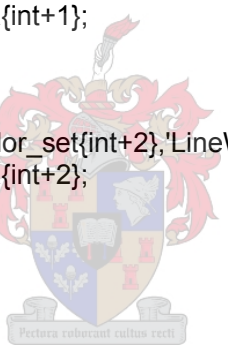


### H.4. Testing symmetry between phase A and phase C

```
clear;
tel = 1;
for tel = 1:2
   text = ['select sensor nr. '  int2str(tel)];
   [filename,pathname] = uigetfile('*.dat',text);
   if isequal(filename,0)
      disp('User selected cancel');
      break;
   else
      disp(['User selected', fullfile(pathname, filename)]);
      Cell_filename(tel) = {filename};
      Cell_pathname(tel) = {pathname};
   end
end

%Declaring properties of plot
```

```
data_scale = {2,1.5,2,2,1.5,2};
figure;
hold on;
Color_set = {'b:', 'r--', 'k-.','k', 'r', 'b'};
Legend_data = {'Phase A - Sensor A','Phase A - Sensor B', 'Phase A - Sensor C', 'Phase C -
Sensor A','Phase C - Sensor B', 'Phase C - Sensor C'};
Legend_used = cell(6,1);

%Design filter
Sf = 100000;                    %Sampling frequency
fn = 500;                       %Cut-off frequency
Wn = 2*pi()*fn/(pi()*Sf);       %Normalized cut-off frequency
[b,a] = butter(2,Wn,'low')      %Design lowpass filter

%Read in Data from file and plot the data
for int = 1:length(Cell_filename)
   work_file = fopen(Cell_filename{int});
   C = textscan(work_file, '%*f %f32 %f32 %f32 %f32 %*f %*f %*f %*f %*f', 'delimiter', ',',
'headerLines', 5)
   fclose(work_file);
   hold on;
   width = 1+int;
   int = 1+(int-1)*3;

   %Plot phase A
   y1=filter(b,a,C{1,2});
   plot(C{1,1},y1*data_scale{int},Color_set{int},'LineWidth',width);
   Legend_used{int} = Legend_data{int};

   %Plot phase B
   y2=filter(b,a,C{1,3});
   plot(C{1,1},y2*data_scale{int+1},Color_set{int+1},'LineWidth',width);
   Legend_used{int+1} = Legend_data{int+1};

   %Plot phase C
   y3=filter(b,a,C{1,4});
   plot(C{1,1},y3*data_scale{int+2},Color_set{int+2},'LineWidth',width);
   Legend_used{int+2} = Legend_data{int+2};
end;

grid on;
axis([0.001 0.021 -0.3 0.3]);
xlabel('Time (sec)','FontSize',16);
ylabel('Voltage (V)','FontSize',16);
legend(Legend_data,'FontSize',16);
```

# Appendix I. Land Survey

## I.1. Land survey background

Surveying is the science and art of measuring distances and angles on or near the surface of the earth. Surveying involves the measurement of distance, both horizontal and vertical, and direction to determine the relative position of points above, on or beneath the surface of the earth [57].

### I.1.1. Equipment used for surveying

To measure the distance between points, the following equipment can be used: tapes; stadia or electronic distance measuring. To measure the direction to a certain point the following instruments can be used: compass; alidade; transit; dumpy level or theodolite [57].

### I.1.2. Theodolite

For the survey that was needed to be done in this project, the theodolite would be adequate. A theodolite is a scientific instrument used for measuring both horizontal and vertical angles, as used in triangular networks. A theodolite consists of a telescope mounted movably within two perpendicular axes, the horizontal axis and the vertical axis. When the telescope is pointed at a desired object, the angle of each of these axes can be measured with great precision [59]. In Figure I.1 a photograph of a typical theodolite and the diagram of the theodolite are illustrated.



**Factors influencing the use of the theodolite [58]**

- A clear line of sight between the instrument and the measured points is essential.
- The precision of the instrument is dependant on the raw repeatability of the angle measurement.
- A well defined measurement point or target /prism is required to obtain the maximum accuracy
- The accuracy of angle measurement is subject to a number of instrumental errors and the correct field procedures.

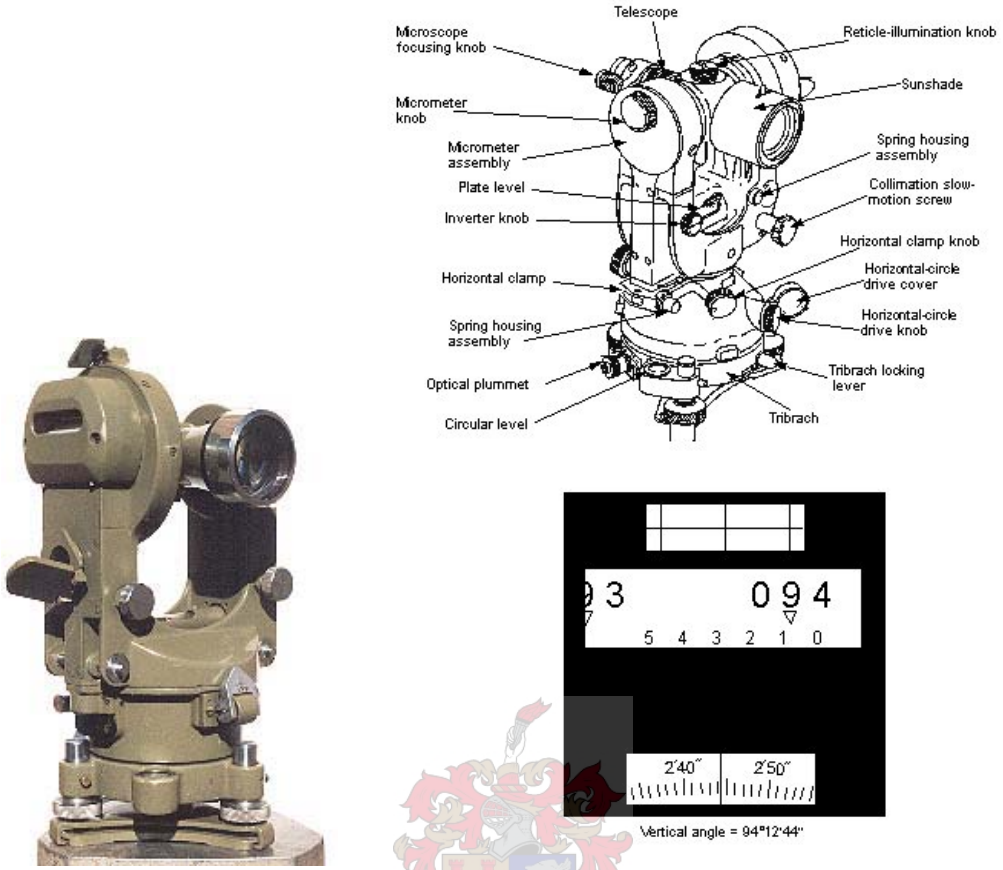


**Figure I.1: (a) Typical theodolite [58] (b) Diagram of an optical Theodolite [59].**

### I.1.3. Concept of operation of the theodolite

Most theodolites are mounted on a tripod centred over a mark on the ground. It is mounted on a centering plate containing three thumbscrews for rapid levelling. Before measuring the theodolite must be placed precisely and vertically over the point to be measured (centering) and its vertical axis aligned with local gravity (levelling). The height of the reference point of the theodolite above the ground bench mark must be measured precisely. The determination of position on a plane can be calculated through simple vector mathematics, breaking the vector into its two constituent components. Both axes of a theodolite are equipped with the graduate circles that can be read through magnifying lenses. The horizontal and vertical axes of a theodolite must be mutually perpendicular. The condition where they deviate from perpendicularity is referred to as horizontal axis error. The optical axis of the telescope, called sight axes and defined by the optical centre of the objective and the centre of the cross-hairs in its focal point, must be perpendicular to the horizontal axis. The deviation from perpendicularity is called the collimation error and is illustrated in Figure I.2. In Figure I.3 the axes and circles of a theodolite was illustrated.

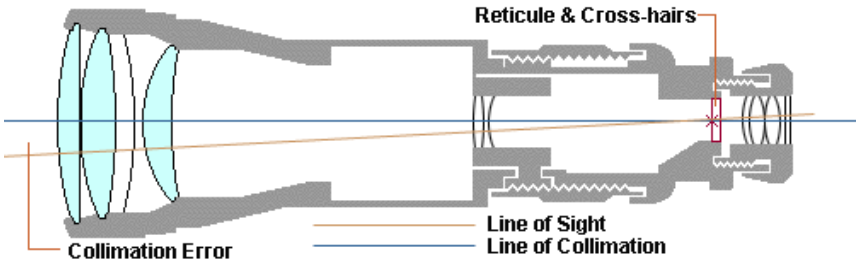


**Figure I.2: Cross section through a theodolite telescope illustrating horizontal axis error [58].**

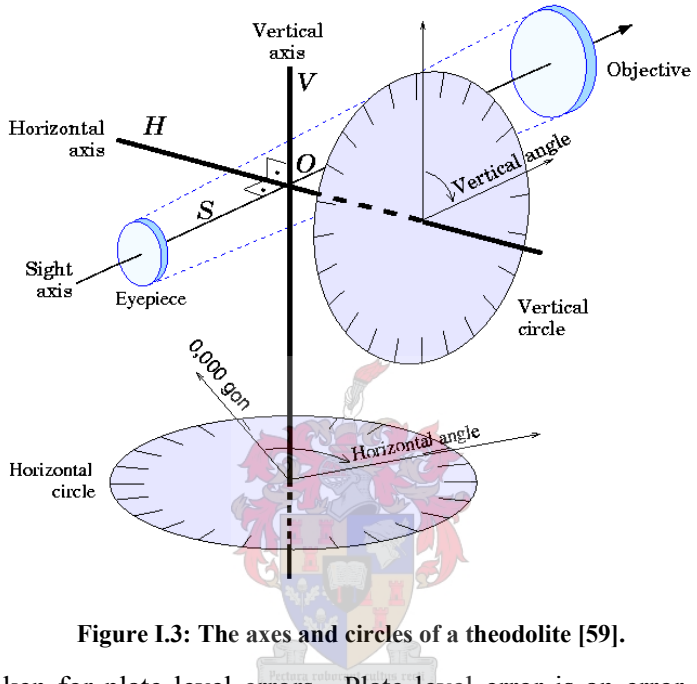


**Figure I.3: The axes and circles of a theodolite [59].**

Care should be taken for plate level errors. Plate level error is an error of adjustment that affects horizontal angles observed to elevated targets as illustrated in Figure I.4. It occurs when the theodolite is not levelled properly, using the plate level bubble. This error is significant when elevated targets (overhead conductors) are observed.


**Figure I.4: Plate level error [58].**

### I.1.4. Measurements of distance and direction

**Angular Measurements**

The combination of a direction and a distance gives a polar vector to a point and hence a unique location of that point in space. The theodolite facilitate in angle measurements [58].

**Tachometry**

This method of survey consists of using a theodolite to make cross hair intercept readings on a levelling staff. As the angle subtended by the cross hairs is known, the distance can be calculated as illustrated in Figure I.5. Tachometry is an optical solution to measuring distance.

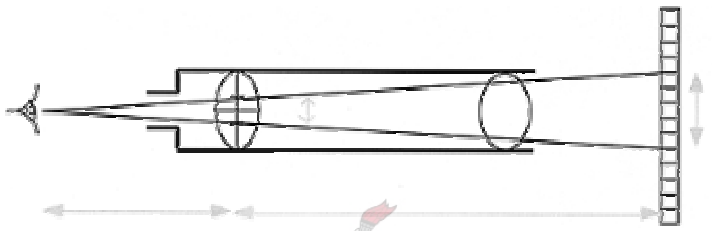

**Figure I.5: Illustrating tachometry [58].**

**Angle – Angle Intersection**

In the simplest case the angle-angle intersection solves a two dimensional triangle. The three known quantities in the triangle are two angles and a distance. The distance is measured between the two stations where the angle measurement takes place. The angles are measured using a theodolite or total stations. The distance between the two stations is the horizontal distance, and horizontal angles are measured. If the third coordinate of the intersected point is needed then additional measurements are necessary to determine the height of the point

For a simple angle-angle intersection, the field procedure is as follows:

1. Locate two control points which are known and from which the intersection points are visible.
2. It is advisable to check the distance measurement between the two control points if possible.
3. Set up the theodolite or total station at the first station. Set up a suitable target over the second station.
4. Measure the horizontal angles subtended by the second station and the intersection points.

5. Swap the instrument and the target. The theodolite or total station is set up at the second station.
6. Measure the horizontal angles subtended by the first station and the intersection points.

Although there are formulae for the solution of a triangle from a side and two angles, the standard mathematical formulae compute other two sides and the remaining angle. The most straightforward way to approach this is to compute the remaining angle (as the three angles sum to 180 degrees) and then use the sine rule.

However in the case of an angle-angle intersection, the requirement is to compute the coordinates of the intersection point, based on the coordinates of the stations and the measured angles. One formula which is widely used is given below:

$$E_P = \frac{E_A \cot\beta + E_B \cot\alpha + (N_B - N_A)}{\cot\beta + \cot\alpha} \tag{I.1}$$

$$N_P = \frac{N_A \cot\beta + N_B \cot\alpha + (E_A - E_B)}{\cot\beta + \cot\alpha} \tag{I.2}$$

### I.1.5. Modern theodolite

In this project the old theodolite was used due to availability. However, newer theodolites can be used that will make the measuring of the overhead conductor heights much simpler. In a modern theodolite the reading out of the horizontal and vertical circles is usually done electrically. Modern theodolites are usually equipped with integrated electro-optical distance measuring devices, allowing the measurement in one go of complete three-dimensional vectors, albeit in instrument-defined polar co-ordinates, which can then be transformed to a pre-existing co-ordinate system in the area by means of a sufficient number of control points. The instruments "intelligent" theodolites, called total stations, perform the necessary operations, saving data into internal registering units, or into external data storage devices. In Figure I.6 an illustration is given for explanation of the mathematics behind the operations.

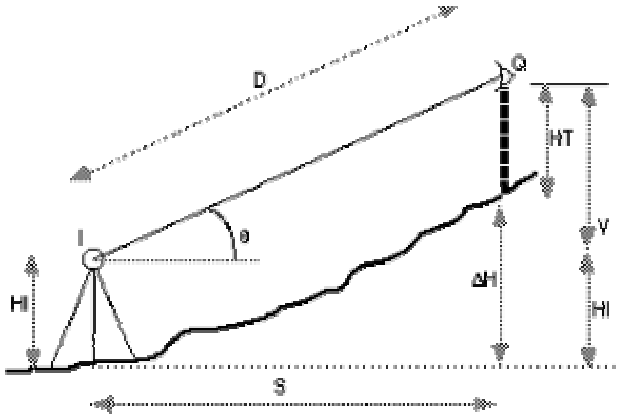


**Figure I.6: Electronic tachometry [58].**

$$S = D\cos(\theta)$$
$$RL = RL_A + HI + D\sin(\theta) - HT \tag{I.3}$$

# Appendix J. Transmission line parameters for three-phase transmission lines

## J.1. Introduction

This chapter discusses transmission line parameters for a three-phase line, the capacitive phase matrix as well as transmission line electric fields. The capacitive phase matrix of a specific transmission line configuration is used to calculate the electric field underneath the transmission line as well as the capacitive coupling between the different elements of the line configuration. The different methods used to determine the capacitive coupling between the overhead transmission lines are discussed. The analytical method of calculating the capacitive matrix of a three-phase system is reviewed in this chapter.

The electric field distribution underneath power lines is a function of the capacitive matrix, which in turn is a function of the transmission line configuration. A review is thus given on various transmission line configurations and tower structures used in practise.

This chapter also gives a review of transmission line parameters, definitions and theory of power system analysis. It provides a discussion on calculating the electric field for single-circuit power lines as well as the scaling of a power system.

## J.1. Power line configurations and structures

Various power line tower structures and transmission line configurations are used in practice. Detailed data on various tower structures and line configurations are given in Appendix D and E. The geometrical positioning of the phase conductors and neutral conductors in the line configuration must be known for calculation of the capacitive matrix.

Power lines are categorized in terms of the nominal operating voltage levels, i.e. such as Medium Voltage (MV) lines denoting voltage levels between 1kV and 44kV, High Voltage (HV) lines denoting voltage levels between 44kV and 220kV, Extra-High Voltage (EHV) lines denoting voltage levels between 220kV and 400kV and Ultra-High Voltage (UHV) denoting voltage levels above 400kV.

The transmission line configuration consists out of the following aspects:

- *Single / multi-circuit line topology*: Power line structures can consist out of more than one set of three phases. These power lines are called multi-circuit lines.
- *Phase configuration*: A relative, physical arrangement of the phase conductors.

- *Phase bundle topology*: The practice of using more than one conductor per phase is called bundling.
- *Conductor configuration*: The physical dimensions of the conductors.

The tower structure, i.e. tower configuration and dimensions, are dependant on the single / multi-circuit line configuration. Figure J.1(a) illustrates a typical single-circuit transmission line and Figure J.1(b) illustrates a typical double-circuit transmission line.

Figure J.2 illustrates different phase arrangements used in practice. A delta, horizontal, vertical and vertical staggered phase arrangement is illustrated respectively. These configurations are dependant on the type of tower structure used for the power line. The distance between the different phases is called the phase spacing and is dependant on the type of phase configuration used.

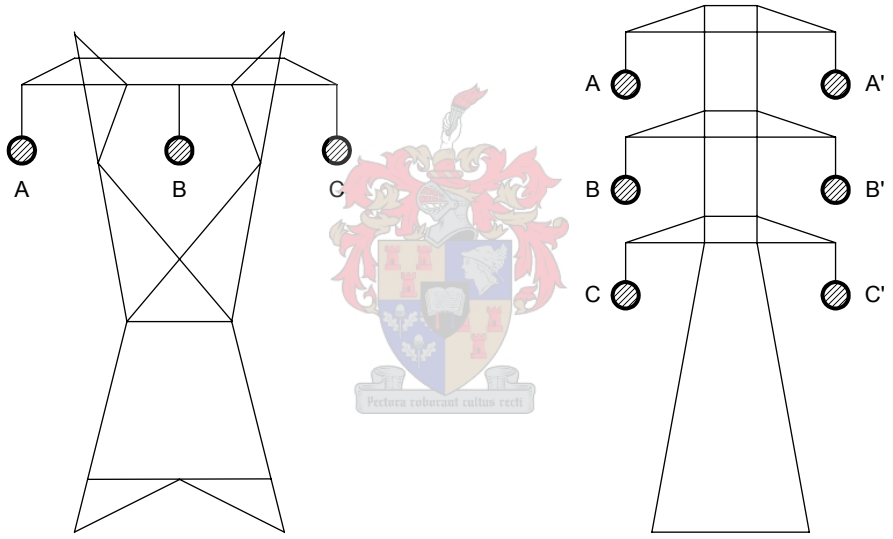


**Figure J.1: (a) A typical 132kV, single-circuit transmission line and (b) a typical 132kV, double-circuit transmission line.**

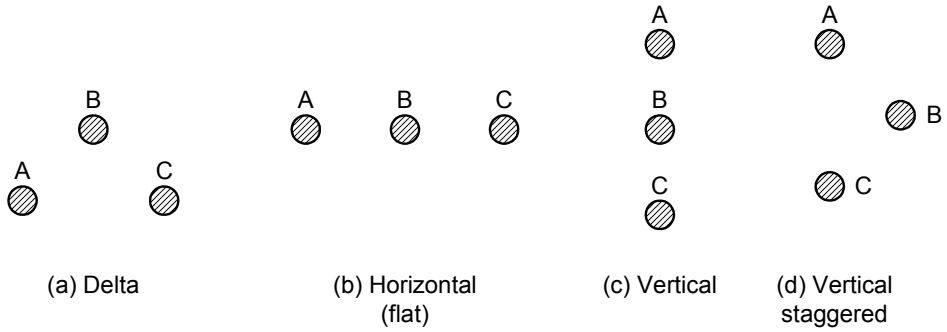


**Figure J.2: Typical phase configurations used for power lines.**

It is common practise for EHV lines to use more than one conductor per phase, a practise called *bundling*. Bundling reduces the electric field strength at the conductor surfaces, which in turn reduces or eliminates corona and its results. Bundling also reduces the series resistance of the line by increasing the Geometric Mean Radius (GMR) of the bundle. The phase spacing can also be reduced if bundled conductors are used. Section J.2.1 discusses bundling in more detail, reviewing the method used for calculating the radius of the bundle. Figure J.3 shows common HV bundles.

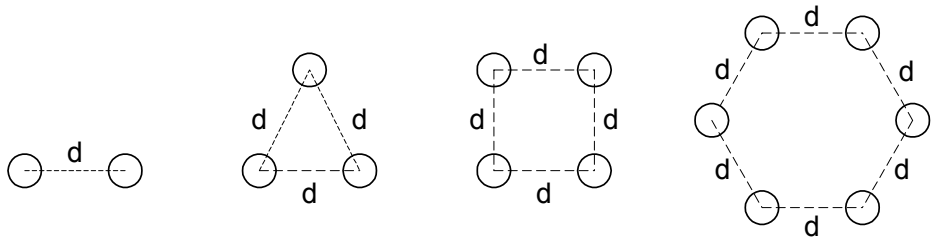


**Figure J.3: Bundle conductor configurations [11].**

Conductors used on power lines are not solid conductors. Power lines make use of what is known as stranded conductors of which Aluminium Conductor, Steel Reinforced (ACSR) is most widely used. For the calculations done in this thesis stranded conductors are replaced with an equivalent solid cylindrical conductor which has an equivalent diameter given by the GMR. Section J.2.1 discusses the evaluation of the GMR. Appendix D.2 illustrates different conductor configurations and detailed data of various conductors, i.e. GMR, mass and total area. These data are available from the cable manufactures.

## J.2. Theory of power system analysis

Transmission lines have four basic parameters namely, series resistance, series inductance, shunt capacitance and shunt conductance. Series impedance, including resistance and inductive reactance, gives rise to voltage drops along the line. Shunt capacitance gives rise to line-charging currents. Shunt conductance accounts for the leakage current at the insulators of overhead lines and through the insulation cables. The shunt conductance is usually ignored as the conductors are well isolated from each other and ground. The conductance and capacitance existing between conductors of a single-phase line or from a conductor to neutral of a three-phase line form the shunt admittance [72]. For purposes of this thesis only the shunt capacitance is discussed.

### J.2.1. Composite conductor calculations

Conductors used on power lines are not solid, but consists of layers of strands surrounding a central core and one of the most common conductor types is ACSR. It consists out of layers of aluminium stands surrounding a core of steel strands. Stranded conductors are easier to manufacture, handle and are more flexible than solid conductors. A stranded conductor is an example of a composite conductor.

For calculation purposes stranded conductors are replaced by an equivalent solid cylindrical conductor which has an equivalent diameter given by the GMR. The GMR of a stranded conductor can be interpreted as the equivalent radius of a single solid conductor with the same total surface charge as the stranded conductor. The GMR of a particular stranded conductor can be obtained from the manufacturer or can be calculated. This section gives a review on GMR calculations.

Composite conductors consist of two or more solid cylindrical sub-conductor (strands) in parallel. For simplicity it is assumed that for each conductor, the strands are identical and share the conductor current equally. Figure J.4 shows a single-phase two-conductor line consisting of two composite conductors $x$ and $y$. Conductor $x$ has $N$ identical strands, each with a radius $r_x$. Similarly, conductor $y$ consists of $M$ identical strands, each with a radius $r_y$. The *geometric mean distance* (GMD) between conductors $x$ and $y$, $D_{xy}$, is given by the relationship

$$D_{xy} = \sqrt[MN]{\prod_{k=1}^{N}\prod_{m=1'}^{M} D_{km}} \tag{J.1}$$

where $N$ is the amount of strands in conductor $x$ and $M$ is the amount of strands in conductor $y$. Associated with each strand $k$ of conductor $x$ are the $M$ distances $D_{k1}'$, $D_{k2}'$,…, $D_{kM}$ to the strands of conductor $y$. For $N$ strands in conductor $x$, there are therefore $MN$ of these distances. $D_{xy}$ is the $MN$th root of the product of $MN$ distances from the strands of conductor $x$ to the strands of conductor $y$ [11].

The *geometric mean radius* (GMR) between the strands of conductor $x$, $D_{xx}$, is given by the relationship

$$D_{xx} = \sqrt[N^2]{\prod_{k=1}^{N}\prod_{m=1}^{N} D_{km}} \tag{J.2}$$

where $N$ is the amount of strands in conductor $x$. Associated with each strand $k$ are the $N$ distances $D_{k1}$, $D_{k2}$,…, $D_{kk} = r'$,...., $D_{kN}$. $D_{xx}$ is the $N^2$ root of the product of the $N^2$ distances

between the strands of conductor $x$. For $N$ strands in conductor $x$, there are therefore $N^2$ of these distances. $D_{yy}$, the GMR of conductor $y$, is the $M^2$ root of the product of the $M^2$ distances between the strands of conductor $y$.

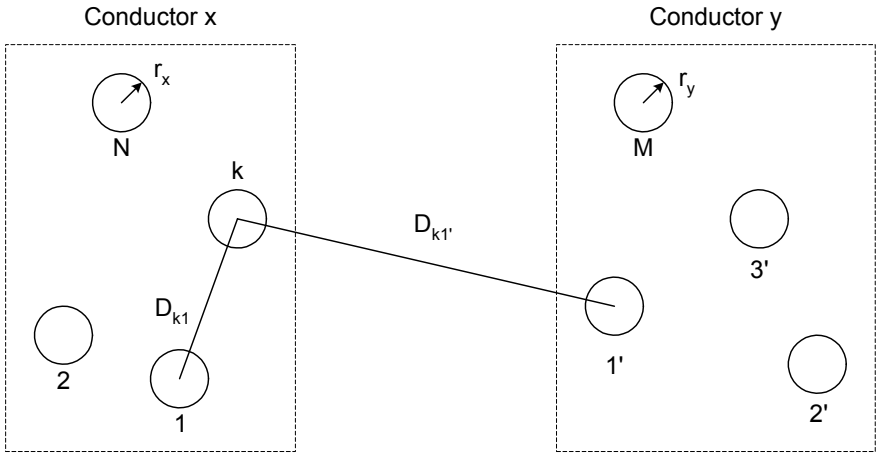


**Figure J.4: Single-phase two-conductor bundle line with composite conductors [11].**

It is seldom necessary to calculate the GMR or the GMD for standard lines. The GMR of standard conductors is provided by the conductor manufactures as illustrated in Appendix D.2. If the distances between conductors are also large compared to the distances between the strands of each conductor, then the GMD between conductors is approximately equal to the distance between conductor centres.

As stated before HV power lines usually make use of more than one conductor per phase. Figure J.3 shows common bundled conductor configurations used for EHV and UHV power lines. If the conductors are stranded and the bundle spacing $d$ is large compared to the conductor outside radius, each stranded conductor is first replaced by an equivalent solid cylindrical conductor with the GMR denoted by $D_s$. The GMR of a stranded conductor can be interpreted as the equivalent radius of a single solid conductor with the same total surface charge as the stranded conductor. The bundle is then replaced by one equivalent conductor with the GMR denoted by $D_{SL}$, given by equation (J.2), with $n$ = 2, 3, 4 or 6 as follows [11]:

Two-conductor bundle:

$$D_{SL} = \sqrt[4]{\left(D_S \times d\right)^2} = \sqrt{D_S d} \tag{J.3}$$

Three-conductor bundle:

$$D_{SL} = \sqrt[9]{\left(D_S \times d \times d\right)^3} = \sqrt[3]{D_S d^2} \tag{J.4}$$

Four-conductor bundle:

$$D_{SL} = \sqrt[16]{\left(D_S \times d \times d \times d\sqrt{2}\right)^4} = 1.091\sqrt[4]{D_S d^3} \tag{J.5}$$

Six-conductor bundle:

$$D_{SL} = \sqrt[36]{\left(D_S \times d \times d \times d\frac{\sqrt{12}}{2} \times d\frac{\sqrt{12}}{2} \times 2d\right)^6} = \sqrt[6]{6D_S d^5}\ . \tag{J.6}$$

Bundle configurations used for EHV lines consist of two, three or four conductors and UHV lines usually use six conductors per bundle. The lower voltage level lines use single stranded conductors. Equations (J.3) to (J.6) are used in Chapter 3 during the construction of transmission line configurations in software packages. It is not possible to simulate every strand, thus the GMR is needed for these simulations.

### J.2.2. Electric field and voltage: solid cylindrical conductor

The capacitance of general transmission line configurations must be calculated. This is the first step in calculating the capacitive coupling between the overhead conductors and objects near ground level, i.e. sensors.

At first the electric field of a uniformly charged, solid cylindrical conductor and the voltage between two points outside the conductor, are computed. The voltage between two conductors in an array of charged conductors is computed as well. Electric charge is a source of electric fields and electric field lines originate from positive charges and terminate at negative charges. From Gauss law the electric field strength, *E*, can be calculated [11].

Figure J.5 shows a solid cylindrical conductor with radius *r* and with charge *q* coulombs per meter (assumed positive in the figure), uniformly distributed on the conductor surface. The electric field is radial to the conductor and due to the uniform charge distribution, the electric field strength $E_x$, is constant on the cylinder. Gauss's law states that the total electric flux leaving a closed surface equals the total charge within the volume enclosed by the surface. Gauss's law is given by the relationship [11]

$$\oiint D_{\perp} ds = \oiint \varepsilon \mathrm{E}_{\perp} ds = Q_{enclosed} \tag{J.7}$$

where $\mathrm{D}_{\perp}$ denotes the normal component of electric flux density, $\mathrm{E}_{\perp}$ denotes the normal component of electric field strength, *ds* denotes the differential surface area and $Q_{enclosed}$ denotes total charge within the volume enclosed by the surface [11]. Appendix J.4 gives a detailed description of the electric field strength underneath power lines. To determine the

electric field outside the conductor, at a distance $x$ from the conductor centre, equation (J.7) is integrated, which yields [11]

$$E_x = \frac{q}{2\pi\varepsilon x} \text{ V/m} \tag{J.8}$$

where $q$ denotes the charge and for a conductor in free space $\varepsilon = \varepsilon_0 = 8.854\text{x}10^{-12}$ F/m.

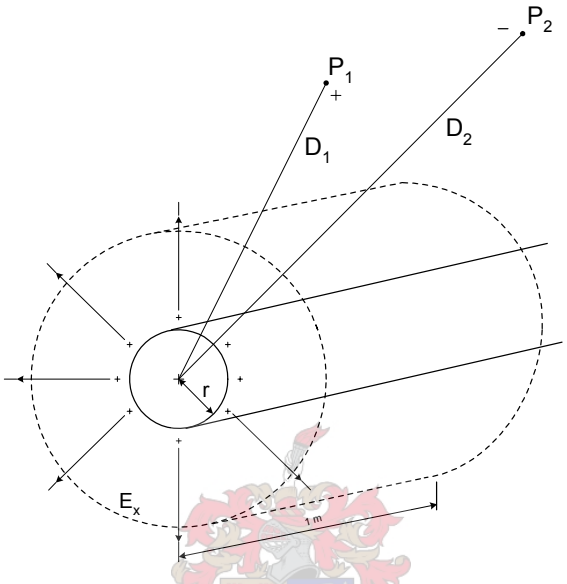


**Figure J.5: Perfectly conducting solid cylindrical conductor with uniform charge distribution [11].**

Concentric cylinders surrounding the conductor are constant potential surfaces. Using equations (J.8) and (J.7), it follows that the voltage $V_{12}$ between two points, $P_1$ and $P_2$, at distance $D_1$ and $D_2$ from the conductor centre, as shown in Figure J.5, is denoted as [11]

$$V_{12} = \int_{D_1}^{D_2} \frac{q}{2\pi\varepsilon x} = \frac{q}{2\pi\varepsilon} \ln \frac{D_2}{D_1}. \tag{J.9}$$

For AC, $V_{12}$ is a phasor voltage and $q$ is a phasor representation of a sinusoidal charge [11].

By applying equation (J.9) to the array of $M$ solid cylindrical conductors shown in Figure J.6 and using superposition, the voltage $V_{ki}$ between conductors $k$ and $i$ due to the constant potential surfaces of all the conductors is given by [11]

$$V_{ki} = \frac{1}{2\pi\varepsilon} \sum_{m=1}^{M} q_m \ln \frac{D_{im}}{D_{km}} \tag{J.10}$$

where $D_{im}$ is the distance between conductor centres $i$ and $m$, $D_{km}$ is the distance between conductor centres $k$ and $m$ and $D_{mm} = r_m$, the conductor radius, when $k = m$ or $i = m$.

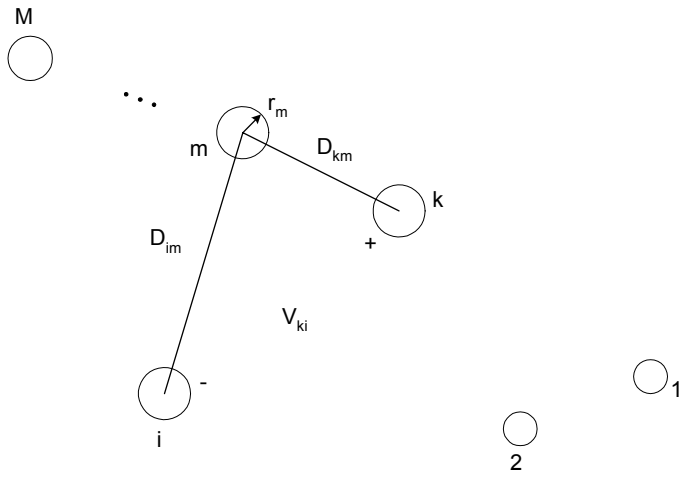


**Figure J.6: Array of *M* solid cylindrical conductors [11].**

**These results are required in determining the capacitance of transmission lines and are used in the following sections.**

### J.2.3. Power lines with neutral conductors and earth return

In this section equations are reviewed for calculation of the shunt admittance of a three-phase overhead line. Numerous assumptions are made during these calculations and these assumptions must be taken into account whenever the results are examined. These assumptions are the following [11]:

- The conductors are solid, cylindrical and have zero resistivity.
- The conductor is sufficient long so that end effects are negligible.
- The conductors are uniformly charged.
- The electric field inside the conductors is zero and the external field is perpendicular to the conductor surface.
- The distortion of the electric field in the vicinity of the other conductors, caused by the fact that the other conductors are constant potential surfaces, is negligible.
- The earth surface is approximated as a perfectly conducting horizontal plane.

When calculating line capacitance the stranded conductors can be replaced by a perfectly conducting solid cylindrical conductor with a radius equal to that of the stranded conductor's GMR.

The method of images is used to take the effect of the earth plane underneath a transmission line into account, as explained in Chapter 2.3.3. Figure J.7 illustrates a three-phase line with *N* neutral conductors, where the perfectly conducting earth plane is replaced by a separate

image conductor for each overhead conductor. The overhead conductors *a, b, c, n1, n2, ..., nN* carry charges $q_a$, $q_b$, $q_c$, $q_{n1}$,…., $q_{nN}$, and the image conductors *a', b', c', n1', n2', ..., nN'* carry charges $-q_a$, $-q_b$, $-q_c$, $-q_{n1}$,…., $-q_{nN}$. Applying equation (J.10) the voltage $V_{kk'}$ between any conductor *k* and its image conductor *k'* is given by the relationship [11]

$$V_{kk'} = \frac{2}{2\pi\varepsilon} \sum_{m=a}^{nN} q_m \ln \frac{H_{km}}{D_{km}} \tag{J.11}$$

where $D_{km}$ denotes the distance between overhead conductors *k* and *m*, $H_{km}$ denotes the distance between overhead conductor *k* and image conductor *m* and *nN* denotes the amount of neutral conductors. If $k = m$, then $D_{kk} = r_k$.

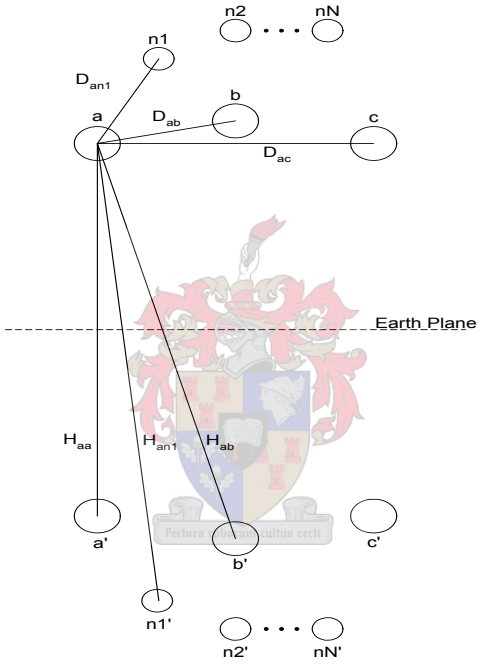


**Figure J.7: Three-phase line with neutral conductors and earth plane replaced by image conductors [11].**

By symmetry, the voltage $V_{kn}$ between conductor *k* and earth is one-half of the voltage $V_{kk'}$. This yields [11]

$$V_{kn} = \frac{1}{2} V_{kk'} = \frac{1}{2\pi\varepsilon} \sum_{m=a}^{nN} q_m \ln \frac{H_{km}}{D_{km}} \tag{J.12}$$

where

$k = a, b, c, n1, n2, ..., nN$

and

$m = a, b, c, n1, n2, ..., nN.$

Since all the neutral conductors are grounded to the earth, voltage $V_{kn}$ is given as

$$V_{kn} = 0 \qquad \textit{(J.13)}$$

for $k = n1, n2, \ldots, nN$ .

Equation (J.12) and (J.13) can be written in matrix format as [11]

$$\begin{bmatrix} \underline{V}_P \\ \mathbf{0} \end{bmatrix} = \begin{bmatrix} \boldsymbol{P}_A & \boldsymbol{P}_B \\ \boldsymbol{P}_C & \boldsymbol{P}_D \end{bmatrix} \begin{bmatrix} \boldsymbol{q}_P \\ \boldsymbol{q}_n \end{bmatrix} \qquad \text{(J.14)}$$

where $\boldsymbol{V_p}$ is the three-dimensional vector of phase-to-neutral voltages, $\boldsymbol{q_p}$ is the three-dimensional vector of phase-conductor charges and $\boldsymbol{q_n}$ is the $N$ vector of neutral conductor charges. The (3+$N$) x (3+$N$) $\boldsymbol{P}$ matrix is partitioned into four separate matrixes, i.e. $\boldsymbol{P}_A$, $\boldsymbol{P}_B$, $\boldsymbol{P}_C$ and $\boldsymbol{P}_D$, which are respectively given as

$$\boldsymbol{P}_A = \begin{bmatrix} \boldsymbol{P}_{aa} & \boldsymbol{P}_{ab} & \boldsymbol{P}_{ac} \\ \boldsymbol{P}_{ba} & \boldsymbol{P}_{bb} & \boldsymbol{P}_{bc} \\ \boldsymbol{P}_{ca} & \boldsymbol{P}_{cb} & \boldsymbol{P}_{cc} \end{bmatrix}, \qquad \text{(J.15)}$$

$$\boldsymbol{P}_B = \begin{bmatrix} \boldsymbol{P}_{an1} & \cdots & \boldsymbol{P}_{anN} \\ \boldsymbol{P}_{bn1} & \cdots & \boldsymbol{P}_{bnN} \\ \boldsymbol{P}_{cn1} & \cdots & \boldsymbol{P}_{cnN} \end{bmatrix}, \qquad \text{(J.16)}$$

$$\boldsymbol{P}_C = \begin{bmatrix} \boldsymbol{P}_{n1a} & \boldsymbol{P}_{n1b} & \boldsymbol{P}_{n1c} \\ \vdots & & \\ \boldsymbol{P}_{nNa} & \boldsymbol{P}_{nNb} & \boldsymbol{P}_{nNc} \end{bmatrix} \qquad \text{(J.17)}$$

and

$$\boldsymbol{P}_D = \begin{bmatrix} \boldsymbol{P}_{n1n1} & \cdots & \boldsymbol{P}_{n1nN} \\ & & \\ \boldsymbol{P}_{nNn1} & \cdots & \boldsymbol{P}_{nNnN} \end{bmatrix}. \qquad \text{(J.18)}$$

The elements of the above $\boldsymbol{P}$ matrixes are denoted as [11]

$$P_{km} = \frac{1}{2\pi\varepsilon} \ln \frac{H_{km}}{D_{km}} \quad \text{m/F} \qquad \text{(J.19)}$$

where

$k = a, b, c, n1, n2, \ldots, nN$

and

$m = a, b, c, n1, n2, \ldots, nN.$

From Sarma and Glover the phase-to-neutral voltages can be denoted as

$$\boldsymbol{V}_P = \left( \boldsymbol{P}_A - \boldsymbol{P}_B \boldsymbol{P}_D^{-1} \boldsymbol{P}_C \right)^{-1} \boldsymbol{q}_P \ . \qquad \text{(J.20)}$$

Equation (J.20) can be rewritten as [11]

$$\boldsymbol{q}_P = \boldsymbol{C}_P \boldsymbol{V}_P \tag{J.21}$$

where

$$\boldsymbol{C}_P = \left( \boldsymbol{P}_A - \boldsymbol{P}_B \boldsymbol{P}_D^{-1} \boldsymbol{P}_C \right)^{-1} \quad \text{F/m.} \tag{J.22}$$

Equation (J.21) relates the phase-conductor charges to the phase-to-neutral voltages. The 3x3 matrix of phase capacitances $\boldsymbol{C_p}$ elements are denoted as [11]

$$\boldsymbol{C}_P = \begin{bmatrix} C_{aa} & C_{ab} & C_{ac} \\ C_{ab} & C_{bb} & C_{bc} \\ C_{ac} & C_{bc} & C_{cc} \end{bmatrix} \quad \text{F/m} \tag{J.23}$$

where $\boldsymbol{C_p}$ is a matrix symmetrical around both diagonals, whose diagonal terms $C_{aa}$, $C_{bb}$, $C_{cc}$ are positive and whose off-diagonal terms $C_{ab}$, $C_{bc}$, $C_{ac}$ are negative. This indicates that when a positive line-to-neutral voltage is applied to one phase, a positive charge is induced on that phase and negative charges are induced on the other phases [11].

The results obtained in this section are used to determine the matrix of capacitance phases for a three-phase transmission line with $N$ neutral conductors. Equation (J.10) can be used to calculate the voltage $V_{ki}$ between conductors $k$ and $i$ for any line configuration.

### J.3. Calculation of electric fields for single-circuit power lines [38]

The electric field in the vicinity of an AC power line is calculated with the assumption that there is no free charge in space and that the earth plane is a perfect conductor. The permittivity of the air surrounding power lines is for all practical reasons independent from weather conditions and thus is equal to the permittivity of free space, $\varepsilon_0 = 8.854 \text{x} 10^{-12}$ F/m.

The phasor charges **Q** present on the phase and neutral conductors are determined by applying the phasor voltages **V** and Maxwell's potential coefficient matrix **P** to the equation

$$\boldsymbol{Q} = \boldsymbol{P}^{-1} \boldsymbol{V} \ . \tag{J.24}$$

where the elements of the **P** matrix is denoted by equation (J.19).

The resulting conductor charges are all phasors, which implies that equation (J.24) can be written for both real and imaginary charges. The charges on each of the sub-conductors of a bundled phase conductor can be determined by solving equation (J.24).

For a bundled phase conductor *a*, with $N_a$ sub-conductors and with charge $\tilde{Q}_a$ C/m present on its equivalent solid cylindrical conductor, the charge per sub-conductor is $\tilde{Q}_a / N_a$ .

Once the real and imaginary components of the charge present on each phase sub-conductor and on each neutral conductor is known, the electric field at a point, *s*, with coordinates ($x_s$, $y_s$) in space can be calculated. The field, due to the charge on a sub-conductor *a1* and to its image inside the earth can be calculated by using Figure J.8 [38].

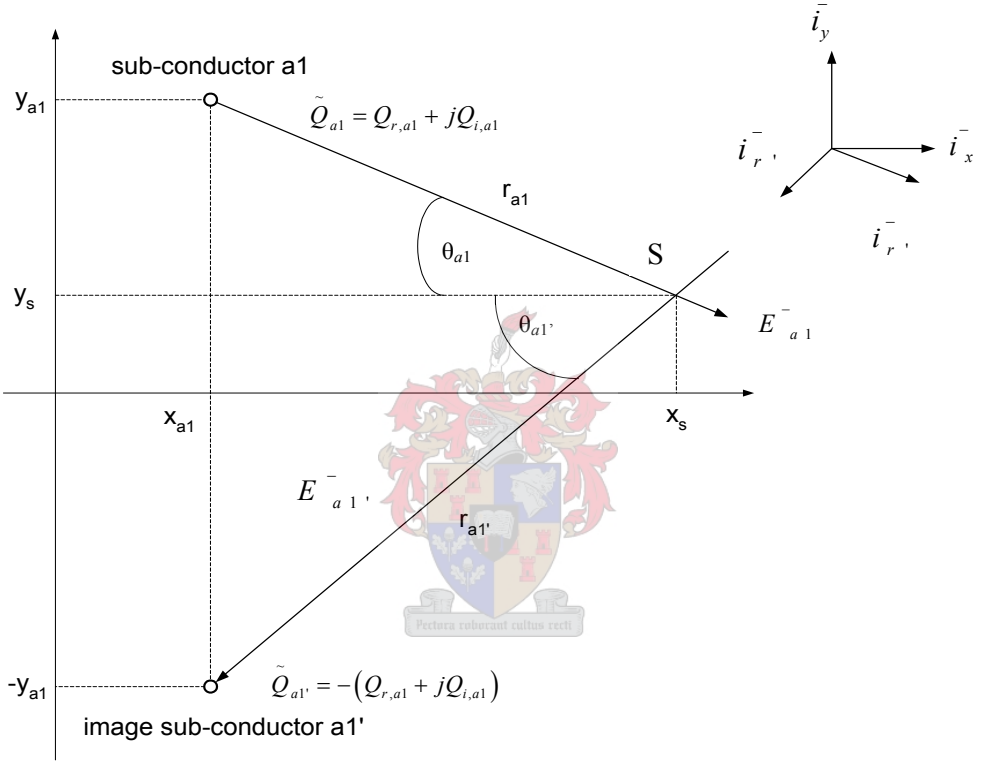


**Figure J.8: Electric field at point *s* caused by a sub-conductor and its image [38].**

The electric field $\bar{E}_{a1}$ due to the charge of an overhead sub-conductor *a*1 and its image conductor *a1'* is denoted as [40]

$$\bar{E}_{a1} = \left(\tilde{E}_{x,a1} + \tilde{E}_{x,a1'}\right)\bar{i}_x + \left(\tilde{E}_{y,a1} + \tilde{E}_{y,a1'}\right)\bar{i}_y = \tilde{E}_{x,a1}\,\bar{i}_x + \tilde{E}_{y,a1}\,\bar{i}_y \qquad \text{(J.25)}$$

where $\bar{i}_x$ and $\bar{i}_y$ are the unit vectors along the horizontal and vertical axes. $\tilde{E}_{x,a1}$ and $\tilde{E}_{y,a1}$ represent the electric field vector components due to both *a1* and its image conductor *a1'*. The horizontal and vertical components are respectively given by [40]

$$\tilde{E}_{x,a1} = \frac{\left(Q_{r,a1} + jQ_{i,a1}\right)\left(x_s - x_{a1}\right)}{2\pi\varepsilon_0\left[\left(x_{a1} - x_s\right)^2 + \left(y_{a1} - y_s\right)^2\right]} - \frac{\left(Q_{r,a1} + jQ_{i,a1}\right)\left(x_s - x_{a1}\right)}{2\pi\varepsilon_0\left[\left(x_{a1} - x_s\right)^2 + \left(y_{a1} + y_s\right)^2\right]} \tag{J.26}$$

and

$$\tilde{E}_{y,a1} = \frac{-\left(Q_{r,a1} + jQ_{i,a1}\right)\left(y_{a1} - y_s\right)}{2\pi\varepsilon_0\left[\left(x_{a1} - x_s\right)^2 + \left(y_{a1} - y_s\right)^2\right]} - \frac{\left(Q_{r,a1} + jQ_{i,a1}\right)\left(y_{a1} + y_s\right)}{2\pi\varepsilon_0\left[\left(x_{a1} - x_s\right)^2 + \left(y_{a1} + y_s\right)^2\right]} \; . \tag{J.27}$$

For a power line with more than one phase conductor, i.e. a three-phase line, superposition is used to calculate the total horizontal component $\tilde{E}_x$ and the total vertical component $\tilde{E}_y$ of the electric field vector at point *s* due to all the charge carrying conductors in the power line.

It is assumed that phase conductor *a* has $N_a$ sub-conductors, phase conductor *b* has $N_b$ sub-conductors, phase conductor *c* has $N_c$ sub-conductors and that there are *N* neutral conductors so that $\tilde{E}_x$ and $\tilde{E}_y$ can be denoted as [38]

$$\tilde{E}_x = \sum_{m=a1}^{nN} \tilde{E}_{x,m} \tag{J.28}$$

and

$$\tilde{E}_y = \sum_{m=a1}^{nN} \tilde{E}_{y,m} \tag{J.29}$$

where $m$ = ($a1$, $a2$,.., $aN_a$, $b1$, $b2$,…, $bN_b$, $c1$, $c2$,…, $cN_c$, $n1$, $n2$,…, $nN_n$). Each of these components is a phasor, expressed by real and imaginary parts denoted as [38]

$$\tilde{E}_x = E_{rx} + jE_{ix} \tag{J.30}$$

and

$$\tilde{E}_y = E_{ry} + jE_{iy} \; . \tag{J.31}$$

The amplitude of the horizontal and vertical component is respectively given by [38]

$$E_x = \sqrt{\left(E_{rx}\right)^2 + \left(E_{ix}\right)^2} \tag{J.32}$$

and

$$E_y = \sqrt{\left(E_{ry}\right)^2 + \left(E_{iy}\right)^2} \; . \tag{J.33}$$

The magnitude of the resultant electric field at point *s* is given by [38]

$$E_r = \sqrt{(E_x)^2 + (E_y)^2} \quad . \tag{J.34}$$

The calculation of the electric field profile is a considerable simplification of the general method of the calculation [38]. If the electric field is calculated near the ground for points along a section perpendicular to the power line, the lateral profile of the power line electric field is obtained. The analysis reviewed in this section is used to obtain a factor relating the different coupling vectors between the transmission lines and the sensors. The analysis above can be extended to include double circuit lines [38].

### J.4. Scaling of the power system model [10]

The electric field derived from a power system at any point in free space can be expressed by the analytical technique; therefore it can be used to examine the effects of scaling of the power system geometry. Gerrard investigated the effects of scaling as, for laboratory investigations, it is frequently impossible to construct a full size model of a power system [10].

A conductor in the full sized system is centred at point ($x_n$, $y_n$) and has diameter $d_n$ and a peak voltage $V_{pn}$. A conductor in the scale system is centred at ($x_n^*$, $y_n^*$), has diameter $d_n^*$ and a peak voltage $V_{pn}^*$. The relationship between the geometry of the two systems is given by the scale factor, $K$ where $x_n = Kx_n^*$, $y_n = Ky_n^*$ and $d_n = Kd_n^*$. Point $P(x_p,y_p)$ in the full sized system is equivalent to point $P^*(x_p^*, y_p^*)$ in the scaled system, where $x_p = Kx_p^*$, $y_p = Ky_p^*$.

For a single conductor, the Maxwell Potential Coefficients $C$ are reduced to a one element matrix and the equivalent line charge in the scaled system $\tilde{Q}^*$ is denoted as

$$\tilde{Q}^* = \frac{\tilde{V}_{P1}^*}{2\pi\varepsilon} \ln\left(\frac{4y_1^*}{d_1^*}\right) \quad . \tag{J.35}$$

Substituting for $y_1^*$ and $d_1^*$ in the above equation gives

$$\tilde{Q}^* = \frac{\tilde{V}_{P1}^*}{2\pi\varepsilon} \ln\left(\frac{4\,y_1/K}{d_1/K}\right). \tag{J.36}$$

Comparing equations (J.35) and (J.36) shows that the equivalent line charge in the scaled system is determined by the scaled voltage, $\tilde{V}_{P1}^*$, and not by the scaled dimensions. Writing the horizontal component of equation (J.27) in terms of the scaled parameters and substituting

for $x_p^*$, $x_n^*$, $y_p^*$ and $y_n^*$ gives the horizontal component of the electric field $\tilde{E}^*_{xpn}$ in the scale model as

$$\tilde{E}^*_{xp} = \frac{\left(Q^*_{rn} + jQ^*_{in}\right)\left(\frac{x_p}{K} - \frac{x_n}{K}\right)}{2\pi\varepsilon\left[\left(\frac{x_n}{K} - \frac{x_p}{K}\right)^2 + \left(\frac{y_n}{K} - \frac{y_p}{K}\right)^2\right]} - \frac{\left(Q^*_{rn} + jQ^*_{in}\right)\left(\frac{x_p}{K} - \frac{x_n}{K}\right)}{2\pi\varepsilon\left[\left(\frac{x_n}{K} - \frac{x_p}{K}\right)^2 + \left(\frac{y_n}{K} + \frac{y_p}{K}\right)^2\right]} \quad . \qquad \text{(J.37)}$$

The horizontal component of equation (J.37) is identical to equation (J.27) if

$$\tilde{Q}_n = K\,\tilde{Q}^*_n \, .$$

This may be achieved by scaling the voltage $\tilde{V}_n$ by the factor $K$. A similar analysis can be applied to equation (J.19) and to the vertical component of equation (J.27) with identical results. Scaling of the system geometry and voltage, by the same amount, results in the absolute magnitudes and directions of the fields, at equivalent points to be identical in the full sized systems and the scaled model. Chapter 8 uses the method of scaling down a full size power system to a model size that could be constructed in the laboratory. This section proved that if the voltage and the geometry of a full size power system are scaled down by the same factor, the electric fields, and hence the capacitive coupling, of the power line will stay the same.



## J.5. Conclusion

Feser & Pfaff [3] indicated that for the measurement of a overhead voltage $v_{HV}(t)$, with an electric field sensor probe, the electric field sensor has to be calibrated for the specific measuring place. As the calibration voltage $V_o$ is related to the electric field strength $E_{so}$, the unknown voltage $v_{HV}(t)$ is given by the calibration factor $k=V_o/E_{so}$ and the measured field $E(t)$ as

$$v_{HV}(t) = kE(t) \, . \qquad \text{(J.38)}$$

As the measured voltage $v_m(t)$ is linear proportional to the overhead power line voltage $v_{HV}(t)$, equation (J.38) can be written as

$$v_m(t) = akE(t) \, . \qquad \text{(J.39)}$$

Thus the measured voltage is a factor $ak$ of the electric field underneath a power line. By using the electric field equations the measured voltage for each sensor can thus be obtained.

By comparing the electric field at the three different sensors, the calibration factor between the different coupling vectors can be obtained.

This chapter stated the theory behind calculating the capacitance phase matrix of a power system as well as calculating the electric field profile underneath a power system. The concept of scaling a power system will be used in construction of a high voltage test facility.

Capacitive coupling tests in this thesis are done on single-circuit, horizontal line configurations. The transmission line configuration determines how many sensors must be used and the positioning of the sensors beneath the transmission line. For double-circuit lines more capacitive sensors will be required for capacitive coupling tests. Other phase configurations will also result in different positioning of the sensors. Electric field profiles underneath power lines can be helpful in determining the optimal placement of these sensors underneath the power lines.